

MODELING EMERGING SOLAR CELL MATERIALS AND DEVICES

By

Non Thongprong

A DISSERTATION

Submitted to  
Michigan State University  
in partial fulfillment of the requirements  
for the degree of

Physics – Doctor of Philosophy

2017

ProQuest Number: 10283324

All rights reserved

INFORMATION TO ALL USERS

The quality of this reproduction is dependent upon the quality of the copy submitted.

In the unlikely event that the author did not send a complete manuscript and there are missing pages, these will be noted. Also, if material had to be removed, a note will indicate the deletion.



ProQuest 10283324

Published by ProQuest LLC (2017). Copyright of the Dissertation is held by the Author.

All rights reserved.

This work is protected against unauthorized copying under Title 17, United States Code  
Microform Edition © ProQuest LLC.

ProQuest LLC.  
789 East Eisenhower Parkway  
P.O. Box 1346  
Ann Arbor, MI 48106 – 1346

## ABSTRACT

### MODELING EMERGING SOLAR CELL MATERIALS AND DEVICES

By

Non Thongprong

Organic photovoltaics (OPVs) and perovskite solar cells are emerging classes of solar cell that are promising for clean energy alternatives to fossil fuels. Understanding fundamental physics of these materials is crucial for improving their energy conversion efficiencies and promoting them to practical applications.

Current density-voltage (JV) curves; which are important indicators of OPV efficiency, have direct connections to many fundamental properties of solar cells. They can be described by the Shockley diode equation, resulting in fitting parameters; series and parallel resistance ( $R_s$  and  $R_p$ ), diode saturation current ( $J_0$ ) and ideality factor ( $n$ ). However, the Shockley equation was developed specifically for inorganic p-n junction diodes, so it lacks physical meanings when it is applied to OPVs. Hence, the purposes of this work are to understand the fundamental physics of OPVs and to develop new diode equations in the same form as the Shockley equation that are based on OPV physics.

We develop a numerical drift-diffusion simulation model to study bilayer OPVs, which will be called the drift-diffusion for bilayer interface (DD-BI) model. The model solves Poisson, drift-diffusion and current-continuity equations self-consistently for charge densities and potential profiles of a bilayer device with an organic heterojunction interface described by the GWWF model. We also derive new diode equations that have JV curves consistent with the DD-BI model and thus will be called self-consistent diode (SCD) equations.

Using the DD-BI and the SCD model allows us to understand working principles of bilayer OPVs and physical definitions of the Shockley parameters. Due to low carrier mobilities in OPVs, space charge accumulation is common especially near the interface and electrodes. Hence, quasi-Fermi levels (i.e. chemical potentials), which depend on charge densities, are modified around the interface, resulting in a splitting of quasi-Fermi levels that works as

a driving potential for the heterojunction diode. This brings about the meaning of  $R_s$  as the resistance that gives rise to the diode voltage equal to the interface quasi-Fermi level splitting instead of the voltage between the electrodes. Quasi-Fermi levels that drop near the electrodes because of unmatched electrode work functions or due to charge injection can also increase  $R_s$ . Furthermore, we are able to study dissociation and recombination rates of bound charge pairs across the interface (i.e. polaron pairs or PPs) and arrive at the physical meaning of  $R_p$  as recombination resistance of PPs. In the dark, PP density is very low, so  $R_p$  is possibly caused by a tunneling leakage current at the interface. Ideality factors are parameters that depend on the split of quasi-Fermi levels and the ratio of recombination rate to recombination rate at equilibrium. Even though they are related to trap characteristics as normally understood, their relations are complicated and careful interpretations of fitted ideality factors are needed. Our models are successfully applied to actual devices, and useful physics can be deduced, for example differences between the Shockley parameters under dark and illumination conditions.

Another purpose of this thesis is to study electronic properties of CsSnBr<sub>3</sub> perovskite and processes of growing the perovskite film using an epitaxy technique. Calculation results using density functional theory reveal that a CsSnBr<sub>3</sub> film that is grown on a NaCl(100) substrate can undergo a phase transition to CsSn<sub>2</sub>Br<sub>5</sub>, which is a wide-bandgap semiconductor material. Actual mechanisms of the transition and the interface between CsSnBr<sub>3</sub> and CsSn<sub>2</sub>Br<sub>5</sub> are interesting for future studies.

## ACKNOWLEDGEMENTS

Every time I look back to the past of my life, I am surprised by how far I have journeyed the academic path and how much I have succeeded. I would not be here if I had not had support from the following persons.

First of all, I would like to thank my advisor, professor Duxbury, for understanding me, correcting my mistakes, and supporting me academically and financially. I would like to thank all members in my guidance committee: professor Pengpeng Zhang for letting me work in her lab for a semester; professor Richard Lunt for being a great collaborator; professor Norman Birge and professor Mark Dykman for being very good teachers in the courses I took and guiding my PhD goals. I would like to thank all professors in the department and the department of Physics and Astronomy for being a great place to study for PhD.

I would like express great gratitude to the Development and Promotion of Science and Technology Talents Project (DPST), which is a program supported by the Royal Thai Government, for recruiting me into this program and for funding me since high school.

I would also like to thank Lili Wang, who is a postdoc in Professor Lunt's group, and Peggy Young, who works with Dr Lunt as well. It has been pleasure to work with you two. Thank you, Gift Kanokkorn Pimcharoen, for giving me the prototype of the numerical model. I would like to mention David Miller and my Thai friend; Thanaphong Phongpreecha, who give me advice about doing DFT simulations in VASP. Thank you all my friends; Dan Olds, Jenny Portman, Bin, Xukun, Brian, Connor and Joe Williams, who make the fourth floor of BPS building a wonderful place to work in.

Lastly, I could not say thanks enough to my mom and dad, who have been raising and taking care of me even when we are thousands of miles away. I would also like to thank all Thai friends, Thai Student Association and Office of Educational Affairs at Royal Thai Embassy in Washington DC for helping me through the years at MSU.

## TABLE OF CONTENTS

LIST OF TABLES . . . . .	viii
LIST OF FIGURES . . . . .	ix
KEY TO ABBREVIATIONS . . . . .	xvii
CHAPTER 1 BACKGROUND AND MOTIVATION . . . . .	1
1.1 Global Warming and the Need for Solar Energy Technologies . . . . .	1
1.2 Introduction to Organic Photovoltaics . . . . .	4
1.3 My Contributions . . . . .	9
1.4 Shockley Equation and Equivalent Electrical Circuit Model . . . . .	10
1.5 Efficiency parameters . . . . .	12
1.6 GWWF Model . . . . .	14
1.7 Shockley-Read-Hall Recombination . . . . .	19
1.8 Shockley-Read-Hall Recombination with Exponential Trap Distributions . .	21
1.9 Dissociation and Recombination Rates of Polaron Pairs . . . . .	24
1.10 Overview . . . . .	25
CHAPTER 2 ANALYTICAL MODEL WITH SPACE CHARGES . . . . .	28
2.1 Self-Consistence Ideal Diode (SCD) Equations . . . . .	28
2.1.1 The f-f Recombination . . . . .	29
2.1.2 The f-t Recombination . . . . .	30
2.1.3 The f-f and f-t Recombination . . . . .	32
2.1.4 The SRH Recombination . . . . .	32
2.2 Diode Voltage, Series and Parallel Resistances . . . . .	33
2.3 Definition of Illumination Conditions . . . . .	35
2.4 Conclusions . . . . .	36
CHAPTER 3 NUMERICAL MODEL . . . . .	37
3.1 the Drift-Diffusion model for Bilayer Interfaces (DD-BI model) . . . . .	37
3.2 Conclusions . . . . .	44
CHAPTER 4 PHYSICS OF OPVS . . . . .	46
4.1 The Differences Between the Current Models and the GWWF Model . . . . .	46
4.1.1 Introduction . . . . .	46
4.1.2 Simulation Details . . . . .	47
4.1.3 Results and Discussion . . . . .	49
4.1.4 Strategies to Improve the GWWF Model . . . . .	54
4.2 Effects of Carrier Mobilities . . . . .	56
4.2.1 Space charge effects and quasi-Fermi levels splitting . . . . .	58
4.2.2 Effect of mobility on space charges . . . . .	60
4.2.3 Dissociation and recombination of polaron pairs: The parallel resistance	61

4.2.4	Effect of mobility on the series resistance . . . . .	64
4.3	Effects of Injection Barriers . . . . .	68
4.3.1	JV Characteristic Response with Varied Injection Barriers . . . . .	68
4.3.2	Reduced Built-in Potential from High Injection Barriers . . . . .	70
4.3.3	Unaffected Interface Densities: Unaffected $V_{oc}$ . . . . .	72
4.4	Metal/Organic Semiconductor Contact . . . . .	73
4.4.1	Mott-Schottky Model With Vacuum Level Shift . . . . .	74
4.4.2	Integer Charge Transfer (ICT) Model . . . . .	76
4.4.3	Organic/Metal Interfaces Under Illumination . . . . .	78
4.4.4	Organic/Metal Interfaces In the Dark . . . . .	81
4.4.5	Components of Series Resistance . . . . .	82
4.4.6	Choosing the Anode and the Cathode . . . . .	85
4.5	Ideality Factor and Trap-assisted Recombination . . . . .	86
4.6	Comparison between the SRH and the f-t Recombination . . . . .	93
4.7	Conclusions . . . . .	97

CHAPTER 5	INTERPRETATION OF SHOCKLEY PARAMETERS : DARK VER-	
	SUS LIGHT . . . . .	100
5.1	Organic Salt Photovoltaic Devices . . . . .	100
5.2	Effects of the Shockley Parameters on Dark JV curves . . . . .	102
5.3	Effects of the Shockley Parameters on illuminated JV curves . . . . .	106
5.4	Parallel Resistance in the Dark . . . . .	108
5.4.1	Trap-to-trap Recombination as the Dark Leakage Current . . . . .	109
5.4.2	Simulating the CyTRIS:C <sub>60</sub> Device . . . . .	110
5.4.3	Including a Constant Dark Parallel Resistance in the DD-BI and the SCD models. . . . .	115
5.5	Complete Equivalent Electrical Circuit Model . . . . .	118
5.5.1	Total Parallel Resistance under Illumination Conditions . . . . .	120
5.6	Shockley Parameters: Dark Versus Light . . . . .	121
5.6.1	Diode Saturation Current ( $J_0$ ) . . . . .	122
5.6.2	Series Resistance ( $R_s$ ) . . . . .	123
5.6.3	Ideality Factor (n) . . . . .	124
5.6.4	Parallel Resistance ( $R_p$ ) . . . . .	125
5.6.5	Errors of Using Dark and Illumination Shockley Parameters Inter-changeably . . . . .	125
5.7	Conclusions . . . . .	126
CHAPTER 6	<i>AB INITIO</i> CALCULATION OF AN EPITAXIAL PEROVSKITE . .	128
6.1	Crystal Structures . . . . .	129
6.1.1	Cubic Perovskite . . . . .	129
6.1.2	CsSn <sub>2</sub> Br <sub>5</sub> Structure . . . . .	131
6.2	Band Structure and Density of States Calculations of CsSnBr <sub>3</sub> and CsSn <sub>2</sub> Br <sub>5</sub> . . . . .	133
6.2.1	Computational Details . . . . .	134
6.2.2	The PBE Calculations . . . . .	137
6.2.2.1	CsSnBr <sub>3</sub> Bands and DOS . . . . .	137

6.2.2.2	CsSn <sub>2</sub> Br <sub>5</sub> Bands and DOS . . . . .	137
6.2.3	The HSE06 Calculations . . . . .	140
6.2.4	Summary and Discussion of Band Gaps . . . . .	142
6.3	Adsorption of the Precursor Atoms Onto the NaCl(100) Surface . . . . .	143
6.4	Effects of the NaCl Substrate on the CsSnBr <sub>3</sub> band structure . . . . .	145
6.5	CsSnBr <sub>3</sub> Film Growing Processes: Layer by Layer Deposition . . . . .	148
6.6	Useful Research Directions : Heteroepitaxy, Critical Thickness and Phase Transition . . . . .	151
6.7	Conclusions . . . . .	152
CHAPTER 7 CONCLUSIONS AND OUTLOOKS . . . . .		154
7.1	Conclusions . . . . .	154
7.2	Outlook . . . . .	158
APPENDIX . . . . .		159
BIBLIOGRAPHY . . . . .		169

## LIST OF TABLES

Table 4.1: Summary of parameters used in the comparison between the GWWF model and the models developed in this study. . . . .	48
Table 4.2: Four cases of GWWF calculations with improved values of $\delta_D$ , $\delta_A$ , $F_I$ and $R_s$ to include space charge effects. . . . .	54
Table 4.3: Summary of parameters used in simulations of P3HT:PCBM bilayer solar cells, with hole mobility as the independent variable . . . . .	57
Table 4.4: Parameters indicating power conversion efficiency; short circuit current ( $J_{sc}$ ), open circuit voltage ( $V_{oc}$ ), and fill factor ( $FF$ ), of the P3HT:PCBM bilayer solar cells with different P3HT hole mobility, obtained from figure 4.6(a). . . . .	58
Table 4.5: Summary of parameters used to study effects of cathode injection barriers $\phi_c$	69
Table 4.6: Summary of parameters used to study effects of hole characteristic trap temperature ( $T_{t,D}$ ) in a P3HT:PCBM bilayer OPV. . . . .	89
Table 4.7: Dependence of device parameters; $J_{sc}$ , $V_{oc}$ and FF, on hole characteristic trap temperature ( $T_{t,D}$ ). . . . .	89
Table 4.8: Summary of the simulation parameters used in the comparison between the SRH recombination (Eq. 1.43) and the f-t recombination (Eq. 1.8). . . . .	94
Table 4.9: Comparisons of the $J_{sc}$ , $V_{oc}$ and $FF$ values between the devices having $R_{SRH}$ (Eq. 1.43) and $R_{f-t}$ (Eq. 1.8) as the interface recombination. The values are measured from the JV curves in Fig. 4.33, and the devices are described by Table 4.8. . . . .	95
Table 5.1: Summary of parameters used to study effects of the trap-to-trap recombination ( $R_{t-t}$ ) in terms of the effective mobility $\mu_{tunn}$ in the CyTRIS:C <sub>60</sub> device[1]. . . . .	112
Table 6.1: Summary of the band gap values and lattice parameters of CsSnBr <sub>3</sub> and CsSn <sub>2</sub> Br <sub>5</sub> . . . . .	142
Table 6.2: Resulting adsorption energies ( $E_{ads}$ ) and perpendicular distances in the study of adsorption of Cs, Sn and Br precursor atoms on the NaCl(100) surface. . . . .	145

## LIST OF FIGURES

<p>Figure 1.1: Energy band diagram and working principles of typical OPVs showing several important steps: (1) exciton generation; (2) exciton diffusion; (3) forming of a charge transfer exciton or a polaron pair (PP); (4) dissociation of PP; (5) charge transport and collection. <i>Adapted from [2, 3].</i></p> <p>Figure 1.2: Equivalent electrical circuit with single diode for a solar cell . . . . .</p> <p>Figure 1.3: Equivalent electrical circuit with double diode for a solar cell . . . . .</p> <p>Figure 1.4: Example of JV characteristic and output power versus voltage of a solar cell with an illustration of squareness of the JV curve. . . . .</p> <p>Figure 1.5: Energy level diagram and possible interactions occurring at the heterointerface between the active layers of a bilayer organic solar cell as proposed by GWWF. <i>Adapted from[4]</i></p> <p>Figure 1.6: Diagram showing the four processes constituting the total Shockley-Read-Hall recombination: electron capture rate (<math>r_{nc}</math>); electron emission rate (<math>r_{ne}</math>); hole capture rate (<math>r_{pc}</math>); and hole emission rate (<math>r_{pe}</math>) . . . . .</p> <p>Figure 1.7: Energy band diagram of an organic semiconductor showing exponential tail state distributions from the LUMO (<math>g_n(E)</math>) and from the HOMO (<math>g_p(E)</math>) that are filled with trapped electrons and holes up to <math>E_{fn}</math> and <math>E_{fp}</math> respectively. . . . .</p> <p>Figure 1.8: Total SRH recombination at the D/A interface as a result of net capture and emission of the interface charges (<math>n_I</math> and <math>p_I</math>) by the interface donor trapped holes and the interface acceptor trapped electrons having energies <math>E_{tp}</math> and <math>E_{tn}</math> respectively. . . . .</p> <p>Figure 2.1: Schematic flow of the constant exciton current (<math>qJ_X</math>) through the PP processes at the interface resulting in the photo-current <math>qJ_X\eta_{PPd}</math> and the recombined exciton current (<math>qJ_X(1-\eta_{PPd})</math>) that is flowing through <math>R_p</math>.</p> <p>Figure 3.1: Flowchart of the numerical DD-BI model. . . . .</p> <p>Figure 4.1: Comparison of JV characteristics generated by the DD-BI model (symbol), the SCD equation in Equation 2.14 (solid line), the GWWF model with <math>\delta_D = 0.9</math> and <math>\delta_A = 0.1</math> (dashed line) and the GWWF model with <math>\delta_D = 0.5</math> and <math>\delta_A = 0.5</math> (dashed and dotted line).</p>	<p>6</p> <p>11</p> <p>12</p> <p>13</p> <p>14</p> <p>19</p> <p>22</p> <p>24</p> <p>35</p> <p>38</p> <p>49</p>
--	--

Figure 4.2: Comparison of JV characteristics generated by the DD-BI model (symbol), the SCD equation in Equation 2.14 (solid line), the GWWF model with $\delta_D = 0.9$ and $\delta_A = 0.1$ (dashed line) and the GWWF model with $\delta_D = 0.5$ and $\delta_A = 0.5$ (dashed and dotted line) for the devices with $\phi_a/\phi_c$ equal to (a) 0.1eV/0.3eV, (b) 0.2eV/0.3eV and (c) 0.3eV/0.3eV. . . . .	49
Figure 4.3: (a) Interface hole ( $p_I$ ) and electron ( $n_I$ ) densities versus the applied voltage calculated by the DD-BI model (filled symbols) and the equations used by GWWF (Eqs. 1.12 and 1.13)(open symbols) that have fractions of potential dropped $\delta_D$ and $\delta_A$ shown in figure (b) as their arguments. . . . .	51
Figure 4.4: Graphs of the interface electric field strengths ( $F_I$ ), polaron pair dissociation rates and probabilities ( $k_{PPd}$ and $\eta_{PPd}$ ) of the device with $\phi_a/\phi_c = 0.1eV/0.6eV$ calculated by the DD-BI models (black), the GWWF model with $\delta_D/\delta_A = 0.9/0.1$ (red) and the GWWF model with $\delta_D$ and $\delta_A$ as a function of $V_a$ derived from the DD-BI model(green). . . . .	52
Figure 4.5: Comparisons of JV characteristics calculated by the DD-BI model, the SCD model and the four cases of modified GWWF calculations that are summarized in Table 4.2, in the devices with $\phi_a/\phi_c$ equal to (a) 0.1eV/0.6eV, (2) 0.0eV/0.0eV and (3) 0.3eV/0.3eV. The values of the fitted $R_s$ that are used in case 4 are written in each plot. . . . .	55
Figure 4.6: (a) J-V curves under illumination conditions of P3HT:PCBM bilayer photovoltaic cells and (b) $\ln J  - V$ curves of the same devices under dark conditions. Parameters used in these simulations are in table 4.3. . . . .	57
Figure 4.7: (a) A comparison of hole (red lines) and electron (black lines) densities at $V_a = 0V$ between dark (or equilibrium) conditions (sold lines) and illuminated conditions (dashed line), of the device with $\mu_p = 10^{-6}m^2/Vs$ . (b) Energy level diagram of the same device under both conditions including equilibrium (dashed line), quasi electron Fermi (green line) and hole (blue line) energy levels. . . . .	59
Figure 4.8: (a) Densities of electron (black) and hole (red) within the devices with different donor hole mobility, under $V_a = 0V$ . Equilibrium charge densities are almost invariant with $\mu_p$ and plotted in the solid lines. (b) Energy level diagram showing different quasi-Fermi levels deviation/splitting in the devices. The top LUMO and bottom HOMO bands are almost invariant with the mobility. . . . .	60
Figure 4.9: Polaron pair dissociation rate ( $k_{PPd}$ ), recombination rate ( $k_{PPr}$ ) and dissociation probability/efficiency ( $\eta_{PPd}$ ), as a function of applied voltage. . . . .	63

Figure 4.10: Plots of (a) $k_{PPd}$ , (b) $k_{PPr}$ , and (c) $\eta_{PPd}$ as a function of voltage in the devices with different hole mobility. . . . .	64
Figure 4.11: Parallel resistances ( $R_p$ ) as a function of applied voltage calculated by equation 2.28 from the devices having different donor $\mu_p$ . . . . .	65
Figure 4.12: Energy diagram showing LUMO level (top solid line) and HOMO level (bottom solid line), including electron and hole quasi-Fermi levels (red dashed and blue dotted-dashed line respectively) of the devices with (a) $\mu_p = 10^{-6} m^2/Vs$ and (b) $\mu_p = 10^{-9} m^2/Vs$ at $V_a = 0.4V$ . . . . .	66
Figure 4.13: Plot of series resistance ( $R_s$ ) functions of the devices with different hole mobility in donor. . . . .	66
Figure 4.14: Plots of the diode voltage ( $V_d = E_{fn,I} - E_{fp,I}$ ) and total change of quasi-Fermi energies from the electrodes to the interface ( $V_d$ ), i.e. $V_a - V_d$ , with respect $V_a$ . . . . .	67
Figure 4.15: (a) JV characteristics of devices under influence of increasing cathode work function (injection barrier), and (b) their extracted $J_{sc}$ , $V_{oc}$ , and FF. . . . .	69
Figure 4.16: Potential profiles ( $\psi(x)$ ) of the devices with different $\phi_c$ at applied voltage (a) 0V and (b) 0.5V. . . . .	70
Figure 4.17: Carrier density profiles ( $n(x)$ and $p(x)$ ) showing only majority carriers, i.e. holes in the donor and electrons in the acceptor, of the devices with $\phi_c = 0.0eV$ , $0.2eV$ and $0.4eV$ at the same applied voltage of 0.5V. . . . .	71
Figure 4.18: Plotting as a function of $\phi_c$ of (a) interface electron and hole densities with their multiplication and (b) open circuit voltages extracted from the DD-BI model simulations (same as in Fig. 4.15b), compared with a calculated one using equation 4.12. . . . .	73
Figure 4.19: Illustration of a Mott-Schottky contact between a metal with work function $\Phi_m$ and an n-type semiconductor with chemical potential $\Phi_s$ , where $\Phi_m > \Phi_s$ , forming a blocking contact and downward band bending. . . . .	74
Figure 4.20: Illustration of an ohmic contact between a metal with work function $\Phi_m$ and a semiconductor with Fermi level $\Phi_s$ , where $\Phi_m < \Phi_s$ , forming an ohmic contact and upward band bending. . . . .	75
Figure 4.21: Integer Charge Transfer (ICT) model describing spontaneous charge tunneling at a metal/organic semiconductor interface of the case (a) $\Phi_m > E_{ICT+}$ , (b) $E_{ICT-} < \Phi_m < E_{ICT+}$ and (c) $\Phi_m < E_{ICT-}$ . . . . .	77

Figure 4.22: A simple diagram showing the bilayer structure and some important positions at the anode and the cathode organic/metal and the hetero-junction interfaces. . . . .	78
Figure 4.23: Band diagram illustrating energy levels of the devices with $\phi_a = 0.2\text{eV}$ and $\phi_c = 0.0\text{eV}, 0.3\text{eV}$ and $0.6\text{eV}$ under illumination. . . . .	79
Figure 4.24: Plots of vacuum level shift ( $\Delta$ ), voltage loss ( $V_{loss}$ ) and acceptor electron quasi-Fermi level ( $E_{fn,L-1}$ ) at the cathode relative to the cathode work function ( $WF_c$ ) as a function of $\phi_c$ . . . . .	79
Figure 4.25: Band diagram illustrating energy levels of the devices with $\phi_c = 0.0\text{eV}, 0.3\text{eV}$ and $0.6\text{eV}$ in the dark. . . . .	81
Figure 4.26: Diagram showing possible deviations of hole quasi-Fermi level at the anode contact and bulk donor and electron quasi-Fermi level at the cathode contact and bulk acceptor, that can be represented by a component of series resistance. . . . .	83
Figure 4.27: Plots of series resistance as a function of voltage under influences of changing cathode injection barrier from $0.0\text{eV}$ to $0.6\text{eV}$ with fixed anode injection barrier at $0.2\text{eV}$ . . . . .	84
Figure 4.28: Plots of the component series resistances $R_{sa}$ , $R_{sD}$ , $R_{sA}$ and $R_{sc}$ , and total $R_s$ being the sum of the four components as a function of applied voltage of the devices with different cathode injection barrier. . . . .	84
Figure 4.29: Ideality factors $n_D$ and $n_A$ in the symmetric device with characteristic trap temperatures of electron ( $T_{t,A}$ ) and hole ( $T_{t,D}$ ) equal to $1000\text{K}$ . . . . .	88
Figure 4.30: JV characteristic responses of the devices with different hole characteristic trap temperature ( $T_{t,D}$ ) but fixed electron characteristic trap temperature ( $T_{t,A}$ ) at $1000\text{K}$ . . . . .	88
Figure 4.31: Plots of the ideality factors (a) $n_D$ and (b) $n_A$ as a function of voltage, calculated using equations 2.17 and 2.18 respectively, under the influences of varying $T_{t,D}$ . The inset shows the interface electron and hole densities in dependence on voltage when $T_{t,D} = 1200\text{K}$ . . . . .	90
Figure 4.32: Plots of JV components, namely, diode currents from free-electron to free-hole recombination (f-f), free-electron to trapped-hole recombination (fn-tp) and free-hole to trapped-electron recombination (fp-tn), and the photo-current ( $qJ_X\eta_{PPd}$ ), of the devices with fixed $T_{t,A} = 1000\text{K}$ and $T_{t,D} = 1200\text{K}, 800\text{K}$ , and $400\text{K}$ . . . . .	91

Figure 4.33: Comparisons between the illuminated JV curves calculated using $R_{f-t}$ (Eq. 1.8) and $R_{SRH}$ (Eq. 1.43) of the devices with $T_{t,D}$ and $T_{t,A}$ equal to a) 1000K and b) 450K. . . . .	94
Figure 4.34: a) Total $R_{SRH}$ and $R_{f-t}$ rates and b) their separate rates from different mechanisms; $R_{SRH} = R_{SRH,D} + R_{SRH,A}$ and $R_{f-t} = R_{rec,n} + R_{rec,p}$ , of the devices with $\mu_n/\mu_p = 100$ and $T_{t,D(A)} = 1000K$ . . . . .	96
Figure 5.1: a) Molecular structures of the heptamethine cation ( $Cy^+$ ) and b) its counter anions: (from left to right) $I^-$ ; $PF_6^-$ ; $SbF_6^-$ ; $TRIS^-$ ; and $TPFB^-$ , that are used as the donor in the device with the architecture shown in c). <i>From Ref. [1]</i> . . . . .	101
Figure 5.2: JV curves under a) nominal 1 sun illumination and b) dark condition from measurements (symbols) and fitting with the generalized Shockley equation (Eq. 1.3) . . . . .	102
Figure 5.3: Effects of the Shockley parameters a) $R_p$ , b) $J_0$ , c) $n$ and d) $R_s$ on the shapes of dark JV curves calculated by the conventional Shockley equation (Eq. 1.3) using each parameter as a constant. Control variables are summarized at the top of each plot. . . . .	103
Figure 5.4: Plots of the total dark currents ( $J$ ), the diode currents ( $J_{diode}$ ) and the leakage currents ( $J_{leak}$ ) where $J = J_{diode} + J_{leak}$ as a function of voltage for the cases of a) $R_p = 3 \times 10^5$ and b) $3 \times 10^4 \Omega m^2$ . . . . .	104
Figure 5.5: A figure showing the three regions in a dark current, namely, the leakage region, the diode region, and the Ohmic region, including how the shape in each region is affected by the Shockley parameters. <i>adapted from [5]</i> .	106
Figure 5.6: Effects of the Shockley parameters a) $R_p$ , b) $J_0$ , c) $n$ and d) $R_s$ on the shapes of illuminated JV curves calculated by the conventional Shockley equation (Eq. 1.3) using each parameter as a constant. Control variables are summarized at the top of each plot. . . . .	107
Figure 5.7: (a) Energy band diagram and the thickness of each layer in the CyTRIS:C <sub>60</sub> device. (b) Fermi-level pinning, vacuum level shifts, and possible hole injecting mechanism at the ITO/MoO <sub>3</sub> /CyTRIS interfaces ( <i>adapted from [6]</i> ). . . . .	111
Figure 5.8: Comparisons between the simulated JV curves of the CyTRIS:C <sub>60</sub> device and the experimental data under a) illumination and b) dark conditions	113
Figure 5.9: Plots of the currents originated from $R_{SRH}$ ( $J_{SRH}$ ) and $R_{tt}$ ( $J_{tun}$ ) defined in Eqs. 5.3 and 5.4 and the total dark currents $J = J_{SRH} + J_{tun}$ for the devices with $\mu_{tun}$ equals to a) $1.0 \times 10^{-11}$ and b) $5.0 \times 10^{-10} m^2/Vs$ .	114

Figure 5.10: Plot of the parallel resistance $R_{p\_tun}$ calculated by Eq. 5.5 as a function of applied voltage in the device with $\mu_{tun} = 5.0 \times 10^{-10} m^2/Vs$ . . . . .	115
Figure 5.11: Comparisons of JV curves of the CyTRIS:C <sub>60</sub> device under (a) illumination and (b) dark conditions between the experimental results (circle symbol), the DD-BI and the SCD results (lines with a symbol) and the Shockley equation's results (Eq. 1.3) (solid lines) using the fitted parameters from Ref. [1] . . . . .	117
Figure 5.12: A schematic showing the bilayer OPV architecture with each important physical mechanism being represented by an electrical circuit component. All the electrical components form the complete EEC model. . . . .	118
Figure 5.13: A comparison between $R_s$ , $R_{p\_PP}$ , $R_{p\_tun}$ and total device resistance calculated by Eqs. 2.27, 2.28, 5.5 and $[\partial J/\partial V_a]^{-1}$ respectively. The device is from Section 5.4 with $\mu_{tun} = 5 \times 10^{-10} m^2/Vs$ and under illumination conditions . . . . .	120
Figure 5.14: JV curves of the CyTRIS:C <sub>60</sub> (black lines with circles) and the P3HT:PCBM (red lines with squares) devices under (a) illumination and (b) dark conditions. . . . .	121
Figure 5.15: Plots of $J_0$ as a function of $V_a$ extracted from (a) the CyTRIS:C <sub>60</sub> and (b) P3HT:PCBM devices ( Figs. 5.14) under dark (black solid lines) and illumination (red dashed line) conditions. . . . .	122
Figure 5.16: Comparisons between illumination and dark conditions of (a) $k_{PPd}(V_a)$ , $k_{PPr}(V_a)$ , (b) $F_I(V_a)$ and $\eta_{PPd} = k_{PPd}/(k_{PPd} + k_{PPr})$ of the CyTRIS:C <sub>60</sub> device. . . . .	123
Figure 5.17: Comparisons between illumination (red dashed lines) and dark (black solid lines) series resistances of (a) the CyTRIS:C <sub>60</sub> and (b) P3HT:PCBM devices. . . . .	123
Figure 5.18: Ideality factor functions calculated by Eq. 2.23 of (a) the CyTRIS:C <sub>60</sub> and (b) the P3HT:PCBM devices under dark and illumination conditions. (inset) zoomed portion of figure (a) for $V_a > 0V$ . . . . .	124
Figure 5.19: Plots of parallel resistances under illumination ( $R_{p\_PP}$ ) of the CyTRIS:C <sub>60</sub> (black with circles) and the P3HT:PCBM (red with squares) devices calculated using Eq. 2.28. . . . .	126
Figure 6.1: (a) Structure of a cubic perovskite showing octahedra of BX <sub>6</sub> and the cation A filling the cuboctahedral void. (b) and (c) Two representations of the perovskite unit cell with the labels of the Cs, Sn, and Br ions in figure (b) for the case of CsSnBr <sub>3</sub> . . . . .	130

Figure 6.2: a) Tetragonal unit cell of $\text{CsSn}_2\text{Br}_5$ with the definitions of the basis vectors and b) its projection onto the $b/c$ plane. c) Projection onto the $a/b$ plane of the $[\text{Sn}_2\text{Br}_5]_n^{n-}$ polymeric sheet. Gray, purple and brown spheres represent Cs, Sn and Br atoms, respectively. . . . .	132
Figure 6.3: Triclinic unit cell of $\text{CsSn}_2\text{Br}_5$ that is projected into a) the $a/c$ plane, b) the $b/c$ plane and c) the $a/b$ plane. Gray, purple and brown spheres represent Cs, Sn and Br atoms, respectively. . . . .	133
Figure 6.4: The first brillouin zones of (a) a cubic, (b) a triclinic and (c) a tetragonal unit cell with a path along the edges of the irreducible brillouin zones. <i>adapted from [7]</i> . . . . .	134
Figure 6.5: Ground state energy ( $E_0$ ) convergence tests of the cubic phase as a function of (a) cut off energy ( $E_{cut}$ ) using a $\Gamma$ -centered k-point grid $9 \times 9 \times 9$ and (b) k-point grid of $N \times N \times N$ where $N$ is the x-axis value with $E_{cut} = 275\text{eV}$ . . . . .	135
Figure 6.6: Ground state energy ( $E_0$ ) convergence tests of the optimized triclinic unit cell of $\text{CsSn}_2\text{Br}_5$ as a function of (a) cut off energy ( $E_{cut}$ ) using a $\Gamma$ -centered k-point grid $13 \times 13 \times 12$ and (b) $\Gamma$ -centered k-point grids with a fixed $E_{cut} = 300\text{eV}$ . . . . .	136
Figure 6.7: Electronic band structure and projected density of states the cubic $\text{CsSnBr}_3$ structure calculated using the PBE functional. . . . .	138
Figure 6.8: Zoomed in projected density of states around the VBM and the CBM of the cubic $\text{CsSnBr}_3$ calculated using the PBE functional. . . . .	139
Figure 6.9: Electronic band structure and projected density of states of $\text{CsSn}_2\text{Br}_5$ calculated using the optimized triclinic unit cell and the PBE functional. . . . .	139
Figure 6.10: Electronic band structure and projected density of states of $\text{CsSn}_2\text{Br}_5$ calculated using the optimized tetragonal unit cell and the PBE functional. . . . .	140
Figure 6.11: Calculated band structures of a) the cubic $\text{CsSnBr}_3$ and b) the triclinic $\text{CsSn}_2\text{Br}_5$ using the HSE06 functional. . . . .	141
Figure 6.12: (a) The unit cell used for the infinite $\text{NaCl}(100)$ surface under 3D periodic boundary conditions. The larger yellow spheres represent Na atoms, and the smaller green spheres represent Cl atoms. (b) Top view of a single-layer $\text{NaCl}(100)$ surface. . . . .	144
Figure 6.13: Structure of the $\text{CsSnBr}_3$ crystal bonded to the $\text{NaCl}(100)$ surface by the $\text{Sn}^{2+}\text{Cl}^-$ ionic bonds. . . . .	145

Figure 6.14: Unit cells of the cubic $\text{CsSnBr}_3$ perovskite films having the thicknesses of 1.7 nm that are used to study effects of the $\text{NaCl}$ substrate. . . . .	146
Figure 6.15: Band structure and PDOS functions of the $\text{CsSnBr}_3$ film that is attached to the $\text{NaCl}$ substrate, calculated using the PBE functional. . . . .	147
Figure 6.16: Band structure and PDOS functions of the $\text{CsSnBr}_3$ film without the $\text{NaCl}$ substrate, calculated using the PBE functional. . . . .	148
Figure 6.17: Simulation results of depositing atomic layers of $\text{CsSnBr}_3$ onto the $\text{NaCl}$ substrate. Na, Cl, Cs, Sn, Br atoms are represented by yellow, green, gray, purple and brown spheres, respectively. . . . .	149
Figure 6.18: Simulation results showing film deposition processes after the third full-cover SnBr layer. Na, Cl, Cs, Sn, Br atoms are represented by yellow, green, gray, purple and brown spheres, respectively. . . . .	151

## KEY TO ABBREVIATIONS

**OPVs** Organic Photovoltaics

**GWWF** the model proposed by Giebink, Wiederrecht, Wasielewski and Forrest

**JV** current density-voltage characteristics

**EEC** the equivalent electrical circuit model

**MPP** maximum power point

**eq** equilibrium conditions (i.e. no light and applied voltage)

**D/A interface** the interface between the donor and the acceptor layers

**DD-BI** the drift-diffusion for bilayer interfaces model

**SCD** the self-consistent diode equations

**HOMO, LUMO** the highest occupied molecular orbital and the lowest unoccupied molecular orbital

**PP** polaron pair at the D/A interface (i.e. charge-transfer exciton)

**CT** charge-transfer exciton at the D/A interface (i.e. polaron pair)

**f-f** recombination between free electrons and free holes at the D/A interface

**fn-tp** recombination between free electrons and trapped holes at the D/A interface

**fp-tn** recombination between free holes and trapped electrons at the D/A interface

**t-t** recombination between trapped electrons and trapped holes at the D/A interface

**SRH** the Shockley-Read-Hall recombination

$J_{sc}$ ,  $V_{oc}$  short-circuit current and open-circuit voltage

$J_{max}$ ,  $V_{max}$  output current density and voltage at the MPP

$J_d$ ,  $J_{diode}$  diode current density

$J_{leak}$  leakage current density

$J_{leak,dark}$  leakage current density in the dark

$J_{ph}$  photo-current density

$J_{tun}$  current density from tunneling processes

$V_a$  the applied voltage (equal to  $WF_c - WF_a$ )

$V_d$  the diode voltage

$V_t$  the thermal voltage

$J_0$  the diode saturation current in the Shockley equation

$J_{s0}$  the diode saturation current from the f-f recombination

$J_{sD}, J_{sA}$  the diode saturation currents arising from donor trapped holes (the fn-tp recombination) and acceptor trapped electrons (the fp-tn recombination)

$R_s$  total series resistance and series resistance in the Shockley equation

$R_{sa}, R_{sD}, R_{sA}, R_{sc}$  series resistances caused by the anode contact, the bulk donor, the bulk acceptor and the cathode contact

$R_p$  total parallel resistance and parallel resistance in the Shockley equation

$R_{p\_tun}$  recombination resistance of tunneling current density

$R_{p\_PP}$  recombination resistance of the recombined exciton current density

$R_{p,dark}, R_{p,illu}$  parallel resistances under dark and illumination conditions

$n$  ideality factor

$n_D, n_A$  ideality factors arising from donor trapped holes (the fn-tp recombination) and acceptor trapped electrons (the fp-tn recombination)

$J_X$  exciton current density reaching the D/A interface

$a_0$  the width of the D/A interface

$\epsilon$  relative dielectric permittivity

$E_b$  polaron pair binding energy

$\zeta$  polaron pair density at the D/A interface

$F_I$  electric field strength at the D/A interface

$k_{PPd}, k_{PPr}$  dissociation and recombination rates of interface polaron pairs

$\eta_{PPd}$  polaron pair dissociation probability

$R$  free carrier recombination at the D/A interface

$\Delta E_{HL}$  interface energy gap

$k_{rec}$  recombination coefficient of the f-f recombination

$k_{rec,n}, k_{rec,p}$  recombination coefficients of the fn-tp and the fp-tn recombinations

$n_i$  intrinsic free carrier density

$n_I, p_I$  free electron and hole densities at the D/A interface

$n_{It}, p_{It}$  trapped electron and hole densities at the D/A interface

$n_c, p_c$  free electron and hole densities at the cathode and the anode contacts

$\delta_D, \delta_A$  fractions of potential dropped across the donor and the acceptor

$V_{bi}$  built-in potential

$WF_a, WF_c$  work functions of the anode and the cathode

$\phi_a, \phi_c$  injection barriers at the anode and the cathode

$N_{LUMO}, N_{HOMO}$  densities of states at the acceptor LUMO and the donor HOMO band edges

$E_f$  equilibrium Fermi energy

$E_{fn}, E_{fp}$  quasi-Fermi energies of electrons and holes

$E_{fn,I}, E_{fp,I}$  quasi-Fermi energies of electrons and holes at the D/A interface

$H_D, H_A$  trap densities of states at the donor HOMO and the acceptor LUMO band edges

$T_{t,D}, T_{t,A}$  characteristic trap temperatures of donor trapped hole and acceptor trapped electron distributions

$l_D, l_A$  characteristic trap parameters of donor trapped hole ( $l_D = T_{t,D}/T$ ) and acceptor trapped electron ( $l_A = T_{t,A}/T$ ) distributions

$E_{t,D}, E_{t,A}$  characteristic trap energies of donor trapped hole ( $E_{t,D} = k_B T_{t,D}$ ) and acceptor trapped electron ( $E_{t,A} = k_B T_{t,A}$ ) distributions

$N_t$  trap density in the SRH recombination

$C_n, C_p$  capture rates of electrons and holes in the SRH recombination

$\mu_n, \mu_p$  electron and hole mobilities

$n(x), p(x)$  electron and hole densities as a function of position (i.e. electron and hole density profiles)

$\psi(x)$  electrostatic potential as a function of position (i.e. potential profile)

# CHAPTER 1

## BACKGROUND AND MOTIVATION

### 1.1 Global Warming and the Need for Solar Energy Technologies

In the book *Sustainable Energy — Without the Hot Air* [8], David JC MacKay points out that there are three main reasons why we have to rethink about our uses of fossil fuels: (1) fossil fuels are limited; (2) we need energy security; and (3) burning fossil fuels causes climate change. Energy security is defined as the ability to access energy resources at an affordable price. Points (1) and (2) may cause economic and political problems, but more importantly, climate change and global warming, caused by by-products of burning fossil fuels, may result in uninhabitable regions and unhealthy climate and environment across the planet.

According to the International Energy Agency[9], in 2014, oil, coal and natural gas; which are the three primary fossil fuels, have their shares at 39.9%, 11.4% and 15.1%, respectively, of the direct global energy consumption of 109,612 terawatt-hours (TWh), where watt-hour is a unit of energy equal to  $3.6 \times 10^3$  Joules. These percentages do not include the additional use of oil, coal or natural gas in producing electricity. Thus, fossil fuels are the primary energy resources consumed by humans. A statistical prediction based on the ratios of world consumption to reserved fossil fuels in 2006 [10] predicts that oil, coal and gas will last about 40, 200 and 70 years, respectively, meaning that we will approximately run out of these resources in 2046, 2206 and 2076. Even though advanced extraction techniques like hydraulic fracturing [11] and discoveries of new crude oil locations and new forms of resources like methane hydrate on the seabed [12] can extend the supply time hundreds of years, the resources will be depleted eventually.

Almost all of the utilizations of fossil fuels involve burning the resources to get heat, and then using the heat to do work. For example, we burn natural gas to warm our houses, burn oil to run the heat engines in our cars, and burn coals to boil water to produce electricity in power plants. These processes are not the most efficient or favorable as we lose energy during

heat transfers, carbon dioxide ( $\text{CO}_2$ ) gas; which is a greenhouse gas, is emitted as a product of combustion reactions (e.g.  $\text{CH}_4 + 2\text{O}_2 \rightarrow \text{CO}_2 + 2\text{H}_2\text{O}$ ). Naturally,  $\text{CO}_2$  gas is a part of atmospheric gases that absorbs and re-emits infrared parts of sunlight so that Earth is livable. Introducing extra  $\text{CO}_2$  content to the atmosphere from human activities undoubtedly results in higher global temperature. There are clear evidences that  $\text{CO}_2$  concentration in the air has increased at an accelerating rate after the industrial revolution [8, 13]. According to the global temperature data by the National Aeronautics and Space Administration (NASA) [14], the year 2016 is the warmest year since 1880, having  $0.99^\circ\text{C}$  higher temperature than the 1951-1980 average. At this rate, global average temperature is predicted to increase by  $2\text{-}6^\circ\text{C}$  within a century; which will result in a sea level rise between 0.5 to 1.5 meters [15]. Due to the problems associated with using fossil fuels, sustainable, renewable and clean energies are necessary.

The amount of sunlight energy hitting Earth in two hours is more than an annual total global energy consumption from all resources combined [16]. This means that, theoretically, we could cut the uses all energies and replace them with solar energy alone. In a qualitative view, assuming that a solar panel can harvest about 20% of solar irradiance (i.e. solar energy per unit time and unit area), whose average is around  $300 \text{ Wm}^{-2}$ [17] and there are 12 hours of daylight, the panel can produce a yearly energy of

$$\frac{20\% \times 300 \text{ Wm}^{-2} \times 60 \text{ seconds} \times 60 \text{ minutes} \times 12 \text{ hours} \times 365 \text{ days}}{3.6 \times 10^6 \text{ J/KWh}} = 262.8 \text{ kWhm}^{-2}. \quad (1.1)$$

In order to have as much energy as the 2014 total global assumption, we need to install

$$\frac{109,612 \times 10^9 \text{ KWh}}{262.8 \text{ kWhm}^{-2}} = 4.17 \times 10^{11} \text{ m}^2 = 4.17 \times 10^5 \text{ km}^2 \quad (1.2)$$

or  $645\text{km} \times 645\text{km}$  of solar panels, which is only about 0.28% of Earth's land area[18]. This futuristic idea can be practical if solar panels are geographically distributed over available areas, like roof surface area [19]. For example, if half of the population in Spain, where average irradiation is  $1,600 \text{ kWh/m}^2$  [20, 21], installed  $14\text{m}^2$ [19] of the 20%-efficiency solar panels on their roofs, 42% of total electricity consumption (i.e. 249 Twh in 2014 [9]) could

be replaced by solar energy; which is equivalent to reduction of fossil fuel usage by 9 million tonnes (i.e. 1 Million Tonnes of Oil Equivalent (MTOE) is 11.63 TWh).

Solar cell technologies have been developed since the mid-20th century, and now we are on the verge of the third generation of solar cells. The first generation solar cells; which are still the most efficient and dominate the solar cell market, are made of silicon (Si). They are classified by the type of silicon used; which can be monocrystalline Si (up to 25% efficiency), polycrystalline Si (up to 20% efficiency) and amorphous Si (less than 10% efficiency) [22]. The second generation of solar cells is based on thin-film technologies. Three main types of solar cells in this generation are thin-film amorphous Si, cadmium telluride (CdTe) (up to 18% efficiency [22]) and copper indium gallium diselenide (CIGS) (up to 16% efficiency[22]). However, solar cells in this generation are not as popular as the first generation's ones, and share less than 1% in the solar panel market [23]. The third generation solar cells, which are at the focal point of this thesis and the research community, are based on solution-processed materials, where promising candidates include organic polymer:fullerene, organic hybrid polymer, dye-sensitized and perovskite solar cells [24, 25].

Apart from the impressive efficiencies and lifetimes of silicon solar cells, pure silicon; which is expensive and energy intensive, is needed[26]. For each kilogram of pure silicon, electrical energy ranging from 15 KWh to 90 KWh is required; which means, in terms of energy profits, silicon-based solar cells may take up to two years to generate the same amount of electricity that was spent in producing them [26].

Organic photovoltaics or solar cells (OPVs or OSCs) are promising for the next generation solar cells because of the following advantages over inorganic solar cell technologies. First, they can be manufactured using all-solution processes at low temperature and standard pressure. These include roll-to-roll printing techniques[27]. Second, they can be light, flexible, transparent, integrable to other products, cheaper to manufacture than inorganic solar cells, have short energy payback time and less environmental impact[28]. Results from a cost analysis indicate that current OPV technologies have price per produced energy at 1.06-

8.90\$ per watt-peak ( $W_p$ ), and can be as low as 0.05-0.64\$ per  $W_p$  on an industrial scale[27]. Watt-peak is defined as the nominal power of a solar cell, measured under *standard Test Conditions*; light intensity of  $1\text{KW/m}^2$ , at latitude  $42^\circ\text{N}$  (airmass 1.5) and temperature  $25^\circ\text{C}$ . These prices per  $W_p$  are comparable to those of silicon solar cells[29]. Energy payback time (EPBT) of OPV cells can be as low as 0.2 years, which is better than many renewable energies, such as, wind (EPBT = 0.39 years), polycrystalline and monocrystalline Si PVs (EPBT = 1.65-4.14 years), hydropower (EPBT = 0.5 years) and biomass (EPBT = 5-10 years)[30]. Furthermore, OPVs are among the cleanest sustainable energies because they produce only 0.01-0.06 kg of  $\text{CO}_2$  per kW of produced electricity, which is comparable to wind and hydropower energies, and less than 10% of  $\text{CO}_2$  amount emitted by natural gas[30].

We can see that OPVs have a lot of potential to be the next generation solar cells, or even applied at a global scale to replace/reduce the uses of fossil fuels. However, low efficiencies (less than 5% under actual operation) and short lifetimes are two main drawbacks of OPVs that make them stay on laboratory shelves, instead of store shelves. These are the reasons why we have to study and understand the physics of OPVS.

## 1.2 Introduction to Organic Photovoltaics

Photovoltaic (PV) cells, or solar cells, are semiconductor devices that generate a current and voltage from the energy of incident photons. The current and the voltage are therefore the most important parameters that need to be maximized. They depend on each other and are often plotted as a current density-voltage (JV) characteristic curve. Having an analytic equation to describe the JV curves is undoubtedly necessary for effective design of modules consisting of many thousands of solar cells.

JV curves are usually diode-like, so the most ubiquitous JV equation is composed of the Shockley p-n junction diode term[31], a photo-current term, and a leakage term. Series and parallel resistances ( $R_s$  and  $R_p$ ) are usually included to represent physical loss mechanisms in PV cells[17, 32]. The resulting equation is generally referred to as the Shockley equation.

It can meaningfully describe p-n junction PV cells, which are p-n junction diodes both when the light is absent and present.

When new types of PV cell emerge, the Shockley equation and the working principles of p-n junction PV cells are also applied to them, for example, organic photovoltaic (OPV) cells[33, 34, 35, 36, 37, 38], dye sensitized solar cells (DSSCs)[39], perovskite solar cells[40, 41], and organic salt solar cells[1], because they all exhibit diode-like behavior similar to the p-n junction. Despite the fact that the Shockley equation fits their JV curves, their working principles and structures are different from the p-n junction PV cells[42, 43]. This has led to a debate on whether the Shockley equation is universal; which is still open, even in 2015[44].

Diode saturation current ( $J_0$ ),  $R_s$ ,  $R_p$  and the ideality factor ( $n$ ) are important Shockley parameters that are usually fitted and extracted by experimentalists to show their devices' physical processes.  $R_s$  is interpreted as the total resistance of the bulk layers and contacts [35, 45, 46, 5], while  $R_p$  is understood to represent leakage current[32] that is caused by either pinholes[5] or direct contact between the electrodes (e.g. anode and cathode) and the active layers[47]. The ideality factor  $n$  is an indicator of the free-carrier recombination type. In the ideal case with  $n = 1$ , free charges recombine via bimolecular recombination[44].  $n$  exactly equal to 2[48] in the p-n junction picture arises from the Shockley-Read-Hall recombination[49, 50] where free charges recombine with trapped charges that act as recombination centers. In reality, any values of  $n$  can be extracted, and  $n > 1$  is interpreted as an evidence of trap-assisted recombination[51, 52].

Thin-film OPV cells are the main focus in this study. A typical energy band diagram and working principles of OPVs are illustrated in Figure 1.1[2, 3]. The active layer, which is the layer that adsorbs photons and produces free carriers, is made of an electron-donor and an electron-acceptor material. They are often called donor and acceptor for short. The donor material can be a macrocyclic compound[38, 53], a polymer[54, 55], etc., and the acceptor is usually a fullerene derivative[38, 54]. The first OPV cell was invented by Tang in 1986[53] in a form of planar heterojunction, or bilayer, structure where the donor and the acceptor are

deposited separately into two layers. Later, the idea of blending the donor and the acceptor in the bulk heterojunction (BHJ) structure [56, 57, 58] was introduced and gained popularity among researchers. Recently, attention has been drawn back to the planar heterojunction because it leads to a superior OPV morphology[59, 60, 61], and novel PV technologies like perovskite solar cells[62, 63, 64] also adopted it. Hence, the bilayer structure is at the focal point in this study.

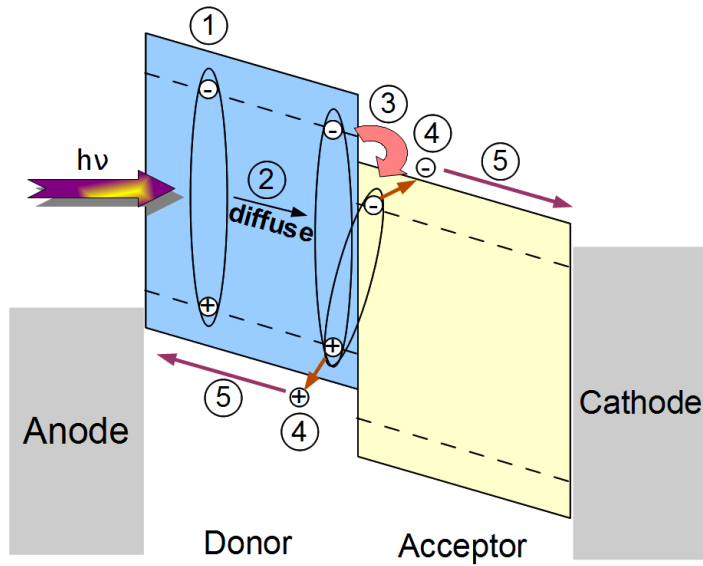


Figure 1.1: Energy band diagram and working principles of typical OPVs showing several important steps: (1) exciton generation; (2) exciton diffusion; (3) forming of a charge transfer exciton or a polaron pair (PP); (4) dissociation of PP; (5) charge transport and collection. *Adapted from [2, 3].*

As illustrated in Fig. 1.1, typical working principles of OPVs are as follows[2, 3]. First, incident photons excite electrons in the donor molecules from the highest occupied molecular orbital (HOMO) to the lowest unoccupied molecular orbital (LUMO). However, because the dielectric permittivities are typically low in organic semiconductors, the excited electrons are coulombically bound to electron holes (or holes) in the HOMO, resulting in tightly bound electron-hole pairs; or **excitons**, that have a large binding energy of around 0.3 - 1.0 eV[65]. Excitons in organic materials are usually confined within the molecular radius and thus are categorized as Frenkel excitons. The exciton generation processes are step (1) in Figure

1.1. These excitons are electrically neutral and diffuse around via hopping mechanisms that are caused by the exciton concentration gradient. Typical exciton diffusion length in organic materials is around 1-10 nm[2]. If the excitons can diffuse to the donor-acceptor (D/A) interface as shown in step (2) in Figure 1.1, the excited electrons undergo charge transfer under the influence of the LUMO energy offset;  $E_{LUMO,D} - E_{LUMO,A}$ , to a more favorable energy level in the acceptor, as labeled by process (3). Electronic relaxations of the donor holes and geometric relaxations of the donor molecules occur, resulting in self-localized states called **hole polarons**[66]. The same relaxations apply to the acceptor electrons and the acceptor molecules, leading to **electron polarons**. After the charge transfer in step (3), electron polarons and hole polarons are still bound together across the D/A interface, and a pair of electron and hole polarons is defined as a **polaron pair** (PP) or a charge-transfer (CT) exciton. The coulombic bond in a PP can be broken by an external electric field (shown step (4)), resulting in a free electron in the acceptor and a free hole in the donor. In the final step, these free carriers are transported under influences of an applied electric field (drift) and charge concentration gradients (diffusion) to the electrodes, so they are collected and utilized. Accordingly, the key mechanism that distinguishes OPV cells from others is dissociation of PPs into free carriers[67, 68].

The paper by Giebink, Wiederrecht, Wasielewski and Forrest (GWWF) [4] was probably the first and one of very few papers trying to derive PV equations from the physics of CT states. The resulting equations are in the same form as the Shockley equation but written in terms of CT dissociation and recombination rates. This work ties the opposite ends of solar cells together and validates the applicability of the Shockley equation to OPV cells. There are, however, some improvements that can be made to the GWWF model to make it more accurate. For example, GWWF calculated the interface charge densities using fractions of potential dropped across the donor and the acceptor, which is strictly valid only when the sum of drift and diffusion currents is zero[69]. The interface electric field which is very important in determining the dissociation of CT excitons is also inaccurate

because it is calculated from the interface charge densities. Additionally, the series resistance, which is an intrinsic property depending on charge transport and contacts, is missing in the GWWF derivation due to some assumptions. Even though it was added manually later so the equations fitted with experimental results better, its physical meaning was still absent. Another OPV characteristic that is hardly included in any OPV equations is the accumulation of charges due to poor transport properties[44], which are referred to as space charge effects.

Numerical simulation solving the Poisson equation and the current continuity equations self-consistently can bring about the correct interface charge densities and the inclusion of space charge effects. It is a widely accepted method used to study OPV cells[70, 71, 72, 73, 74]. Barker *et al.* [69] developed a numerical model for bilayer OPV cells that include interface processes similar to the GWWF model but with the space charge effects included. It is able to reproduce OPV behaviors such as dependence of  $V_{oc}$  on incident light intensity. Nonetheless, it needs some modifications that make it more suitable for OPV cells. For instance, Langevin-like bimolecular recombination[75, 76] that was used for free carrier recombination can be replaced by a trap-assisted recombination[4, 77]. Most importantly, it would be more helpful to have an analytic JV equation to go with the numerical simulation.

In this study, a numerical simulation for thin-film bilayer OPV cells is developed and utilized; and new JV equations in the same form as the Shockley equation with quasi-Fermi energies are developed. They will be called the Drift-Diffusion model for Bilayer Interfaces (DD-BI model) and the Self-Consistent Ideal Diode (SCD) models/equations respectively. The DD-BI model; which has space charge effects included, can calculate the right interface charge densities, the right interface electric field and the right D/A CT rates. Using these quantities as a function of the PV voltage in the SCD equations not only makes them able to reproduce the DD-BI's JV curves, but also able to provide physical meanings of the Shockley parameters (e.g  $R_s$ ,  $R_p$ ,  $n$ ). This is the proof that the Shockley form equations are appropriate to describe OPV JV curves[44]. However, each parameter in the equations

is not constant in general but a function of applied voltage as well as other parameters in the model.

### 1.3 My Contributions

There are two parts in this thesis. The first part is simulating bilayer OPVs using a computer program and models that we develop ourselves, and the second part is calculating electronic properties of a perovskite and related materials using density functional theory with a commercial software.

For the first part, as stated earlier, the Shockley equation that was developed for inorganic p-n junctions can fit OPV JV curves regardless of their different natures, so I started this part with curiosity of origins of the Shockley equation and its parameters in terms of organic semiconductor physics. I took a Fortran code of 1D drift-diffusion simulation that was written by Kanokkorn Pimcharoen; another PhD candidate in our group, and included the bilayer interface as suggested in the GWWF model; which is a Shockley equation model for OPVs, resulting in the DD-BI model in Chapter 3. However, JV results from the DD-BI model do not agree with GWWF diode equations, so I made comparisons between the two models and found that the GWWF model does not treat many OPV properties correctly, especially interface densities, space charge effects and series resistance (see Section 4.1). Thus, I derived new diode equations for OPVs using charge densities as a function of quasi-Fermi levels, resulting in the SCD equations in Chapter 2; which are always consistent with the DD-BI model. Using the DD-BI and SCD models allows me to understand principles of bilayer OPVs in terms of quasi-Fermi levels and define actual meanings of all the Shockley parameters for OPVs. Many characters of OPVs are studied (see Chapter 4) and new interesting results are observed. For example, injection barriers smaller than about 0.2eV do not affect JV curves, and increasing injection barriers almost do not affect open-circuit voltage. I can show by using the DD-BI and the SCD models that small injection barriers result in quasi-Fermi level pinning, so they do not affect JV curves, and interface densities; which mainly determine

$V_{oc}$ , are not significantly affected by increasing injection barriers. I can also show that ideality factor functions that I derived are actually general forms of a famous ideality factor equation but provide more details about trap characteristics. In Chapter 5, I include more mechanisms governing leakage current in the dark and thus arrive at a complete diode model from OPVs. My models can fit and explain actual devices and provide more understanding of the Shockley parameters both under illumination and dark conditions.

My contributions in the second part of the thesis are that I use the program VASP to calculate band structures and band gaps of  $\text{CsSnBr}_3$  and  $\text{CsSn}_2\text{Br}_5$  in DFT levels in order to confirm experimental results of growing a  $\text{CsSnBr}_3$  film on a  $\text{NaCl}(100)$  substrate using a vapor phase heteroepitaxy technique. Another purpose; which is still in progress, is to find the atomic configuration at the interface between  $\text{CsSnBr}_3$  and  $\text{CsSn}_2\text{Br}_5$  in order to verify that  $\text{CsSnBr}_3$  can transform into  $\text{CsSn}_2\text{Br}_5$  during the growth process.

## 1.4 Shockley Equation and Equivalent Electrical Circuit Model

Most inorganic solar cells nowadays are based on p-n junction architectures that have been developed and studied since the 1950s[78]. For this reason, the ideal diode equation of a p-n junction, which was developed by Shockley[31], has always been applied to solar cells to describe their current-voltage (JV) response. The generalized form of the Shockley equation that includes photogenerated current ( $J_{ph}$ ), series resistance ( $R_s$ ), and parallel resistance ( $R_p$ ) is given by

$$J = J_0 \left[ \exp \left( \frac{q(V_a - JR_s)}{nk_B T} \right) - 1 \right] - J_{ph} + \frac{V_a - JR_s}{R_p}, \quad (1.3)$$

where  $J_0$  is the saturation current of minority carriers,  $q$  is the elementary charge,  $V_a$  is applied voltage as well as the voltage that a solar cell produces at a corresponding  $J$ ,  $n$  is the ideality factor,  $k_B$  is the Boltzmann constant, and  $T$  is temperature[32, 17].  $R_s$  is a resistance from contacts and bulk materials, and  $R_p$  comes from leaking current at the p-n junction that can be represented by a shunt path. This conventional definition of  $R_p$

applies to OPVs only in the dark because  $R_p$  under illumination conditions is dominated by recombination resistance of interface PPs (See Section 2.2 and 5.5). The ideality factor  $n$  is an indicator of charge transport/recombination mechanisms. Conventionally, the recombination current gives rise to  $n = 2$  while the current from charge diffusion has  $n = 1$ [48]. There are three terms on the right hand side of Eq. 1.3, i.e. diode current( $J_d$ ), photocurrent, and leakage current( $J_{leak}$ ), from left to right. Each of these terms can be represented by an electrical component in the equivalent electrical circuit (EEC) model, shown in Fig. 1.2.

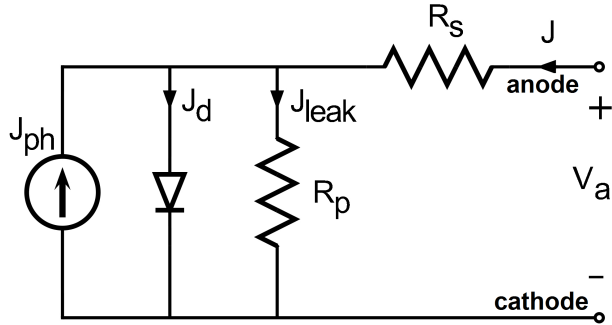


Figure 1.2: Equivalent electrical circuit with single diode for a solar cell

However, the Shockley equation and the EEC model sometimes cannot accurately fit experimental data. A double diode model was introduced to capture both recombination and diffusion currents[79], with the Shockley equation modified accordingly to

$$J = J_{01} \left[ \exp\left(\frac{q(V_a - JR_s)}{n_1 k_B T}\right) - 1 \right] + J_{02} \left[ \exp\left(\frac{q(V_a - JR_s)}{n_2 k_B T}\right) - 1 \right] - J_{ph} + \frac{V_a - JR_s}{R_p}, \quad (1.4)$$

where the first diode term represents diffusion current having  $n_1 = 1$  and the second term represents recombination current having  $n_2 = 2$ [79, 48]. Later, it was shown that  $n_1 = 1$  and  $n_2 = 2$  are not always true, and both of them should also be fitting parameters to get a better fit to actual devices[80]. Figure 1.3 depicts the EEC model for the double diode case.

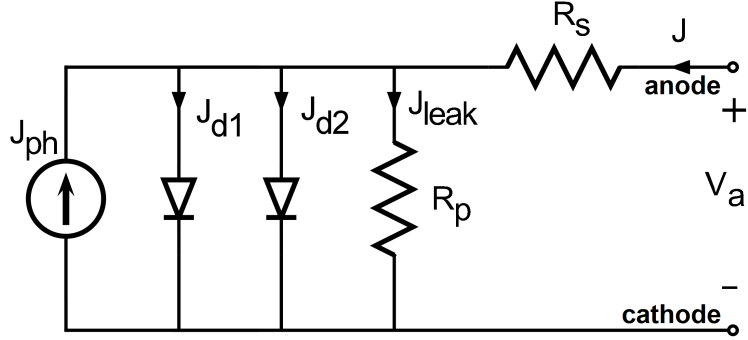


Figure 1.3: Equivalent electrical circuit with double diode for a solar cell

## 1.5 Efficiency parameters

One of the simplest ways to measure and display how well a solar cell can convert sunlight energy into electrical energy is to use efficiency parameters associated with a JV characteristic curve. If a solar cell is connected to an external load, the relation between current and voltage that it can deliver is often plotted as the lower part of Figure 1.4, where negative current is defined as a current flowing out of the anode under illumination. Load or external resistance will determine the current and voltage. If the cell produces large current, the produced voltage has to be small, and *vice versa*. The point where maximum current is achieved is the point where the voltage is zero and is called short circuit (sc) conditions. The current here is short circuit current ( $J_{sc}$ ). On the other hand, the cell will have maximum voltage if the current is zero. This condition is called open circuit (oc), having the voltage of open circuit voltage ( $V_{oc}$ ).

Different points on the JV curve correspond to different output power defined by  $Power = J \times V$  (see upper part of Fig. 1.4). There is one point where the output power is maximum. This is the point where solar cells operate, and it is called maximum power point (MPP). The associated voltage and current are  $V_{max}$  and  $J_{max}$ , respectively. Efficiency of a solar cell is exhibited by power conversion efficiency (PCE) which is the ratio of electrical output of the solar cell at the MPP to the power of incident sunlight. The power of sunlight per

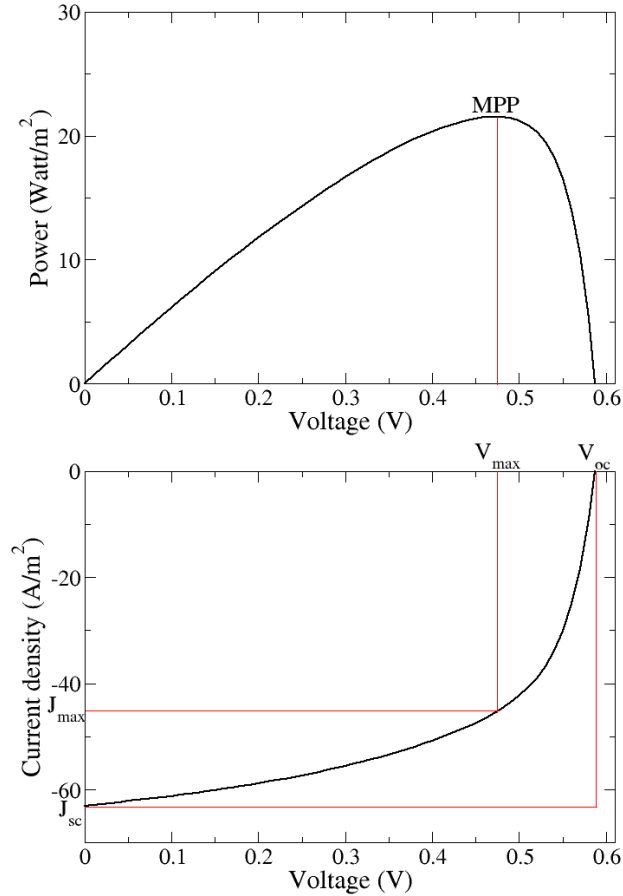


Figure 1.4: Example of JV characteristic and output power versus voltage of a solar cell with an illustration of squareness of the JV curve.

unit area; irradiance, is  $G$  with the unit  $\text{Watt}/\text{m}^2$ . PCE is given by

$$PCE = \frac{J_{max}V_{max}}{G}. \quad (1.5)$$

However, it is more useful to correlate the MPP with  $J_{sc}$  and  $V_{oc}$  so that the shape of the JV curve can be roughly presented. Another parameter, named Fill Factor (FF), is introduced and defined by  $FF = J_{max}V_{max}/J_{sc}V_{oc}$ . According to the lower part of Fig. 1.4, FF is the ratio of the area of the inner red rectangle to the area of the outer red rectangle. FF is then *squareness* of JV characteristics. Consequently, it is more general to calculate PCE with the following form.

$$PCE = \frac{J_{sc}V_{oc}FF}{G} \quad (1.6)$$

Ultimately, larger  $J_{sc}$ ,  $V_{oc}$  and FF, give higher PCE and a better solar cell. It is the primary goal of researchers to develop solar cell technology so that these parameters are as high as possible.

## 1.6 GWWF Model

Giebink, Wiederrecht, Wasielewski and Forrest (GWWF) proposed a model for organic heterojunctions that includes important interface processes and derived ideal diode equations from the model[4]. Below is an overview of this model.

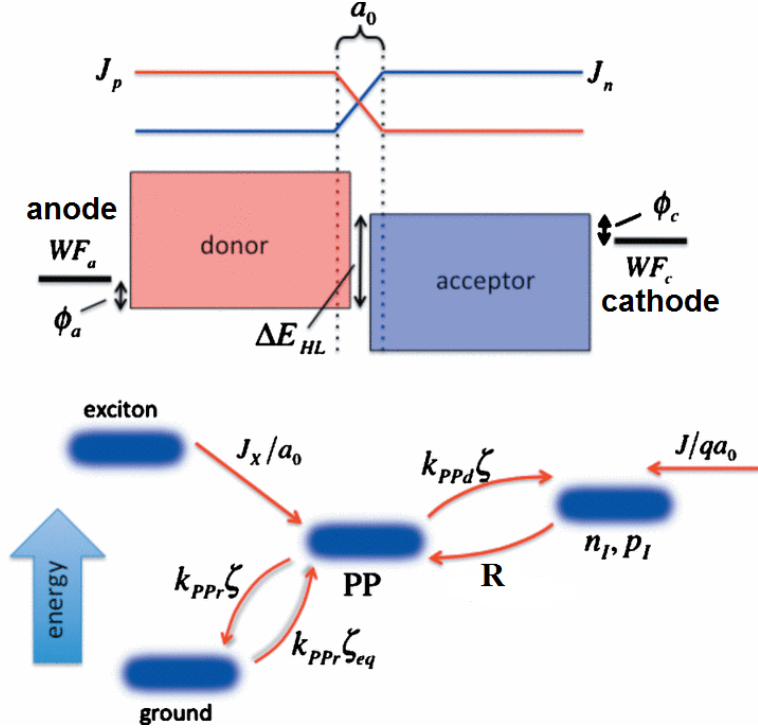


Figure 1.5: Energy level diagram and possible interactions occurring at the heterointerface between the active layers of a bilayer organic solar cell as proposed by GWWF. *Adapted from[4]*

The GWWF model can be depicted by Fig. 1.5. Photoexcited donors produce bound excited electron-hole pairs, or excitons[81], that can diffuse to the donor-acceptor (D/A) interface with a current density  $J_X$ . The electrons transfer from the lowest unoccupied molecular orbital (LUMO) of the donor to the LUMO of the acceptor, but they are still

coulombically bound with the donor holes[56]. This forms paired charges called charge transfer (CT) excitons or polaron pairs (PPs). The D/A interface is  $a_0$  thick, where  $a_0$  is the PP binding length. The PPs, having total density of  $\zeta$ : can either recombine to ground states with a rate  $k_{PPr}$ , the polaron pair recombination rate[82]; or dissociate to be free charge carriers with a rate  $k_{PPd}$ , the Onsager-Bruan electric field assisted dissociation rate[83]. Two more interactions affect  $\zeta$ . One is thermally activated PP from the ground states with a rate  $k_{PPr}\zeta_{eq}$ . The other is recombination of free charges at the interface, denoted by  $R$  in this work. Competition between total recombination rate and total dissociation rate will result in the current density ( $J$ ) flowing outward or inward at the interface, and it is this current that will be calculated.

Two possible mechanisms of the recombination ( $R$ ) are considered. The first one is free-carrier to free-carrier Langevin bimolecular recombination[75, 76]. It is denoted by f-f recombination, which follows the same notation as in Ref.[84]. The rate is given by

$$R_{f-f} = k_{rec} n_I p_I, \quad (1.7)$$

where  $k_{rec}$  is the Langevin bimolecular recombination coefficient, and  $n_I(p_I)$  is the interface free electron (hole) density.  $k_{rec}$  is given by  $k_{rec} = q(\mu_n + \mu_p)/\epsilon\epsilon_0$ , where  $\mu_n(\mu_p)$  is the electron (hole) mobility,  $\epsilon$  is the dielectric constant, and  $\epsilon_0$  is dielectric permittivity of free space. The second recombination mechanism is trapped-assisted recombination which is a recombination between free-carriers and trapped-charges (f-t). Its expression is given by

$$R_{f-t} = k_{rec,n} n_I p_{It} + k_{rec,p} p_I n_{It}, \quad (1.8)$$

where  $k_{rec,n}$  is the recombination coefficient of free-electrons to trapped-holes (fn-tp),  $k_{rec,p}$  is the recombination coefficient of free-holes to trapped-electrons (fp-tn), and  $n_{It}(p_{It})$  is the interface trapped electron (hole) density.

Assuming steady state conditions of  $\zeta$ ,  $n_I$  and  $p_I$ , the following rate equations are obtained.

$$\frac{J_X}{a_0} - k_{PPr}(\zeta - \zeta_{eq}) - k_{PPd}\zeta + R = 0. \quad (1.9)$$

$$k_{PPd}\zeta - R + \frac{J}{qa_0} = 0. \quad (1.10)$$

Solving these equations leads to an expression for the current density  $J$  as

$$J = qa_0(1 - \eta_{PPd}) \left( R - \frac{k_{PPd}}{k_{PPd,eq}} R_{eq} \right) - qJ_X\eta_{PPd}, \quad (1.11)$$

where  $\eta_{PPd}$  is PP dissociation probability expressed as  $\eta_{PPd} = k_{PPd}/(k_{PPd} + k_{PPr})$  [83, 85],  $k_{PPd,eq}$  is the equilibrium polaron pair dissociation rate, and  $R_{eq}$  is the interface free carrier recombination rate under equilibrium. Equilibrium here refers to when there is no light;  $J_X = 0$ , and no applied voltage;  $V_a = 0$ . In order to have an explicit equation for  $J$ , expressions for  $R$  in Eq. 1.7 or Eq. 1.8 and for the interface densities  $n_I$  and  $p_I$  are needed. GWWF used the following relations to relate  $n_I$  and  $p_I$  with cathode electron density ( $n_c$ ) and anode hole density ( $p_c$ ).

$$n_I = n_c \exp \left[ \frac{\delta_A q(V_a - V_{bi})}{k_B T} \right]. \quad (1.12)$$

$$p_I = p_c \exp \left[ \frac{\delta_D q(V_a - V_{bi})}{k_B T} \right], \quad (1.13)$$

where  $\delta_A$  and  $\delta_D$  are fractions of potential dropped across donor and acceptor respectively, and  $V_{bi}$  is the built-in potential given by

$$V_{bi} = WF_a - WF_c = \Delta E_{HL} - \phi_a - \phi_c, \quad (1.14)$$

where  $WF_a$  and  $WF_c$  are anode and cathode work function respectively,  $\Delta E_{HL}$  is the interface energy gap defined by  $\Delta E_{HL} = E_{LUMO,A} - E_{HOMO,D}$ , and  $\phi_c$  and  $\phi_a$  are cathode and anode injection barriers, respectively. Equations 1.12 and 1.13 are strictly valid only when current density vanishes, i.e. at around the open circuit conditions;  $V_a = V_{oc}$  [4, 69], but they are applied to all  $V_a$  in the GWWF model. Contact charge densities  $n_c$  and  $p_c$  can be approximated by

$$n_c = N_{LUMO} \exp(-\phi_c/k_B T), \quad (1.15)$$

and

$$p_c = N_{HOMO} \exp(-\phi_a/k_B T), \quad (1.16)$$

where  $N_{LUMO}$  is the density of states of electrons at the acceptor LUMO band edge, and  $N_{HOMO}$  is the hole density of states at the highest occupied molecular orbital (HOMO) band edge of donor.

In the case of f-f recombination, GWWF derived an ideal diode equation for organic heterojunctions that is given by

$$J = J_{s0} \left[ \exp\left(\frac{q(V_a - JR_s)}{k_B T}\right) - 1 \right] - qJ_X \eta_{PPd}, \quad (1.17)$$

where  $J_{s0}$  is the diode saturation current. It is given by

$$J_{s0} = qa_0 k_{rec} N_{HOMO} N_{LUMO} (1 - \eta_{PPd}) \exp(-\Delta E_{HL}/k_B T), \quad (1.18)$$

where series resistance  $R_s$  is *manually* added here. This equation resembles the Shockley ideal equation for solar cells that was derived from the physics of inorganic p-n junction in 1949[31].

In the case of trap-assisted recombination, expressions for trapped charge densities  $n_{It}$  and  $p_{It}$  have to be formulated first. However, it is important to introduce the physics of quasi-Fermi levels prior to that. Under equilibrium conditions, the total chemical potential of an electron in a substance is the Fermi level  $E_f$ . In semiconductors, the Fermi level designates the amount of free electrons in the LUMO bands and free holes in the HOMO bands through the relations;

$$n = N_{LUMO} \exp\left(\frac{-(E_{LUMO} - E_f)}{k_B T}\right), \quad (1.19)$$

and

$$p = N_{HOMO} \exp\left(\frac{-(E_f - E_{HOMO})}{k_B T}\right). \quad (1.20)$$

However, once a semiconductor is disturbed from equilibrium by either illumination or applied voltage, electrons from the HOMO will be excited to the LUMO and holes will be produced in the HOMO. These two excited free charge densities cannot be described by just one Fermi level as in Eq. 1.19 and Eq. 1.20, but two quasi-Fermi levels are needed, namely, the electron quasi-Fermi level ( $E_{fn}$ ) and the hole quasi-Fermi level ( $E_{fp}$ )[17]. In simple

words, the electron and hole densities change as they have their own Fermi levels, which are given by

$$n = N_{LUMO} \exp\left(\frac{-(E_{LUMO} - E_{fn})}{k_B T}\right), \quad (1.21)$$

and

$$p = N_{HOMO} \exp\left(\frac{-(E_{fp} - E_{HOMO})}{k_B T}\right). \quad (1.22)$$

Assuming an exponential trap distribution with characteristic trapped electron energy  $E_{t,A} = k_B T_{t,A}$  and characteristic trapped hole energy  $E_{t,D} = k_B T_{t,D}$ , where  $T_{t,A}$  and  $T_{t,D}$  are corresponding characteristic trap temperatures, trapped electron and hole densities can be approximated by

$$n_t \approx H_A \exp\left(\frac{-(E_{LUMO} - E_{fn})}{k_B T_{t,A}}\right) \approx H_A \left(\frac{n}{N_{LUMO}}\right)^{(1/l_A)}, \quad (1.23)$$

and

$$p_t \approx H_D \exp\left(\frac{-(E_{fp} - E_{HOMO})}{k_B T_{t,D}}\right) \approx H_D \left(\frac{p}{N_{HOMO}}\right)^{(1/l_D)}, \quad (1.24)$$

where  $H_D$  and  $H_A$  are the total trap densities in donor and acceptor respectively, and  $l_A = T_{t,A}/T$  and  $l_D = T_{t,D}/T$ . These equations are actually true only at  $T = 0K$ , where the injected or photo-generated charges are trapped and fill up the DOS up to the quasi-Fermi levels[86]. However, they can be applicable to any temperature if  $T < T_{t,D}$  and  $T_{t,A}$ , and if Fermi-Dirac distributions of free electrons and holes are established and  $n < n_t$  and  $p < p_t$ [86]. More details about the exponential trap distribution can be found in Section 1.8.

As a result, the ideal diode equation with trap-assisted recombination in the GWWF model is given by

$$J = J_{sD} \left[ \exp\left(\frac{q(V_a - JR_s)}{n_D k_B T}\right) - 1 \right] + J_{sA} \left[ \exp\left(\frac{q(V_a - JR_s)}{n_A k_B T}\right) - 1 \right] - q J_X \eta_{PPd}, \quad (1.25)$$

where  $J_{sD}$  and  $J_{sA}$  are diode saturation currents, and  $n_D$  and  $n_A$  are ideality factors. They are a function that have  $\delta_D$  and  $\delta_A$  as one of the arguments. Detailed expressions for  $J_{sD}$ ,  $J_{sA}$ ,  $n_D$ , and  $n_A$  in the GWWF model can be found in the original work[4].

## 1.7 Shockley-Read-Hall Recombination

In addition to the trap-assisted recombination in Eq. 1.8, the Shockley-Read-Hall (SRH) recombination [49, 50] is a widely accepted recombination theory in disordered materials. Even though it was originally derived using inorganic semiconductor physics, it can be extended to organic devices[87, 88, 89].

The integral part of the SRH recombination is that defects in a disordered solid can capture (or trap) free electrons or holes from transport levels. They can then either be emitted (or detrapped) back to the transport levels or act as recombination centers, recombining with other free carriers. The defects or traps are localized states having trap energy ( $E_t$ ) lying within the forbidden energy gap

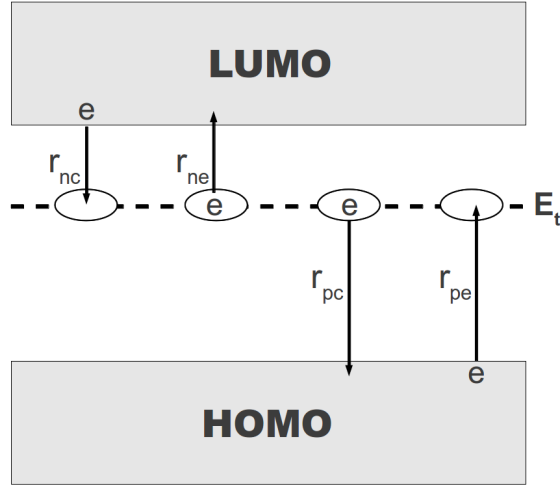


Figure 1.6: Diagram showing the four processes constituting the total Shockley-Read-Hall recombination: electron capture rate ( $r_{nc}$ ); electron emission rate ( $r_{ne}$ ); hole capture rate ( $r_{pc}$ ); and hole emission rate ( $r_{pe}$ )

The derivation of the SRH recombination equation is done by applying the detailed balance principle to the competing trapping and detrapping rates of both electrons and holes. Figure 1.6 shows the four rates associated with a single trap energy level at  $E_t$ . For  $N_t$  as the density of trap states, the probability that the states are occupied by trapped electrons  $f_t$ ; the rate at which free electrons (with density  $n$ ) are captured by the unoccupied

traps is

$$r_{nc} = C_n n N_t (1 - f_t), \quad (1.26)$$

where  $C_n$  is the electron capture coefficient. The occupied traps can also emit the trapped electrons back to the LUMO bands by the rate

$$r_{ne} = e_n N_t f_t, \quad (1.27)$$

where  $e_n$  is the electron emission coefficient. At the equilibrium conditions where  $r_{nc} = r_{ne}$ , a relation between  $C_n$  and  $e_n$  is established and leads to

$$r_{ne} = C_n n_1 N_t f_t, \quad (1.28)$$

where  $n_1$  is the number of electrons in the LUMO bands when the electron Fermi level equals to  $E_t$ [49], i.e.

$$n_1 = N_{LUMO} \exp\left(\frac{E_t - E_{LUMO}}{k_B T}\right). \quad (1.29)$$

When the semiconductor is not at equilibrium, the total electron capture rate is

$$U_{nc} = r_{nc} - r_{ne} = C_n n N_t (1 - f_t) - C_n n_1 N_t f_t. \quad (1.30)$$

Similarly, following the same considerations gives rise to the hole capture and emission rates that can be expressed by

$$r_{pc} = C_p p N_t f_t, \quad (1.31)$$

and

$$r_{pe} = C_p p_1 N_t (1 - f_t), \quad (1.32)$$

respectively.  $p_1$  is the number of holes in the HOMO bands when  $E_f = E_t$ , so

$$p_1 = N_{HOMO} \exp\left(\frac{E_{HOMO} - E_t}{k_B T}\right). \quad (1.33)$$

Consequently, the net hole capture rate is

$$U_{pc} = r_{pc} - r_{pe} = C_p p N_t f_t - C_p p_1 N_t (1 - f_t). \quad (1.34)$$

Under steady-state conditions where  $n$  and  $p$  are invariant with time, the rate  $U_{nc}$  must equal  $U_{pc}$  which also equal the total SRH recombination rate ( $R_{SRH}$ ). Solving  $U_{nc} = U_{pc}$  for  $f_t$  in terms of the other variables, the famous  $R_{SRH}$  rate is obtained and given by

$$R_{SRH} = \frac{C_n C_p N_t (np - n_1 p_1)}{C_n (n + n_1) + C_p (p + p_1)}. \quad (1.35)$$

From Equations 1.29 and 1.33,

$$\begin{aligned} n_1 p_1 &= N_{LUMO} N_{HOMO} \exp((E_{HOMO} - E_{LUMO})/k_B T) \\ &= N_{LUMO} N_{HOMO} \exp(-E_g/k_B T) = n_i^2, \end{aligned} \quad (1.36)$$

where  $E_g = E_{LUMO} - E_{HOMO}$  is the semiconductor energy gap and  $n_i$  is the intrinsic carrier density.

The values of the capture rates  $C_n$  and  $C_p$  have to be specified. Here we use the assumption that stationary traps and free carriers recombine under the influence of their mutual coulomb field, so the rates can be described by the Langevin bimolecular recombination[51, 77], i.e.

$$C_p = q \frac{\mu_p}{\epsilon} = k_{rec,p}, \quad (1.37)$$

and

$$C_n = q \frac{\mu_n}{\epsilon} = k_{rec,n}. \quad (1.38)$$

We can see that many aspects of the SRH recombination are similar to the f-t recombination in Eq. 1.8. However, the two theories are actually different, and the differences will be discussed thoroughly in Section 4.6.

## 1.8 Shockley-Read-Hall Recombination with Exponential Trap Distributions

In the previous section, trap states are represented by only a single trap energy level at  $E_t$ . In reality, there are many trap energy levels distributed in the band gap, so the trap states need to be described by a trap density of states function. Gaussian and exponential

distributions are the two most acknowledged trap distribution functions[90], and because of their shapes in the gap, traps are frequently referred to as tail states. In this section, the SRH recombination is extended to include the exponential trap distribution by integrating over electron trap energy  $E_{tn}$  in acceptor and hole trap energy  $E_{tp}$  in donor.

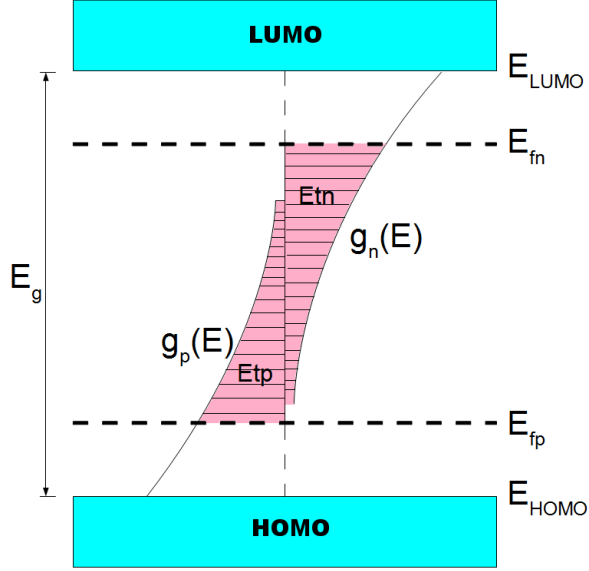


Figure 1.7: Energy band diagram of an organic semiconductor showing exponential tail state distributions from the LUMO ( $g_n(E)$ ) and from the HOMO ( $g_p(E)$ ) that are filled with trapped electrons and holes up to  $E_{fn}$  and  $E_{fp}$  respectively.

Consider the exponential tail states in the band gap in Fig. 1.7 of a semiconductor that is disturbed from equilibrium so that electron and hole densities are described by their own quasi-Fermi levels  $E_{fn}$  and  $E_{fp}$ . Non-intrinsic electrons and holes that are introduced to the system have to fill up the traps to the energies  $E_{fn}$  and  $E_{fp}$ . An exponential DOS of trapped electrons per unit energy range  $E_{tn}$  can be given by [86, 91]

$$g_n(E_{tn}) = \frac{H_A}{k_B T_{t,A}} \exp\left(\frac{E_{tn} - E_{LUMO}}{k_B T_{t,A}}\right), \quad (1.39)$$

where  $H_A$  and  $T_{t,A}$  are the total trapped electron density at the LUMO edge and the characteristic trapped electron temperature, respectively. They are the same as in Eq. 1.23 in the GWWF model section. Similarly, an exponential DOS function of trapped holes is

given by

$$g_p(E_{tp}) = \frac{H_D}{k_B T_{t,D}} \exp\left(\frac{E_{HOMO} - E_{tp}}{k_B T_{t,D}}\right), \quad (1.40)$$

where  $H_D$  and  $T_{t,D}$  have the same definitions as in Eq. 1.24. Assuming that traps occupy the states according to a Fermi-Dirac distribution function  $f(E_{tn,p}) = 1/[1 + \exp((E_{tn,p} - E_{fp})/k_B T)]$ , trapped electron and hole densities ( $n_t$  and  $p_t$ ) can be calculated from Eqs. 1.39 and 1.40 by

$$n_t = \int_{-\infty}^{E_{fn}} g_n(E_{tn}) f(E_{tn}) dE_{tn} \approx H_A \frac{k_B T_{t,A}}{k_B T_{t,A} - k_B T} \exp\left(\frac{E_{fn} - E_{LUMO}}{k_B T_{t,A}}\right), \quad (1.41)$$

and

$$p_t = \int_{E_{fp}}^{\infty} g_p(E_{tp}) [1 - f(E_{tp})] dE_{tp} \approx H_D \frac{k_B T_{t,D}}{k_B T_{t,D} - k_B T} \exp\left(\frac{E_{HOMO} - E_{fp}}{k_B T_{t,D}}\right), \quad (1.42)$$

as similarly proved by Ref. [92]. Generally, for  $T < T_{t,D(A)}$ ,  $n < n_t$  and  $p < p_t$ , Equations 1.41 and 1.42 can be approximated by Equations 1.23 and 1.24 respectively.

Each trap level in the DOS functions  $g_n(E_{Tn})$  and  $g_p(E_{tp})$  serves as a trapping/detrapping or recombination center as described in the SRH theory. Trapped hole density is much higher than trapped electron density in a donor and *vice versa* for trapped electron density in an acceptor; so that the interface carriers  $n_I$  and  $p_I$  are most probably captured and emitted by donor trapped holes at  $E_{tp}$  and acceptor trapped electrons at  $E_{tn}$  as illustrated by Figure 1.8. Consequently, the total SRH recombination rate at the D/A interface is calculated by the integration[51, 93];

$$R_{SRH} = \int_{E_{HOMO,A}}^{E_{fn}} \frac{g_n(E_{tn}) C_n C_p (n_I p_I - n_{i,A}^2)}{C_n [n_I + n_{1A}(E_{tn})] + C_p [p_I + p_{1A}(E_{tn})]} dE_{tn} \\ + \int_{E_{fp}}^{E_{LUMO,D}} \frac{g_p(E_{tp}) C_n C_p (n_I p_I - n_{i,D}^2)}{C_n [n_I + n_{1D}(E_{tp})] + C_p [p_I + p_{1D}(E_{tp})]} dE_{tp}, \quad (1.43)$$

where  $n_{1D(A)}$  and  $p_{1D(A)}$  are  $n_1$  and  $p_1$  as Eqs. 1.29 and 1.33 in the donor(acceptor), and  $n_{i,A(D)}^2 = N_{LUMO,A(D)} N_{HOMO,A(D)} \exp(-E_{g,A(D)}/k_B T)$ , where  $E_{g,A(D)}$  is the intrinsic energy gap of the acceptor(donor). For simplicity,  $N_{LUMO} = N_{LUMO,A} = N_{LUMO,D}$  and  $N_{HOMO} = N_{HOMO,A} = N_{HOMO,D}$  are used throughout this study.

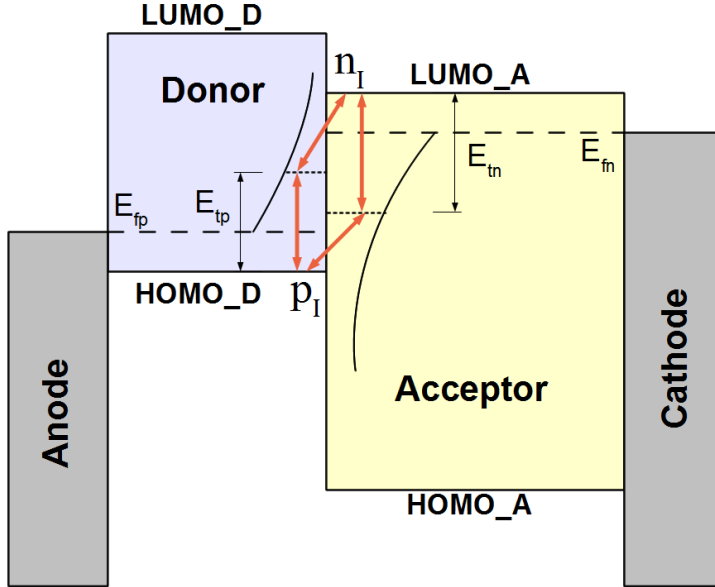


Figure 1.8: Total SRH recombination at the D/A interface as a result of net capture and emission of the interface charges ( $n_I$  and  $p_I$ ) by the interface donor trapped holes and the interface acceptor trapped electrons having energies  $E_{tp}$  and  $E_{tn}$  respectively.

## 1.9 Dissociation and Recombination Rates of Polaron Pairs

Interface polaron pairs, or the lowest lying charge transfer state, can either dissociate or recombine. Both of these rates are a function of the interface electric field ( $F_I$ ) as used in the GWWF model and in our analytical and numerical models. First, for the field that points out of the interface (i.e. dissociating field), the dissociation rate ( $k_{PPd}$ ) is described by the Bruan model[83]. It can be expressed by a dissociation rate at zero field ( $k_{PPd,0}$ ) multiplied by a field dependent term suggested by Onsager[94]. The resulting rate is sometimes called Onsager-Bruan (OB) dissociation rate, which is given by

$$k_{PPd} = k_{PPd,0} \frac{J_1[2\sqrt{-2b}]}{\sqrt{-2b}}, \quad (1.44)$$

where  $J_1$  is the first order Bessel function of the first kind and  $b = q^3 F_I / 8\pi\epsilon k_B^2 T^2$ , where  $\epsilon$  is spatially averaged dielectric constant. The rate ( $k_{PPd,0}$ ) is derived from dissociation of

an ion pair accompanied by consideration of detailed balance of the CT state. It is given by

$$k_{PPd,0} = \frac{3}{4\pi a_0^3} k_{rec} \exp(-E_b/k_B T), \quad (1.45)$$

where  $k_{rec}$  is Langevin bimolecular rate constant and  $E_b$  is polaron pair binding energy described by

$$E_b = \frac{q^2}{4\pi\epsilon a_0}. \quad (1.46)$$

Secondly, when the field points to the interface and suppresses the dissociation, an additional barrier is added to the PP binding energy, and  $k_{PPd}$  is averaged over the half sphere at the D/A interface[4]. The mathematical expression is given by

$$k_{PPd} = \frac{1}{\pi} \int_{-\pi/2}^{\pi/2} \frac{3}{4\pi a_0^3} k_{rec} \exp\left[\frac{-E_b + F_I r_c \cos\theta}{V_t}\right] d\theta, \quad (1.47)$$

where  $F_I r_c \cos\theta$  is the additioanl barrier,  $r_c = q^2/(4\pi\epsilon k_B T)$  is the Onsager radius, and  $\theta$  is the angel between the PP separation length vector and the D/A interface normal vector.

Another fate of the PPs is that they recombine with the rate  $k_{PPr}$ . According to paper II of GWWF [82], experimental data allowed them to formulate a field dependent  $k_{PPr}$  that is given by

$$k_{PPr} = k_{PPr0} \exp\left(\frac{-qF_I a_0}{k_B T}\right), \quad (1.48)$$

where  $k_{PPr0}$  is PP recombination in zero field. Note that the exponential term has opposite sign from the original paper because here the positive field is defined as the field that helps charge separation.

## 1.10 Overview

The contents in this thesis are organized as follows. In **Chapter 1**, introductions to solar cells, organic solar cells, the Shockley equation and its parameters, typical solar cell JV curves and the GWWF model are provided. Physics of charge distributions, trap densities and charge recombination processes are explained. The chapter ends with the interface polaron pair rates that are used in the GWWF model and our models.

In **Chapter 2**, we present our analytical models, namely the self-consistent diode (SCD) models, using different types of free carrier recombination. Physical definitions of saturated diode currents, ideality factors, series and parallel resistances, the diode voltage are formulated and explained.

In **Chapter 3**, the computational drift-diffusion for bilayer interfaces (DD-BI) model that is developed in this dissertation is presented. Basics of the drift-diffusion model and how to solve the equations in the model computationally are explained.

**Chapter 4** focuses on using the SCD and the DD-BI models to elucidate fundamental physics of bilayer OPVs. This chapter starts with advantages of the DD-BI and the SCD models when they deal with space charge effects, interface properties, series and parallel resistances as compared with the GWWF model. We show how charge densities distribute as a function of a distance from an electrode and how these distributions affect quasi-Fermi levels (chemical potentials) as a function of the distance. Effects of carrier mobilities on the charge distributions and quasi-Fermi levels are explained and connected to physical definitions of measurable series and parallel resistances. After that, physics regarding the electrodes' work functions, e.g. injection barriers and organic-semiconductor/metal contacts, are studied. Relations between ideality factors and trap characteristic energies are presented, and remarks on interpretations of fitted ideality factors are given. Finally, the SRH recombination is compared with its reduced forms.

**Chapter 5** copes with applications of our models on actual bilayer devices through use of the Shockley parameters  $R_s$ ,  $R_p$ ,  $J_0$  and  $n$  to explain the shapes of JV curves under illumination and dark conditions. Additional leakage current and  $R_p$  in the dark are proposed and compared with those under illumination conditions. The Shockley parameters as a function of applied voltage in the presence and absence of light are compared. Finally, remarks on relations between fitted Shockley parameters and physical properties are given.

In **Chapter 6**, we show *ab initio* calculations of growing a  $\text{CsSnBr}_3$  perovskite film; which is a promising material for bilayer photovoltaics, using a heteroepitaxy technique.

Band structures and densities of states of  $\text{CsSnBr}_3$  and  $\text{CsSn}_2\text{Br}_5$  are simulated using density functional theory. Processes of growing the epitaxial  $\text{CsSnBr}_3$  film are studied, and possible future works regarding a phase transition from  $\text{CsSnBr}_3$  to  $\text{CsSn}_2\text{Br}_5$  are suggested.

## CHAPTER 2

### ANALYTICAL MODEL WITH SPACE CHARGES

#### 2.1 Self-Consistence Ideal Diode (SCD) Equations

The interface densities in the GWWF model (Equations 1.12 and 1.13) are valid only at the open circuit conditions and do not take space charge effects into account. More accurate forms of the ideal diode equation with a better representation of space charge effects can be derived using more accurate interface densities calculations. In order to do this, Equations 1.12 and 1.13 are replaced by Equations 1.21 and 1.22, respectively. The latter have space charge effects included in terms of quasi-Fermi levels.

Here, we use the intermediate equation of  $J$  (Eq. 1.11) in the GWWF model as a general form of  $JV$  equation. It can be rewritten as

$$J = qa_0(1 - \eta_{PPd})R_{eq} \left( \frac{R}{R_{eq}} - \frac{k_{PPd}}{k_{PPd,eq}} \right) - qJ_X\eta_{PPd}. \quad (2.1)$$

This equation is an exact solution for any recombination types, based on the detailed balance conditions of the GWWF interface rates. With the approximation  $k_{PPd}/k_{PPd,eq} \approx 1$ [4] and  $R$  usually depends on the voltage exponentially, we will show in this section that it is in the same form as the Shockley equation with the term  $qa_0(1 - \eta_{PPd})R_{eq}$  equivalent to the saturation diode current ( $J_0$ ) and  $qJ_X\eta_{PPd}$  containing information about the leakage photocurrent.

In this part, ideal diode equations with space charge effects (or SCD equations) for bilayer solar cells with the f-f recombination (Eq. 1.7) and the f-t recombination (Eq. 1.8) are derived analytically. They will be compared and used cooperatively with the numerical DD-BI model summarized in Chapter 3, to elucidate the OPV physics in Chapter 4

### 2.1.1 The f-f Recombination

For the f-f recombination processes,  $R$  is given by (from Eqs. 1.7, 1.21, 1.22)

$$R_{f-f} = k_{rec} N_{LUMO} N_{HOMO} \exp\left(-\frac{E_{LUMO,A,I} - E_{HOMO,D,I}}{k_B T}\right) \exp\left(\frac{E_{fn,I} - E_{fp,I}}{k_B T}\right), \quad (2.2)$$

where  $E_{LUMO,A,I} - E_{HOMO,D,I}$  is the interface acceptor LUMO energy minus the interface donor HOMO energy. It is identical to the interface energy gap  $\Delta E_{HL}$  in the GWWF model and can be used interchangeably. At the equilibrium conditions where  $J_X = 0$  and  $V_a = 0$ , electron and hole quasi-Fermi levels do not split from the intrinsic Fermi level and  $E_{fn} = E_{fp} = E_f$ . For this reason, recombination rate at equilibrium is given by

$$R_{f-f,eq} = k_{rec} N_{LUMO} N_{HOMO} \exp\left(-\frac{E_{LUMO,A,I} - E_{HOMO,D,I}}{k_B T}\right). \quad (2.3)$$

Substituting  $R_{f-f}$  and  $R_{f-f,eq}$  into Eq. 2.1 yields a new ideal diode equation;

$$\begin{aligned} J = & q a_0 (1 - \eta_{PPd}) k_{rec} N_{LUMO} N_{HOMO} \exp\left(-\frac{E_{LUMO,A,I} - E_{HOMO,D,I}}{k_B T}\right) \\ & \times \left[ \exp\left(\frac{E_{fn,I} - E_{fp,I}}{k_B T}\right) - \frac{k_{PPd}}{k_{PPd,eq}} \right] - q J_X \eta_{PPd}. \end{aligned} \quad (2.4)$$

With the same assumption in the GWWF model that  $k_{PPd}/k_{PPd,eq} \approx 1$ [4], it is reduced to

$$J = J_{s0} \left[ \exp\left(\frac{E_{fn,I} - E_{fp,I}}{k_B T}\right) - 1 \right] - q J_X \eta_{PPd}, \quad (2.5)$$

where the diode saturation current is given by

$$\begin{aligned} J_{s0} &= q a_0 (1 - \eta_{PPd}) k_{rec} N_{LUMO} N_{HOMO} \exp\left(-\frac{E_{LUMO,A,I} - E_{HOMO,D,I}}{k_B T}\right) \\ &= q a_0 (1 - \eta_{PPd}) k_{rec} n_{I,eq} p_{I,eq} \\ &= q a_0 (1 - \eta_{PPd}) R_{f-f,eq} \end{aligned} \quad (2.6)$$

The ideal diode equation (Eq. 2.5) is similar to the one in the GWWF model except the diode voltage that equals to  $E_{fn,I} - E_{fp,I}$  instead of  $V_a - JR_s$ .

### 2.1.2 The f-t Recombination

For the f-t recombination, Eq. 1.8 is written in two separate terms as

$$R = R_{\text{fn-tp}} + R_{\text{fp-tn}} = k_{\text{rec},n} n_I p_{I,t} + k_{\text{rec},p} p_I n_{I,t} \quad (2.7)$$

for simplicity of derivation. Use this form of  $R$  to rewrite Equation 1.11 as

$$\begin{aligned} J &= q a_0 (1 - \eta_{PPd}) \left[ R_{\text{fn-tp}} + R_{\text{fp-tn}} - \frac{k_{PPd}}{k_{PPd,eq}} (R_{\text{fn-tp,eq}} + R_{\text{fp-tn,eq}}) \right] - q J_X \eta_{PPd} \\ &= q a_0 (1 - \eta_{PPd}) R_{\text{fn-tp,eq}} \left[ \frac{R_{\text{fn-tp}}}{R_{\text{fn-tp,eq}}} - \frac{k_{PPd}}{k_{PPd,eq}} \right] \\ &+ q a_0 (1 - \eta_{PPd}) R_{\text{fp-tn,eq}} \left[ \frac{R_{\text{fp-tn}}}{R_{\text{fp-tn,eq}}} - \frac{k_{PPd}}{k_{PPd,eq}} \right] - q J_X \eta_{PPd}. \end{aligned} \quad (2.8)$$

This equation has two diode terms having different physical origins that are in the same form as the general  $JV$  equation (Eq. 2.1). Using the interface charge densities in Eqs. 1.21 and 1.22 along with the trapped charge densities in terms of quasi-Fermi levels in Eqs. 1.23 and 1.24, the electron capture rate by trapped holes is

$$R_{\text{fn-tp}} = k_{\text{rec},n} N_{\text{LUMO}} H_D \exp \left[ -E'_{\text{LUMO},A,I} + E'_{\text{HOMO},D,I}/l_D + E'_{f,n,I} - E'_{f,p,I}/l_D \right], \quad (2.9)$$

and the free hole capture rate by trapped electrons is

$$R_{\text{fp-tn}} = k_{\text{rec},p} N_{\text{HOMO}} H_A \exp \left[ -E'_{\text{LUMO},A,I}/l_A + E'_{\text{HOMO},D,I} + E'_{f,n,I}/l_A - E'_{f,p,I} \right]. \quad (2.10)$$

Here the characteristic trap energy  $E_{t,D(A)}$  is written as  $l_{D(A)} k_B T$  and  $E' = E/k_B T$ . Under the equilibrium conditions, these two equations are given by

$$R_{\text{fn-tp,eq}} = k_{\text{rec},n} N_{\text{LUMO}} H_D \exp \left[ -E'_{\text{LUMO},A,I} + E'_{\text{HOMO},D,I}/l_D + (1 - 1/l_D) E'_f \right] \quad (2.11)$$

and

$$R_{\text{fp-tn,eq}} = k_{\text{rec},p} N_{\text{HOMO}} H_A \exp \left[ -E'_{\text{LUMO},A,I}/l_A + E'_{\text{HOMO},D,I} + (1/l_A - 1) E'_f \right]. \quad (2.12)$$

Using Eqs. 2.9 - 2.12 in 2.8 yields the ideal diode equation with space charges;

$$\begin{aligned}
J = & \quad qa_0(1-\eta_{PPd})k_{rec,n}N_{LUMO}H_D \exp \left[ -E'_{LUMO,A,I} + \frac{E'_{HOMO,D,I}}{l_D} + \left(1 - \frac{1}{l_D}\right) E'_f \right] \\
& \times \left\{ \exp \left[ (E'_{fn,I} - E'_{fp,I}) \left( 1 + \frac{(E_{fp,I} - E_f)(1 - 1/l_D)}{E_{fn,I} - E_{fp,I}} \right) \right] - \frac{k_{PPd}}{k_{PPd,eq}} \right\} \\
+ & \quad qa_0(1-\eta_{PPd})k_{rec,p}N_{HOMO}H_A \exp \left[ \frac{-E'_{LUMO,A,I}}{l_A} + E'_{HOMO,D,I} + \left( \frac{1}{l_A} - 1 \right) E'_f \right] \\
& \times \left\{ \exp \left[ (E'_{fn,I} - E'_{fp,I}) \left( 1 + \frac{(E_{fn,I} - E_f)(1/l_A - 1)}{E_{fn,I} - E_{fp,I}} \right) \right] - \frac{k_{PPd}}{k_{PPd,eq}} \right\} \\
- & \quad qJ_X\eta_{PPd}.
\end{aligned} \tag{2.13}$$

It can be written in a simple form as,

$$J = J_{sD} \left[ \exp \left( \frac{E_{fn,I} - E_{fp,I}}{n_D k_B T} \right) - 1 \right] + J_{sA} \left[ \exp \left( \frac{E_{fn,I} - E_{fp,I}}{n_A k_B T} \right) - 1 \right] - qJ_X\eta_{PPd}, \tag{2.14}$$

where  $J_{sD}$  and  $J_{sA}$  are respectively saturation currents associated with the fn-tp and the fp-tn processes, which are given by

$$\begin{aligned}
J_{sD} &= qa_0(1-\eta_{PPd})k_{rec,n}N_{LUMO}H_D \exp \left[ -E'_{LUMO,A,I} + \frac{E'_{HOMO,D,I}}{l_D} + \left(1 - \frac{1}{l_D}\right) E'_f \right] \\
&= qa_0(1-\eta_{PPd})k_{rec,n}n_{I,eq}p_{It,eq} \\
&= qa_0(1-\eta_{PPd})R_{fn-tp,eq},
\end{aligned} \tag{2.15}$$

and

$$\begin{aligned}
J_{sA} &= qa_0(1-\eta_{PPd})k_{rec,p}N_{HOMO}H_A \exp \left[ \frac{-E'_{LUMO,A,I}}{l_A} + E'_{HOMO,D,I} + \left( \frac{1}{l_A} - 1 \right) E'_f \right] \\
&= qa_0(1-\eta_{PPd})k_{rec,p}p_{I,eq}n_{It,eq} \\
&= qa_0(1-\eta_{PPd})R_{fp-tn,eq},
\end{aligned} \tag{2.16}$$

and  $n_D$  and  $n_A$  are ideality factors associated with the two recombination processes formulated as

$$n_D = \left( 1 + \frac{(E_{fp,I} - E_{f,I})(1 - 1/l_D)}{E_{fn,I} - E_{fp,I}} \right)^{-1} \tag{2.17}$$

and

$$n_A = \left( 1 + \frac{(E_{fn,I} - E_{f,I})(1/l_A - 1)}{E_{fn,I} - E_{fp,I}} \right)^{-1}. \tag{2.18}$$

### 2.1.3 The f-f and f-t Recombination

In the previous cases,  $n_I$  and  $p_I$  are designated to recombine either with other free carriers with the rate  $k_{rec}$  or with trapped charges with the rate  $k_{rec,n(p)}$ . However, it is possible that the f-f and the f-t recombination processes coexist, leading to the total recombination rate of

$$R_{f-f + f-t} = k_{rec}n_I p_I + k_{rec,n} n_I p_{It} + k_{rec,p} p_I n_{It}. \quad (2.19)$$

The ideal diode equation is then given,

$$\begin{aligned} J = & J_{s0} \left[ \exp\left(\frac{E_{fn,I} - E_{fp,I}}{k_B T}\right) - 1 \right] + J_{sD} \left[ \exp\left(\frac{E_{fn,I} - E_{fp,I}}{n_D k_B T}\right) - 1 \right] \\ & + J_{sA} \left[ \exp\left(\frac{E_{fn,I} - E_{fp,I}}{n_A k_B T}\right) - 1 \right] - q J_X \eta_{PPd}, \end{aligned} \quad (2.20)$$

where all the parameters are explained above. This equation is similar to the double diode EEC model in section 1.4. There are multiple diode currents where one of them has the ideality factor of unity ( $n = 1$ ), and the diode term from trap-assisted recombination is split into two distinct processes; fn-tp and fp-tn.

We should emphasize that the derived ideal equations in Eqs. 2.5, 2.14 and 2.20 come explicitly from fundamental physics. Each term has mathematical expression that has physical meaning. They do not have any extra terms for the resistances  $R_s$  and  $R_p$  because these are intrinsic properties and already included in the Fermi-Dirac charge distributions (Eqs. 1.21 and 1.22) and the PP rates. Unlike many other theoretical works that view  $R_s$  and  $R_p$  as extrinsic or fitting parameters, we instead extract them and their physical meanings from the equations. This is shown analytically in the next section and numerically in Chapter 4.

### 2.1.4 The SRH Recombination

For the SRH recombination in the integral form (Eq. 1.43), an explicit SCD equation like Eq. 2.5 for the f-f recombination or Eq. 2.14 for the f-t recombination cannot be written. However, we can use the general form of current density proposed by GWWF (Eq. 2.1) to

obtain an implicit SCD equation for the SRH process; which is

$$J = qa_0(1 - \eta_{PPd})R_{SRH,eq} \left( \frac{R_{SRH}}{R_{SRH,eq}} - \frac{k_{PPd}}{k_{PPd,eq}} \right) - qJ_X\eta_{PPd}, \quad (2.21)$$

where  $R_{SRH,eq}$  is the total SRH recombination rate under equilibrium conditions. Assuming that the term  $R_{SRH}/R_{SRH,eq}$  is in the same form as in the f-f and the f-t cases, i.e.  $R_{SRH}/R_{SRH,eq} = \exp((E_{fn,I} - E_{fp,I})/n_{SRH}k_B T)$ , where  $n_{SRH}$  is the ideality factor from the SRH recombination, Equation 2.21 can be reduced to the generalized Shockley form;

$$J = J_{s,SRH} \left[ \exp \left( \frac{E_{fn,I} - E_{fp,I}}{n_{SRH}k_B T} \right) - 1 \right] - qJ_X\eta_{PPd}, \quad (2.22)$$

where  $J_{s,SRH} = qa_0(1 - \eta_{PPd})R_{SRH,eq}$  is the diode saturation current, and  $n_{SRH}$  is given by

$$n_{SRH} = \frac{E_{fn,I} - E_{fp,I}}{k_B T \ln \left( \frac{R_{SRH}}{R_{SRH,eq}} \right)}. \quad (2.23)$$

## 2.2 Diode Voltage, Series and Parallel Resistances

As seen in the generalized Shockley equation and the EEC model (see section 1.4), series ( $R_s$ ) and parallel ( $R_p$ ) resistance are as important as  $J_{sc}$ ,  $V_{oc}$ , and  $FF$  as efficiency parameters. Experimentalists usually fit the Shockley equation (Eq. 1.3) with their JV data to extract  $R_s$  and  $R_p$ . Conventionally,  $R_s$  represents total resistance of all bulk materials and contacts, and  $R_p$  is interpreted as leakage current at the interface due to imperfect contact. Smaller  $R_s$  is preferable as well as higher  $R_p$ . In order to understand the physical meaning of  $R_s$  and  $R_p$  in the OPV point of view, the diode voltage ( $V_d$ ) has to be discussed first.

The diode equation is usually given by

$$J_d = J_0(\exp(V_d/nV_t) - 1), \quad (2.24)$$

where  $J_d$  is a current flowing through the diode,  $V_d$  is diode voltage and  $V_t = k_B T/q$  is thermal voltage.  $V_d$  is defined as a voltage right across the junction or interface, that drives the current  $J_d$  through it. In the case of p-n junctions, it is originally and sometimes called

junction voltage[31]. It is the applied voltage ( $V_a$ ) across anode and cathode reduced by the total series resistance loss;

$$V_d = V_a - JR_s. \quad (2.25)$$

Comparing this to equation 2.20 for organic heterojunctions, we have

$$V_d = E_{fn,I} - E_{fp,I}. \quad (2.26)$$

Hence, what drives a current through the D/A interface is the quasi-Fermi level splitting, which equals the difference between the interface electron quasi-Fermi level in acceptor ( $E_{fn,I}$ ) and the interface hole quasi-Fermi level in donor ( $E_{fp,I}$ ). It should be noted that, by saying driving a current through the interface, holes in the donor and electrons in the acceptor are driven to the interface to recombine, resulting in a hole current in the donor and an electron current in the acceptor that are equal to each other. The splitting  $E_{fn,I} - E_{fp,I}$  actually promotes interface free carrier recombination ( $R$ ), and hence both holes and electrons are driven to the interface. Because the bilayer device is unipolar, i.e. current density is conducted by holes in the donor and by electrons in the acceptor, higher recombination  $R$  implies that more current is flowing in the device.

The relations for  $V_d$  lead to  $R_s$  that is given by

$$R_s = \frac{V_a - (E_{fn,I} - E_{fp,I})}{J} = \frac{(WF_c - E_{fn,I}) + (E_{fp,I} - WF_a)}{J}, \quad (2.27)$$

where the second form is obtained by using  $V_a = WF_c - WF_a$  where  $WF_c$  and  $WF_a$  are the work functions of cathode and anode, respectively. According to the first form, one can view  $R_s$  as a resistance that reduces the voltage difference  $V_a$  between the anode and cathode to become the actual diode voltage  $E_{fn,I} - E_{fp,I}$  at the interface. More precisely, according to the second form,  $R_s$  causes total deviation of energy levels from  $WF_a$  to  $E_{fp,I}$  and from  $WF_c$  to  $E_{fn,I}$ . It will be shown later that quasi-Fermi levels can be reduced by charge transfer at the contacts and bulk materials due to space charges. This agrees with the conventional meaning of  $R_s$ .

For  $R_p$ , by writing the term  $qJ_X\eta_{PPd}$  in both the GWWF model and Eq. 2.20 as  $qJ_X + qJ_X(1 - \eta_{PPd})$  to represent a constant photo-generated and a leakage current, a simple comparison between this and the generalized Shockley equation (Eq. 1.3) results in

$$R_p = \frac{V_d}{qJ_X(1 - \eta_{PPd})} = \frac{E_{fn,I} - E_{fp,I}}{qJ_X(1 - \eta_{PPd})}. \quad (2.28)$$

Figure 2.1 is an illustration of the following  $R_p$  explanation. The term  $qJ_X$  can be interpreted as a constant supply of PPs as if the interface is connected to a reservoir of incoming PPs. The term  $(1 - \eta_{PPd}) = k_{PPr}/(k_{PPr} + k_{PPd})$  is the probability of geminate PP recombination via  $k_{PPr}$ . Thus,  $qJ_X(1 - \eta_{PPd})$  is a recombination current that is like a fictitious leakage flowing backward against the photocurrent. Due to that the interface has a voltage of  $V_d = E_{fn,I} - E_{fp,I}$ , the parallel resistance is then a fictitious resistance that controls the recombination current.

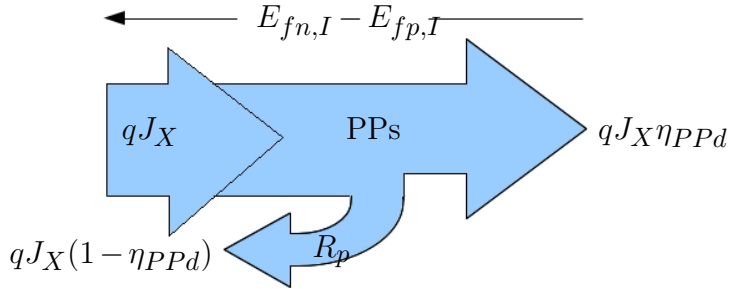


Figure 2.1: Schematic flow of the constant exciton current ( $qJ_X$ ) through the PP processes at the interface resulting in the photo-current  $qJ_X\eta_{PPd}$  and the recombined exciton current ( $qJ_X(1 - \eta_{PPd})$ ) that is flowing through  $R_p$ .

## 2.3 Definition of Illumination Conditions

Solar cells are usually tested under *standard test conditions* (stc) where the solar cell temperature is kept at  $25^\circ$ , solar irradiance is  $1000 \text{ W/m}^2$  and the testing location is at latitude  $42^\circ\text{N}$ . The latter is usually referred to as air-mass 1.5 (AM1.5), which is defined as the ratio of optical path length to the Sun to optical path length to the Sun when the Sun is directly above, i.e.  $\text{AM1.5} = 1/\sin(42^\circ) = \text{cosec}(42^\circ) = 1.5$ .

There are many factors affecting the amount of excitons that are created by exposing a solar cell to sunlight. These include the light reflectivity, the light adsorptivity, refractive index and exciton generation rate per unit volume as a function of the depth from the surface of the solar cell. In this study, these factors are not taken into account, and the illumination conditions are represented by a constant exciton current  $J_X$  which is a fitting parameter and approximately equal to the short circuit current (i.e.  $J_{sc} \approx qJ_X$ ).

## 2.4 Conclusions

In this chapter, we show derivations of our analytic JV equations; the self-consistent diode (SCD) equations. The derivations are similar to those in the GWWF model, but instead of using the problematic interface charge relations in Equations 1.12 and 1.13 (see Section 4.1), we use the ones that obey quasi Fermi-Dirac statistics in Equations 1.21 and 1.22. For the f-f recombination, Equations 2.4, 2.5 and 2.6 are the SCD equations. For the f-t recombination, the SCD equation is shown in Equation 2.14, and the definitions of the saturated diode currents and ideality factors are given by Equations 2.15, 2.16, 2.17 and 2.18. If the recombination does not have an explicit expression (e.g. the SRH recombination), Equations 2.22 and 2.23 are general SCD equations that can be applied for any recombination types.

Additionally, physical meanings of series and parallel resistances are obtained. Based on the SCD equations, series resistance is the resistance that results in the diode voltage of  $E_{fn,I} - E_{fp,I}$  (i.e.  $V_a - JR_s = E_{fn,I} - E_{fp,I}$ ), and parallel resistance under illumination conditions is the recombination resistance for the recombined exciton current ( $qJ_X(1 - \eta_{PPd})$ ).

## CHAPTER 3

### NUMERICAL MODEL

#### 3.1 the Drift-Diffusion model for Bilayer Interfaces (DD-BI model)

The DD-BI model is a combination of the numerical drift-diffusion model and the GWWF interface model. The drift-diffusion model is a computational iterative scheme, comprising solving the Poisson equation, the current continuity equations, and the drift-diffusion equations. This model has been widely applied to many semiconductor applications[69, 70, 71, 72, 73, 74] with the main purpose of including space charge effects. Because of the very small thickness-to-surface area ratio of OPV films, one-dimensional modeling along the thickness dimension is often sufficient to represent an OPV device. The Poisson equation in one dimension is given by

$$\frac{\partial^2}{\partial x^2} \psi(x) = \frac{q}{\epsilon} [n(x) - p(x)], \quad (3.1)$$

where  $\psi(x)$  is electrostatic potential at a distance  $x$  from the anode. The time-independent current continuity equations are given by

$$\begin{aligned} \frac{\partial}{\partial x} J_n(x) &= -qU(x), \\ \frac{\partial}{\partial x} J_p(x) &= qU(x), \end{aligned} \quad (3.2)$$

where  $J_{n(p)}$  is electron (hole) current density and  $U(x)$  is total free carrier generation rate, which is equal to  $k_{PPd}\zeta - R$ . These equations are normally coupled with the following drift-diffusion equations.

$$\begin{aligned} J_n &= -qn\mu_n \frac{\partial}{\partial x} \psi + q\mu_n V_t \frac{\partial}{\partial x} n, \\ J_p &= -qp\mu_p \frac{\partial}{\partial x} \psi - q\mu_p V_t \frac{\partial}{\partial x} p, \end{aligned} \quad (3.3)$$

where the argument  $x$  is dropped for convenience. One can couple Eqs. 3.2 with Eq. 3.3 by finding derivatives of Eq. 3.3 with respect to  $x$  and comparing to the charge generation rate

$\pm qU(x)$ . Current density equations containing both drift and diffusion terms in Eq. 3.3 are also used in calculations of total current density ( $J$ ), which is the sum of  $J_n$  and  $J_p$ .

In computer programming, the continuous distance  $x$  is discretized into a mesh. In this study, the zeroth mesh point is at the anode and the  $L^{th}$  mesh point is at the cathode. Adjacent  $x$  nodes are separated by the mesh width ( $\delta x$ ) of around 1-2 nm. The total film thickness is, hence,  $L\delta x$ . The D/A interface is between the point  $l^{th}$  and  $(l+1)^{th}$ . For simplicity, the mesh width is assigned to be equal to the interface width, which is 1.5nm according to the GWWF model.

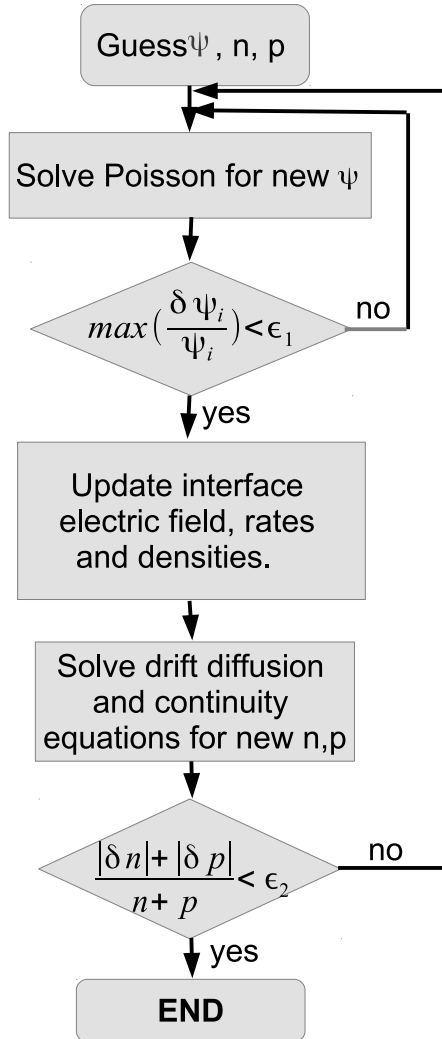


Figure 3.1: Flowchart of the numerical DD-BI model.

The DD-BI model is implemented into a computer code using the flowchart as shown in

Fig. 3.1. It is developed based on the Gummel scheme[95] and a work by Koster et al.[70]. Firstly, initial and boundary conditions of charge densities and potential profile are set using the following conditions.

$$p_0 = N_{HOMO}, \quad p_L = N_{HOMO} \exp(-(E_{LUMO,A} - E_{HOMO,A})/V_t). \quad (3.4)$$

$$n_L = N_{LUMO}, \quad n_0 = N_{LUMO} \exp(-(E_{LUMO,D} - E_{HOMO,D})/V_t). \quad (3.5)$$

$$\psi_L - \psi_0 = V_{bi} - V_a. \quad (3.6)$$

The subscripts refer to the  $n^{th}$  mesh points and  $V_{bi}$  is built-in potential defined by

$$V_{bi} = WF_a - WF_c = \Delta E_{HL} - \phi_a - \phi_c. \quad (3.7)$$

The built-in potential is a potential that helps move free carriers from the interface to the electrodes where they can be extracted to an external circuit. For initial values of  $n_i$ ,  $p_i$ , and  $\psi_i$  where  $i$  does not belong to one of the above boundary conditions, data from a pre-converged calculation with similar  $V_a$  can be used. If they are not available, the smallest value in Eq. 3.4 and Eq. 3.5 is a good initial value for any  $n_i$  and  $p_i$ . For  $\psi_i$ , a linear function from  $\psi_0$  to  $\psi_L$  is also a good guess for the initial potential.

After setting the initial conditions, the Poisson equation in Eq. 3.1 is solved numerically. In order to do this, it has to be discretized. First, consider the following Taylor series expansions.

$$\psi(x + \delta x) = \psi(x) + \delta x \psi'(x) + \frac{\delta x^2}{2} \psi''(x) + \frac{\delta x^3}{6} \psi^{(3)}(x) + \frac{\delta x^4}{24} \psi^{(4)}(x) + \dots \quad (3.8)$$

$$\psi(x - \delta x) = \psi(x) - \delta x \psi'(x) + \frac{\delta x^2}{2} \psi''(x) - \frac{\delta x^3}{6} \psi^{(3)}(x) + \frac{\delta x^4}{24} \psi^{(4)}(x) + \dots \quad (3.9)$$

One can have an approximation for  $\partial^2 \psi / \partial x^2$  by adding the two Taylor expansions.

$$\frac{\partial^2}{\partial x^2} \psi = \frac{\psi(x - \delta x) - 2\psi(x) + \psi(x + \delta x)}{\delta x^2} + O(\delta x^4), \quad (3.10)$$

where  $O(\delta x^4)$  is an error proportional to  $\delta x^4$ , which is very small compared to the other terms. Consequently, the discrete form of the Poisson equation is obtained as

$$\frac{\psi_{i-1} - 2\psi_i + \psi_{i+1}}{\delta x^2} = \frac{q}{\epsilon} [n_i - p_i], \quad (3.11)$$

for  $i = 1, 2, \dots, L - 1$ . However, numerical difference between  $n_i$ ,  $p_i$  and  $\psi_i$  can be problematic and causes instability in numerical calculations. This can be alleviated by scaling all the variables so they are in comparable orders of magnitude. Here, the scaled variables are  $\psi'_i = \psi_i/V_t$ ,  $n'_i = n_i/N$ , and  $p'_i = p_i/N$  where  $N \approx N_{LUMO}$  or  $N_{HOMO}$ . Please note that the prime marks here indicate numerical scaling, not the first derivative. Ultimately, the solvable Poisson equation is given by

$$\psi'_{i-1} - 2\psi'_i + \psi'_{i+1} = \frac{qN\delta x^2}{\epsilon V_t} [n'_i - p'_i]. \quad (3.12)$$

If trapped charges are taken into account,  $n'_i$  and  $p'_i$  are total densities including the trapped charges. There are  $L - 1$  equations of Eq. 3.12 from the 1<sup>st</sup> to  $L - 1$ <sup>th</sup> node, which can be written in a matrix form as

$$\begin{pmatrix} -2 & 1 & 0 & 0 & \cdots & 0 \\ 1 & -2 & 1 & 0 & \cdots & 0 \\ 0 & 1 & -2 & 1 & \cdots & 0 \\ \vdots & & & \ddots & & \vdots \\ 0 & \cdots & 0 & 0 & 1 & -2 \end{pmatrix} \begin{pmatrix} \psi'_1 \\ \psi'_2 \\ \psi'_3 \\ \vdots \\ \psi'_{L-1} \end{pmatrix} = \frac{qN\delta x^2}{\epsilon V_t} \begin{pmatrix} n'_1 - p'_1 \\ n'_2 - p'_2 \\ n'_3 - p'_3 \\ \vdots \\ n'_{L-1} - p'_{L-1} \end{pmatrix} - \begin{pmatrix} \psi'_0 \\ 0 \\ 0 \\ \vdots \\ \psi'_L \end{pmatrix}, \quad (3.13)$$

or

$$\mathbf{A}_\psi \psi = \mathbf{b}_\psi, \quad (3.14)$$

where  $\mathbf{A}_\psi$  is a tridiagonal matrix. Here Poisson's equation in Eq. 3.14 is solved for a potential profile  $\psi$  from known charge profiles  $\mathbf{n}$  and  $\mathbf{p}$ . This can be done by taking the matrix inverse to obtain  $\psi = \mathbf{A}_\psi^{-1} \mathbf{b}_\psi$ . The mathematics theorem that is used for inverting a tridiagonal matrix in this study was proposed by R.A. Usmani[96]. This step is repeated until the highest percentage change of  $\psi_i$  is less than a small number ( $\epsilon_1 \approx 1.0 \times 10^{-18}$  or  $1.0 \times 10^{-16}$ ). This is usually easy to converge to  $\epsilon_1$  within only one repeat.

New converged values, or updated,  $\psi_i$  provide a new electrostatic field at the interface ( $F_I$ ) by

$$F_I = F_{l+1/2} = -(\psi_{l+1} - \psi_l)/a_0. \quad (3.15)$$

This new field will update the interface rates in the GWWF model. Three rates,  $k_{PPd}$ ,  $k_{PPr}$  and  $R$ , are taken into consideration. Let's define the positive field as the field pointing from acceptor to donor; i.e. the field that promotes charge dissociation and extraction, and *vice versa* for negative field. Equation 1.44, written in terms of a Bessel function expansion is

$$k_{PPd} = \frac{3}{4\pi a_0^3} k_{rec} \exp(-E_b/k_B T) \left[ 1 + b + \frac{b^2}{3} + \frac{b^3}{18} + \frac{b^4}{180} \right], \quad (3.16)$$

which is useful to calculate the  $k_{PPd}$  rate under a positive field. If  $F_I$  is negative, Eq. 1.47 is used instead. The rate  $k_{PPr}$  expressed in Eq. 1.48 is also straightforwardly updated. For the free carrier recombination  $R$ , Eqs. 1.7 and/or 1.8 or 1.43 are applied, depending on the recombination type at the interface. After that, the polaron pair density ( $\zeta$ ) is accordingly updated using detailed balance conditions suggested in the GWWF model. It is simply given by

$$\zeta = \frac{J_X/a_0 + k_{PPr}\zeta_{eq} + R}{k_{PPr} + k_{PPd}}. \quad (3.17)$$

Ultimately, net generation rate of free carriers is updated using the relation  $U_l = U_{l+1} = k_{PPd}\zeta - R$ .

The current continuity equations coupled with the drift diffusion equations are solved in the following step using new  $\psi_i$  and  $U_{l(l+1)}$  as one of the arguments. However, according to Scharfetter and Gummel[97], when the potential difference between two adjacent mesh points exceeds  $2V_t$ , numerical instability may occur and the standard finite difference approach is unable to solve the problem. They suggested a method to mitigate this problem by considering charge densities as a function of  $x$  in the form  $n(x) = a + be^{cx}$  which finally leads to more stable discretized current density equations;

$$J_{p,i+1/2} = -\frac{qV_t N \mu_{p,i+1}}{\delta x} (B(-\delta\psi'_{i+1})p'_{i+1} - B(\delta\psi'_{i+1})p'_i), \quad (3.18)$$

$$J_{n,i+1/2} = \frac{qV_t N \mu_{n,i+1}}{\delta x} (B(\delta\psi'_{i+1})n'_{i+1} - B(-\delta\psi'_{i+1})n'_i), \quad (3.19)$$

where  $\delta\psi'_{i+1} = \psi'_{i+1} - \psi'_i$  and  $B()$  is the Bernouli function defined by

$$B(x) = \frac{x}{\exp(x) - 1}. \quad (3.20)$$

Any energy offsets (e.g.  $E_{LUMO,A} - E_{LUMO,D}$  for an electron at the interface) and barriers (e.g. injection barriers  $\phi_a$  and  $\phi_c$ ) are simply added to  $\delta\psi'_i$  at the corresponding  $i^{th}$  point. The discrete current density relations are now solvable by the standard central finite difference, i.e.

$$\frac{\partial J_{n(p),i}}{\partial x} \approx \frac{J_{n(p),i+1/2} - J_{n(p),i-1/2}}{\delta x}, \quad (3.21)$$

and results in the final formulas to be solved iteratively as

$$\begin{aligned} -\frac{qV_t N}{\delta x^2} \left[ \mu_{n,i+1} B(\delta\psi'_{i+1}) n'_{i+1} - (\mu_{n,i+1} B(-\delta\psi'_{i+1}) + \mu_{n,i} B(\delta\psi'_i)) n'_i + \mu_{n,i} B(-\delta\psi'_i) n'_{i-1} \right] &= qU_i, \\ -\frac{qV_t N}{\delta x^2} \left[ \mu_{p,i+1} B(-\delta\psi'_{i+1}) p'_{i+1} - (\mu_{p,i+1} B(\delta\psi'_{i+1}) + \mu_{p,i} B(-\delta\psi'_i)) p'_i + \mu_{p,i} B(\delta\psi'_i) p'_{i-1} \right] &= qU_i. \end{aligned} \quad (3.22)$$

Similarly to Poisson equation, they form matrix equations

$$\mathbf{A}_n \mathbf{n} = \mathbf{b}_n \quad (3.23)$$

and

$$\mathbf{A}_p \mathbf{p} = \mathbf{b}_p, \quad (3.24)$$

respectively, where

$$\mathbf{A}_n = \begin{pmatrix} -(\mu_{n,2}B(-\delta\psi'_2) + \mu_{n,1}B(\delta\psi'_1)) & \mu_{n,2}B(\delta\psi'_2) & 0 & \cdots & 0 \\ \mu_{n,2}B(-\delta\psi'_2) & -(\mu_{n,3}B(-\delta\psi'_3) + \mu_{n,2}B(\delta\psi'_2)) & \mu_{n,3}B(\delta\psi'_3) & \cdots & 0 \\ \vdots & & & \ddots & \\ 0 & \cdots & \mu_{n,L-1}B(-\delta\psi'_{L-1}) & -(\mu_{n,L}B(-\delta\psi'_L) + \mu_{n,L-1}B(\delta\psi'_{L-1})) & \end{pmatrix}, \quad (3.25)$$

$$\mathbf{A}_p = \begin{pmatrix} -(\mu_{p,2}B(\delta\psi'_2) + \mu_{p,1}B(-\delta\psi'_1)) & \mu_{p,2}B(-\delta\psi'_2) & 0 & \cdots & 0 \\ \mu_{p,2}B(\delta\psi'_2) & -(\mu_{p,3}B(\delta\psi'_3) + \mu_{p,2}B(-\delta\psi'_2)) & \mu_{p,3}B(-\delta\psi'_3) & \cdots & 0 \\ \vdots & & & \ddots & \\ 0 & \cdots & \mu_{p,L-1}B(\delta\psi'_{L-1}) & -(\mu_{p,L}B(\delta\psi'_L) + \mu_{p,L-1}B(-\delta\psi'_{L-1})) & \end{pmatrix}, \quad (3.26)$$

$$\mathbf{n} = \begin{pmatrix} n'_1 \\ n'_2 \\ \vdots \\ n'_{L-1} \end{pmatrix}, \quad \mathbf{b}_n = -\frac{\delta x^2}{V_t N} \begin{pmatrix} U_1 \\ U_2 \\ \vdots \\ U_{L-1} \end{pmatrix} - \begin{pmatrix} \mu_{n,1}B(-\delta\psi'_1)n'_0 \\ 0 \\ \vdots \\ \mu_{n,L}B(\delta\psi'_L)n'_L \end{pmatrix}, \quad \mathbf{p} = \begin{pmatrix} p'_1 \\ p'_2 \\ \vdots \\ p'_{L-1} \end{pmatrix}, \quad \mathbf{b}_p = -\frac{\delta x^2}{V_t N} \begin{pmatrix} U_1 \\ U_2 \\ \vdots \\ U_{L-1} \end{pmatrix} - \begin{pmatrix} \mu_{p,1}B(\delta\psi'_1)p'_0 \\ 0 \\ \vdots \\ \mu_{p,L}B(-\delta\psi'_L)p'_L \end{pmatrix}. \quad (3.27)$$

The matrices  $\mathbf{A}_n$  and  $\mathbf{A}_p$  are tridiagonal and can be solved with the same method as used for solving the Poisson equation.

The algorithm is an iterative scheme. Starting from guessed charge density profiles  $[\mathbf{n}]_i$  and  $[\mathbf{p}]_i$ , Poisson's equation yields a new potential profile  $[\psi]_i$ , that is inserted in the current continuity equations to be solved for new charge density profiles, which starts another loop of the scheme. These will be repeated until the percentage change of  $[\mathbf{n}]_i$  and  $[\mathbf{p}]_i$  are very small, which is normally around the significant decimal digits of the numerical format used in the program. Double-precision floating-point format, having about 15-17 significant decimal digits, is used in this study, so the convergence condition is

$$\max \left( \frac{|n_{i,new} - n_{i,old}| + |p_{i,new} - p_{i,old}|}{n_{i,old} + p_{i,old}} \right) \lesssim 10^{-14}, \quad (3.28)$$

where the subscripts *old* and *new* refer to values from the previous and current loop, respectively. After the simulation is converged, total current density  $J$  is calculated by summing Eq. 3.18 and Eq. 3.19, at any mesh point  $i$ .

It should be noted that, even using the Scharfetter-Gummel method[97], numerical instability is still a problem. This problem is alleviated by setting charge densities for the next iteration with mixed values from the old densities, e.g.,  $n_{i,new} = w n_{i,new} + (1-w)n_{i,old}$ , where  $w$  is the mixing parameter. It is normally less than 0.1 or as small as  $10^{-5}$  in hard-to-converge circumstances such as at high  $V_a$ , where numerical instability is severe. Here, the DD-BI model works well up to  $V_a$  a little higher than  $V_{oc}$ , after which convergence is difficult.

## 3.2 Conclusions

In this chapter, we present our numerical model; the drift-diffusion for bilayer interface (DD-BI) model, which is an extension of the GWWF but interface properties, such as interface densities, interface electric field, dissociation and recombination rates of polaron pairs, are solved self-consistently using an iterative numerical method instead of an approximation.

The advantages of the DD-BI model are better treatments of space charge effects and more correct interface properties.

The algorithm of the model is illustrated in Figure 3.1. The central part of the program is to solve the Poisson equation (Eq. 3.12) and the drift-diffusion equations coupled with current continuity equations (Eq. 3.22) iteratively until the charge density profiles ( $n(x)$  and  $p(x)$ ) converge. The equations are written in tridiagonal matrices and can be solved using a mathematical theorem to invert the tridiagonal matrices. Contributions of the GWWF model are the interface rates and polar pair density in Eq. 3.17. Once a simulation converges, Equations 3.18 and 3.19 are used to calculate total current density, resulting in a  $J - V_a$  characteristic.

## CHAPTER 4

### PHYSICS OF OPVS

Fundamental physics of OPVs is studied in this chapter using the DD-BI and the SCD models that are described in Chapter 3 and 2, respectively. We start this chapter by comparing our models with the GWWF model to show that better treatments of interface densities, space charge effects, series resistance and interface electric field are included in our models. In Section 4.2, effects of carrier mobilities are explained in terms of spatial charge distributions, quasi-Fermi levels, interface rates, series and parallel resistances. In Section 4.3 and 4.4, we explain effects of injection barriers using our models in conjunction with the ICT and Mott-Schottkey models. Understanding how quasi-Fermi levels drop across injection barriers leads to better understanding of series resistance. In Section 4.5, relations between ideality factors and trap characteristics are studied. Lastly, in Section 4.6, we show differences between the SRH recombination and the f-t recombination which is understood as a reduced form the SRH recombination.

## 4.1 The Differences Between the Current Models and the GWWF Model

### 4.1.1 Introduction

Interface charge densities ( $n_I$  and  $p_I$ ) are very crucial in describing the D/A interface because they determine the interface recombination,  $R$ , in Eqs. 1.7, 1.8, 1.35 and 1.43 and the interface electric field ( $F_I$ ); which is an important contributer to the rates  $k_{PPd}$  (Eqs. 1.44 and 1.47),  $k_{PPr}$  (Eq. 1.48) and, most importantly, the polaron pair dissociation efficiency,  $\eta_{PPd} = k_{PPd}/(k_{PPd} + k_{PPr})$ . The densities  $n_I$  and  $p_I$  are obtained from solving the charge transport equations (Eqs. 3.1, 3.2 and 3.3), using electrode charge densities ( $n_C$  and  $p_C$ ) and the terminal voltage ( $V_{bi} - V_a$ ) as boundary conditions. However, because of the low mobilities in OPVs, spatial charge accumulation (i.e. space charge effect) is common and

complicates the charge transport, so the equations have to be solved self-consistently.

The GWWF model; which is not a self-consistent model, uses Eqs. 1.12 and 1.13, that require voltage drops across donor ( $\delta_D$ ) and acceptor ( $\delta_A$ ) as inputs, to estimate  $n_I$ ,  $p_I$  and  $F_I$ . As we will show in this section, Eqs. 1.12 and 1.13 are invalid and result in misinterpretations in the following aspects: (i) Interface densities and rates; (ii) Space charge effects; (iii) Series resistance ( $R_s$ ); (iv) Injection barriers ( $\phi_a$  and  $\phi_c$ ); (v)  $\delta_D$  and  $\delta_A$ ; (vi) Traps in the bulk and at the interface.

In contrast, the DD-BI model; which is the computational model developed in this study, is based on the numerical self-consistent drift-diffusion simulation and the D/A interface described by the GWWF model. The purpose of combining these models is to provide a self-consistent extension of the GWWF model. The SCD equations which are analytic forms of the DD-BI model also have the self-consistency if each parameter is an actual function of  $V_a$ , extracted from the DD-BI model. Accordingly, advantages of the DD-BI and the SCD models are that they treat the aspects (i)-(vi) self-consistently. This part of thesis shows the differences between the DD-BI/SCD model and the GWWF model.

#### 4.1.2 Simulation Details

The models are compared by generating JV characteristics based on the same set of parameters; which are taken from Table II of the GWWF paper, and are summarized in Table 4.1. It should be remarked that the injection barriers ( $\phi_a$  and  $\phi_c$ ) cancel out in the GWWF derivation, so no information about them or their effects can be found in the paper. From the interfacial energy gap ( $\Delta E_{HL}$ ) of 1.2eV and the built-in potential ( $V_{bi}$ ) of 0.5eV, the summation of  $\phi_c$  and  $\phi_a$  has to be 0.7eV according to  $V_{bi} = \Delta E_{HL} - \phi_c - \phi_a$ . For this reason, three sets of  $\phi_a$  and  $\phi_c$  are analyzed: (1)  $\phi_a = 0.1\text{eV}$  and  $\phi_c = 0.6\text{eV}$ ; (2)  $\phi_a = 0.2\text{eV}$  and  $\phi_c = 0.5\text{eV}$ ; (3)  $\phi_a = 0.3\text{eV}$  and  $\phi_c = 0.4\text{eV}$ . However, these high injection barriers are not desirable for efficiency OPVs, so we include three more cases of lower  $\phi_a/\phi_c$ : (1) 0.1eV/0.3eV; (2) 0.2eV/0.3eV; and (3) 0.3eV/0.3eV. Another remark is that in the GWWF model, series

resistance ( $R_s$ ) is inserted manually ( $R_s = 1 \times 10^{-4} \Omega m^2$ ). In the DD-BI model,  $R_s$  is an intrinsic property, arising from the mobilities of the donor and acceptor and the contacts at the anode and the cathode (more discussion can be found in Section 4.4.5). Hence,  $R_s$  is not added to the DD-BI model simulations, but is instead a result of the analysis. Additionally, the DD-BI model solves drift-diffusion equations for the interface charge densities, but the GWWF model uses Equations 1.12 and 1.13 with empirical values of the fractions of potential dropped  $\delta_D = 0.9$  and  $\delta_A = 0.1$ . We find that for devices with the same thicknesses and mobilities in donor and acceptor,  $\delta_D = \delta_A = 0.5$  is more reasonable, so we include this value into the simulations. The final remark is that the interface electric field is obtained from Poisson equation's solutions in the DD-BI and the SCD models, but in the GWWF JV calculations it is calculated using the method summarized at the end of the GWWF paper[4], based on  $p_C$  and  $p_I$  that are predicted by Eqs. 1.16 and 1.13 .

Parameter	Value
Donor and acceptor thickness	40nm.
$\mu_p = \mu_n$	$10^{-7} m^2/Vs$
$\phi_a/\phi_c$	Figure 4.1: 0.1eV/0.6eV; 0.2eV/0.5eV; 0.3 eV/0.4eV, Figure 4.2: 0.1eV/0.3eV; 0.2eV/0.3eV; 0.3 eV/0.3eV.
$R_s^\dagger$	$1 \times 10^{-4} \Omega m^2$
$\delta_D/\delta_A^\dagger$	0.9/0.1 and 0.5/0.5
$\epsilon$	$3\epsilon_0$
$T_{t,A} = T_{t,D}$	1000K
$k_{PPr}$	$(1\mu s)^{-1}$ (constant)
$N_{HOMO}/N_{LUMO}$	$1E27 m^{-3}$
$H_D/H_A$	$1E24 m^{-3}$
$J_X$	$4.3E20 m^{-2}s^{-1}$
$a_0$	1.5nm
$\Delta E_{HL}$	1.2eV
$V_{bi}$	0.5eV
recombination type	the f-t recombination (Eq. 1.8)

<sup>†</sup>  $R_s$ ,  $\delta_D$ , and  $\delta_A$  are used in the GWWF model only.

Table 4.1: Summary of parameters used in the comparison between the GWWF model and the models developed in this study.

### 4.1.3 Results and Discussion

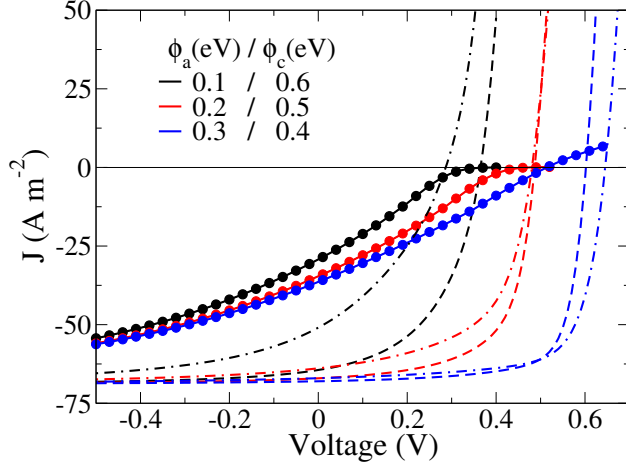


Figure 4.1: Comparison of JV characteristics generated by the DD-BI model (symbol), the SCD equation in Equation 2.14 (solid line), the GWWF model with  $\delta_D = 0.9$  and  $\delta_A = 0.1$  (dashed line) and the GWWF model with  $\delta_D = 0.5$  and  $\delta_A = 0.5$  (dashed and dotted line).

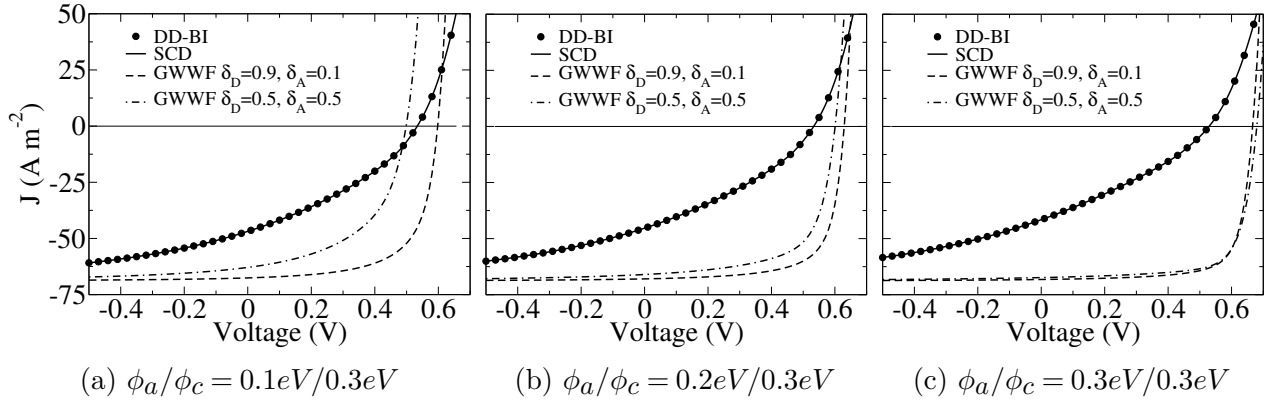


Figure 4.2: Comparison of JV characteristics generated by the DD-BI model (symbol), the SCD equation in Equation 2.14 (solid line), the GWWF model with  $\delta_D = 0.9$  and  $\delta_A = 0.1$  (dashed lines) and the GWWF model with  $\delta_D = 0.5$  and  $\delta_A = 0.5$  (dashed and dotted lines) for the devices with  $\phi_a/\phi_c$  equal to (a)  $0.1\text{eV}/0.3\text{eV}$ , (b)  $0.2\text{eV}/0.3\text{eV}$  and (c)  $0.3\text{eV}/0.3\text{eV}$ .

The resulting JV curves are compared in Figures 4.1 and 4.2 for the two sets of  $\phi_a$  and  $\phi_c$ . The GWWF JV curves both with  $\delta_D = 0.9$  and  $\delta_A = 0.1$  (dashed lines) and  $\delta_D = 0.5$  and  $\delta_A = 0.5$  (dashed and dotted lines) are completely different from the DD-BI (symbols) and the SCD (solid lines) curves that are consistent with each other. The differences can be categorized into two aspects: (1) the currents at  $V_a > V_{oc}$  in the GWWF results are much higher than the DD-BI and the SCD cases; and (2) the DD-BI and the SCD models show

severe s-shaped behaviors if the injection barriers are too high or reduced FFs if the injection barriers are moderate, while the GWWF results show high FFs in most cases.

The prime variables that give rise to the discrepancies between the GWWF model and the DD-BI/SCD model are the interface charge densities ( $n_I$  and  $p_I$ ). Equations 1.12 and 1.13, which are used in the GWWF model, have  $\delta_D$  and  $\delta_A$  as one of their arguments, where  $\delta_D + \delta_A = 1$  is assumed. However, there are several disadvantages to making this assumption.

First, as stated in the GWWF paper, Eqs. 1.12 and 1.13 are valid only when  $J = 0$  (open circuit conditions). Using the equations at any other  $V_a$  results in  $n_I$  and  $p_I$  that are inaccurate and do not include space charge effects. Comparisons of  $n_I$  and  $p_I$  calculated by Eqs. 1.12 and 1.13 and the DD-BI model in the device with  $\phi_a = 0.1\text{eV}$  and  $\phi_c = 0.6\text{eV}$  are given in Figure 4.3(a). The DD-BI self-consistent values of  $\delta_D$  and  $\delta_A$  are functions of applied voltage as shown in Figure 4.3(b). We can see that, even with the actual functions of  $\delta_D(V_a)$  and  $\delta_A(V_a)$ , the GWWF Equations 1.12 and 1.13 fail to predict the interface densities except for  $p_I$  in the small voltage range at high  $V_a$ . One important feature that is shown in the DD-BI results is that  $n_I$  and  $p_I$  do not change with  $V_a$  in the small and reverse bias regimes. This indicates accumulation of charge in space which is common for OPVs due to the low mobilities and the low dielectric permittivity. The accumulation is often referred to as space charge accumulation or space charge effect; which is not included in the GWWF model. It is interesting that  $\delta_D$  and  $\delta_A$  can change dramatically over the whole range of voltage. They diverge when  $V_a = V_{bi}$ , and may have negative values when the direction of the averaged electric field in an active layer is switched due to space charge effects. The topic will be discussed in Section 4.3.2.

Inaccurate values of  $n_I$  and  $p_I$  bring about an erroneous interface recombination, interface electric field,  $k_{PPd}$  and, most importantly,  $\eta_{PPd}$  in the GWWF calculation. The interface electric field ( $F_I$ ) is one of the most important parameters in determining the rate  $k_{PPd}$  as seen in Eqs. 1.44 and 1.47. In Figures. 4.1 and 4.2,  $k_{PPr}$  is used as a constant, but  $k_{PPr}$  as a function of  $F_I$  (Eq. 1.48) is more accurate to describe the PP recombination and often

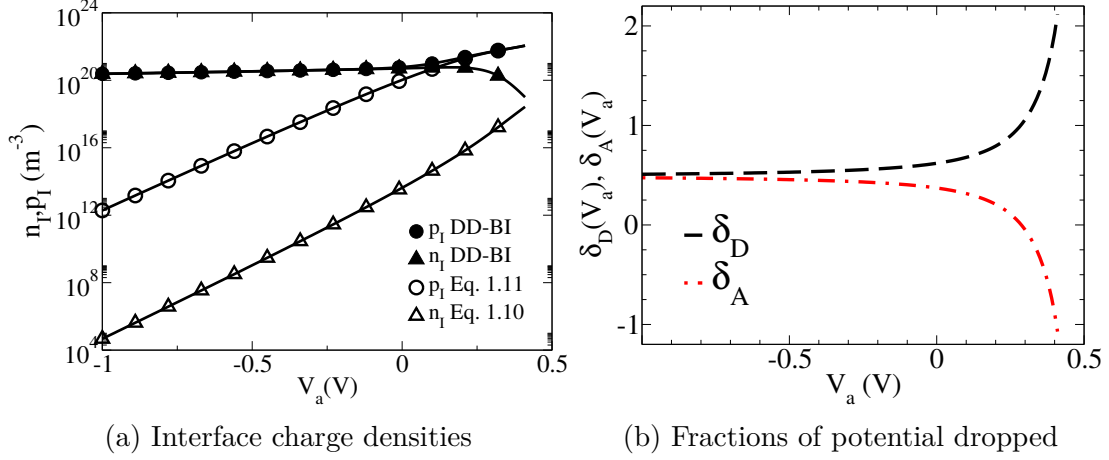


Figure 4.3: (a) Interface hole ( $p_I$ ) and electron ( $n_I$ ) densities versus the applied voltage calculated by the DD-BI model (filled symbols) and the equations used by GWWF (Eqs. 1.12 and 1.13)(open symbols) that have fractions of potential dropped  $\delta_D$  and  $\delta_A$  shown in figure (b) as their arguments.

used[82]. We can see that  $\eta_{PPd} = k_{PPd}/(k_{PPd} + k_{PPr})$ , which has a major impact on fill factor through the photo-current density ( $qJ_X\eta_{PPd}$ ), is directly affected by  $F_I$ . The DD-BI model solves the Poisson equation for a potential profile ( $\psi(x)$ ), so  $F_I$  can be calculated by  $F_I = -\partial\psi(x)/\partial x$  at the interface. On the other hand, because the GWWF model does not use any iterative numerical scheme to solve for  $\psi(x)$ ,  $F_I$  has to be approximated using a method that relates  $F_I$  with differences between the electrode charge densities ( $n_c$  and  $p_c$ ) and the interface charge densities ( $n_I$  and  $p_I$ ). However, Eqs. 1.12 and 1.13 greatly underestimate  $n_I$  and  $p_I$  because of the lack of treatment of the space charge accumulation at the interface. Thus, the GWWF model overestimates  $F_I$ ,  $k_{PPd}$  and  $\eta_{PPd}(F_I)$ , resulting in a JV curve with high FF and efficiency. Figure 4.4 shows  $F_I$ ,  $k_{PPd}$  and  $\eta_{PPd}$  as a function of  $V_a$  in the device with  $\phi_a/\phi_c = 0.1\text{eV}/0.6\text{eV}$  from three different models: the DD-BI model; the GWWF model with  $\delta_D/\delta_A = 0.9/0.1$ ; and the GWWF model with actual values of  $\delta_D(V_a)$  and  $\delta_A(V_a)$  from the DD-BI results. Strengths of the  $F_I$  fields predicted by the GWWF method are always higher than the DD-BI results, regardless of the choices of  $\delta_D$  and  $\delta_A$ . This leads to  $k_{PPd}$  that can be much higher than it should be and  $\eta_{PPd}$  that is close to a hundred percent (i.e. almost all of the excitons are dissociated and turned into

the photo-current). We note the similarities between the  $\eta_{PPd}$  graphs and the shapes (fill factors) of the JV Curves in Fig. 4.1.

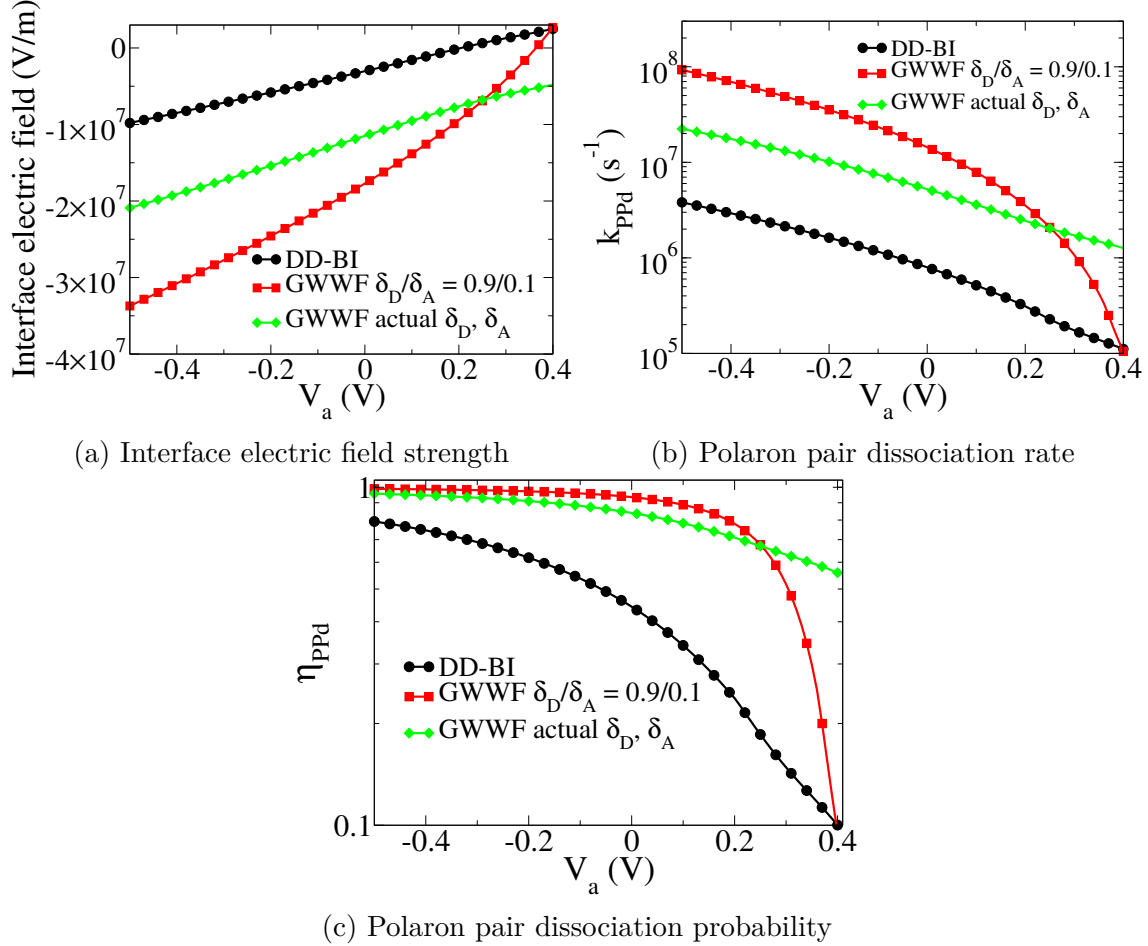


Figure 4.4: Graphs of the interface electric field strengths ( $F_I$ ), polaron pair dissociation rates and probabilities ( $k_{PPd}$  and  $\eta_{PPd}$ ) of the device with  $\phi_a/\phi_c = 0.1eV/0.6eV$  calculated by the DD-BI models (black), the GWWF model with  $\delta_D/\delta_A = 0.9/0.1$  (red) and the GWWF model with  $\delta_D$  and  $\delta_A$  as a function of  $V_a$  derived from the DD-BI model(green).

Thirdly,  $R_s$ , which is an intrinsic property associated charge densities and quasi-Fermi levels, is removed by the assumption  $\delta_D + \delta_A = 1$ . The product of  $n_I$  and  $p_I$  is given by

$$n_I p_I = n_c p_c \exp \left[ \frac{q(V_a - V_{bi})}{k_B T} \right] \approx N_{LUMO} N_{HOMO} \exp \left[ \frac{-q\Delta E_{HL}}{k_B T} \right] \exp \left[ \frac{qV_a}{k_B T} \right], \quad (4.1)$$

or

$$n_I p_I \approx n_i^2 \exp \left[ \frac{qV_a}{k_B T} \right], \quad (4.2)$$

where  $n_c$  and  $p_c$  are charge densities at the electrodes given by Equations 1.15 and 1.16, and  $n_i = [N_{LUMO}N_{HOMO}\exp(-q\Delta E_{HL}/k_B T)]^{1/2}$  is intrinsic charge density. However, this is not true in general because when the device is under illumination or bias, the electron and hole densities will change according to their quasi-Fermi levels, so that[17]

$$n_I p_I = n_i^2 \exp \left[ (E_{fn,I} - E_{fp,I}) / k_B T \right]. \quad (4.3)$$

The voltage in the exponential term of  $n_I p_I$  is the diode voltage;  $V_d = V_a - JR_s$ , as shown in Chapter 2. The assumption  $\delta_D + \delta_A = 1$  removes  $R_s$  from the model, so it has to be included manually at the end of the GWWF derivation.

Furthermore, the summation  $\delta_D + \delta_A = 1 + F_I a_0 / (V_{bi} - V_a)$  instead of one as assumed in the GWWF model where  $a_0$  is the interface width. By definition in the GWWF model,  $\delta_D(\delta_A)$  is based on the potential drop from the anode(cathode) to the edge of donor(acceptor) at the interface. This leaves the potential drop across the interface itself out, hence a term of magnitude of  $F_I a_0$  is omitted. Since  $F_I$  is of the order of  $10^6 - 10^7 V/m$  as shown in Fig. 4.4 and  $a_0 \approx 10^{-9} m$ , the error of using  $\delta_D + \delta_A = 1$  could be as high as 10% assuming that  $V_{bi} - V_a$  is of the order of 0.1V. In addition,  $\delta_D$  and  $\delta_A$  change drastically from one system to another and can take many values. They also depend on the cathode work function[98], donor/acceptor thicknesses, the device voltage[99], and the mobilities.

For the conclusions of this section, we now go back to the two aspects of the JV differences that were raised earlier. For aspect (1), the steep JV curves calculated by the GWWF method are the absence of  $R_s$  which is most relevant at high voltage[32]. In-depth discussion about the effects of  $R_s$  on JV curves can be found in Sections 5.2 and 5.3. For aspect (2), the s-shaped JV characteristics are mainly caused by the accumulation of space charge[100, 101] that can reduce  $F_I$  and  $\eta_{PPd}$ , and is not included in the GWWF model. It will be showed in Section 4.3.2 that reduced built-in potential from high injection barriers can also cause s-shaped JV behaviors, which are observed experimentally when high work function electrodes are used[102].

#### 4.1.4 Strategies to Improve the GWWF Model

In order to prove the points about  $F_I$  and  $R_s$  in the previous section, in this section we would like to show that GWWF JV curves can be consistent with DD-BI and SCD curves if space charge effects are included, by using more reasonable values of  $\delta_D$ ,  $\delta_A$ ,  $F_I$  and  $R_s$ . It is also interesting to see the conditions in which the GWWF model is a good approximation.

Here, we simulate devices having the same parameters as in Table 4.1, and with the injection barriers  $\phi_a/\phi_c = 0.1eV/0.6eV$ ,  $0.0eV/0.0eV$  and  $0.3eV/0.3eV$ . The latter two cases of the injection barriers represent symmetric devices with Ohmic contacts and contacts with small Schottky barriers, respectively. Four cases of modified GWWF calculations, which are summarized in Table 4.2, are calculated and compared to the DD-BI and the SCD results. From case 1 to case 4, we correct the parameters' values one at a time, to clearly show effects of each parameter. In case 1, we use the original values of  $\delta_D$ ,  $\delta_A$ ,  $F_I$  and  $R_s$  as suggested by GWWF. According to the results shown in Fig. 4.3(b),  $\delta_A = \delta_D = 0.5$  is more appropriate if the thicknesses of the donor and the acceptor are equal, so we start using this value from case 2. Up to this point,  $F_I$  is still calculated from the approximation method in the GWWF paper that is based on  $\delta_D$  and Eq. 1.13. Accordingly, in case 3, we use  $F_I$  as a function of  $V_a$  that is derived from the DD-BI simulations. Finally, in case 4, a fitted  $R_s$  is used instead of  $1 \times 10^{-4}\Omega m^2$

case	$\delta_D$ , $\delta_A$	$F_I$	$R_s$
1	0.9, 0.1	GWWF method	$1 \times 10^{-4}\Omega m^2$
2	0.5, 0.5	GWWF method	$1 \times 10^{-4}\Omega m^2$
3	0.5, 0.5	DD-BI results	$1 \times 10^{-4}\Omega m^2$
4	0.5, 0.5	DD-BI results	Fitted

Table 4.2: Four cases of GWWF calculations with improved values of  $\delta_D$ ,  $\delta_A$ ,  $F_I$  and  $R_s$  to include space charge effects.

The calculated GWWF, DD-BI and SCD JV curves are shown and compared in Fig. 4.5. Some interesting remarks about the results are as follows. Firstly, the SCD and the DD-BI results are always consistent with each other. Secondly, the original GWWF calculations

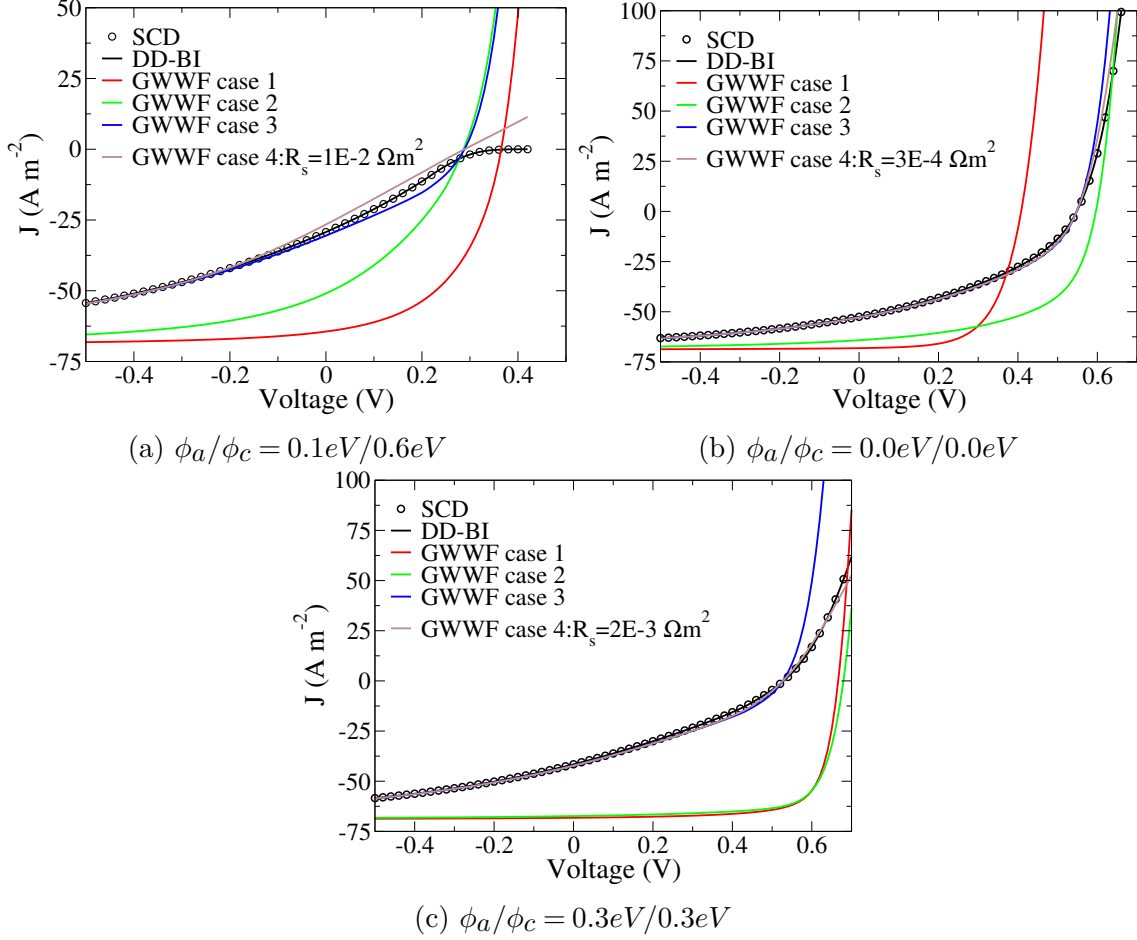


Figure 4.5: Comparisons of JV characteristics calculated by the DD-BI model, the SCD model and the four cases of modified GWWF calculations that are summarized in Table 4.2, in the devices with  $\phi_a/\phi_c$  equal to (a)  $0.1\text{eV}/0.6\text{eV}$ , (2)  $0.0\text{eV}/0.0\text{eV}$  and (3)  $0.3\text{eV}/0.3\text{eV}$ . The values of the fitted  $R_s$  that are used in case 4 are written in each plot.

(case 1) are not consistent with the drift-diffusion DD-BI results in any  $\phi_a/\phi_c$  cases and also result in the curves with the highest FFs. As discussed earlier, this is because the GWWF method overestimates  $F_I$ ,  $k_{PPd}$  and  $\eta_{PPd}$  from the underestimated  $n_I$  and  $p_I$ . Thirdly, using  $\delta_D = \delta_A = 0.5$  alone does not give rise to a better JV prediction because Equations 1.12 and 1.13 that have  $\delta_D$  and  $\delta_A$  as arguments are invalid to calculate  $n_I$ ,  $p_I$ , and the resulting  $F_I$ . However, using  $\delta_D = \delta_A = 0.5$  concurrently with the right  $F_I$  function from the DD-BI results drastically improves the GWWF results, as we can see from the case-3 graphs. This is another indication of how important the right  $F_I$  is in predicting JV curves. Finally, the case-3 GWWF graphs still have inconsistent currents at high  $V_a$  that have to be

corrected by using the more appropriate values of  $R_s$ .

In conclusion, we proved that a correct function  $F_I(V_a)$  and a fitted  $R_s$  are needed in the GWWF model in order to make it a reasonable model. Moreover, even with the invalidities of Eqs. 1.12, 1.13 and the assumptions regarding  $\delta_D$  and  $\delta_A$ ,  $\delta_D = \delta_A = 0.5$  is the best set up if the interface sits in the middle of the active layer. All of the physical quantities, such as spatial charge densities ( $n(x)$  and  $p(x)$ ), potential profile ( $\psi(x)$ ) and electric field ( $F(x)$ ), are highly correlated with each other according to the laws of Electrostatics. Hence, it is best to avoid using the problematic approximations (Eqs. 1.12, 1.13,  $\delta_D$  and  $\delta_A$ ) altogether.

## 4.2 Effects of Carrier Mobilities

Free carrier mobilities are clearly one of the most important factors limiting OPV efficiency. It is commonly known that they directly affect charge transport, so the higher they are the better. Somehow, it is less known in what way they affect other less obvious properties like charge recombination, space charge accumulation, charge-transfer state recombination and dissociation, etc. This leads to the purpose of this section; studying effects of free carrier mobilities.

One of the benchmark materials that have been extensively studied is poly-3-hexyl thiophene (P3HT):phenyl-C61-butyric acid methyl ester (PCBM) donor-acceptor system. Parameters from these materials will be mainly used in this section. In practice, the "true" bilayer structure is difficult to achieve in this system[60, 61] due to fast interpenetration of the two materials even at low temperature. Hole mobility in P3HT intrinsically depends on its regioregularity (order of repeating monomers) and molecular weight of the P3HT solution, which was shown to be around  $10^{-4} - 10^{-5} \text{ cm}^2/\text{Vs}$ [103]. Consequently, hole mobility in P3HT within this range and above will be studied to develop a detailed mechanistic picture of the benefits of higher mobility.

Table 4.3 summarizes important parameters used in the simulations. Simulated JV curves both under illumination and dark conditions are shown in figure 4.6. Efficiency parameters

Parameter	Value
$\mu_p$	$10^{-6} - 10^{-9} m^2/Vs$
$\mu_n$	$2.0 \times 10^{-7} m^2/Vs$ [104]
Donor/acceptor thickness	50nm/22nm [59]
$\phi_a/\phi_c$	0.2 eV [105], 0.2 eV
$\epsilon$	$3.9\epsilon_0$
$E_{t,A} = E_{t,D}$	58 meV [103]
$k_{PPr,0}$	$1\mu s^{-1}$
Donor $E_{LUMO}/E_{HOMO}$	-4.9eV/-3.0eV
Acceptor $E_{LUMO}/E_{HOMO}$	-6.1eV/-3.7eV
$N_{HOMO}/N_{LUMO}$	$1E27 m^{-3}$
$H_D/H_A$	$1E24 m^{-3}$
$J_X$	$4.3E20 m^{-2}s^{-1}$
$a_0 = \delta x$	1.0nm
recombination type	Bimolecular + trap-assisted

Table 4.3: Summary of parameters used in simulations of P3HT:PCBM bilayer solar cells, with hole mobility as the independent variable

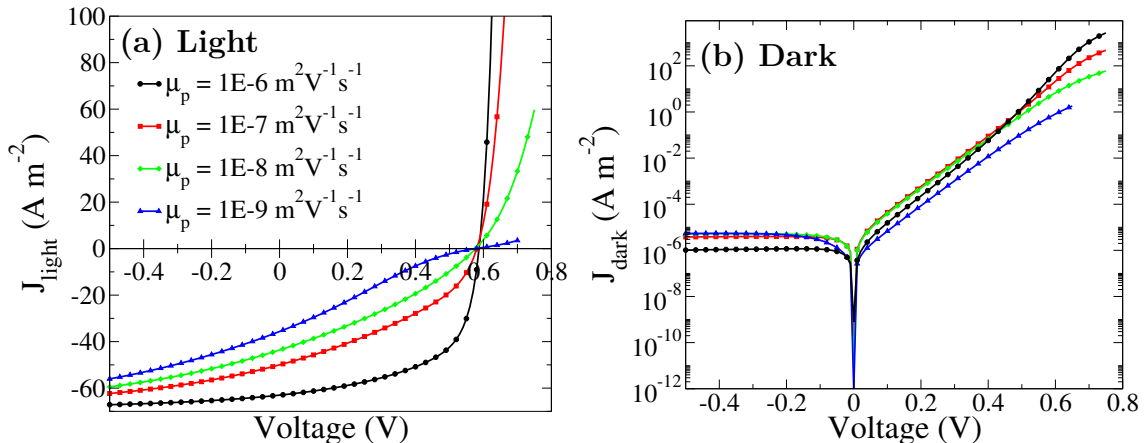


Figure 4.6: (a) J-V curves under illumination conditions of P3HT:PCBM bilayer photovoltaic cells and (b)  $\ln|J| - V$  curves of the same devices under dark conditions. Parameters used in these simulations are in table 4.3.

from the illuminated cells are listed in table 4.4. As expected, energy conversion efficiency is reduced with the reduced hole mobility. Short circuit current and fill factor are affected heavily while  $V_{oc}$  is surprisingly left intact. At the open circuit point, slopes of the graphs are very steep in the high mobility devices and become less steep as the mobility is lowered, especially with  $\mu_p = 10^{-9} m^2/Vs$ . The slope of a JV curve at open circuit voltage is often a good indication of series resistance ( $R_s$ ) [32]. This agrees with the results and can be simply

understood by decreased donor electrical conductivity ( $\sigma = qp\mu_p$ ). However, deeper understanding the mechanism behind the slope change reveals more insights. On the other hand, slope at short circuit conditions is connected to the parallel resistance ( $R_p$ )[32]. Leakage current is the cause of  $R_p$  in the conventional picture, whereas polaron pair (or charge-transfer state) recombination is more likely the reason in the OPV context under illumination. The least slope as occurs in the high  $\mu_p$  devices is preferred at this point. There are a lot of details regarding  $R_s$  and  $R_p$  that will be further discussed in this section and Section 5.5. There are, however, a couple most important and fundamental aspects that have to be understood first; space charge effects, quasi-Fermi levels and polaron pair dissociation.

$\mu_p$ [ $m^2 V^{-1} s^{-1}$ ]	$J_{sc}$ [ $Am^{-2}$ ]	$V_{oc}$ [V]	FF [%]
1E-6	63.03	0.59	58.19
1E-7	49.99	0.58	38.46
1E-8	43.62	0.58	32.44
1E-9	35.65	0.58	22.68

Table 4.4: Parameters indicating power conversion efficiency; short circuit current ( $J_{sc}$ ), open circuit voltage ( $V_{oc}$ ), and fill factor (FF), of the P3HT:PCBM bilayer solar cells with different P3HT hole mobility, obtained from figure 4.6(a).

#### 4.2.1 Space charge effects and quasi-Fermi levels splitting

This part is devoted to explain space charge accumulation and quasi-Fermi levels splitting at the D/A interface, which causes the driving potential of the diode current. Heterojunctions of organic donor-acceptor are similar, but not the same, as the inorganic p-n junctions[42]. Quasi-Fermi levels splitting is also found in a p-n junction, but the regions near the junction are depletion regions due to charge transfer across the interface. This does not occur in a D/A interface because charge densities are much lower, and there are barriers from the donor and acceptor energy levels differences. Therefore, it is crucial to understand the D/A heterojunction from the organic point of view itself.

Figure 4.7 shows a comparison of charge densities and energy levels of the device with

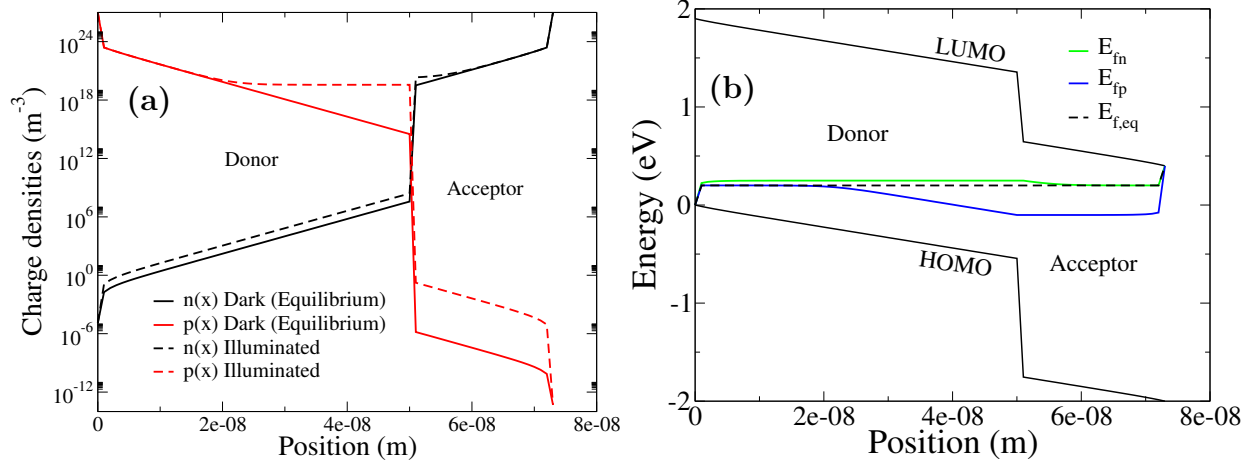


Figure 4.7: (a) A comparison of hole (red lines) and electron (black lines) densities at  $V_a = 0V$  between dark (or equilibrium) conditions (solid lines) and illuminated conditions (dashed line), of the device with  $\mu_p = 10^{-6} m^2/Vs$ . (b) Energy level diagram of the same device under both conditions including equilibrium (dashed line), quasi electron Fermi (green line) and hole (blue line) energy levels.

$\mu_p = 10^{-6} m^2/Vs$  under dark and illumination conditions at  $V_a = 0V$ . The former conditions will be referred to as equilibrium conditions. Under these conditions, holes and electrons, that are injected from the anode and the cathode, diffuse until they reach the interface where they are blocked by a barrier (e.g.  $E_{LUMO_D} - E_{LUMO_A}$ ). The quasi-Fermi energies of electron and hole (dashed line in Fig. 4.7(b)) are equal and equilibrated throughout the device when there is no illumination. Equilibrated , or aligned, Fermi levels ( $E_{f,eq}$ ) are necessary otherwise currents would flow as;[17]

$$J_n(r) = \mu_n n \nabla E_{fn} \quad (4.4)$$

$$J_p(r) = \mu_p p \nabla E_{fp}, \quad (4.5)$$

, but it is obvious that there is no net current at the equilibrium conditions. The LUMO and HOMO bands are almost linear from the anode to the cathode as shown in Fig. 4.7(b), due to the linear potential. Hence  $E_{LUMO} - E_{fn}$  and  $E_{fp} - E_{HOMO}$  are also a linear function of position. As a result, according to equations 1.21 and 1.22, charge densities spread exponentially from the injection sources (see Figure 4.7(a)).

In the case of illuminated conditions, the D/A interface is now another source of charge

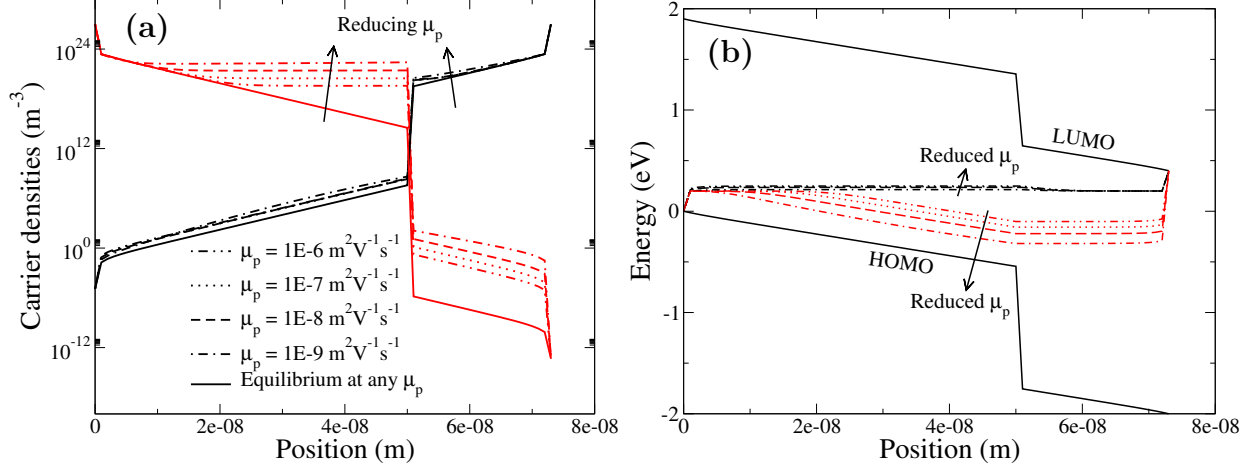


Figure 4.8: (a) Densities of electron (black) and hole (red) within the devices with different donor hole mobility, under  $V_a = 0V$ . Equilibrium charge densities are almost invariant with  $\mu_p$  and plotted in the solid lines. (b) Energy level diagram showing different quasi-Fermi levels deviation/splitting in the devices. The top LUMO and bottom HOMO bands are almost invariant with the mobility.

from the dissociation of polaron pairs. Interface charges move toward the electrodes under the influences of the built-in potential or bias (drift) and diffusion, until steady state conditions (time-independent) of charges and any interface rates are reached. There are now two regions of charge distribution, namely an exponential decay region near the electrodes (e.g. the first 20 nm near both the donor and acceptor) and a constant charge region near the interface (e.g. from 20-50 nm in the donor and a few nanometers in the acceptor). According to equations 1.21 and 1.22, in the constant charge regions, donor  $E_{HOMO}$  and  $E_{fp}$  are parallel, as well as acceptor  $E_{LUMO}$  and  $E_{fn}$ . This makes the quasi-Fermi levels  $E_{fn}$  and  $E_{fp}$  split and deviate from  $E_{f,eq}$ , giving rise to the quasi-Fermi level difference  $E_{fn,I} - E_{fp,I}$  at the D/A interface, which is the actual diode voltage.

#### 4.2.2 Effect of mobility on space charges

The origins of quasi-Fermi level splitting have been discussed in the previous part. This part will be about how hole mobility affects space charge accumulation and energy splitting at the interface.

Figure 4.8 shows how charge densities and energy levels are affected by varying the hole

mobility. First of all, under equilibrium conditions for  $\mu_p = 10^{-6}$  to  $10^{-8} m^2/Vs$ , equilibrium charge densities and energy levels are almost invariant, but for  $\mu_p = 10^{-9} m^2/Vs$  there is a small change caused by band bending. It is not shown in the figure and will be discussed in detail later under the band-bending section (Section 4.4). Therefore, solid red and black lines in Fig. 4.8(a) respectively represent equilibrium hole and electron densities in all cases of  $\mu_p$ . When there are incident photons, the two distinct regions, i.e. the exponential charge distribution and the constant charge distribution, can be seen in all cases (see figure 4.8(a)). The impacts of lower  $\mu_p$  is that dissociated free carriers are more difficult to move and collected at the electrodes, so they accumulate more and raise the amount of charge in the constant charge distribution region. This is normally viewed as reduced charge transport and collection coefficient caused by low mobility. The raised hole density in the constant density region decreases the hole quasi-Fermi level since holes are unoccupied electron states, so electrons can be added or removed using lower energies. Then,  $E_{fp}$  is closer, but still parallel, to  $E_{HOMO}$  (see Eq. 1.22), resulting in more splitting of the quasi-Fermi levels  $E_{fn,I} - E_{fp,I}$  at the interface as can be seen in Fig. 4.8(b).

The D/A heterojunction which behaves like a diode is biased with more diode voltage  $V_d = E_{fn,I} - E_{fp,I}$  from the lowered mobility. According to ideal equations in Shockley equation form (for example Eqs. 1.3 and 2.20), the diode conducts more current and subtracts more from the photocurrent, so the reduction of photocurrent is observed in Fig. 4.6(a). Physically speaking, lowered mobility worsens charge transport so there is more accumulation near the interface. This forces dissociated charges from polaron pairs to recombine back to polaron pairs, and finally are lost by polaron pair recombination ( $k_{PPr}\zeta$ ).

#### 4.2.3 Dissociation and recombination of polaron pairs: The parallel resistance

Polaron pair (PP) recombination and dissociation are vital parts of OPV physics. Let's first see how their rates vary as a function of applied voltage in Figure 4.9.

The rate  $k_{PPd}$  is the polaron pair dissociation rate, governing the amount of polaron

pairs to be dissociated into free carriers ( $k_{PPd}\zeta$ ); while  $k_{PPr}$  is the rate for recombining PP to the ground state, leading to loss of carriers. Introduction to  $k_{PPd}$  and  $k_{PPr}$  can be found in section 1.9. Maximized  $k_{PPd}$  and minimized  $k_{PPr}$  are undoubtedly primary goals of OPV research. They depend on interface electric field ( $F_I$ ), but oppositely and  $k_{PPd}$  is more sensitive to it. It changes more than one order of magnitude as seen in Fig. 4.9. Within the reverse or small bias regimes, built-in potential provides large  $F_I$  that points from acceptor to donor, breaking the coulombic bond of a PP, hence promoting dissociation and also pulling carriers away from the interface. This makes  $k_{PPd}$  high and  $k_{PPr}$  low. As the voltage increases into the working solar cell regime, the applied voltage counters the built-in potential and lessens  $F_I$  or even reverses its direction. Charges are driven to the interface and recombine, reducing  $k_{PPd}$  and enlarging  $k_{PPr}$ . The combination,  $\eta_{PPd} = k_{PPd}/(k_{PPd} + k_{PPr})$  is a very important parameter, capturing the competition of the two PP rates. One might consider the D/A interface as an exciton current separator, splitting the incoming exciton current  $J_X$  into usable photocurrent  $qJ_X\eta_{PPd}$  and wasted current  $qJ_X(1 - \eta_{PPd})$  leaking to ground states. In Fig. 4.9,  $\eta_{PPd}$  is close to one at low voltage because of the built-in potential. In this device, the maximum power point is at 0.47V, where only about 60% of exciton flux becomes free charge flux.

Figure 4.10 shows how the three parameters ( $k_{PPd}$ ,  $k_{PPr}$ ,  $\eta_{PPd}$ ) react to a lowered hole mobility. The dissociation rate,  $k_{PPd}$ , drops rapidly with decreasing hole mobility; however, from  $\mu_p = 10^{-8}$  to  $10^{-9} m^2/Vs$  and at high  $V_a$ ,  $k_{PPd}$  almost does not change. Surprisingly,  $k_{PPr}$  is not influenced by the mobility from  $\mu_p = 10^{-6}$  down to  $10^{-8} m^2/Vs$ , but it is when  $\mu_p = 10^{-9} m^2/Vs$ . Nonetheless, the increment at this mobility is small as compared to the reduction of  $k_{PPd}$  (notice that the scale of  $k_{PPr}$  is linear, not logarithmic). In terms of PP rates, OPV efficiency is thus impacted from poor charge transport through diminished  $k_{PPd}$ , but less severely from elevated  $k_{PPr}$ . Noticeably, since  $k_{PPr}$  is weakly affected by  $\mu_p$ , the  $\eta_{PPd}$  plots in figure 4.10(c) follow the trends of  $k_{PPd}$ . Reduced  $\eta_{PPd}$  greatly affects the harvestable exciton flux. It was discussed already that only 60% of  $J_X$  is harvestable

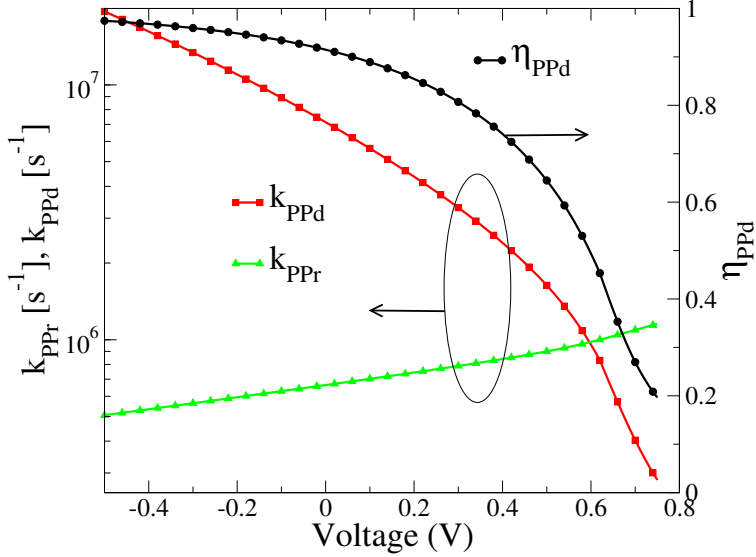


Figure 4.9: Polaron pair dissociation rate ( $k_{PPd}$ ), recombination rate ( $k_{PPr}$ ) and dissociation probability/efficiency ( $\eta_{PPd}$ ), as a function of applied voltage.

for  $\mu_p = 10^{-6} m^2/Vs$  at maximum power point. For  $\mu_p = 10^{-9} m^2/Vs$ , the MPP point is at 0.25V, having only about 30% of excitons leading to free carriers coming out of the interface. Note that, further losses occur from free carrier recombination.

Parallel resistance ( $R_p$ ), based on the theory in section 2.2, mostly depends  $\eta_{PPd}$ . In the conventional interpretation,  $R_p$  is due to leakage current from one electrode to the other[5], which can be caused by manufacturing defects like pinholes. We will show in Chapter 5 that an OPV cell without actual shorting electrodes can have leakage currents both under illumination and dark conditions, but these leakage currents are more likely recombination currents at the D/A interface. Illumination  $R_p$  is related to recombinations of interface polaron-pairs, and dark  $R_p$  is possibly from trap-related tunneling processes.  $R_p$  is usually extracted at  $V_a = 0V$  or lower, and at this voltage, the total photocurrent  $qJ_X\eta_{PPd}$  is higher than the diode current many orders of magnitude. The slope of a graph, which is understood as  $R_p^{-1}$  [32], is accordingly the slope of  $\eta_{PPd}$  ( $d\eta_{PPd}/dV$ ).

Figure 4.11 is a comparison plot of  $R_p$  as a function of  $V_a$  showing the effects of donor hole mobility. They are calculated using Equation 2.28;

$$R_p = \frac{E_{fn,I} - E_{fp,I}}{qJ_X(1 - \eta_{PPd})}. \quad (4.6)$$

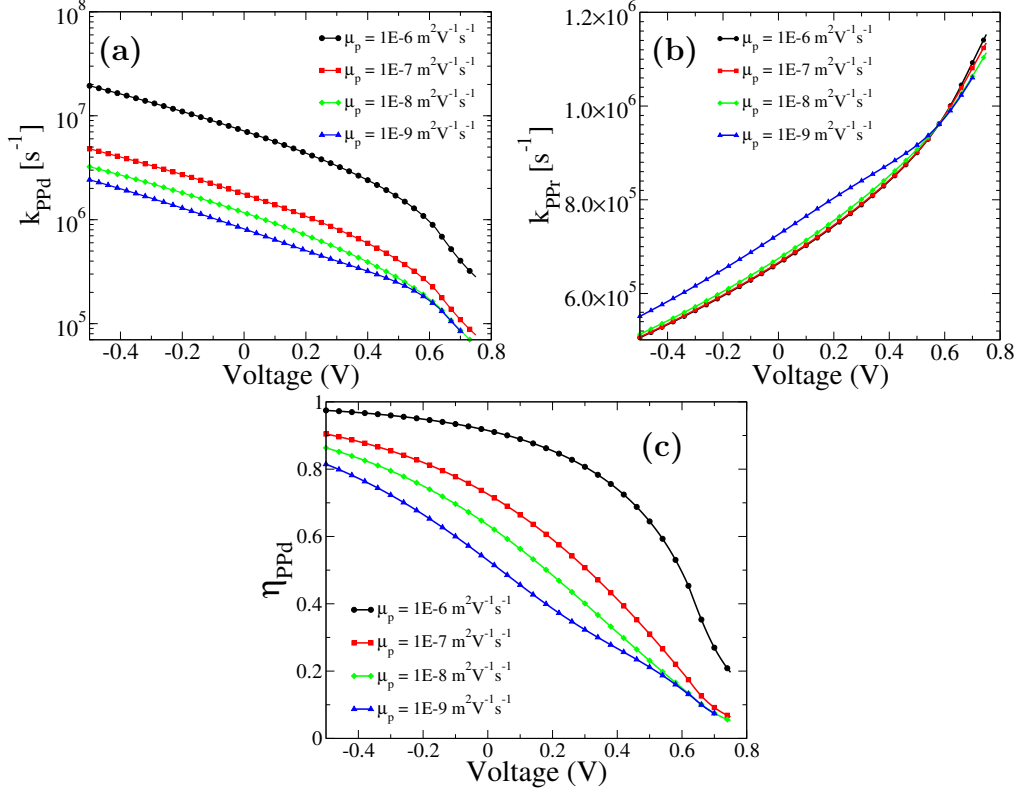


Figure 4.10: Plots of (a)  $k_{PPd}$ , (b)  $k_{PPr}$ , and (c)  $\eta_{PPd}$  as a function of voltage in the devices with different hole mobility.

In the  $V_a < 0V$  range where  $R_p$  is most in effect,  $R_p$  is reduced with the same trend as  $k_{PPd}$  and  $\eta_{PPd}$  in figure 4.10 (a) and (c). Lower PP dissociation caused by the decreased  $\mu_p$  makes the "virtual" leakage current of  $qJ_x(1 - \eta_{PPd})$  higher and, hence,  $R_p$  smaller. In the DD-BI model,  $R_p$  is thus predominantly due to PP recombination, and it is inversely related to it. A low recombination rate leads to large  $R_p$ .

#### 4.2.4 Effect of mobility on the series resistance

Another resistance that is more directly related to mobilities is series resistance ( $R_s$ ). Since the applied voltage is the difference between anode and cathode work functions;  $V_a = WF_c - WF_a$ , then the relation  $V_d = V_a - JR_s = E_{fn,I} - E_{fp,I}$  leads to equation 2.27, i.e.

$$R_s = \frac{(WF_c - E_{fn,I}) + (E_{fp,I} - WF_a)}{J}. \quad (4.7)$$

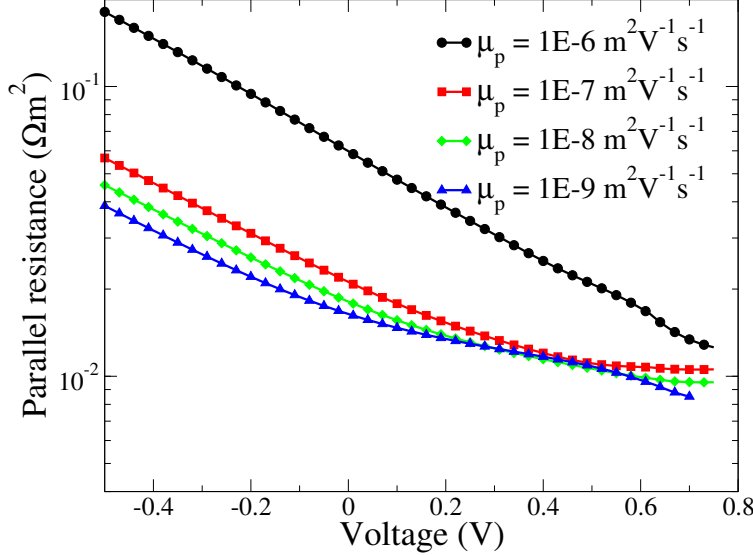


Figure 4.11: Parallel resistances ( $R_p$ ) as a function of applied voltage calculated by equation 2.28 from the devices having different donor  $\mu_p$ .

Typically, if the injection barriers are not higher than about 0.2eV,  $E_{fn}$  near the cathode ( $E_{fn,c}$ ) will be pinned to  $WF_c$  and  $E_{fp}$  near the anode ( $E_{fp,a}$ ) will be also pinned to  $WF_a$  because they are in the Fermi level pinning regime[106]. This will be discussed further in the injection barrier section (Section 4.4). Hence, one can write  $R_s$  as

$$R_s = \frac{(E_{fn,c} - E_{fn,I}) + (E_{fp,I} - E_{fp,a})}{J}. \quad (4.8)$$

Consequently,  $R_s$  causes  $E_{fn,I}$  and  $E_{fp,I}$  at the interface to be changed from  $E_{fn,c}$  and  $E_{fp,a}$  at the cathode and anode respectively.

Energy levels at  $V_a = 0.4V$  of the devices with  $\mu_p = 10^{-6}m^2/Vs$  and  $10^{-9}m^2/Vs$  are chosen as examples and shown in figure 4.12. It can be seen that  $E_{LUMO}$ ,  $E_{HOMO}$  and  $E_{fn}$  are not much different between the two cases, but  $E_{fp}$  in the bulk donor moves more from the anode level in the device with  $\mu_p = 10^{-9}m^2/Vs$  than the other. This shifting is caused by more accumulation of space charge as seen in figure 4.8(a), due to the lower mobility of this device.

Finally,  $R_s$  as a function of applied voltage of the different  $\mu_p$  devices are plotted in figure 4.13, calculated using equation 2.27. The high  $V_a$  region is where  $R_s$  is usually most relevant and experimentally extracted. For  $\mu_p = 10^{-6} - 10^{-7}m^2/Vs$ ,  $R_s$  values here agree

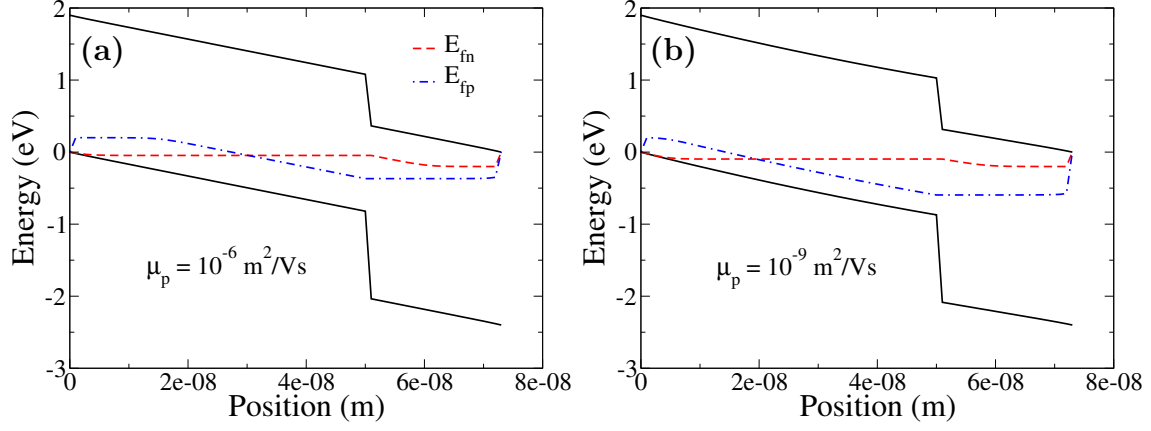


Figure 4.12: Energy diagram showing LUMO level (top solid line) and HOMO level (bottom solid line), including electron and hole quasi-Fermi levels (red dashed and blue dotted-dashed line respectively) of the devices with (a)  $\mu_p = 10^{-6} m^2/Vs$  and (b)  $\mu_p = 10^{-9} m^2/Vs$  at  $V_a = 0.4V$

with typical experimentally extracted values of  $1\Omega cm^2$  or  $10^{-4}\Omega m^2$ . It is also increased by orders of magnitude as  $\mu_p$  decreases. One interesting thing is that  $R_s(V_a)$  itself varies considerably (two orders of magnitude) in the high mobility devices, but it changes much less (factors of five) in the lowest mobility device. This raises the question of when the constant value  $R_s$  Shockley equation can be applicable, which will be discussed in Chapter 5.

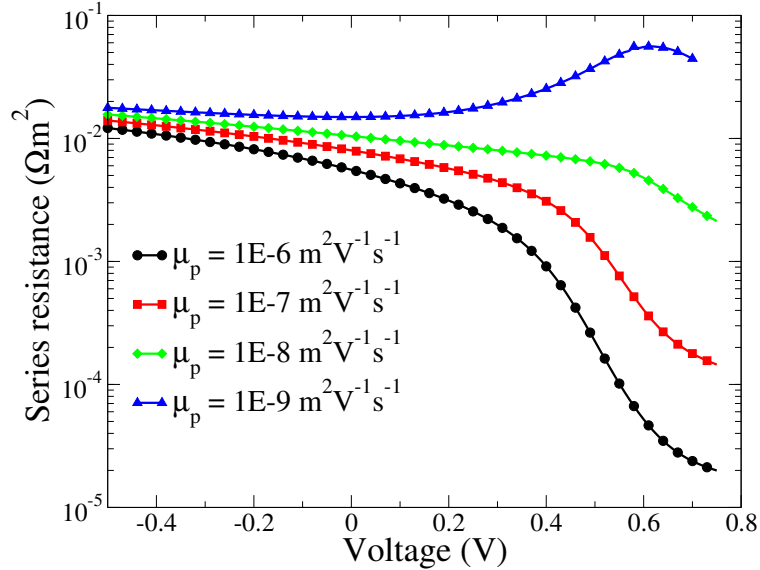


Figure 4.13: Plot of series resistance ( $R_s$ ) functions of the devices with different hole mobility in donor.

The reason why  $R_s(V_a)$  values decrease at high  $V_a$  in high mobility devices is as follows. From Eq. 2.27,  $R_s = [V_a - (E_{fn,I} - E_{fp,I})] / J$ , where  $J$  is the total current, which is negative in the fourth quadrant of JV plot, and  $E_{fn,I} - E_{fp,I}$  is the diode voltage ( $V_d$ ). Consider  $V_d$  and  $V_a - V_d$  of the device with  $\mu_p = 10^{-6} m^2/Vs$  in Figure 4.14. The term  $V_a - V_d$  indicates how much quasi-Fermi levels change over the bulk layers to the actual voltage biasing the interface ( $V_d$ ). For  $V_a < 0.4V$ ,  $V_d$  shows little variation with  $V_a$  because of space charge accumulation, so  $V_a - V_d$  is almost a linear function of  $V_a$  and highly negative. At  $V_a = 0.4V$ , a lot of charges are injected so the interface quasi-Fermi levels start to align with the electrode values. This makes  $V_d \approx V_a$  and  $V_a - V_d$  approaching zero. As a result,  $R_s$  that depends on  $V_a - V_d$  decreases at high  $V_a$ . This can be simply viewed as, at high  $V_a$ , there are more free carriers to conduct currents so the electrical resistivity of the device decreases. On the other hand,  $R_s(V_a)$  of the device with  $\mu_p = 10^{-9} m^2/Vs$  does not follow the same trend as the others because of the stronger degree of space charge effects and the s-shaped JV behavior.

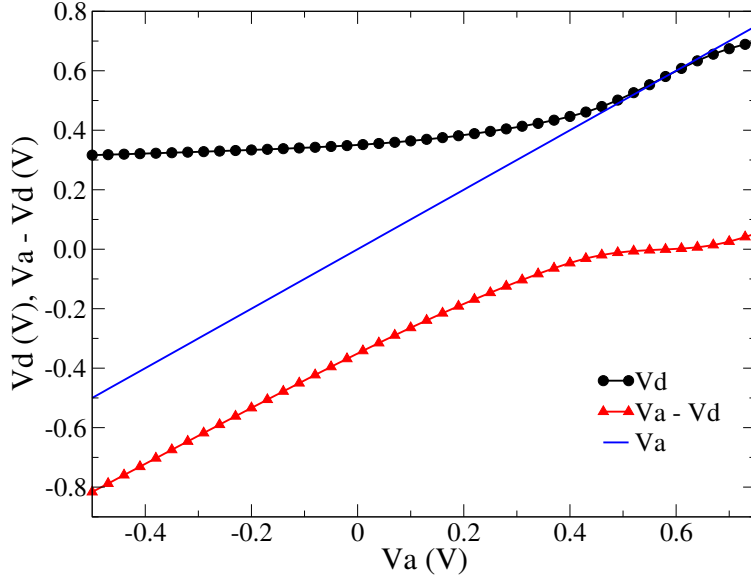


Figure 4.14: Plots of the diode voltage ( $V_d = E_{fn,I} - E_{fp,I}$ ) and total change of quasi-Fermi energies from the electrodes to the interface ( $V_d$ ), i.e.  $V_a - V_d$ , with respect  $V_a$

## 4.3 Effects of Injection Barriers

Injection barriers at the anode ( $\phi_a$ ) and the cathode ( $\phi_c$ ) are defined by  $WF_a - E_{HOMO,D}$  and  $E_{LUMO,A} - WF_c$ , where  $WF_a$  and  $WF_c$  are the anode and the cathode work function, respectively. In this study, only positive values of  $\phi_a$  and  $\phi_c$  are taken into consideration. A stack of indium tin oxide (ITO) and poly(3,4-ethylenedioxythiophene) polystyrene sulfonate (PDOT:PSS) is ubiquitously used as the transparent hole extracting layer (anode) for the P3HT:PCBM system [59, 107, 108, 109]. In some cases, ITO/MoO<sub>X</sub> and other material systems are used as the anode[1, 110]. On the other hand, Ca, Mg, Al LiF/Al, and Au are metallic elements usually chosen to be the cathode[111]. The question why some materials/elements perform better than the others have been partially answered by considering alignment of energy levels[66, 110], but a complete understanding including space charge effects, charge recombination, interface polaron pair recombination, etc. has not been achieved. In order to make the right choices of anode and cathode that optimize the efficiency, effects of injection barriers on OPV are of importance to understand.

### 4.3.1 JV Characteristic Response with Varied Injection Barriers

JV responses of the devices with parameters summarized in table 4.5 under illumination conditions are simulated and showed in figure 4.15a, as well as their efficiency parameters in figure 4.15b. The active layer is P3HT/PCBM bilayer. The anode is ITO/PDOT:PSS, having the injection barrier ( $\phi_a$ ) around 0.2eV.[105]. Cathode work function serves as the independent variable in this study, and is varied from 0.0 to 0.4eV; resulting in many interesting responses of the JV curves. First, photocurrent is reduced with the increasing  $\phi_c$ , giving rise to a lower FF and the s-shape JV behavior which are main reasons for the degraded efficiency. As seen in figure 4.15b, FF is only at 0.48 when  $\phi_c = 0.4eV$ , which is reduced by 26% relative to when  $\phi_c = 0eV$ , while  $J_{sc}$  is reduced by less than 4%. Second,  $V_{oc}$  is affected very slightly by the  $\phi_c$ . Third and most importantly,  $\phi_c \leq 0.2eV$  does not have noticeable effects on the JV curves. Before investigating any of these behaviors, it should be

noted that these s-shape JV characteristics with unchanged  $V_{oc}$  being induced by changing cathode work function are commonly observed in experiments[102, 112, 113].

Parameter	Value
$\mu_p$	$1.0 \times 10^{-8} m^2/Vs$
$\mu_n$	$2.0 \times 10^{-7} m^2/Vs$ [104]
Donor/acceptor thickness	40nm/40nm
$\phi_a$	0.2 eV[105]
$\phi_c$	0.0, 0.1, 0.2, 0.3, 0.35, 0.4 eV
$\epsilon$	$3.9\epsilon_0$
$E_{t,A} = E_{t,D}$	58 meV[103]
$k_{PPr,0}$	$(20\mu s)^{-1}$
Donor $E_{LUMO}/E_{HOMO}$	-4.9eV/-3.0eV
Acceptor $E_{LUMO}/E_{HOMO}$	-6.1eV/-3.7eV
$N_{HOMO}/N_{LUMO}$	$10^{28}/10^{26} m^{-3}$
$H_D = H_A$	$10^{24} m^{-3}$
$J_X$	$4.3 \times 10^{20} m^{-2}s^{-1}$
$a_0 = \delta x$	1.0nm
recombination type	Bimolecular + trap-assisted

Table 4.5: Summary of parameters used to study effects of cathode injection barriers  $\phi_c$

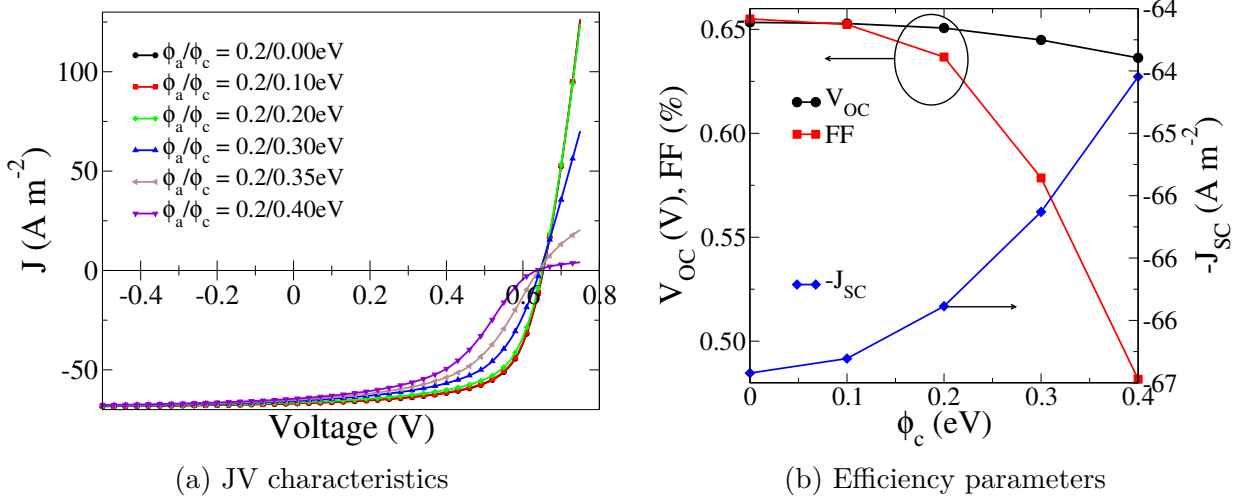


Figure 4.15: (a) JV characteristics of devices under influence of increasing cathode work function (injection barrier), and (b) their extracted  $J_{sc}$ ,  $V_{oc}$ , and FF.

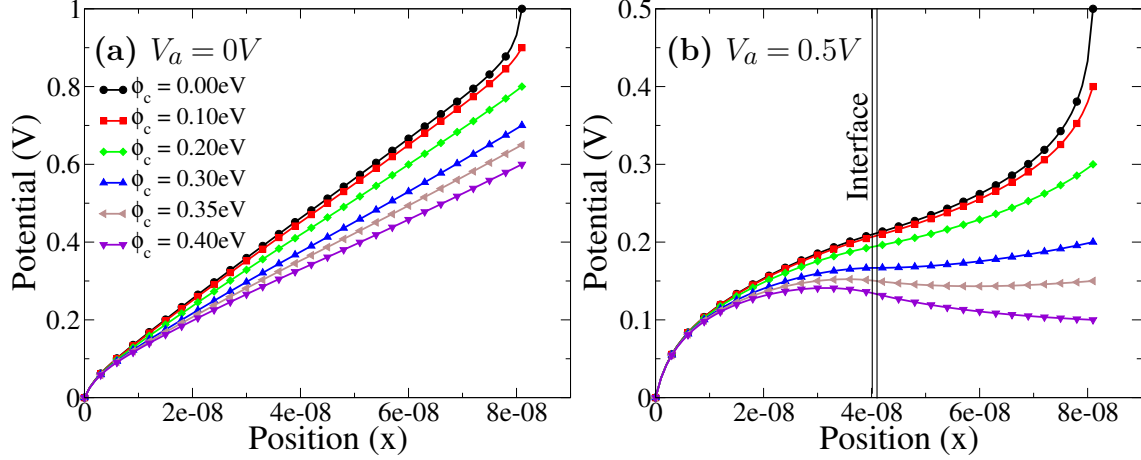


Figure 4.16: Potential profiles ( $\psi(x)$ ) of the devices with different  $\phi_c$  at applied voltage (a) 0V and (b) 0.5V.

#### 4.3.2 Reduced Built-in Potential from High Injection Barriers

The most obvious reason for the reduced photocurrent is that the built-in potential is lessened by higher  $\phi_c$  (i.e. work functions). Built-in potential ( $V_{bi}$ ) is integrated into an OPV from the difference of the electrodes' work function. It is often given by  $V_{bi} = WF_c - WF_a$ , which is also  $V_{bi} = \Delta E_{HL} - \phi_a - \phi_c$ . This potential difference helps pulling photo-generated holes and electrons from the D/A interface to be collected at the anode and the cathode respectively. High work function materials are consequently chosen for the anode, and low work function materials are used as cathodes. Figure set 4.16 shows potential profiles at (a)  $V_a = 0V$  and (b)  $V_a = 0.5V$ , under illumination. This potential ( $\psi(x)$ ) drives free carriers along its gradient resulting in the drift currents;  $qp(x)\mu_p(x)E$  for hole and  $qn(x)\mu_n(x)E$  for electron, where  $E = -\partial\psi(x)/\partial x$  is the electric field. In the figures, the anode and the cathode are at  $x = 0m$  and  $x = 80nm$  respectively. Non-linear  $\psi(x)$  can be seen at the anode for any  $\phi_c$  and at the cathode for  $\phi_c = 0.0eV$ . This is caused by band bending from spontaneous charge transfer at the electrodes, which will be discussed later. Total potential difference between the anode and the cathode is  $WF_c - WF_a$  (i.e.  $V_{bi}$ ). Hence, increasing  $\phi_c$  from 0.1eV to 0.4eV linearly reduces  $V_{bi}$  and results in smaller electric field  $E = -\partial\psi/\partial x$  from the smaller slopes of potential profiles. With less help from the built-in field, less

drift photocurrents can reach the electrodes. Situations at  $V_a = 0.5V$  in figure 4.16(b) are more obvious and severe. The potential profiles are more curved by accumulation of photo-generated charges at the interface, further reducing electric field and drift currents out of the interface. For  $\phi_c \geq 0.3eV$ ,  $V_{bi}$  is low enough so that the direction of the acceptor electric field is switched, driving free charges back to the interface. This is confirmed in Figure 4.17 where majority electron and hole densities are plotted as a function of position, in the devices with  $\phi_c = 0.0$ ,  $0.2$ , and  $0.4$  eV. In the case of  $\phi_c = 0.0eV$ , electron density is high near the cathode due to high drift current as explained earlier and significant carrier injection from the cathode. Electron density near the contact can be approximated by Eq. 1.15 stating that  $n_c = N_{LUMO}exp(-\phi_c/k_B T)$ . Conversely, when  $\phi_c = 0.4eV$ , even though  $n(x)$  near the cathode is very sparse because of the high  $\phi_c$ , free electrons from PP dissociation do not diffuse to the cathode because they are impeded by the inverted electric field, i.e. backward drift current wins over the diffusion current. Thus, dissociated electrons are harder to extract and cause the reduction of photo-current, due to increased free carrier recombination.

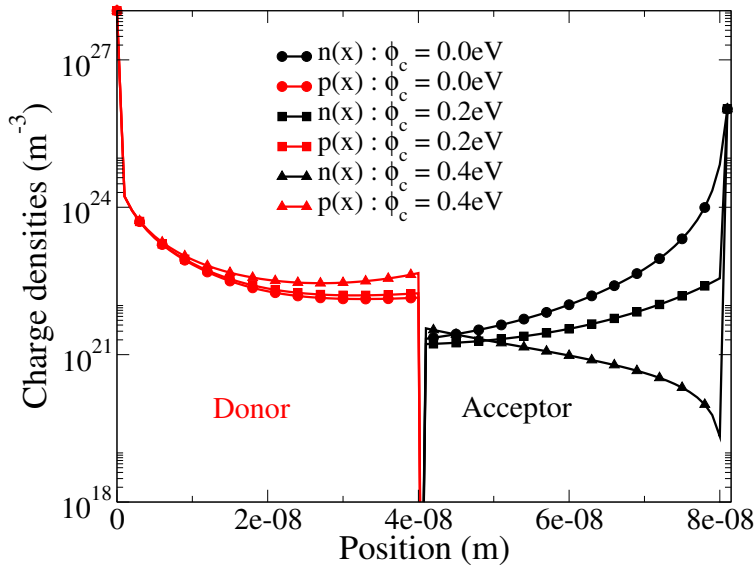


Figure 4.17: Carrier density profiles ( $n(x)$  and  $p(x)$ ) showing only majority carriers, i.e. holes in the donor and electrons in the acceptor, of the devices with  $\phi_c = 0.0eV$ ,  $0.2eV$  and  $0.4eV$  at the same applied voltage of  $0.5V$ .

### 4.3.3 Unaffected Interface Densities: Unaffected $V_{oc}$

From the lack of driving potential at high  $\phi_c$ , interface charge densities are not changed much compared to the contact densities (see figure 4.17). This leads to the origins of another character seen in the JV curves in figure 4.15a, namely the unaffected  $V_{oc}$ .

Open circuit voltage is related to the quasi-Fermi levels through[114];

$$qV_{oc} = (E_{fn} - E_{fp})|_{V_a=V_{oc}}. \quad (4.9)$$

This agrees with the diode voltage derived in this study that  $V_d = E_{fn,I} - E_{fp,I} = V_a - JR_s$ . Under open circuit conditions, the fact that  $J = 0$  results in  $V_a = V_{oc} = E_{fn,I} - E_{fp,I} = V_d$ . At this point,  $E_{fn}$  in acceptor and  $E_{fp}$  in donor are invariant with the position, being aligned from the electrodes to the interface. In order to approximate  $V_{oc}$ , consider the expressions for charge densities in equations 1.21 and 1.22. Interface quasi-Fermi levels can be obtained by taking a logarithm;

$$E_{fn,I} = E_{LUMO,A,I} + k_B T \ln \left( \frac{n_I}{N_{LUMO}} \right), \quad (4.10)$$

$$E_{fp,I} = E_{HOMO,D,I} - k_B T \ln \left( \frac{p_I}{N_{HOMO}} \right). \quad (4.11)$$

The subscripts D, A, and I refer to the donor, the acceptor and the interface respectively.

Substitute these into the  $V_{oc}$  equation.

$$V_{oc} = \Delta E_{HL} - \frac{k_B T}{q} \ln \left( \frac{N_{LUMO} N_{HOMO}}{n_I p_I} \right), \quad (4.12)$$

where  $\Delta E_{HL} = E_{LUMO,A,I} - E_{HOMO,D,I}$  is interface energy gap in eV. All the variables in Eq. 4.12 are independent of  $\phi_c$ , except  $n_I p_I$ . The larger  $n_I p_I$  is, the closer  $E_{fn,I}$  is to  $E_{LUMO,A,I}$ , and  $E_{fp,I}$  to  $E_{HOMO,D,I}$ , leading to larger  $V_{oc}$ . Figure 4.18(a) shows plots of  $n_I$  and  $p_I$  at  $V_{oc}$  as a function of  $\phi_c$ . Even with the reversed acceptor electric field at higher  $\phi_c$ ,  $n_I$  only decreases slightly from diffusion out of the interface. Interface holes then face less recombination from the lesser electrons and accumulate more. With one density goes down and the other goes up,  $n_I p_I$  does not change much as  $\phi_c$  increases (notice that the  $n_I p_I$  scale

is linear), so is the  $V_{oc}$ . Figure 4.18(b) shows a comparison between  $V_{oc}$  obtained from the JV curves in Fig. 4.15a and approximated by Eq. 4.12 using  $n_I p_I$  from Fig. 4.18(a). It should be stressed that the y-scale is very narrow. Both graphs indicate that  $V_{oc}$  changes less than 20mV while  $\phi_c$  changes by 0.4eV. The approximated  $V_{oc}$  is close and agrees with the extracted one with a small constant error arising from using  $\Delta E_{HL} = 1.2\text{eV}$  as a constant. In reality, there is band bending at the interface[66] making  $\Delta E_{HL} \neq E_{LUMO,A,I} - E_{HOMO,D,I}$ .

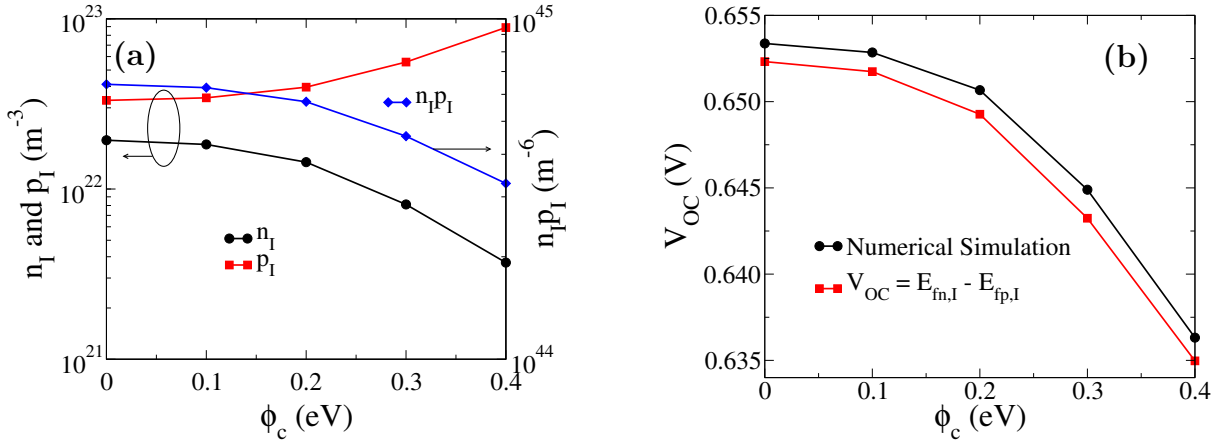


Figure 4.18: Plotting as a function of  $\phi_c$  of (a) interface electron and hole densities with their multiplication and (b) open circuit voltages extracted from the DD-BI model simulations (same as in Fig. 4.15b), compared with a calculated one using equation 4.12.

In conclusion,  $n_I p_I$  is not affected significantly by the reduced built-in field resulting from an increased  $\phi_c$ . Open circuit voltage which entirely depends on  $n_I p_I$  is also not greatly affected. Optimizing OPVs by using matching electrode work functions (small injection barriers) does not improve  $V_{oc}$  but significantly improves FF and  $J_{sc}$ .

#### 4.4 Metal/Organic Semiconductor Contact

The question why  $\phi_c \leq 0.2\text{eV}$  does not have any noticeable effects on the JV curves will be investigated in this part. The main role is played by the metal/organic semiconductor contact at the cathode where a lot of physics is going on. This section will be for possible explanations of the nature of the contact, starting from Mott-Schottky model to Integer Charge Transfer Model. Band bending, the intrinsic property that has been mentioned

many times, will also be discussed. The simulation results will be compared and explained with these established theories.

#### 4.4.1 Mott-Schottky Model With Vacuum Level Shift

The original Mott-Schottky (MS) model was proposed in the 1940s in two separate papers by N. F. Mott and W. Schottky. The model was developed for metal/inorganic semiconductor contacts, but had been applied, without serious verification, to the field of organic semiconductor during its boom period[115]. Until around in 2000, there were many experimental evidences of an interface dipole that induces a vacuum level shift, so the model was slightly modified by including it.

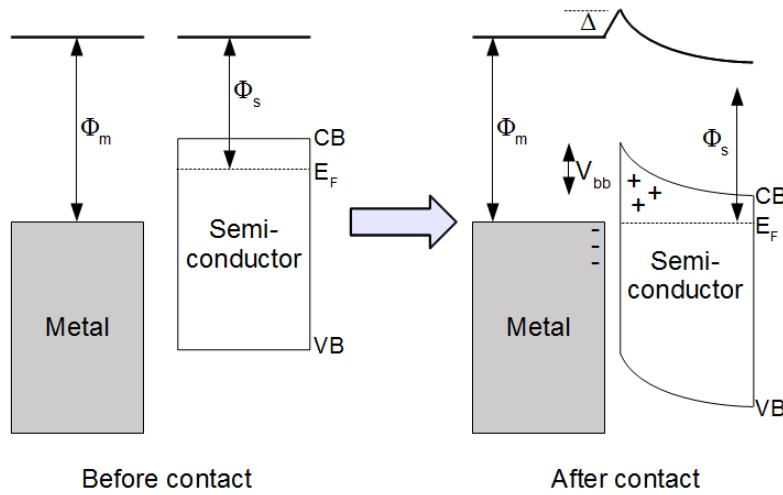


Figure 4.19: Illustration of a Mott-Schottky contact between a metal with work function  $\Phi_m$  and an n-type semiconductor with chemical potential  $\Phi_s$ , where  $\Phi_m > \Phi_s$ , forming a blocking contact and downward band bending.

Figure 4.19 is a schematic conclusion of one example of the MS contacts. A metal with the work function  $\Phi_m$  is brought into contact with an n-type inorganic semiconductor with the Fermi level (chemical potential)  $\Phi_s$ , where  $\Phi_m > \Phi_s$ . After the contact, Fermi level has to be equilibrated at the interface and aligned throughout the bulk semiconductor. To

achieve this, electrons have to flow from the semiconductor (higher energy) to the metal (lower energy), giving rise to energy levels bending, or band bending. In the original MS model, interface vacuum level alignment is assumed. However, this does not hold in most organic/metal interfaces due to an interface dipole modifying vacuum level, so a vacuum level shift ( $\Delta$ ) was added to the model[115]. Potential drop from the band bending ( $V_{bb}$ ) is  $|\Phi_m - \Phi_s|$ , and total potential loss ( $V_{loss}$ ) including the vacuum shift is  $V_{bb} + \Delta$ . In this example, a Mott-Schottky (blocking) barrier is formed, making the contact rectifying. In the opposite circumstances shown in figure 4.20 where  $\Phi_m < \Phi_s$ , electrons flow from the metal to the semiconductor, inducing upward band bending instead of downward. There is no Mott-Schottky barrier and the contact is ohmic (non-rectifying). Possible vacuum level shift is also included in the figure.

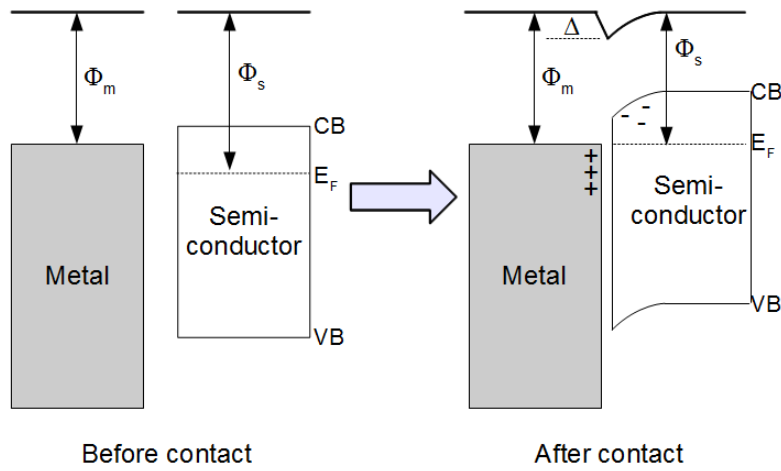


Figure 4.20: Illustration of an ohmic contact between a metal with work function  $\Phi_m$  and a semiconductor with Fermi level  $\Phi_s$ , where  $\Phi_m < \Phi_s$ , forming an ohmic contact and upward band bending.

#### 4.4.2 Integer Charge Transfer (ICT) Model

Integer Charge Transfer (ICT) model has gained more popularity than the MS model recently as it is more applicable and able to describe organic/metal interfaces, and it has been confirmed by experiments [106]. There are many models describing different types of organic/metal interfaces, but the ICT model is suitable for interfaces of a solution processed (spin-coating, ink-jet printing) polymer coating on oxide passivated metal[66]. This type of interface is the most common in OPVs due to the ease of the solution process.

Organic  $\pi$ -conjugated molecules and polymers have a soft geometric structure so that when they receive or give away an electron, both electronic and geometric states are relaxed[66]. Hence, free holes and electrons in an organic polymer are considered as polarons. Their local polaronic states can have energies within the forbidden energy gap[66]. Based on the ICT model,  $E_{ICT+}$  is defined as an energy loss when an electron is transferred out of the organic material. This level lies just above the HOMO band edge, within the energy gap. Similarly,  $E_{ICT-}$  is an amount of energy gained by the organic semiconductor if there is an electron transferred into it. This level is below and close the LUMO edge.

When a substrate with a work function  $\Phi_m$  is brought into contact with an organic semiconductor, three possible cases as shown in figure 4.21 may occur.

(a) If  $\Phi_m > E_{ICT+}$ , electron polarons in the  $E_{ICT+}$  states tunnel through the interface to the substrate, creating hole polarons and reducing total energy of the organic semiconductor. This continues until  $E_{ICT+}$  is equilibrated with the substrate work function, usually referred to as Fermi level pinning. There is a potential dipole from the unbalanced charges, producing a shift of vacuum level ( $\Delta$ ) at the interface, equal to  $\Phi_m - E_{ICT+}$ .

(b) If  $E_{ICT-} < \Phi_m < E_{ICT+}$ , spontaneous charge transfer does not occur due to unfavorable energy loss and gain of the organic material[66]. Once taken into contact, all energy levels are the same as when they are separated, making their vacuum level aligned. This situation is consequently called Vacuum Level Alignment in the ICT model.

(c) If  $\Phi_m < E_{ICT-}$ , electrons from the substrate will spontaneously tunnel to the organic

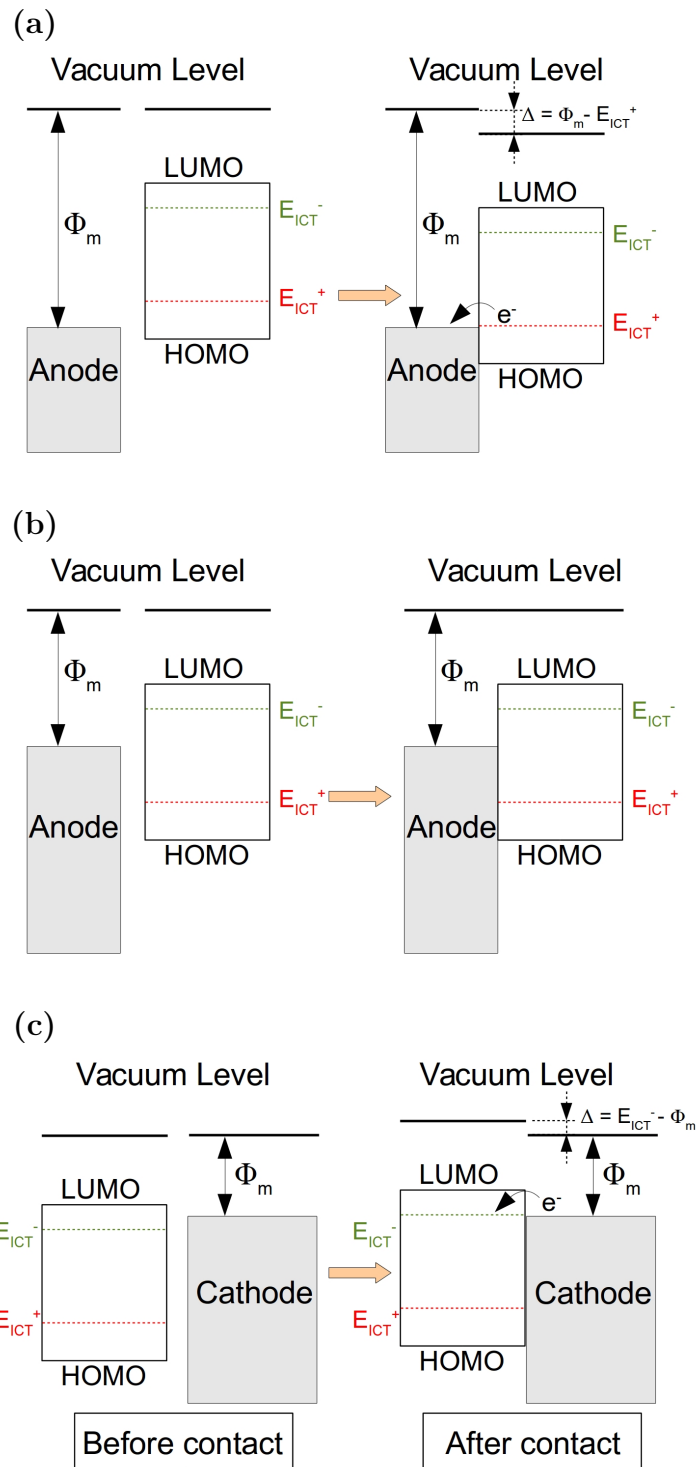


Figure 4.21: Integer Charge Transfer (ICT) model describing spontaneous charge tunneling at a metal/organic semiconductor interface of the case (a)  $\Phi_m > E_{ICT}^+$ , (b)  $E_{ICT}^- < \Phi_m < E_{ICT}^+$  and (c)  $\Phi_m < E_{ICT}^-$ .

layer, raising its  $E_{ICT^-}$  and all other energy levels. Similar to the case (a), this continues until the  $E_{ICT^-}$  level equals the substrate work function, so the Fermi level is pinned. Upward vacuum level shift;  $\Delta = E_{ICT^-} - \Phi_m$ , also occurs at the interface.

#### 4.4.3 Organic/Metal Interfaces Under Illumination

It was found that the computational results have distinct properties between under illumination and the dark. Thus, a cathode organic/metal interface under illumination is investigated first in this part. The cathode injection barrier is taken to be 0.6eV to clearly show its influence. Other parameters are the same as in table 4.5. Analysis of  $\phi_c$  effects will involve referring to important spatial positions in the device. Figure 4.22 is a simple diagram of the bilayer structure and some important positions (nodes). As stated in the computational theory chapter (Chapter 3), the position in the direction of film thickness is divided into nodes (mesh). The anode is at the node 0; the donor is from the 1<sup>st</sup> to the  $l^{th}$  node. The acceptor at the vicinity of the hetero-junction is at the  $l+1^{th}$  node. Most importantly, the node  $L-1$  is the acceptor node next to the organic/metal interface, and the  $L^{th}$  node is the cathode. Based on the MS and the ICT models, the vacuum level shift given by  $\Delta = \psi_{L-1} - \psi_L$ . Fermi level pinning can be checked by comparing  $E_{fn,L-1} - WF_c$  with zero. If it is zero, then the Fermi level, or more correctly quasi-Fermi level, is pinned. If there is band bending in the acceptor bulk, it will be  $V_{bb} = \psi_{l+1} - \psi_{L-1}$ . Lastly, total potential drop from the cathode to the hetero-interface is  $V_{bb} + \Delta = \psi_{l+1} - \psi_L$ .

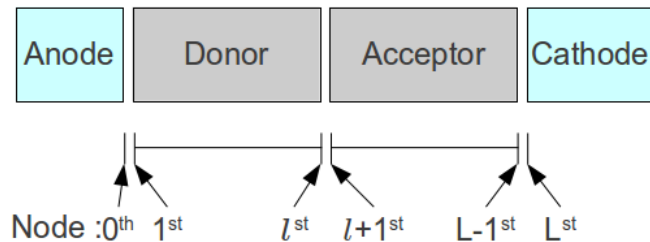


Figure 4.22: A simple diagram showing the bilayer structure and some important positions at the anode and the cathode organic/metal and the hetero-junction interfaces.

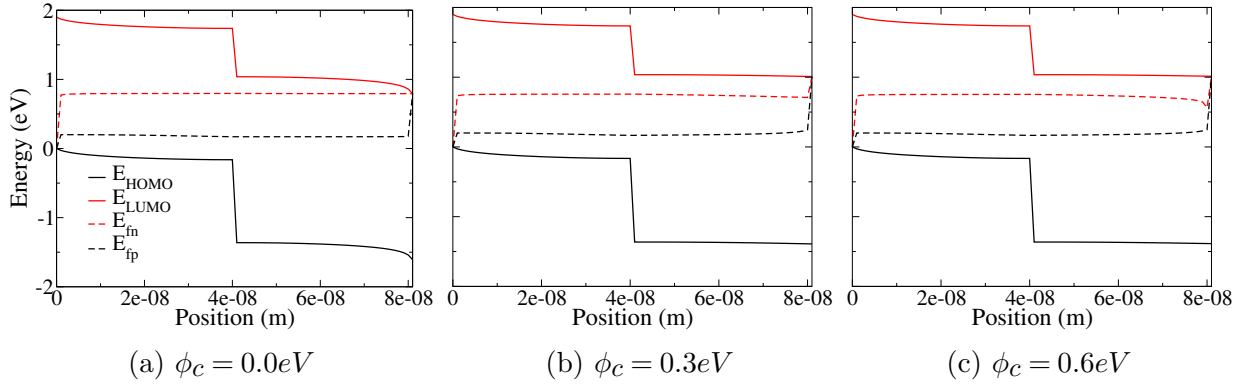


Figure 4.23: Band diagram illustrating energy levels of the devices with  $\phi_a = 0.2\text{eV}$  and  $\phi_c = 0.0\text{eV}$ ,  $0.3\text{eV}$  and  $0.6\text{eV}$  under illumination.

Figure 4.23 shows energy band diagrams from anode to cathode of the devices with  $\phi_c = 0.0\text{eV}$ ,  $0.3\text{eV}$  and  $0.6\text{eV}$  under flat band conditions and illumination. Flat band conditions are when the applied voltage cancels out the built-in potential so the bands are flat and drift currents vanish. However, there is unavoidable band bending that makes completely flat bands impossible in some cases. The applied voltages to achieve flat bands in figure 4.23 are  $0.594\text{V}$ ,  $0.509\text{V}$  and  $0.214\text{V}$  respectively. Total potential drop from the cathode to the D/A interface under flat band conditions will be called voltage loss ( $V_{loss}$ ) in donor. The name is taken from the fact that  $V_{bi}$  is lost due to  $V_{bb}$  and  $\Delta$ , producing less built-in electric field.

Figure 4.24 shows  $\Delta$  at the cathode,  $V_{loss}$  and  $E_{fn,L-1} - WF_c$  as a function of  $\phi_c$ .

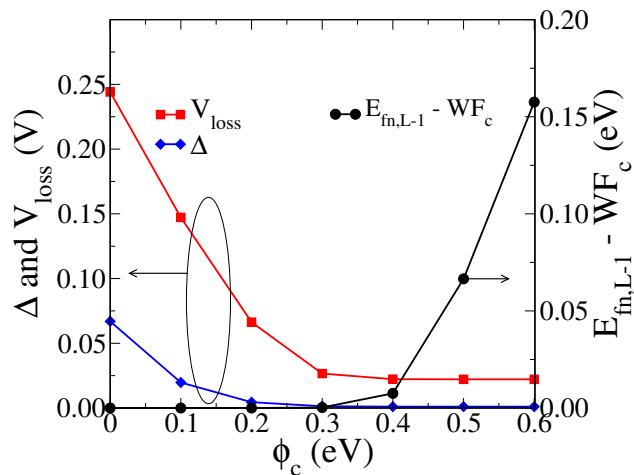


Figure 4.24: Plots of vacuum level shift ( $\Delta$ ), voltage loss ( $V_{loss}$ ) and acceptor electron quasi-Fermi level ( $E_{fn,L-1}$ ) at the cathode relative to the cathode work function ( $WF_c$ ) as a function of  $\phi_c$ .

According to figures 4.23 and 4.24, some conclusions can be drawn as follows. Firstly, Two regimes of  $\phi_c$ , i.e. Fermi level pinning (with vacuum level shift) and vacuum level alignment (with unpinned Fermi level) as suggested by the ICT model, are observed. The black and blue curves in figure 4.24 clearly exhibit these cases. At low  $\phi_c$ ,  $E_{fn,L-1}$  is close to  $WF_c$  and moves along with it when it is varied. Vacuum level shift is also visible in this range. However at  $\phi_c \approx 0.3eV$ ,  $E_{fn,L-1}$  starts to unpin from  $WF_C$  when it moves down further into the acceptor energy gap. At the same time,  $\Delta$  approaches and remains zero. This gives a rough prediction that the  $E_{ICT-}$  is around 0.3eV. Secondly, unlike the ICT model stating that band bending should not occur[66], band banding is clearly seen in both figures 4.24 and 4.23(a). Band bending is caused by accumulation of space charges and should be inevitable in OPVs because of the low mobilities. It is usually observed experimentally, for example, Ishii et al. [115] saw band banding in a C<sub>60</sub> film on a Copper substrate by using Kelvin probe measurements. However, there is only upward band bending when  $\phi_c$  is low, but no downward one to be found when  $\phi_c$  is high, as predicted by the MS model. At high  $\phi_c$ , band banding and vacuum level shift are less significant (see figure 4.24) and the bands seem to be more flat (see figure 4.23(b) and (c)). Not much change of the bands can be observed when increases  $\phi_c$  from 0.3eV to 0.6eV. The positions of  $E_{fn}$  and  $E_{fp}$  in the bulk as well as their split at the D/A interface also do not alter notably. These are other proofs of the unchanged  $V_{oc}$  that was discussed previously. Thirdly, vacuum level shift is not as high as expected by the MS and ICT models. They predict that the shift should be about  $|0.3 - \phi_c|$  V, taken into account that  $E_{ICT-} \approx 0.3V$ . However, it is just tens of mV from the simulation results. However, when include band bending into the shift leading to  $V_{loss}$ , it is in an agreeable range as predicted by the ICT and MS models. This discrepancy may arise from different assumptions and the way each model approaches the problem. The MS model was originally developed for inorganic/metal interfaces, but can work reasonably well with organic interfaces, if small modifications are included. The ICT model was empirically developed from a lot of photoelectron spectroscopy data. Some theoretical works at the

molecular level might be needed to verify and correct the model. The DD-BI model is based on more fundamental Physics like Poisson equation, but better organic descriptions, for example at the organic/metal interfaces, are needed. Nevertheless, they all work well to describe OPVs to some extent.

#### 4.4.4 Organic/Metal Interfaces In the Dark

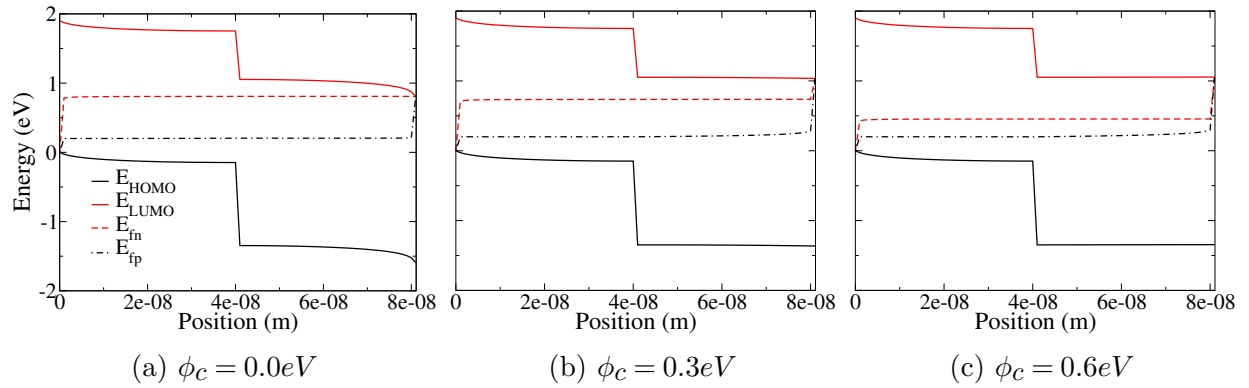


Figure 4.25: Band diagram illustrating energy levels of the devices with  $\phi_c = 0.0\text{eV}$ ,  $0.3\text{eV}$  and  $0.6\text{eV}$  in the dark.

Figure 4.25 shows energy band diagrams in the dark under flat band conditions of the devices with  $\phi_c = 0.0\text{eV}$ ,  $0.3\text{eV}$  and  $0.6\text{eV}$ . The flat band voltages are  $0.609\text{V}$ ,  $0.536\text{V}$  and  $0.255\text{V}$  respectively. These are slightly different from the one under illumination because there is no space charge accumulation at the D/A interface in the dark.

The most important trait of the interface in the dark is that the electron quasi-Fermi level in the donor is always pinned at the cathode, regardless of  $\phi_c$ . Figures 4.23(c) and 4.25(c) illustrate this. Figure 4.25(a), (b) and (c) show  $E_{fn,L-1}$  being exactly at  $0.0\text{eV}$ ,  $0.3\text{eV}$  and  $0.6\text{eV}$  respectively below the energy of the  $L^{th}$  node. There are no separated  $\phi_c$  regimes like in the devices under illumination within the ICT model. The results are more agreeable, but not entirely, with the MS model where Fermi level pinning is always assumed. Band bending and vacuum level shift similar to the illumination cases in figure 4.24 are also expressed under the dark.

#### 4.4.5 Components of Series Resistance

Series resistances ( $R_s$ ) was discussed in section 4.2.4 without any effects of the organic/metal interface at the cathode or the anode, so only the bulk donor and acceptor contributed to the  $R_s$ . It is commonly known that not only the bulk parts, but also any contacts are factors influencing  $R_s$ . There is an experiment by Y. Shen et al.[46], studying effects of film thickness on the series resistance. The results show that  $R_s$  does come from the two contributions, with about 17% from the contacts and 83% from the bulk.

Since  $R_s$  is controlled by changes in the quasi-Fermi levels, as explained in section 4.2.4, it is important to consider four possible causes of changes in the quasi-Fermi energies: (1) anode contact; (2) bulk donor; (3) bulk acceptor; and (4) cathode contact. These give rise to four components of  $R_s$  that will be named as  $R_{sa}$ ,  $R_{sD}$ ,  $R_{sA}$  and  $R_{sc}$  respectively. See figure 4.26 for an illustration. At the anode or the cathode contact, if the injection barrier is too high so that the quasi-Fermi level is not pinned, there will be a drop of the quasi-Fermi energies. This can be represented by the contact series resistances  $R_{sa}$  and  $R_{sc}$ . To view this from another angle, high injection barriers bring about a Mott-Schottky blocking barrier, which resists charge injection/extraction. For the bulk donor and acceptor, poor charge transport (mobility) gives rise to lower conductivity and reduces/changes the quasi-Fermi levels in the regions around the D/A interface. These cause the donor and acceptor to have the resistance  $R_{sD}$  and  $R_{sA}$  respectively. Since this topic was discussed quite expansively in section 4.2.4, effects of injection barriers will only be focused on. Similar to total  $R_s$  equation in Eq. 2.27, each  $R_s$  component is simply given by

$$R_{s,i-j} = \frac{E_{fn(p),j} - E_{fn(p),i}}{J_{i-j}}, \quad (4.13)$$

where  $R_{s,i-j}$  and  $J_{i-j}$  are series resistance and total current density between the node  $i^{th}$  and  $i+1^{th}$ , respectively.

Figure 4.27 shows how  $R_s$  changes with increasing  $\phi_c$ , under illumination. For  $\phi_c = 0.0\text{eV}$  to  $0.2\text{eV}$ , the change of  $R_s$  is negligible. The graph for  $\phi_c = 0.1\text{eV}$  sits on top and entirely covers the graph of  $\phi_c = 0.0\text{eV}$ . Since mobilities are fixed, the  $R_s$  change is only caused by

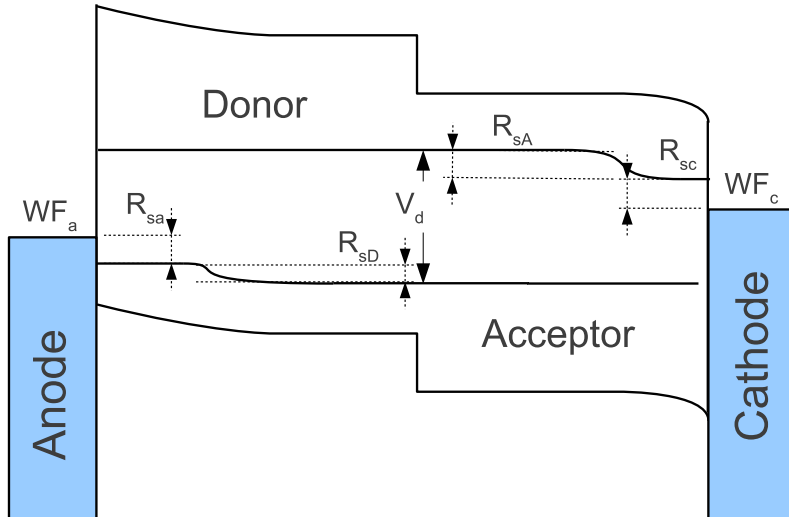


Figure 4.26: Diagram showing possible deviations of hole quasi-Fermi level at the anode contact and bulk donor and electron quasi-Fermi level at the cathode contact and bulk acceptor, that can be represented by a component of series resistance.

the cathode and anode interfaces. However, in this range of  $\phi_c$ , quasi-Fermi level pinning occurs and there is no drop of the  $E_{fn}$  at the cathode, so there is no contribution of  $R_{sc}$  at all. Then total  $R_s$  is not affected by  $\phi_c$  and/or  $\phi_a$  that are in Fermi level pinning regime. Starting at  $\phi_c = 0.3\text{eV}$ ,  $R_s$  at high voltage begins to increase. As stated earlier,  $R_s$  matters more at the high-voltage than low-voltage regimes. Thus, this  $R_s$  increment affects the OPV efficiency as seen in figure 4.15a, even though  $R_s$  values at low voltage are the same.

Change of  $R_s$  from  $\phi_c = 0.2\text{eV}$  to  $0.6\text{eV}$  is interesting to look further how those four components of  $R_s$  play their role. Figure 4.28 shows plots of  $R_{sa}$ ,  $R_{sD}$ ,  $R_{sA}$  and  $R_{sc}$  as a function of voltage of the devices with  $\phi_c = 0.2\text{eV}$ ,  $0.4\text{eV}$  and  $0.6\text{eV}$ . They are calculated by equation 4.13. Anode injection barrier is fixed at  $0.2\text{eV}$ . Firstly, it can be seen that  $R_{sa}$  is negligibly small and not changed at all. This is because of the unchanged  $\phi_a$  and pinning of  $E_{fp}$  at the anode. Secondly, bulk donor resistance  $R_{sD}$  is also not affected noticeably by the increased  $\phi_c$ , due to the fixed  $\phi_a$  and donor hole density that is not disturbed much. Thirdly,  $R_{sD}$  is high and composes most of the  $R_s$  when both  $\phi_a$  and  $\phi_c$  equal to  $0.2\text{eV}$ . This is because of the lower hole mobility in the donor as compared to electron mobility.

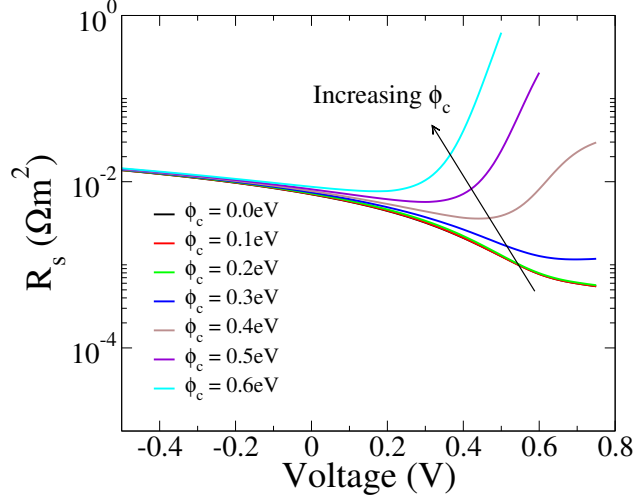


Figure 4.27: Plots of series resistance as a function of voltage under influences of changing cathode injection barrier from 0.0eV to 0.6eV with fixed anode injection barrier at 0.2eV.

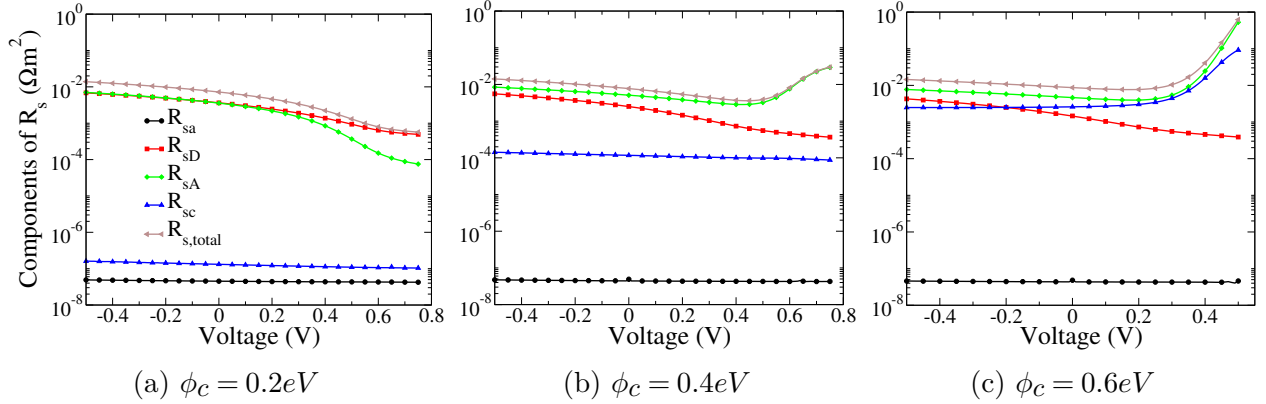


Figure 4.28: Plots of the component series resistances  $R_{sa}$ ,  $R_{sd}$ ,  $R_{sa}$  and  $R_{sc}$ , and total  $R_s$  being the sum of the four components as a function of applied voltage of the devices with different cathode injection barrier.

However, higher  $\phi_c$  greatly reduces electron density in the acceptor, making  $E_{fn}$  deviation in the acceptor much more significant. This raises  $R_{sa}$  so that it becomes a major part of the total  $R_s$ . Fourthly  $R_{sc}$  increases its importance as  $\phi_c$  increases. From  $\phi_c = 0.2\text{eV}$  where  $E_{fn}$  is pinned with  $WF_c$  and  $R_{sc}$  is negligible to  $\phi_c = 0.4\text{eV}$ , the barrier  $\phi_c$  has entered the vacuum level alignment regime, dropping  $E_{fn,L-1} - WF_c$  a little from  $WF_c$ . The resistance  $R_{sc}$  increases many orders of magnitude, but is still insignificant compared to the bulk resistances  $R_{sd}$  and  $R_{sa}$ . At  $\phi_c = 0.6\text{eV}$ , the drop of  $E_{fn,L-1} - WF_c$  becomes substantial as seen in figure 4.24, so that  $R_{sc}$  is more than the donor resistance  $R_{sd}$  and considerably contributes

to the total  $R_s$ .

In conclusion, if both  $\phi_c$  and  $\phi_a$  barriers are in the Fermi level pinning regime, i.e. less than about 0.3eV, contacts resistances  $R_{sa}$  and  $R_{sc}$  are negligible. Series resistance depends on the bulk layer having smaller carrier mobility. Increasing any injection barrier over this limit augments the resistant components associated with it. One is its contact, and the other is the charge density it injects into the bulk. For the case of  $\phi_c$ , it increases  $R_{sA}$  because less electrons can be injected into the acceptor and  $R_{sc}$  because the Fermi level is not pinned but dropped across the organic/metal interface.

#### 4.4.6 Choosing the Anode and the Cathode

Effects of injection barriers have been discussed from many standpoints such as built-in potential, band bending, organic/metal interfaces and contact series resistances. The most important question that remains unanswered is: What are the right values of the anode and the cathode work functions that maximize the OPV efficiency?

Speaking in terms of built-in potential;  $V_{bi} = |WF_a - WF_c|$ , so maximizing this by using the highest  $WF_a$  and the lowest  $WF_c$  seems to be a right strategy. However, this is not true if  $WF_a$  is higher than the donor HOMO level and/or  $WF_c$  is lower than acceptor LUMO level. All energies here are measured relative to the vacuum level. Effects of negative  $\phi_a$  and  $\phi_c$  that are beyond the scope of this study was investigated experimentally by Y.S. Eo et al.[111]. They studied effects of cathode work function in a bulk hetero-junction P3HT:PCBM OPV using PDOT:PSS as the anode. Following materials were used as the cathode: Ca ( $WF_c = 2.89\text{eV}$ ), Mg ( $WF_c = 3.66\text{eV}$ ), Al ( $WF_c = 4.20\text{eV}$ ), LiF/Al ( $WF_c = 4.30\text{eV}$ ) and Au ( $WF_c = 5.10\text{eV}$ ). With the PCBM LUMO level around 4.3eV, Ca, Mg and Al having a negative  $\phi_c$  resulted in worse OPV efficiency than LiF/Al that has about zero  $\phi_c$ , with descending efficiency from Al to Mg to Ca. The worst efficiency belonged to gold that has  $\phi_c \approx 0.8\text{eV}$ . Hence, small positive  $\phi_a$  and  $\phi_c$  are preferred values for high efficiency.

There is, however, room that  $\phi_c$  and  $\phi_a$  can vary around without affecting the efficiency.

If  $\phi_c$  is between  $E_{LUMO,A}$  and acceptor  $E_{ICT^-}$  and  $\phi_a$  is between  $E_{HOMO,D}$  and donor  $E_{ICT^+}$ , charge transfer and Fermi level pinning will make  $\phi_a$  and  $\phi_c$  irrelevant because the injection barriers are countered/compensated by band bending and vacuum level shift. The PCBM  $E_{ICT^-}$  is about 0.3eV according to this study. Using  $\phi_a$  and  $\phi_c$  in these ranges also benefits the  $R_s$  by minimizing contact resistances.

## 4.5 Ideality Factor and Trap-assisted Recombination

The ideality factor ( $n$ ), or quality factor when specifically used with p-n junction diodes in old literature [116], is another fitting parameter in the Shockley equation which is as important as the other parameters in the model. Despite the fact that it is just a single number, typically ranging around 1-2, it is a useful indicator of the recombination mechanism in microscopic levels.  $n$  equal to 1 is commonly understood as an indication of bimolecular recombination, while  $n > 1$  indicates that trap-assisted recombination dominates [52]. In this part, the origins of  $n$  will be discussed. Their equations developed in this study (equations 2.17 and 2.18) will be showed to be generalized forms of famous expressions for  $n$ . Effects of trap states on the ideality factors will be investigated. Later, the origins of  $n = 1$  and errors from interpreting a fitted  $n$  will be discussed.

Recombination of free carriers and trapped charges brings about a value of  $n$  larger than one. Following is a well acknowledged analytic theory that connects  $n$  to the trap characteristic[116, 52, 51]. Let  $n_f$  be the free carrier density, where it could belong to either electrons or holes. Trapped charge density ( $n_t$ ) can be approximated by the exponential trap distribution through[52, 51]

$$n_t \propto n_f^{k_B T/E_U}, \quad (4.14)$$

where  $E_U$  is the characteristic Urbach tail energy. Assuming that the hole and the electron densities are close to each other, then the trap-assisted recombination depends on  $n_f^{1+k_B T/E_U}$ . Note that Eq. 4.14 is the same as the trapped charge densities in Equations 1.23 and 1.24 used in the GWWF model and this work, but the characteristic trapped electron and

hole energies are expressed separately through  $E_{t,A} = k_B T_{t,A}$  and  $E_{t,D} = k_B T_{t,D}$  respectively, instead of  $E_U$ . Using the fact that the diode current originates from the recombination[116], the relation

$$n = \left( \frac{1}{2} + \frac{k_B T}{2E_U} \right)^{-1} \quad (4.15)$$

is obtained[116, 52, 51]. Thus an extracted  $n$  can be used to calculate the Urbach tail energy  $E_U$ .

In this study, there are two ideality factors;  $n_D$  in Eq. 2.17 from the trapped-hole to free-electron recombination (fn-tp) and  $n_A$  in Eq. 2.18 from the trapped-electron to free-hole recombination (fp-tn). They are indeed general forms of Eq. 4.15 if total symmetry is assumed. It means that, for example:  $\mu_n = \mu_p$ ; donor and acceptor thicknesses are equal; both injection barriers are the same.  $n_D$  is rewritten here for convenience

$$n_D = \left( 1 + \frac{(E_{fp,I} - E_{f,I})(1 - 1/l_D)}{E_{fn,I} - E_{fp,I}} \right)^{-1}, \quad (4.16)$$

where,  $l_D = T_{t,D}/T$ . In the symmetric case,  $E_{fp,I}$  and  $E_{fn,I}$  split equally from the equilibrium  $E_{f,I}$  under influences of bias or illumination and hence the magnitude of  $E_{fp,I} - E_{f,I}$  is half of  $E_{fn,I} - E_{fp,I}$ . Note that  $E_{f,I}$  is higher than  $E_{fp,I}$ . Thus,

$$n_D = \left( 1 - \frac{(1 - 1/l_D)}{2} \right)^{-1} = \left( \frac{1}{2} + \frac{T}{2T_{t,D}} \right)^{-1} = \left( \frac{1}{2} + \frac{k_B T}{2E_{t,D}} \right)^{-1}, \quad (4.17)$$

where  $E_{t,D} = E_{t,A} = E_U$  and  $n_D = n_A = n$ .

To prove the claim in the previous paragraph computationally, a symmetric device with only trap-assisted recombination was simulated with the following parameters: the thicknesses were 40 nm for both donor and acceptor;  $\phi_a = \phi_c = 0.2\text{eV}$ ;  $\mu_p = \mu_n = 2 \times 10^{-7}\text{m}^2/\text{Vs}$ ;  $\epsilon = 3.5\epsilon_0$ ; most importantly,  $T_{t,D} = T_{t,A} = 1000K$ .  $n_D$  and  $n_A$  calculated by Equations 2.17 and 2.18 are plotted in Figure 4.29. Please notice the very fine scale on the y-axis. They are very close to each other, with small variations at high voltage. Using  $n_D = n_A \approx 1.5384$  to calculate the characteristic trap energy in Equations 4.15,  $E_U = 86.16\text{meV}$  is obtained, which exactly is  $k_B T_{t,D}$  or  $k_B T_{t,A}$  when  $T_{t,D} = T_{t,A} = 1000K$ .

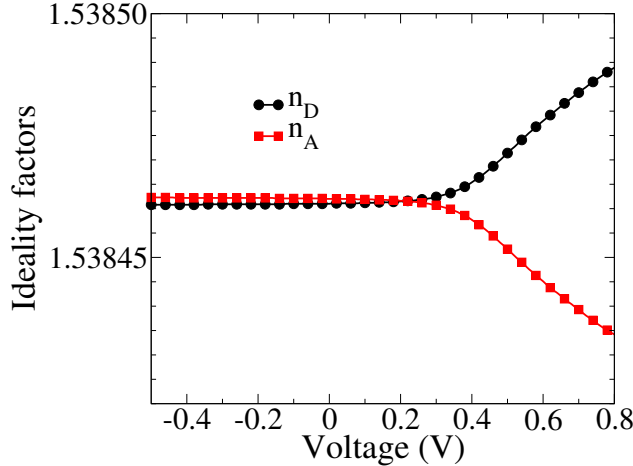


Figure 4.29: Ideality factors  $n_D$  and  $n_A$  in the symmetric device with characteristic trap temperatures of electron ( $T_{t,A}$ ) and hole ( $T_{t,D}$ ) equal to 1000K.

Knowing that the  $n_D$  and  $n_A$  equations are general forms of  $n$  in the established theory, studying their responses to the characteristic trap energies in general is the next step. Devices with different  $T_{t,D}$  varying from 400K to 1200K but the same  $T_{t,A}$  at 1000K were simulated. Other parameters are listed in Table 4.6. Their JV curves are plotted in Figure 4.30, and their efficiency are summarized in Table 4.7. According to the results,  $J_{sc}$  shows little variation across the  $T_{t,D}$  change.  $V_{oc}$  improves around 50mV from the diminishing trapped holes. FF is also slightly improved. Interestingly, there is not much change of the efficiency from reducing  $T_{t,D}$  from 800K to 400K.  $n_D$  and  $n_A$  in dependence on voltage are also plotted in Figure 4.31.

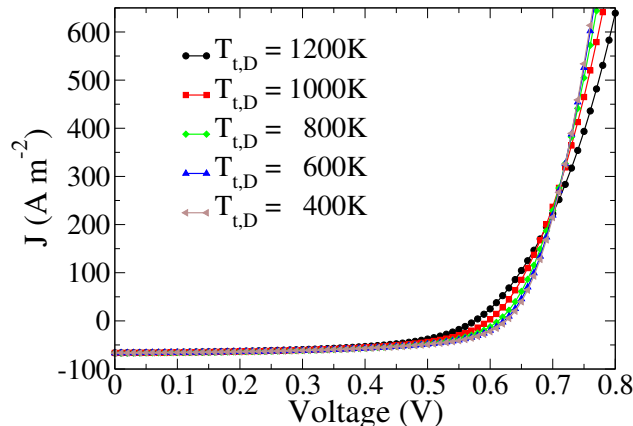


Figure 4.30: JV characteristic responses of the devices with different hole characteristic trap temperature ( $T_{t,D}$ ) but fixed electron characteristic trap temperature ( $T_{t,A}$ ) at 1000K.

Parameter	Value
$\mu_p$	$2.0 \times 10^{-8} m^2/Vs$ [103]
$\mu_n$	$2.0 \times 10^{-7} m^2/Vs$ [104]
Donor/acceptor thickness	50nm/22nm [59]
$\phi_a/\phi_c$	0.2 eV[105], 0.0 eV
$\epsilon$	$3.5\epsilon_0$
$T_{t,D}$	400K-1200K
$T_{t,A}$	1000K
$k_{PPr,0}$	$(20\mu s)^{-1}$
Donor $E_{LUMO}/E_{HOMO}$	-4.9eV/-3.0eV
Acceptor $E_{LUMO}/E_{HOMO}$	-6.1eV/-3.7eV
$N_{HOMO}/N_{LUMO}$	$1E27 m^{-3}$
$H_D/H_A$	$1E24 m^{-3}$
$J_X$	$4.3E20 m^{-2}s^{-1}$
$a_0 = \delta x$	1.0nm
recombination type	Bimolecular + trap-assisted

Table 4.6: Summary of parameters used to study effects of hole characteristic trap temperature ( $T_{t,D}$ ) in a P3HT:PCBM bilayer OPV.

$T_{t,D}$ [K]	$E_{t,D}$ [meV]	$T_{t,A}$ [K]	$E_{t,A}$ [meV]	$J_{sc}$ $[Am^{-2}]$	$V_{oc}$ [V]	FF [%]
1200	103.4	1000	86.2	63.326	0.575	56.527
1000	86.2	1000	86.2	66.542	0.597	57.535
800	69.0	1000	86.2	66.677	0.613	58.275
600	51.7	1000	86.2	66.741	0.622	58.692
400	34.5	1000	86.2	66.757	0.625	58.800

Table 4.7: Dependence of device parameters;  $J_{sc}$ ,  $V_{oc}$  and FF, on hole characteristic trap temperature ( $T_{t,D}$ ).

There are some interesting characters of  $n_D$  and  $n_A$  in Figure 4.31 that are worth discussing. First,  $n_D$  and  $n_A$  are not constant, but a function of voltage and many other parameters that impact the charge densities. However, higher characteristic trap temperatures/energies make the corresponding ideality factors more susceptible to the variations. For instance,  $n_D$  at  $T_{t,D} = 1200K$  changes considerably from 1.7 at low voltage to 1.4 at  $V_a = 0.8V$ , but  $n_D$  at  $T_{t,D} = 400K$  is more or less constant around 1.15 across the whole range of voltage. The reasons behind the variations of  $n_D$  and  $n_A$  are the interface free

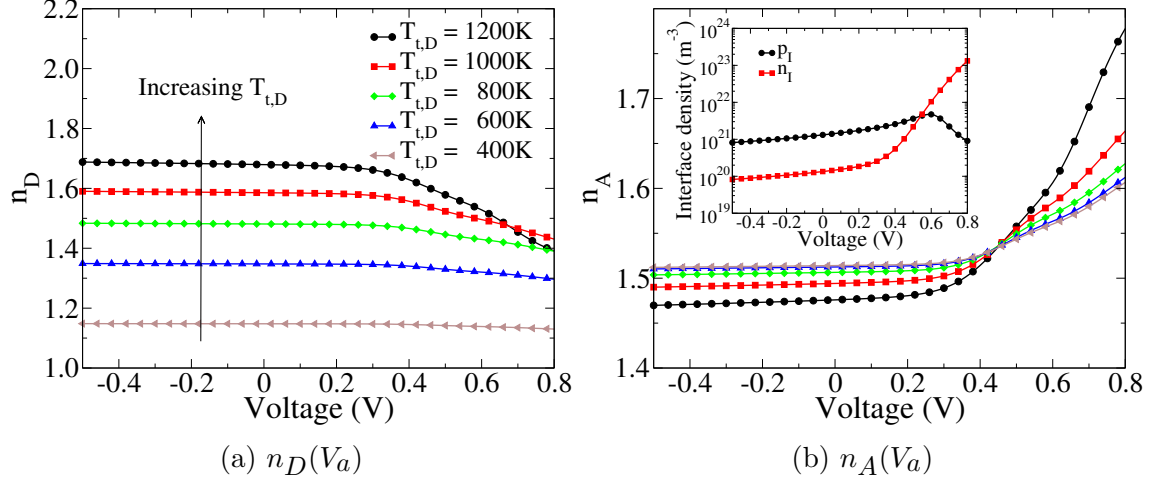


Figure 4.31: Plots of the ideality factors (a)  $n_D$  and (b)  $n_A$  as a function of voltage, calculated using equations 2.17 and 2.18 respectively, under the influences of varying  $T_{t,D}$ . The inset shows the interface electron and hole densities in dependence on voltage when  $T_{t,D} = 1200K$ .

charge densities. Let's rewrite  $n_D$  and  $n_A$  in Equations 2.17 and 2.18 by

$$n_D = \left( 1 - \frac{|E_{fp,I} - E_{f,I}|(1 - 1/l_D)}{E_{fn,I} - E_{fp,I}} \right)^{-1}, \quad n_A = \left( 1 - \frac{|E_{fn,I} - E_{f,I}|(1 - 1/l_A)}{E_{fn,I} - E_{fp,I}} \right)^{-1}. \quad (4.18)$$

From these equations, when either electron or hole has substantially higher density than the other, its quasi-Fermi level splits from the equilibrium level farther than the other, making the terms  $|E_{fp,I} - E_{f,I}|$  and  $|E_{fn,I} - E_{f,I}|$  more different. Thus,  $n_D$  and  $n_A$  will be affected oppositely. Let's consider the case of  $T_{t,D} = 1200K$  for example. The inset of Figure 4.31(b) shows the interface electron ( $n_I$ ) and hole ( $p_I$ ) densities as a function of voltage. Starting at about 0.4V,  $n_I$  rises many orders of magnitude because of the higher injection through the cathode. This shifts  $E_{fn,I}$  farther from  $E_{f,I}$ . Hence, the term  $|E_{fn,I} - E_{f,I}|$  becomes greater than  $|E_{fp,I} - E_{f,I}|$ , so  $n_A$  is increased and  $n_D$  is decreased.

Secondly,  $n_D$  does decrease with the decreased  $T_{t,D}$ , suggesting that ideality factors can be used as indicators of the recombination process. To elucidate this more clearly, see Figure 4.32 where each component of the total current densities of the devices with  $T_{t,D} = 1200K, 800K$ , and  $400K$  is plotted separately. Each curve is calculated by the corresponding term in Equation 2.20. It should be stressed that Eq. 2.20 is the analytic solution that can precisely reproduce numerical JV results. In the plots, there are three diode currents

stemming from three possible recombination processes: (i) free-electron to free-hole (f-f); (ii) free-electron to trapped-hole (fn-tp); (iii) free-hole to trapped-electron (fp-tn). The term  $qJ_X\eta_{PPd}$  is the photo-current including the polaron pair recombination. At  $T_{t,D} = 1200K$ ,  $J_{D,fn-tp}$  dominates over the entire graph due to the high concentration of trapped holes. The total current density can be approximated by  $J \approx J_{sD}[\exp((E_{fn,I} - E_{fp,I})/n_Dk_BT) - 1] - qJ_X\eta_{PPd}$ , which is in the form of the Shockley equation. If this graph is fitted to the Shockley equation, the fitted n should be correlated to  $n_D$  and contain information about  $E_{t,D}$ . In the case of  $T_{t,D} = 400K$ , the importance of fn-tp recombination is abated greatly, so that  $J_{D,fn-tp}$  is now negligible.  $J_{D,fp-tn}$  increases only slightly as there are less trapped electrons due to their higher mobility. Accordingly,  $n_A$  will not greatly influence the fitted n although it is as high as 1.6.

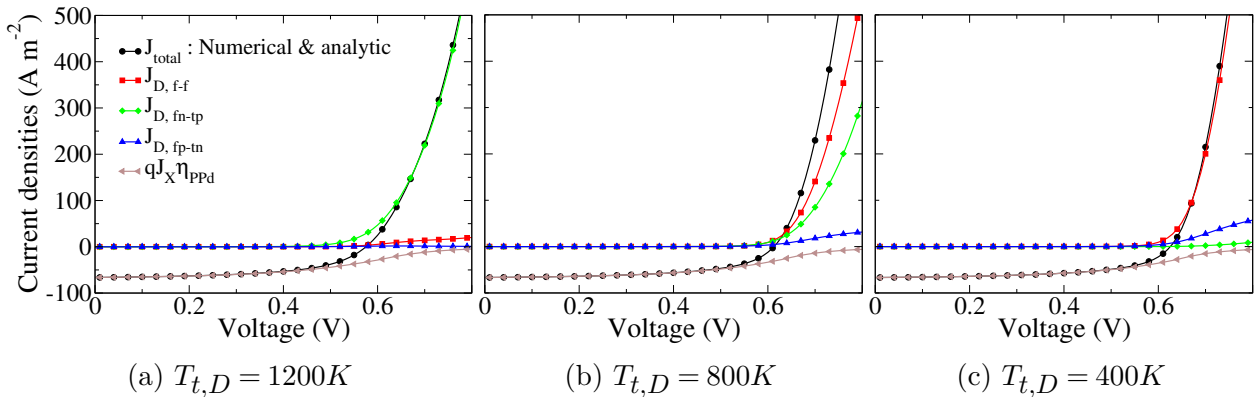


Figure 4.32: Plots of JV components, namely, diode currents from free-electron to free-hole recombination ( $f-f$ ), free-electron to trapped-hole recombination ( $fn-tp$ ) and free-hole to trapped-electron recombination ( $fp-tn$ ), and the photo-current ( $qJ_X\eta_{PPd}$ ), of the devices with fixed  $T_{t,A} = 1000\text{K}$  and  $T_{t,D} = 1200\text{K}$ ,  $800\text{K}$ , and  $400\text{K}$ .

The device with  $T_{t,D} = 800K$  brings us to the third point, which is about complexity and errors of interpreting fitted  $n$ . In reality there is not just one dominant diode current similar to the cases of  $T_{t,D} = 1200K$  and  $400K$ , but a couple of them, all contributing to the total diode current. For  $T_{t,D} = 800K$ , or equivalently  $E_{t,D} = 69meV$ , which is in the typical range of the characteristic trap energy found in OPVs [103, 52, 84, 117], both  $J_{D,f-f}$  and

$J_{D,fn-tp}$  are comparable. Ignoring  $J_{D,fp-tn}$ , the total current density is approximately

$$J \approx J_{sD}[\exp((E_{fn,I} - E_{fp,I})/n_D k_B T) - 1] + J_{s0}[\exp((E_{fn,I} - E_{fp,I})/k_B T) - 1] - qJ_X \eta_{PPd},$$

where  $J_{sD}$ ,  $J_{s0}$ , and  $n_D$  are functions of the voltage. Fitting this graph to the Shockley equation;

$$J = J_0[\exp(V_a - JR_s)/nk_B T - 1] - J_{ph} + (V_a - JR_s)/R_p,$$

where  $J_0$ ,  $R_s$ ,  $R_p$  and  $n$  are constant, will result in considerable error. Note that different methods of extracting parameters give values of the parameters that can differ by orders of magnitude [118, 119]. One might fit the device with  $T_{t,D} = 800K$  and get  $n \approx 1$ , leading to the conclusion that trap states were irrelevant and free charges recombine via bimolecular recombination, which is not true. Ultimately, fitting JV curves to the Shockley equation using the same fitting method are useful for comparison purposes among the devices, but may offer wrong physics if the extracted numbers are used in quantitative analysis, unless the fitted devices are in some specific conditions like the cases of  $T_{t,D} = 1200K$  or  $400K$ .

If a device is dominated by only one recombination mechanism, such as the device with  $T_{t,D} = 1200K$  where the recombination between free electrons and trapped holes dominates and in the device with  $T_{t,D} = 400K$  where trapped holes are not significant and the total recombination is governed by  $R_{f-f}$ , fitting to the standard Shockley equation using one ideality factor can be useful. For example, if the donor layer of a bilayer device is an amorphous polymer and the acceptor is crystalline C<sub>60</sub>, recombination between trapped holes in the donor and free electrons in the acceptor is likely the dominant process and results in only one dominant diode current. One ideality factor is sufficient to describe its JV curves and provides information about the recombination.

Finally, is it possible that there are devices with  $n = 1$ , exactly? Theoretically yes but practically no. A device with only bimolecular recombination can be simulated and has the analytic expression (Eq. 2.5) with  $n = 1$  to describe it. However, all other parameters have to be correct functions of the voltage. Without delicate measuring tools, these functions are unknown in reality. With literature evidence that bimolecular recombination usually

overestimates recombination rate and recombination coefficient [76], extracting  $n = 1$  from an OPV and concluding that bimolecular recombination is dominant can be misleading.

## 4.6 Comparison between the SRH and the f-t Recombination

The terms  $n_1$ ,  $p_1$  and  $n_1p_1$  in the SRH recombination (Eq. 1.35) are almost always assumed to be negligible in the literature[77, 87, 88].  $n_1$  and  $p_1$  are the densities of electrons and holes in the LUMO and the HOMO when their Fermi levels sit at  $E_t$  respectively (see Eqs. 1.29 and 1.33)[49], and  $n_1p_1 = n_i^2$ . The SRH recombination equation is then reduced to

$$R_{SRH} = \frac{C_n C_p N_t n_I p_I}{C_n n_I + C_p p_I}. \quad (4.19)$$

Kuik *et al.*[77] show that if the limiting cases  $C_n \gg C_p$  or  $C_p \gg C_n$  are applied, the equation further reduces to

$$R_{SRH} = C_p N_t p_I, \quad (4.20)$$

or

$$R_{SRH} = C_n N_t n_I. \quad (4.21)$$

Each of these equations is exactly one of the terms in the f-t recombination in Eq. 1.8. This brings about questions: Is the f-t recombination a simplified model of the SRH recombination? Are there any relations between the two models? These questions are answered in this section by the DD-BI model's simulations.

The simulations are carried out using the parameters summarized in Table 4.8. We choose three different sets of the mobilities, i.e.  $\mu_n/\mu_p = 1, 10$  and  $100$  where  $\mu_n = 1 \times 10^{-7} m^2/Vs$ , and  $T_{t,D} = T_{t,A} = 1000K$  and  $450K$  to represent devices with deep and shallow tail states, respectively. One group of the devices has the SRH recombination in the integral form (Eq. 1.43) as the interface free-carrier recombination, while the other has the f-t recombination (Eq. 1.8). The same capture rates as described in Eqs. 1.37 and 1.38 are used.

Figures 4.33a and 4.33b show comparisons between the simulated JV curves under illumination conditions for  $T_{t,D} = T_{t,A} = 1000K$  and  $450K$  respectively. Table 4.9 summarizes

Parameter	Value
$\mu_p$	$1.0 \times 10^{-7} m^2/Vs, 1.0 \times 10^{-8} m^2/Vs, 1.0 \times 10^{-9} m^2/Vs$
$\mu_n$	$1.0 \times 10^{-7} m^2/Vs$
Donor/acceptor thickness	40nm/40nm
$\phi_a/\phi_c$	0.20 eV/0.20 eV
$\epsilon$	$3.0\epsilon_0$
$T_{t,D} = T_{t,A}$	450K, 1000K
$k_{PPr}$	Eq. 1.48 with $k_{PPr,0} = 10\mu s^{-1}$
Donor $E_{LUMO}/E_{HOMO}$	-4.9eV/-3.0eV
Acceptor $E_{LUMO}/E_{HOMO}$	-6.1eV/-3.7eV
$N_{HOMO}/N_{LUMO}$	$1.0E27 m^{-3}$
$H_D/H_A$	$1.0E24 m^{-3}$
$J_X$	$4.3E20 m^{-2}s^{-1}$
$a_0 = \delta x$	1.5nm
recombination type	Shockley-Read-Hall or f-t

Table 4.8: Summary of the simulation parameters used in the comparison between the SRH recombination (Eq. 1.43) and the f-t recombination (Eq. 1.8).

the devices'  $J_{sc}$ ,  $V_{oc}$  and FF values. There are a couple of interesting points that can be concluded as follows.

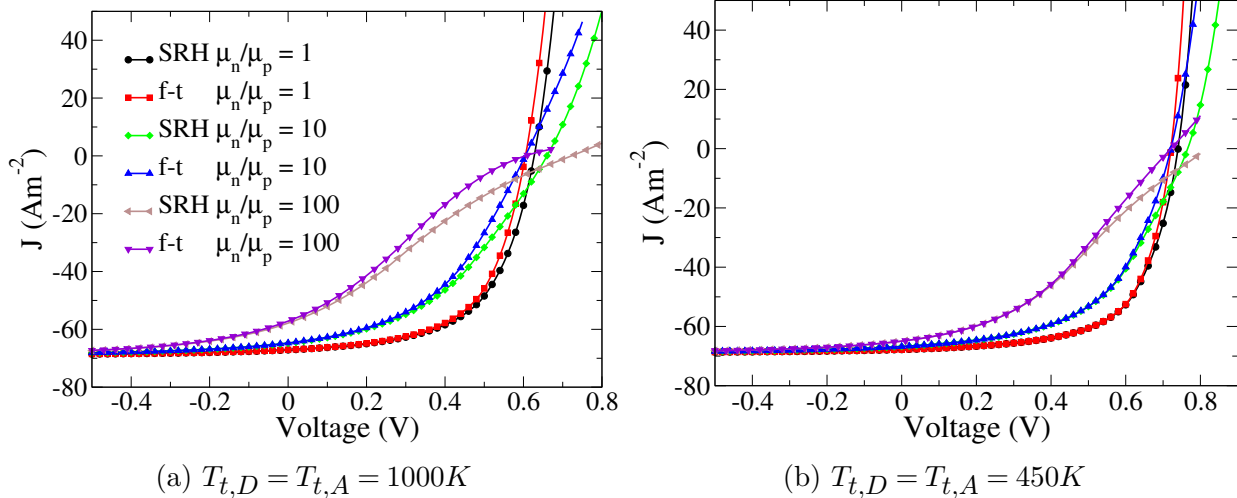


Figure 4.33: Comparisons between the illuminated JV curves calculated using  $R_{f-t}$  (Eq. 1.8) and  $R_{SRH}$  (Eq. 1.43) of the devices with  $T_{t,D}$  and  $T_{t,A}$  equal to a) 1000K and b) 450K.

First, the two recombination types create similar illuminated JV curves in the reverse and the small bias regimes, but the f-t recombination results in a higher diode current at high bias. As we discussed earlier that the diode current is caused by the interface free-carrier

$T_{t,D}, T_{t,A}$ [K]	$\mu_n$ [ $m^2/Vs$ ]	$\mu_p$ [ $m^2/Vs$ ]	Recombination	$J_{sc}$ [ $Am^{-2}$ ]	$V_{oc}$ [V]	FF [%]
1000	$1 \times 10^{-7} m^2/Vs$	$1 \times 10^{-9} m^2/Vs$	SRH	57.84	0.7225	23.80
			f-t	57.16	0.6045	25.97
1000	$1 \times 10^{-7} m^2/Vs$	$1 \times 10^{-8} m^2/Vs$	SRH	64.82	0.6599	43.38
			f-t	64.72	0.6045	45.55
1000	$1 \times 10^{-7} m^2/Vs$	$1 \times 10^{-7} m^2/Vs$	SRH	67.11	0.6273	58.78
			f-t	67.08	0.6050	59.29
450	$1 \times 10^{-7} m^2/Vs$	$1 \times 10^{-9} m^2/Vs$	SRH	64.96	0.8167	34.91
			f-t	64.95	0.7210	39.09
450	$1 \times 10^{-7} m^2/Vs$	$1 \times 10^{-8} m^2/Vs$	SRH	66.76	0.7658	52.38
			f-t	66.76	0.7210	55.55
450	$1 \times 10^{-7} m^2/Vs$	$1 \times 10^{-7} m^2/Vs$	SRH	67.77	0.7401	63.64
			f-t	67.77	0.7212	65.22

Table 4.9: Comparisons of the  $J_{sc}$ ,  $V_{oc}$  and  $FF$  values between the devices having  $R_{SRH}$  (Eq. 1.43) and  $R_{f-t}$  (Eq. 1.8) as the interface recombination. The values are measured from the JV curves in Fig. 4.33, and the devices are described by Table 4.8.

recombination, all the plots indicate that  $R_{f-t}$  is higher than  $R_{SRH}$  when  $C_n = k_{rec,n}$  and  $C_p = k_{rec,p}$ . This agrees with Figure 4.34a that shows the total recombination rates as a function of voltage of the device with  $\mu_p = 10^{-9} m^2/Vs$ ,  $\mu_n = 10^{-7} m^2/Vs$  and  $T_{t,D} = T_{t,A} = 1000k$ . The rate  $R_{f-t}$  is about 2-3 times as high as the rate  $R_{SRH}$  for the whole voltage range.

Secondly, the terms  $n_1$ ,  $p_1$  and  $n_1p_1$  in the SRH equation (Eqs. 1.35 or 1.43) can actually be ignored. The simulation results for all six devices show that  $n_1p_1 = n_i^2$  has no effects on the JV curves both under illumination and dark conditions, and the terms  $n_1$  and  $p_1$  cause only negligible changes on the curves (not shown here). Hence, the reduced SRH equation (Eq. 4.19) is valid. We would like to emphasize that this is not caused by  $n_1 < n$  or  $p_1 < p$  because  $n_1$  and  $p_1$  can be more than or comparable to  $n$  and  $p$  at some values of  $E_t$ , but by that the thermal emissions of the trapped charges are negligible if  $E_t$  is between  $E_{fn}$  and  $E_{fp}$ [87]. Only small regions of trap states close to  $E_{fn}$  or  $E_{fp}$  can thermally emit the trapped charges to the transport levels.

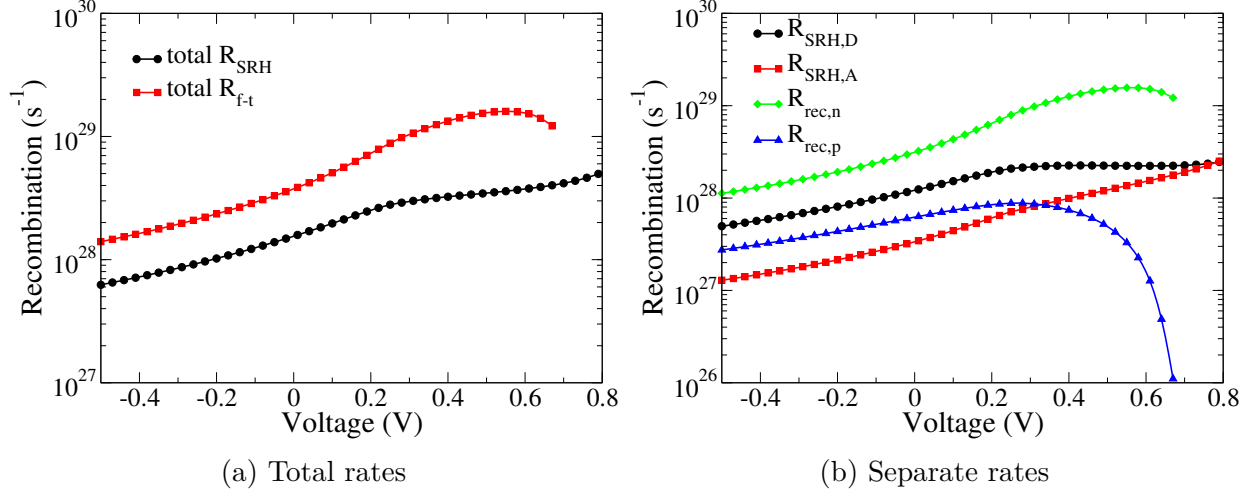


Figure 4.34: a) Total  $R_{SRH}$  and  $R_{f-t}$  rates and b) their separate rates from different mechanisms;  $R_{SRH} = R_{SRH,D} + R_{SRH,A}$  and  $R_{f-t} = R_{rec,n} + R_{rec,p}$ , of the devices with  $\mu_n/\mu_p = 100$  and  $T_{t,D(A)} = 1000K$ .

Thirdly, the f-t recombination is not a simplified form of the SRH recombination but a different model. There are two main reasons. First, the assumptions  $C_n \gg C_p$  and  $C_p \gg C_n$  are not always valid since  $\mu_n$  and  $\mu_p$  at the D/A interface are not necessarily very different. Second, even if they are significantly different,  $R_{SRH}$  does not reduce to  $R_{f-t}$  because it has an extra process related to the unoccupied trap states that  $R_{f-t}$  does not have. Based on the SRH theory, not only the occupied trap states (trapped electrons) can capture free holes, but the unoccupied trap states can also capture free electrons. This is shown in Figure 4.34b where separate rates of the total  $R_{SRH}$  and the total  $R_{f-t}$  of the device with  $\mu_n/\mu_p = 100$  and  $T_{t,D(A)} = 1000K$  in Fig. 4.34a are plotted.  $R_{SRH,A}$  and  $R_{SRH,D}$  are the SRH rates originated from the donor and the acceptor trap states (the first and the second terms of Eq. 1.43), respectively.  $R_{rec,n} = k_{rec,n} n_I p_{It}$ , and  $R_{rec,p} = k_{rec,p} p_I n_{It}$ . Note that  $R_{SRH,A}$  has physical meanings similar to  $R_{rec,p}$ , so  $R_{SRH,A}$  is expected to reduce to  $R_{rec,p}$  when  $C_n \gg C_p$ , and *vice versa* for  $R_{SRH,D}$  and  $R_{rec,n}$ . According to the results,  $R_{rec,p}$  is greatly reduced at high voltage because  $p_I$  becomes depleted from its exceedingly recombination with the injected electrons. However,  $R_{SRH,A}$  does not decrease from the lack of  $p_I$  because the unoccupied traps can still capture the interface electrons. A similar situation happens

to  $R_{SRH,D}$  and thus explains the differences between  $R_{SRH,D}$  and  $R_{rec,n}$ .

Surprisingly, even with the different fundamental physics of  $R_{SRH}$  and  $R_{f-t}$ , the total rates differ by just a factor of 2-3. According to Table 4.9 and Fig. 4.33b, the calculated JV curves can be very close for  $V_a < V_{oc}$  especially in the devices with more balanced mobilities and narrow tail states.

We have shown in this section that  $R_{SRH}$  and  $R_{f-t}$  are different by their natures, but their values are not far apart when  $C_n = k_{rec,n}$  and  $C_p = k_{rec,p}$ . However, they are considerably different at  $V_{oc}$ , so using the reduced forms  $R_{SRH} = C_p N_t p_I$  or  $R_{SRH} = C_n N_t n_I$  are not recommended at this voltage. Additionally, the terms  $n_1$ ,  $p_1$  and  $n_1 p_1$  in the SRH rate (Eq. 1.35) are negligible due to the irrelevant thermal charge emission processes.

## 4.7 Conclusions

In this chapter, fundamental physics of bilayer OPVs are studied using the DD-BI and the SCD models. The purpose is to gain more insights and make connections between the fundamental physics and measurable Shockley parameters;  $R_s$ ,  $R_p$  and  $n$ .

In Section 4.1, comparisons between our models and the GWWF model are made. The advantages of the DD-BI and the SCD models are that they solve for spatial charge densities and potential profile self-consistently, so they have better treatments of interface charge densities, interface electric field, space charge effects and series resistance. On the other hand, the GWWF model uses Equations 1.12 and 1.13 to estimate the interface electric field which is an important argument in  $k_{PPd}$  and  $\eta_{PPd}$ . However, Equations 1.12 and 1.13 do not have accumulation of space charges and series resistance included, so the GWWF model tends to overestimate the interface electric field,  $k_{PPd}$  and  $\eta_{PPd}$ , resulting in overestimated device efficiencies.

In Section 4.2, we present simulation results regarding effects of carrier mobilities on device efficiencies, charge transport and quasi-Fermi levels. First, we show that there are two regions of spatial charge distribution: (1) exponential decay regions near the elec-

trodes; (2) constant density regions near the D/A interface, which are caused by space charge accumulations due to low carrier mobilities. The constant charge regions give rise to changes in quasi-Fermi levels and split the quasi-Fermi levels at the interface; which is the diode voltage ( $V_d = E_{fn,I} - E_{fp,I}$ ), and bring about the definition of series resistance ( $E_{fn,I} - E_{fp,I} = V_a - JR_s$ ). In terms of interface rates, we show that mobilities effect  $k_{PPd}$  the most, resulting in a reduction of dissociation efficiency ( $\eta_{PPd}$ ), which can be represented by an increased parallel resistance.

In Section 4.3, effects injection barriers are presented. Increased injection barriers reduce the device efficiency through reductions of fill factor and short-circuit current, but open-circuit voltage almost does not change. This is because interface charge densities; which are directly related to open-circuit voltage, are not significantly affected by the increased injection barriers.

One interesting feature that is observed in Section 4.3 is that injection barriers smaller than about 0.3eV do not effect JV curves noticeably. In Section 4.4, we focus on this aspect by considering organic semiconductor/metal contacts at the electrodes. The results show that, under illumination, physics at the contacts are similar to that in the ICT model, i.e. small injection barriers result in charge transfer and quasi-Fermi level pinning, but large injection barriers result in significant drops of quasi-Fermi levels over the barriers. These explain the JV behaviors caused by small injection barriers. However, under dark conditions, the contacts are more likely explained by the Mott-Schottkey model because charge transfer and quasi-Fermi level pinning always occur. Ultimately, the knowledge of organic semiconductor/metal contacts allows us to understand and formulate each component of series resistance explicitly.

In Section 4.5, we study origins of ideality factors and show that our expressions of ideality factors in Equation 2.17 and 2.18 are general forms of a famous ideality factor expression [51]. We also show that ideality factor functions change accordingly with characteristic trap energies and can be used as indicators of trap-assisted recombination.

In Section 4.6, the f-t recombination, which is understood as a reduced form of the SRH recombination, is compared with the SRH recombination using exponential trap distributions. The results show that their recombination rates are comparable at applied voltage below  $V_{oc}$ , but they are actually different models and result in different JV curves especially in terms of  $V_{oc}$ 's. This is because the f-t model only considers recombination with occupied trap states, but the SRH model also includes capturing of free carriers by unoccupied trap states.

## CHAPTER 5

### INTERPRETATION OF SHOCKLEY PARAMETERS : DARK VERSUS LIGHT

Despite the fact that each property of a solar cell needs to be described by a complicated function, using a set of constant Shockley parameters;  $J_0$ ,  $R_s$ ,  $R_p$  and  $n$ , is still one of the most preferable methods for describing a solar cell device and its JV curves because it is simple, yet sufficiently descriptive. However, the parameters are always used interchangeably between illumination and dark conditions, despite the different physics of the two conditions. A question then arises: are there any errors associated with using only one set of the parameters interchangeably? In order to answer this question, we simulate and compare functions of the Shockley parameters under both conditions using our models, but first we have to include another mechanism for leakage current and  $R_p$  in the dark because our illumination  $R_p$  model in Eq. 2.28, which is the recombination resistance of the recombined exciton current;  $qJ_X(1 - \eta_{PPd})$ , does not apply when  $J_X = 0$  in the dark.

This chapter starts with an introduction of a new type of solar cell from our collaborators; organic salt solar cells. We then explain effects of the Shockley parameters on JV curves under illumination and dark conditions using the standard Shockley equation (Eq. 1.3) with constant parameters. After proposing possible leakage mechanisms, we apply the models to one of the organic salt solar cells and the P3HT:PCBM device in Chapter 4, and then discuss the differences of dark and illumination Shockley parameters.

#### 5.1 Organic Salt Photovoltaic Devices

One particular bilayer system that is interesting because of its transparency and ability to utilize near-infrared parts of the light spectrum is the organic salt solar cell [1, 120]. Our collaborators in Department of Chemical Engineering and Materials Science, Michigan State University, are focusing on this system, so their work in Ref.[1] will be used and analyzed in

this chapter.

The architecture of the device is a bilayer donor-acceptor so that the DD-BI and the SCD models are applicable. The donor is composed of a heptamethine or cyanine cation ( $Cy^+$ ) and a small molecule anion. The molecular structures are shown in Fig. 5.1. There are many choices of the anion, and  $PF_6^-$ ,  $SbF_6^-$ ,  $\Delta$ -tris(tetrachloro-1,2 benzenediolato)phosphate(V) ( $\Delta$ -TRISPHAT $^-$  or TRIS $^-$ ) and Tetrakis(pentafluorophenyl)borate (TPFB $^-$ ) are used in Ref. [1]. The acceptor is a  $C_{60}$  film. A stack of indium tin oxide (ITO) and MoO<sub>3</sub> serves as the anode and Ag is the cathode.

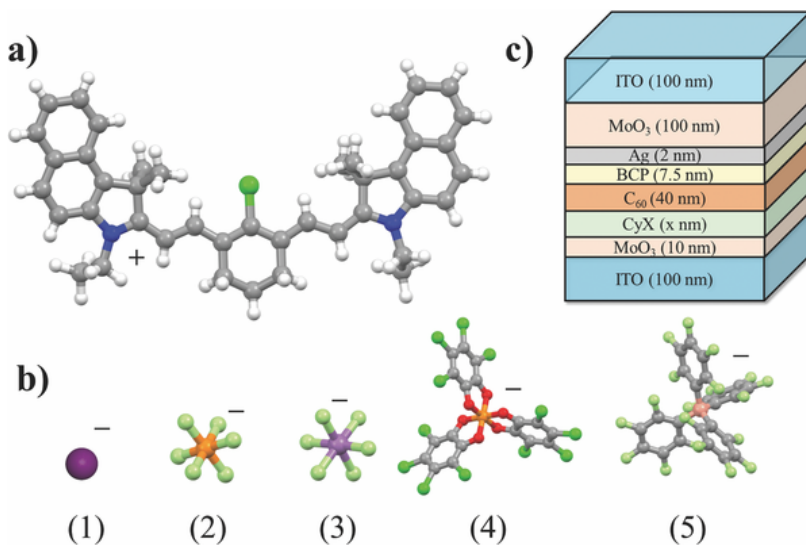


Figure 5.1: a) Molecular structures of the heptamethine cation ( $Cy^+$ ) and b) its counter anions: (from left to right)  $I^-$ ;  $PF_6^-$ ;  $SbF_6^-$ ; TRIS $^-$ ; and TPFB $^-$ , that are used as the donor in the device with the architecture shown in c). *From Ref. [1]*

Figure 5.2 shows  $JV$  characteristics, measured under nominal 1 sun and dark conditions. Solar cell efficiency under illumination is improving from CyPF<sub>6</sub> to CySbF<sub>6</sub> to CyTRIS and to CyTPFB. According to the paper[1], there are several possible reasons for the improvement including: (1) the donor HOMO and LUMO levels are tuned so they are more favorable, (2) the interface size is increased, abating polaron pair recombination, (3) exciton diffusion length increases and (4) trap states are not very dominating. The CyTRIS and especially the CyTPFB devices also show kink-shaped behaviors in their dark JV curves. Because the HOMO and LUMO levels of the CyTRIS: $C_{60}$  device (see supplementary materials of Ref.

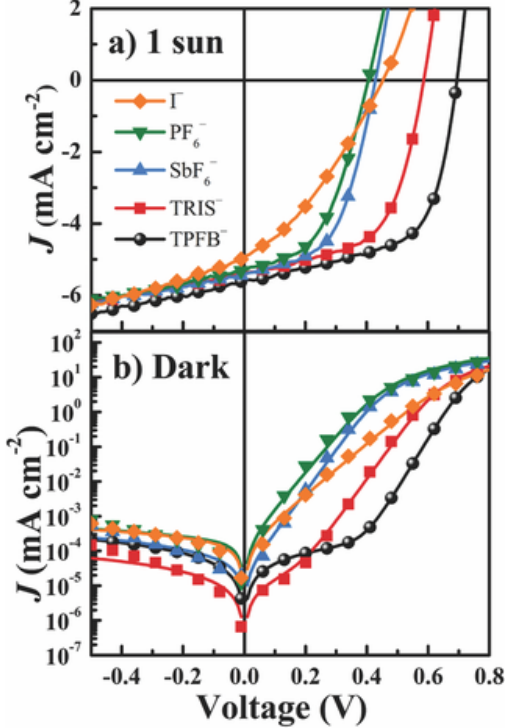


Figure 5.2: JV curves under a) nominal 1 sun illumination and b) dark condition from measurements (symbols) and fitting with the generalized Shockley equation (Eq. 1.3)

[1]) are suitable for simulating with the DD-BI and the SCD models, the device will be fitted, so the Shockley parameters are extracted and analyzed.

## 5.2 Effects of the Shockley Parameters on Dark JV curves

In the upcoming sections, the analyses of dark currents require discussions in terms of the Shockley parameters, namely,  $J_0$ ,  $R_s$ ,  $R_p$  and  $n$ , and how they affect the diode and the leakage currents. In addition to their physical meanings that are discussed in detail in Chapters 2 and 4, simple understanding of their effects on the shapes of dark currents is important for analyzing experimental JV data. This section presents how the shapes of dark currents are changed by those parameters using graphical methods.

Figure 5.3 shows impacts of the Shockley parameters on dark currents' shapes calculated by the conventional Shockley equation in Eq. 1.3. The values of the parameters are typical for the cyanine organic salt solar cells[1].

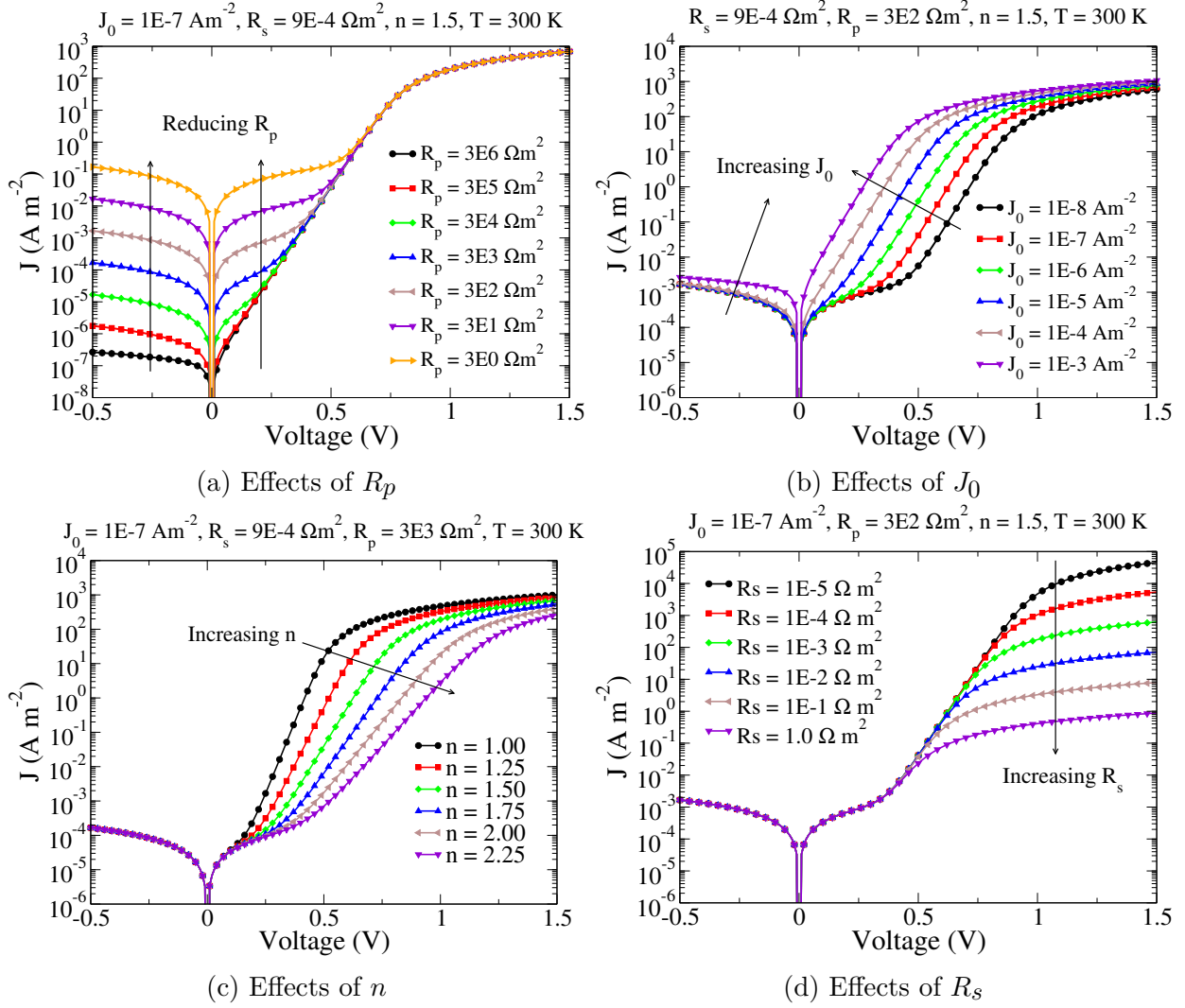


Figure 5.3: Effects of the Shockley parameters a)  $R_p$ , b)  $J_0$ , c)  $n$  and d)  $R_s$  on the shapes of dark JV curves calculated by the conventional Shockley equation (Eq. 1.3) using each parameter as a constant. Control variables are summarized at the top of each plot.

In order to understand the  $R_p$  effects in Figure 5.3a where  $R_p$  varies from  $3 \times 10^6 \Omega m^2$  (high  $R_p$ ) to  $3 \Omega m^2$  (low  $R_p$ ), consider the total current ( $J$ ) as a summation of the diode current;  $J_{diode} = J_0 [exp(q(V_a - JR_s)/k_B T) - 1]$ , and the leakage current;  $J_{leak} = (V_a - JR_s)/R_p$ . They are plotted in Fig. 5.4 for the cases of  $R_p = 3 \times 10^5$  and  $3 \times 10^1 \Omega m^2$  as examples. Because  $J_{diode}$  exponentially depends on the voltage while  $J_{leak}$  is a linear function of it,  $J_{leak}$  is comparable to  $J_{diode}$  only when the voltage is low or reversed. Lowering  $R_p$  increases  $J_{leak}$ . Since  $J_{diode}$  is not affected by  $R_p$ , reducing  $R_p$  is like *vertically*

lifting the  $J_{leak}$  graph up while keeping the  $J_{diode}$  graph unchanged. This increases the total current at low and reverse voltage where  $J_{leak}$  dominates, so that the overall JV curve is kink-shaped.

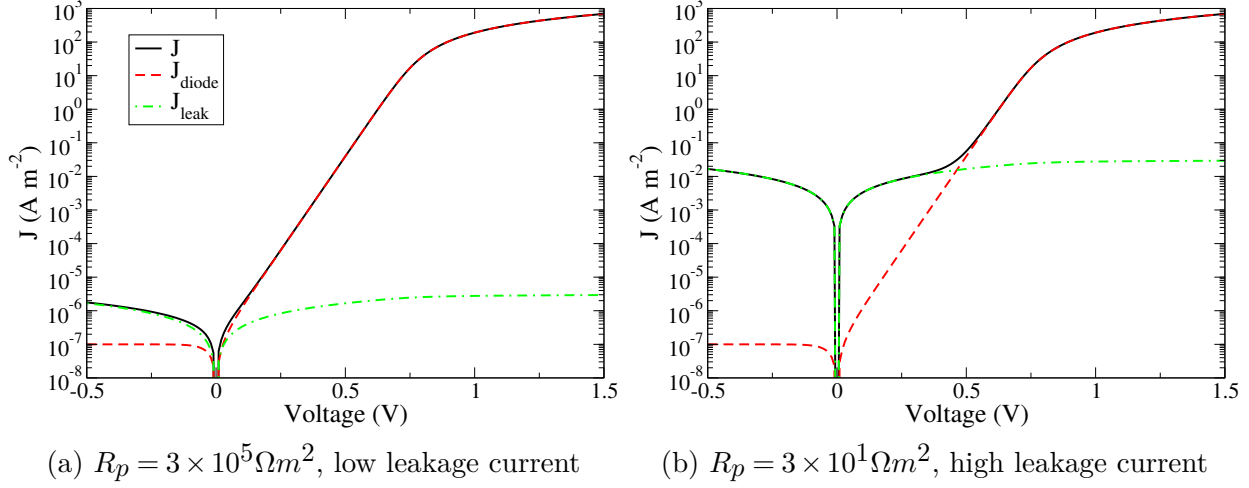


Figure 5.4: Plots of the total dark currents ( $J$ ), the diode currents ( $J_{diode}$ ) and the leakage currents ( $J_{leak}$ ) where  $J = J_{diode} + J_{leak}$  as a function of voltage for the cases of a)  $R_p = 3 \times 10^5$  and b)  $3 \times 10^1 \Omega m^2$

For the effects of  $J_0$ , consider Figure 5.3b where  $J_0$  varies from  $1 \times 10^{-3}$  to  $1 \times 10^{-8} \text{ Am}^{-2}$ .

Since  $J_0$  is the prefactor of the diode term, it simply determines the magnitude  $J_{diode}$  but does not change its slope or the leakage current. Graphically,  $J_0$  can be viewed as a *shifting* parameter of  $J_{diode}$ . Increasing  $J_0$  is like shifting the diode current up along the y-axis and toward the origin of the x-axis. If  $J_{diode}$  at low voltage is high enough, it becomes the dominant current, so the kink-shaped behavior caused by  $R_p$  cannot be seen.

The ideality factor  $n$  is another parameter that affects  $J_{diode}$ , but in a different way. Figure 5.3c shows dark JV curves having different  $n$  values ranging from 1 to 2.25. Assuming that the diode voltage;  $V_d = V_a - JR_s$ , is a linear function of  $V_a$ , so  $V_d = aV_a + b$ , where  $a$  and  $b$  are constant. The slope of the logarithmic diode current can be approximated by  $\partial \ln(J_{diode}) / \partial V_a \approx \partial \ln[J_0 \exp(qV_d/nk_B T)] / \partial V_a \approx qa/nk_B T$ . Hence,  $n^{-1}$  is associated with the slope of dark current in the region where  $J_{diode} \gg J_{leak}$  and dominates the curve.  $n$  can be graphically viewed as a *tilting* parameter of  $J_{diode}$ . As seen in Fig. 5.3c, the dark

JV curves are tilted downward by the higher values of  $n$ , while the reverse currents or the kink-shaped characteristics are less affected

It is clear from Fig. 5.3d that  $R_s$  is very important at high voltage. In order to understand this, consider the Shockley equation in Eq. 1.3 along with its equivalent circuit in Fig. 1.2. At low or reverse bias, the diode is not conductive, so it can be excluded from the circuit.  $R_p$  is then connected to  $R_s$  in series, which is negligible due to  $R_p \gg R_s$ . At high applied voltage, the diode is conductive, so  $J_{diode} \gg J_{leak}$ . The shunt path with  $R_p$  that conducts  $J_{leak}$  can be neglected. The circuit is reduced to the diode connected in series with  $R_s$ . If the diode is fully conducting, the entire circuit is reduced to just the biased  $R_s$ . Hence, Ohm's law applies and the dark current is  $J \approx V_a/R_s$ . In a graphical sense,  $R_s$  is most important after the  $J_{diode}$  dominating regime, by *vertically lifting/lowering* the total dark current curves.

A dark JV curve can have up to three regions with different slopes[5]. For example, Fig. 5.4b shows different slopes in the ranges:  $V_a < 0.5V$ ;  $0.5V < V_a < 1.0V$ ; and  $V_a > 1.0V$ . According to the discussions above, the slope at  $V_a < 0.5V$  belongs to  $J_{leak}$ . The slope at  $0.5V < V_a < 1.0V$  is governed by  $J_{diode}$ . For  $V_a > 1.0V$ , the current obeys Ohm's law, so that the slope is  $[\partial J / \partial V_a]^{-1} \approx R_s$ .

In conclusion, a dark JV curve can be divided into the leakage region, the diode region, and the Ohmic region, as illustrated by Figure 5.5. In the leakage region, the curve is lifted or lowered by  $R_p$ , causing the kink-shaped characteristic if  $R_p$  is low enough. In the diode region, the magnitude of the graph is controlled by  $J_0$ , and the slope is controlled by  $n$ .  $J_0$  and  $n$  can be graphically viewed as shifting and tilting parameters, respectively. Finally,  $R_s$  affects dark currents at very high  $V_a$  by lowering or raising the currents according to Ohm's law.

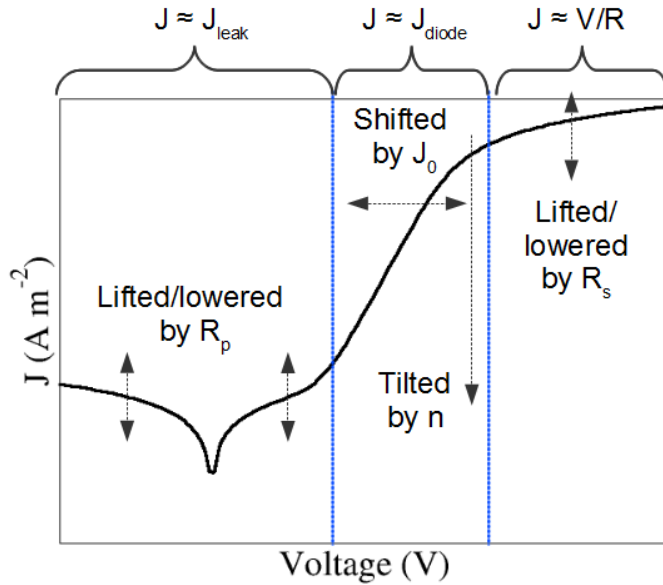


Figure 5.5: A figure showing the three regions in a dark current, namely, the leakage region, the diode region, and the Ohmic region, including how the shape in each region is affected by the Shockley parameters. *adapted from [5]*

### 5.3 Effects of the Shockley Parameters on illuminated JV curves

JV curves under illumination can also provide basic information about the Shockley parameters and physical properties, but not as clearly and informatively as dark JV curves. Figure 5.6 shows the effects of the parameters  $R_p$ ,  $J_0$ ,  $n$  and  $R_s$  on illuminated JV curves calculated by the conventional Shockley equation (Eq. 1.3). The values of the control variables are the same as in Section 5.2 where the parameters' effects are studied under dark conditions. An additional constant photo-current term ( $J_{ph}$ ) equal to  $70\text{Am}^{-2}$  is added in all the plots to represent the photogeneration processes, so  $J = J_{diode} + J_{leak} - J_{ph}$ .

There are a couple of interesting points about  $R_p$  in Fig. 5.6a. First,  $R_p$  under illumination has to be very low compared to  $R_p$  under dark in order to fit this data to the Shockley model. The dark  $R_p$  values in Fig. 5.3a are typical for organic solar cells, which are about tens to hundreds  $\Omega\text{m}^2$ [1, 121, 122], but  $R_p$  under illumination in Fig. 5.6a does not show any effects unless it is lower than  $10^{-2}\Omega\text{m}^2$  (i.e. about four orders of magnitude lower than those in the dark). This topic will be examined thoroughly in Sections 5.4 and 5.5. The

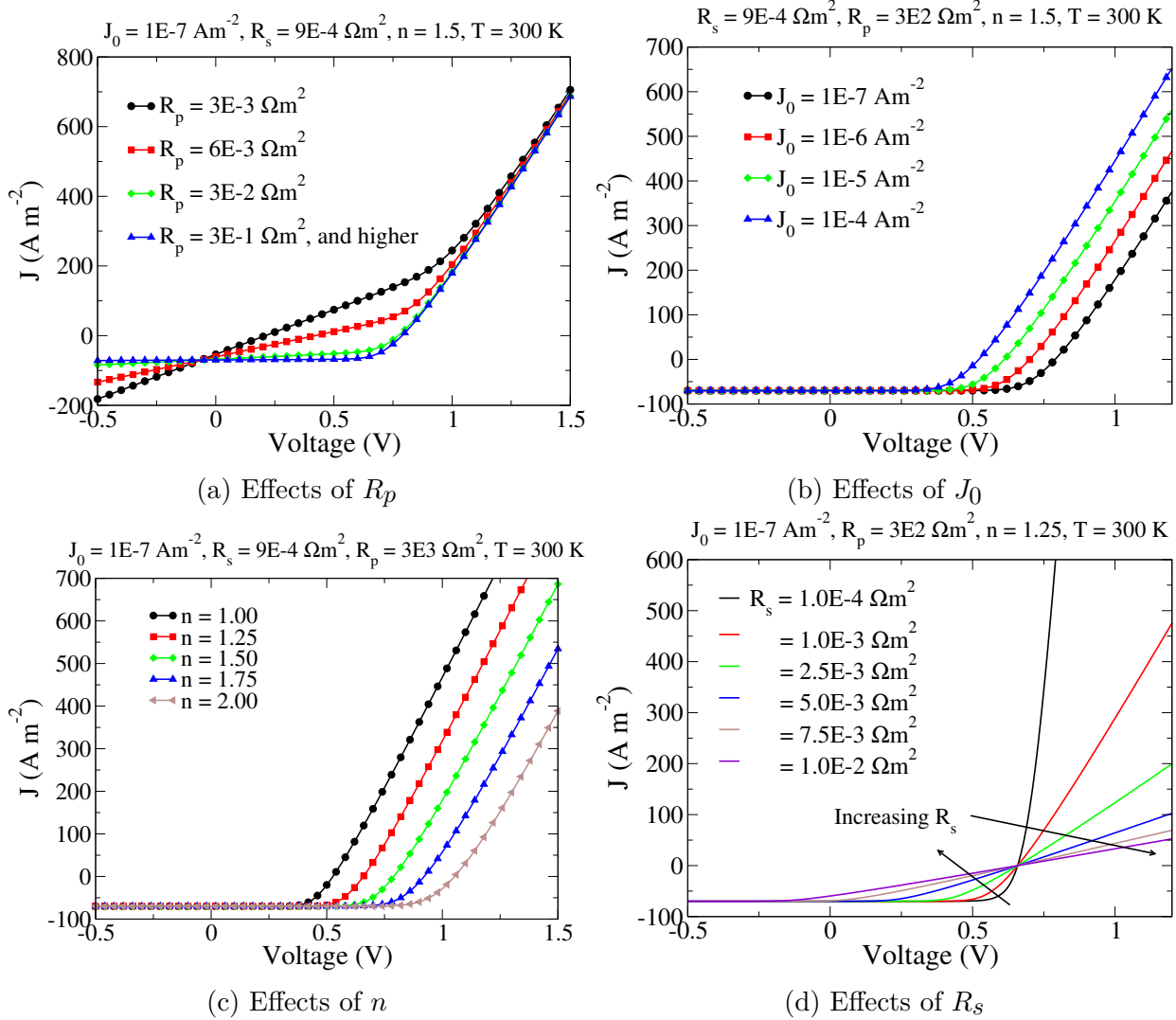


Figure 5.6: Effects of the Shockley parameters a)  $R_p$ , b)  $J_0$ , c)  $n$  and d)  $R_s$  on the shapes of illuminated JV curves calculated by the conventional Shockley equation (Eq. 1.3) using each parameter as a constant. Control variables are summarized at the top of each plot.

conclusion is that parallel resistances under dark and illumination conditions arise from two different physical processes; the dark  $R_p$  is connected to trap-related tunneling processes which are insignificant compared to the illuminated  $R_p$  that virtually depicts the resistivity of the recombined exciton current (see Sections 2.2 and 4.2.3). Secondly, the slope at around the short circuit point is affected the most by  $R_p$ , as shown in Fig. 5.6a. This can be a helpful guide in determining properties of an actual device or possible ranges of parameters. For example, if the slope at  $V_a = 0V$  is very flat, one could conclude that the rate  $k_{PPr}$  is

not very high, and thus the PP dissociation probability ( $\eta_{PPd}$ ) should approach a hundred percent.  $k_{PPr}$  can be set at around  $(1\text{-}100 \mu\text{s})^{-1}$  in this case. On the other hand, if the slope is very steep,  $k_{PPr}$  can be as high as  $(10\text{-}100 \text{ ns})^{-1}$ , making the PP recombination the main loss mechanism.

According to Figs. 5.6b and 5.6c, effects of  $J_0$  and  $n$  are not easily distinguishable, in contrast to the dark cases where  $n$  controls the slope of the diode current and  $J_0$  shifts the current toward the graph origin. We can only deduce that higher  $J_0$  and lower  $n$  increase the diode current, so it responds at lower voltage. More information about  $n$  and  $J_0$  requires a fitting.

Finally,  $R_s$  is the resistance that reduces the slope around  $V_{oc}$  and higher, which accordingly reduces fill factor. The reasons why  $R_s$  affects at high voltage are discussed in the previous section. The behavior shown in Fig. 5.6d agrees with the numerical results in Figs. 4.6a and 4.15a where  $R_s$  is changed by changing the mobility and the contact component of  $R_s$ , respectively.

In summary, even though the reactions of illuminated JV curves to the changes of the Shockley parameters are not as clear as for dark JV curves', the slopes at  $V_a = 0V$  and at  $V_{oc}$  which are affected by  $R_p$  and  $R_s$  can be simple clues of related physical parameters and properties, such as, PP recombination rate, mobility and injection barriers.

## 5.4 Parallel Resistance in the Dark

The experimental dark JV curves of the CyTRIS and CyTPFB devices in Fig. 5.2 are particularly interesting because they clearly show the kink-shaped behavior. According to Section 5.2, the kink-shaped trait is caused by low  $J_0$  and low  $R_p$ , so that the total current in the small and reverse bias regime is dominated by the leakage current. However, the mechanisms governing the leakage current and  $R_p$  under dark conditions have not been included in the models yet. According to the  $R_p$  expression (Eq. 2.28),  $R_p$  is a recombination due to a fraction of the current ( $qJ_X(1 - \eta_{PPd})$ ) that is lost at the D/A interface. This

definition of  $R_p$  does not apply to devices under dark conditions because it predicts that there is no leakage current when  $J_X = 0$ .

In the following sections, mechanisms for the dark leakage current are proposed and added to the numerical models. Numerical JV curves containing these mechanisms will be compared to the experimental results for the CyTRIS case.

#### 5.4.1 Trap-to-trap Recombination as the Dark Leakage Current

Charge tunneling and trap states have been demonstrated to be the primary cause of the leakage current in inorganic semiconductor devices[123, 124, 125, 126, 127]. If there are trap states in the forbidden energy gap, charges from one side of the semiconductor do not have to tunnel through the whole thickness but to the trap states that can capture the tunneling charges and emit them to the other side of the semiconductor. This is the well established trap-assisted tunneling (TAT) theory[125, 126, 127], which is necessary in reproducing the low-bias JV curves in computational simulations[128, 129], where the leakage current dominates. Recently, the TAT model was used to describe the tunneling leakage current in a thin organic layer[130], implying that trap states and tunneling processes play important roles in the organic devices' leakage current.

In addition to the f-f and the f-t recombination mechanisms that are discussed extensively in Chapters 2 and 4, recombination between localized or trap states can be taken into consideration[84, 87]. Though some studies suggest that this recombination should not happen[87], we will show that it results in a dark leakage current that has similar behaviors to those of the dark leakage current caused by  $R_p$  in the Shockley model. The recombination also brings about an extra parallel resistance in the SCD equations that has values close to experimentally extracted  $R_p$  values from dark JV curves.

Here, we model the recombination between localized states in a similar way to that in Ref.[84]. We consider the tunneling and recombination of trapped charges through the D/A interface and that the traps have an effective mobility  $\mu_{tun}$ . Using the same notation as in

Ref.[84], the trap-to-trap (t-t) recombination can be modeled as a bimolecular recombination between  $n_{It}$  and  $p_{It}$  with the mobility  $\mu_{tun}$ ;

$$R_{t-t} = \frac{q\mu_{tun}}{\epsilon\epsilon_0} n_{It} p_{It}, \quad (5.1)$$

where  $\mu_{tun}$  is used as a constant and a fitting parameter, for simplicity.

#### 5.4.2 Simulating the CyTRIS:C<sub>60</sub> Device

We choose to simulate the CyTRIS:C<sub>60</sub> device (Fig. 5.1) to study the effects of the t-t recombination and dark  $R_p$ . Figure 5.7a shows the energy band diagram of each layer and the device architecture; which is indium tin oxide (ITO) (100nm)/MoO<sub>3</sub> (10nm)/CyTRIS (12 nm)/ C<sub>60</sub> (40 nm)/bathocuproine (BCP) (7.5 nm)/Ag (100 nm). The CyTRIS and C<sub>60</sub> layers are the active layers that convert photons into free electrons and holes. MoO<sub>3</sub> and BCP work as the protective inter-layers between the active layers and the electrodes ( i.e. ITO and Ag).

MoO<sub>3</sub> has deep-lying electronic states; the conduction band minimum and the valence band maximum are at 6.7eV and 9.68eV below the vacuum level respectively [6]. Including a thin MoO<sub>3</sub> layer helps improving hole injection from anode[6]. The mechanism, which is illustrated in Fig. 5.7b, is that charge transfer between ITO and MoO<sub>3</sub> gives rise to the Fermi-level pinning between the two layers and a vacuum level shift ( $\Delta_1$ ), making the MoO<sub>3</sub> a strongly n-type semiconductor. Once an ITO/MoO<sub>3</sub> layer is brought into contact with a donor (CyTRIS in this case), instead of injecting holes directly from the ITO, electrons are injected from the donor HOMO to the MoO<sub>3</sub> LUMO, leaving holes in the donor HOMO bands[6]. As a result, an ohmic contact and another vacuum level shift ( $\Delta_2$ ) occur at the interface between ITO/MoO<sub>3</sub> and CyTRIS, making the quasi-Fermi level aligned in all three layers. Based on Section 4.4, we model the ITO/MoO<sub>3</sub>/CyTRIS contacts as an injecting contact with a small injection barrier.

On the other hand, a thin BCP layer is usually deposited between the electron acceptor (C<sub>60</sub>) and the metal cathode to prevent thermal damage during the cathode deposition and

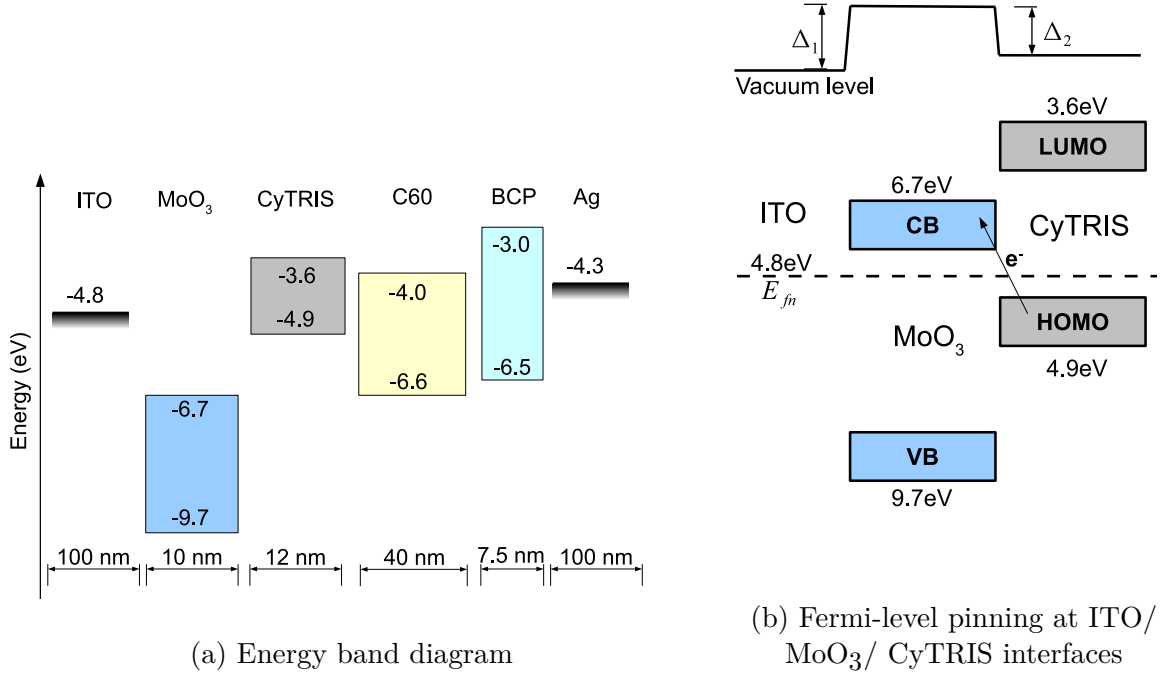


Figure 5.7: (a) Energy band diagram and the thickness of each layer in the CyTRIS:C<sub>60</sub> device. (b) Fermi-level pinning, vacuum level shifts, and possible hole injecting mechanism at the ITO/MoO<sub>3</sub>/CyTRIS interfaces (*adapted from [6]*).

to serve as an exciton blocking layer[131]. Based on the energy band diagrams in Fig. 5.7a, electrons cannot transport through the LUMO of BCP because of the high barrier between C<sub>60</sub> and BCP. However, chemical interaction between BCP and the metal cathode results in induced transport levels and trap states in the BCP gap that electrons can transport through [132]. For simplicity, we model the BCP/Ag layer as an injecting cathode with the work function close to that of Ag.

Simulations for the CyTRIS:C<sub>60</sub> device are performed with the parameters listed in Table 5.1.  $\mu_n$  and  $\mu_p$  are the estimated mobilities of electrons in C<sub>60</sub> and holes in CyTRIS, respectively.  $\mu_{tun}$  is empirically chosen to be around  $10^{-9}$  to  $10^{-11} m^2/Vs$ . The dielectric constant is estimated from the real ( $n'$ ) and imaginary ( $k$ ) parts of the refractive indices shown in the supplementary material of Ref. [1], using the relation [133]

$$\epsilon = \epsilon_0(n'^2 - k^2). \quad (5.2)$$

The total recombination rate is a summation of the SRH recombination with the exponential trap distributions summarized in Section 1.8 and  $R_{t-t}$  in Eq. 5.1.

Parameter	Value
$\mu_p$	$1.0 \times 10^{-7} m^2/Vs$
$\mu_n$	$1.0 \times 10^{-6} m^2/Vs$
$\mu_{tun}$	$0, 10^{-9} - \times 10^{-11} m^2/Vs$
Donor/acceptor thickness	12nm/40nm[1]
$\phi_a/\phi_c$	0.20 eV/0.25 eV
$\epsilon$	$4.2\epsilon_0$
$T_{t,D} = T_{t,A}$	1200K
$k_{PPr,0}$	$5 \times 10^5 s^{-1}$
Donor $E_{LUMO}/E_{HOMO}$	-4.9eV/-3.6eV [1]
Acceptor $E_{LUMO}/E_{HOMO}$	-6.6eV/-4.0eV [1]
$N_{HOMO}/N_{LUMO}$	$3.2E24 m^{-3}$
$H_D/H_A$	$2.0E23 m^{-3}$
$J_X$	$3.5E20 m^{-2}s^{-1}$
$a_0 = \delta x$	1.0nm
recombination type	Shockley-Read-Hall + trap-to-trap

Table 5.1: Summary of parameters used to study effects of the trap-to-trap recombination ( $R_{t-t}$ ) in terms of the effective mobility  $\mu_{tunn}$  in the CyTRIS:C<sub>60</sub> device[1].

The simulation results under illumination and dark conditions are respectively plotted in Figs. 5.8a and 5.8b including the experimental data for comparisons. For the illumination cases,  $\mu_{tun}$  from  $10^{-9}$  to  $10^{-11} m^2/Vs$  does not have any noticeable effects on the JV curves, and they agree well with the experimental one for the whole range of  $V_a$ . For the dark cases, the simulated curves in the range  $V_a > 0.3V$ , i.e. the diode regime, are consistent with the experimental result, with  $\mu_{tun} \approx 5 \times 10^{-10} m^2/Vs$  giving a reasonable fit at lower  $V_a$ . The curves in the reverse bias, however, are quite erroneous as they are flatter and lower than the measured values. Based on the discussions in section 5.2, negative- and low-voltage current is governed by the dark leakage current which is separable from the diode current (see Fig. 5.4). Since the diode term contains all the physical parameters, and the graphs agree well in the diode dominating regime, the parameters in Table 5.1 are good approximations for the actual ones.

Including  $R_{t-t}$  influences JV curves in identical ways to including the dark  $R_p$ . This can

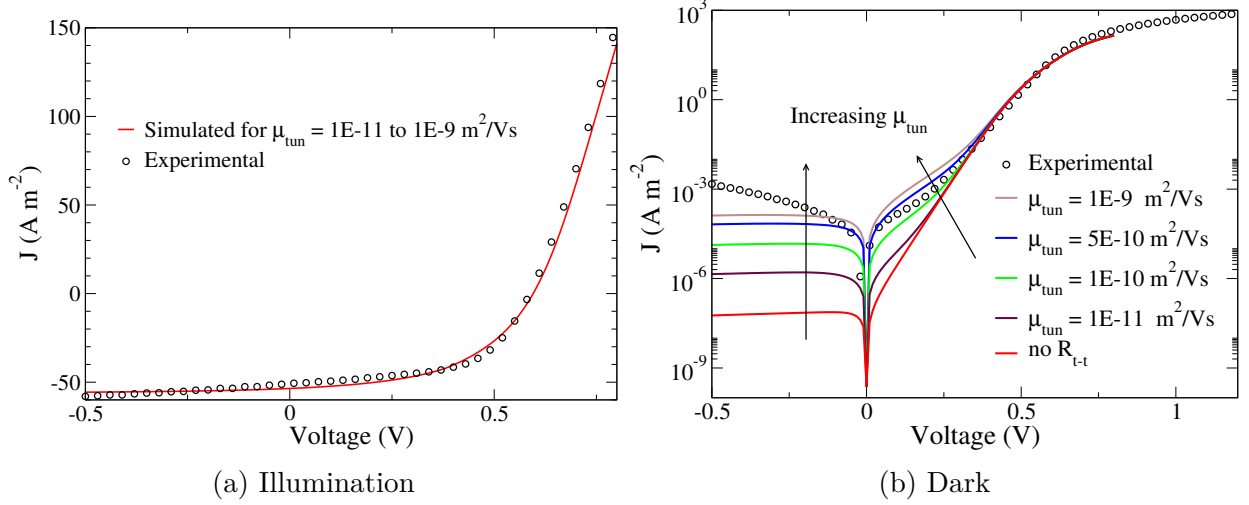


Figure 5.8: Comparisons between the simulated JV curves of the CyTRIS:C<sub>60</sub> device and the experimental data under a) illumination and b) dark conditions

be shown by the following explanations. Firstly,  $R_{t-t}$  graphically affects the illuminated and dark JV curves in Figs. 5.8a and 5.8b analogously to those in Figs. 5.6a and 5.3a, i.e. it does not affect the illuminated JV curves but affects the low- and negative-voltage parts of the dark currents.

Secondly, an extra current term originated from  $R_{t-t}$  has similar properties to the leakage current. Because we use the integral form of  $R_{SRH}$  (Eq. 1.43), in order to separate currents from different origins, the general GWWF JV relation in the analytic form (Eq. 1.11) has to be used instead of Eq. 3.3. Using  $R = R_{SRH} + R_{t-t}$  in Eq. 1.11 yields

$$\begin{aligned} J &= qa_0(1 - \eta_{PPd})R_{SRH,eq} \left( \frac{R_{SRH}}{R_{SRH,eq}} - \frac{k_{PPd}}{k_{PPd,eq}} \right) \\ &\quad + qa_0(1 - \eta_{PPd}) \left( R_{t-t} - \frac{k_{PPd}}{k_{PPd,eq}} R_{t-t,eq} \right) - qJ_X\eta_{PPd} \\ &= J_{SRH} + J_{tun} - qJ_X\eta_{PPd}, \end{aligned} \quad (5.3)$$

where

$$J_{tun} = qa_0(1 - \eta_{PPd})(R_{t-t} - \frac{k_{PPd}}{k_{PPd,eq}} R_{t-t,eq}) \quad (5.4)$$

is the tunneling current from  $R_{t-t}$ , and each parameter is a function of  $V_a$  and taken from numerical simulations. This equation results in exactly the same currents as numerically calculated by Eq. 3.3. Figure 5.9 shows plots of  $J$ ,  $J_{SRH}$  and  $J_{tun}$  of the devices with  $\mu_{tun} =$

$1 \times 10^{-11}$  and  $5 \times 10^{-10} m^2/Vs$  under dark conditions. The diode-like  $J_{SRH}$  is invariant upon changing  $\mu_{tun}$  and equals to the total current curve when  $R_{t-t}$  is excluded. The shapes of  $J_{tun}$  in both graphs are also unchanged but shifted up by the higher  $\mu_{tun}$ . These behaviors are similar to Fig. 5.4 when  $J_{leak}$  is lifted by reducing the dark  $R_p$ .

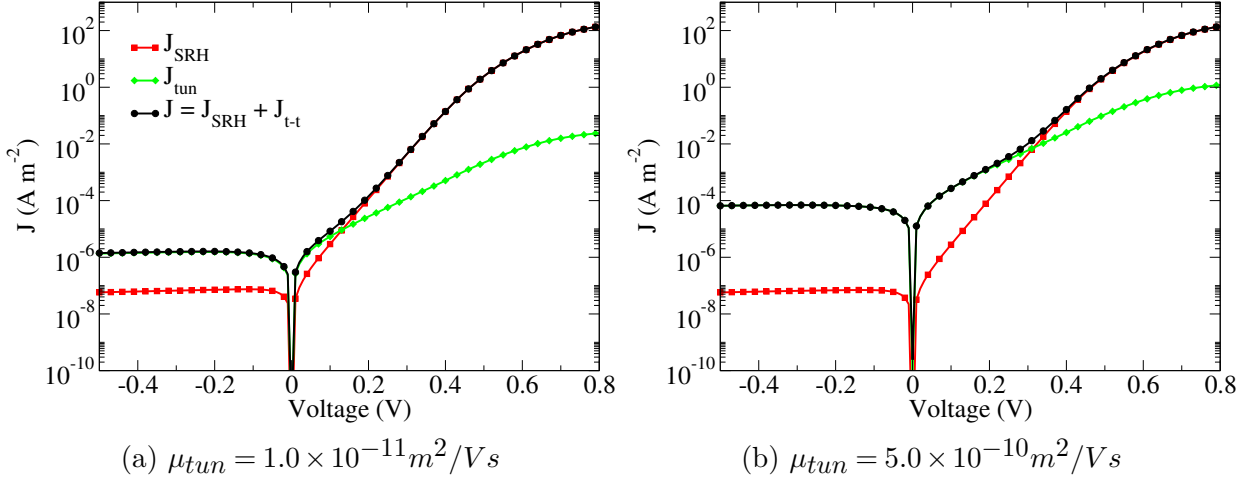


Figure 5.9: Plots of the currents originated from  $R_{SRH}$  ( $J_{SRH}$ ) and  $R_{tt}$  ( $J_{tun}$ ) defined in Eqs. 5.3 and 5.4 and the total dark currents  $J = J_{SRH} + J_{tun}$  for the devices with  $\mu_{tun}$  equals to a)  $1.0 \times 10^{-11}$  and b)  $5.0 \times 10^{-10} m^2/Vs$ .

Thirdly, if the current  $J_{tun}$  is considered as the dark leakage current flowing through a parallel resistance  $R_{p\_tun}$ , the  $R_{p\_tun}$  value will be in accordance with the experimental one. Using the same definition of  $R_p$  as in Section 2.2, i.e. that it is biased by the interface voltage difference  $E_{fn,I} - E_{fp,I}$  yields

$$R_{p\_tun} = \frac{E_{fn,I} - E_{fp,I}}{J_{tun}}. \quad (5.5)$$

A plot of  $R_{p\_tun}$  as a function of voltage in the device with  $\mu_{tun} = 5 \times 10^{-10} \Omega m^2$  is shown in Figure 5.10. In the range  $0.0V < V_a < 0.3V$  where the leakage current  $J_{tun}$  caused by  $R_{p\_tun}$  dominates, the resistance values are around hundreds to a thousand of  $\Omega m^2$  which agree well with the extracted value of  $1,920 \Omega m^2$  from the actual device.[1]

Therefore, it can be concluded that the trap-to-trap recombination can describe the trap-related tunneling processes that cause the dark leakage current.  $R_{t-t}$  gives rise to  $J_{tun}$

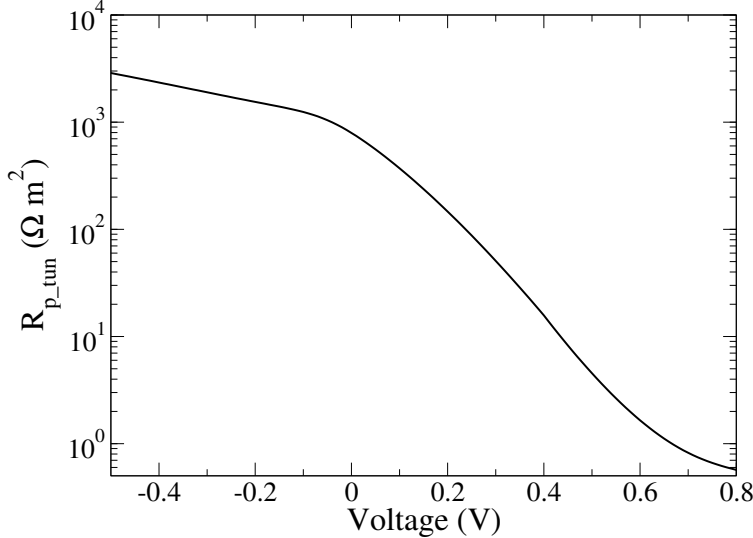


Figure 5.10: Plot of the parallel resistance  $R_{p\_tun}$  calculated by Eq. 5.5 as a function of applied voltage in the device with  $\mu_{tun} = 5.0 \times 10^{-10} \text{ m}^2/\text{Vs}$

that behaves similarly to the dark leakage current and  $R_{p\_tun}$  that has values close to the typically measured parallel resistance in the dark.

However,  $R_{t-t}$  and  $\mu_{tun}$  oversimplify the actual tunneling processes, and cannot reproduce reverse-bias dark JV curves. More sophisticated theories have to be applied. For example, using the Miller-Abrahams rate[91] or a more correct form of charge hopping rate between localized states[134] in the master equation[135] to derive the mobility across the D/A interface is one possibility. The second possibility is to consider charge tunneling through the whole donor layer which is only 12-nanometer thick, by using the TAT current and energy-level-dependent tunneling coefficient[130]. Additionally, one could use the electric-field-dependent mobility[136] in the modified SRH recombination to include the TAT processes[126, 127]. These topics are useful directions for future work.

#### 5.4.3 Including a Constant Dark Parallel Resistance in the DD-BI and the SCD models.

In this part, we propose another method of including a leakage current under dark conditions ( $J_{leak,dark}$ ) to the DD-BI and the SCD models. Here, we use the Shockley form (Eq. 1.3)

of the leakage current;

$$J_{leak,dark} = \frac{V_a - JR_s}{R_{p,dark}} = \frac{E_{fn,I} - E_{fp,I}}{R_{p,dark}}, \quad (5.6)$$

where the parallel resistance  $R_{p,dark}$  is manually included.

Including Eq. 5.6 in the SCD equations (Eqs. 2.5, 2.14, or 2.22) is straightforward. For the case of the SRH recombination, the SCD equation (Eq. 2.22) becomes

$$J = J_{s,SRH} \left[ \exp \left( \frac{E_{fn,I} - E_{fp,I}}{n_{SRH} k_B T} \right) - 1 \right] - q J_X \eta_{PPd} + \frac{E_{fn,I} - E_{fp,I}}{R_{p,dark}}. \quad (5.7)$$

To include the dark leakage current in the self-consistent DD-BI model, some modifications have to be made to the model. First, the total current  $J$  in the GWWF interface model (Fig. 1.5) has to include  $J_{leak,dark}$  by simply replacing  $J$  with  $J - J_{leak,dark}$ . According to the rate equation 1.10, the interface free carrier generation rate ( $U$ ) is modified to

$$U = k_{PPd} \zeta - R - \frac{J_{leak,dark}}{qa_0} = k_{PPd} \zeta - R - \frac{E_{fn,I} - E_{fp,I}}{qa_0 R_{p,dark}} \quad (5.8)$$

to cover the loss from the leakage current. Hence,  $E_{fn,I} - E_{fp,I}$  has to be updated after solving the Poisson equation in the computer algorithm (Fig. 3.1). This can be done by using Equations 1.19 and 1.20 to express  $E_{fn,I} - E_{fp,I}$  in terms of the interface densities ( $n_I$  and  $p_I$ ), i.e.

$$E_{fn,I} - E_{fp,I} = \Delta E_{HL} - F_I a_0 + V_t \ln \left( \frac{n_I p_I}{N_{LUMO} N_{HOMO}} \right), \quad (5.9)$$

where the potential drop across the D/A interface ( $F_I a_0$ ) is included.

The CyTRIS:C<sub>60</sub> device is simulated, using the same parameters as in Table 5.1 except that the t-t recombination is replaced by the leakage processes through the constant  $R_{p,dark}$ , which is chosen to be 80 to  $8 \times 10^4 \Omega m^2$ . Figure 5.11 shows the simulation results, and for comparison purposes, JV curves calculated by the generalized Shockley equation (Eq. 1.3) using fitted Shockley parameters from Ref. [1]:  $J_0 = 1.3 \times 10^{-6} A/m^2$ ;  $R_s = 9 \times 10^{-4} \Omega m^2$ ;  $R_p = 1920 \Omega m^2$ ;  $J_{ph} \approx J_{sc} = 48 A/m^2$ ; and  $n = 1.34$  and  $1.36$  under illumination and dark conditions respectively, are also included. Note that these parameters are extracted from

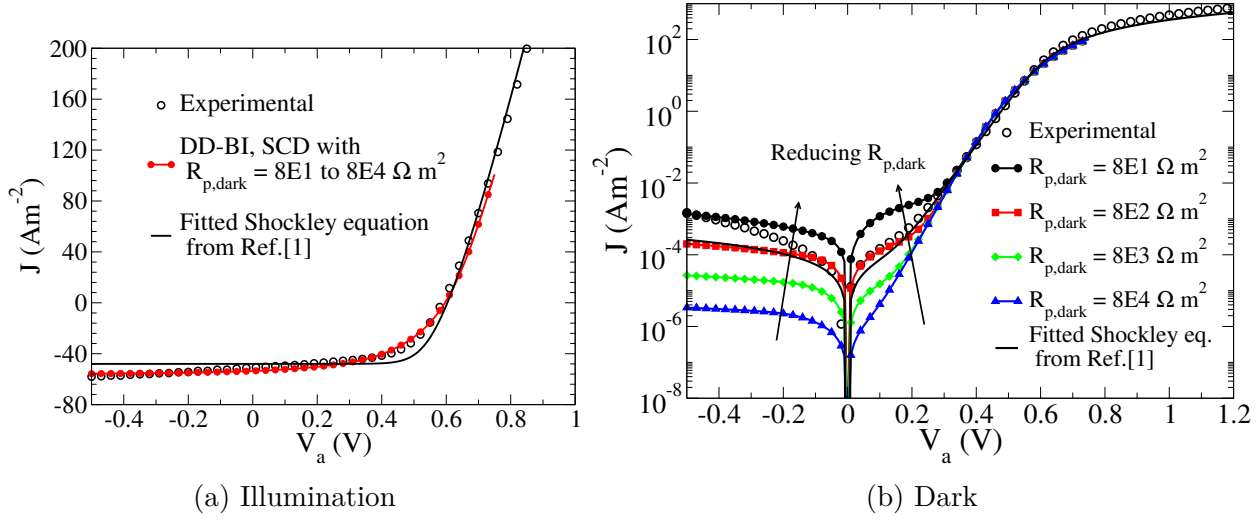


Figure 5.11: Comparisons of JV curves of the CyTRIS: $C_60$  device under (a) illumination and (b) dark conditions between the experimental results (circle symbol), the DD-BI and the SCD results (lines with a symbol) and the Shockley equation's results (Eq. 1.3) (solid lines) using the fitted parameters from Ref. [1].

the measured dark curve, but they are used to describe the device both under dark and illumination conditions.

Following points can be deduced from the comparisons. First, the graphs calculated by the SRH SCD equation with  $R_{p,dark}$  included are consistent with the DD-BI simulations in all the cases of  $R_{p,dark}$ . The DD-BI and the SCD JV curves respond to the change of  $R_{p,dark}$  similarly to the Shockley equation results in Sections 5.2 and 5.3. Second, according to the results in the dark, the DD-BI/SCD curve with  $R_{p,dark} \approx 800\Omega m^2$  fits reasonably well with the experimental one, and is very close to the standard Shockley curve using the parameters from Ref. [1]. However, both plots do not agree well with the experimental result in the reverse bias regime, where the actual slope is steeper. This implies that a more correct description of  $J_{leak,dark}$  is needed. Thirdly, the Shockley equation using only the dark  $R_p$  cannot reproduce the illumination JV curve because the leakage mechanisms under the two conditions are different. Two  $R_p$  values are needed, and the one under illumination has to be much lower than the one in the dark in order to have a leaking photo-current and a sloping JV at low  $V_a$ . This topic and the errors of using only one set of Shockley parameters under both conditions will be discussed in the upcoming sections.

## 5.5 Complete Equivalent Electrical Circuit Model

With more insights of  $R_p$  in the dark and the physical definitions of the Shockley parameters in Chapter 2 and 4, we now have a complete picture of the equivalent electrical circuit model (Complete EEC) in Fig. 5.12.

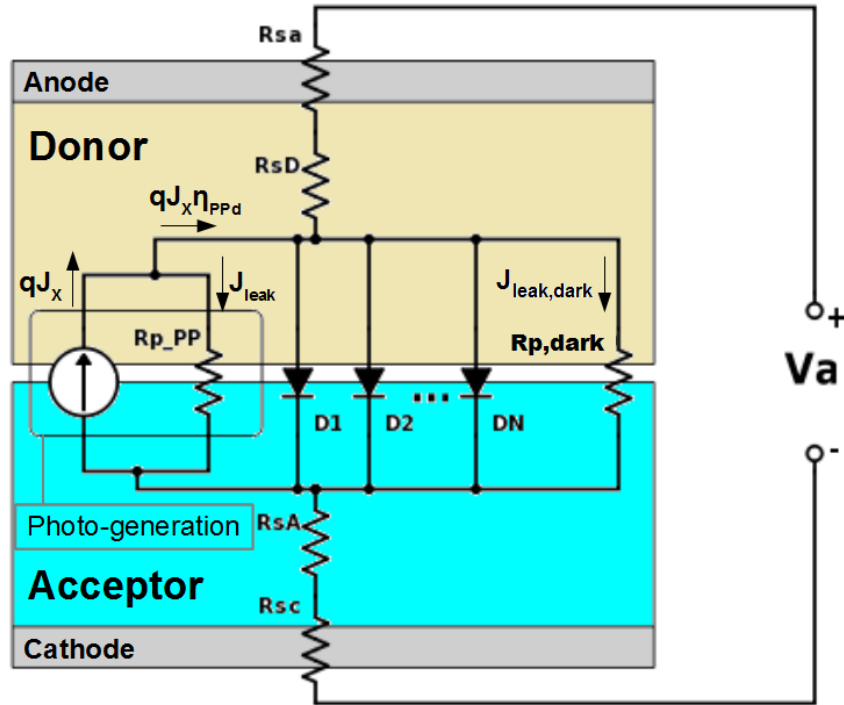


Figure 5.12: A schematic showing the bilayer OPV architecture with each important physical mechanism being represented by an electrical circuit component. All the electrical components form the complete EEC model.

First of all, we would like to emphasize that each electrical component does represent an actual physical mechanism. Starting from the top of Fig. 5.12, series resistance portrays the drops of quasi-Fermi levels caused by the anode contact, bulk donor, bulk acceptor and the cathode contact, so there are four  $R_s$  components (See Section 4.4.5). There are three main processes at the D/A interface, from left to right: (1) photo-generation processes enclosed by the gray box; (2) free-carrier recombination pathways with a diode representing each pathway; (3) the leakage in the dark which is possibly caused by the trap-related

tunneling. For process (1), the current source (the circle symbol with an arrow) produces a constant current of  $qJ_X$ , but  $qJ_X(1 - \eta_{PPd})$  recombines as if it leaks through a virtual parallel resistance ( $R_{p\_PP}$ ) so that only  $qJ_X\eta_{PPd}$  comes out as the voltage-dependent photocurrent. If the device is under dark conditions, the whole gray box disappears, leaving only process (3) governing the dark leakage current. For process (2), if the recombination is  $R_{SRH}$ , one diode suffices. If  $R_{SRH}$  is separated into  $R_{fn\text{-}tp}$  and  $R_{fp\text{-}tn}$ , there have to be two diodes, but they may not conduct currents equally. An extra diode is included if the f-f recombination is taken into account. Lastly, the clear evidences of dark leakage current ( $J_{leak,dark}$ ) that are discussed in Section 5.4 bring about another parallel resistance which is denoted by  $R_{p,dark}$  (or  $R_{p,tun}$  in Eq. 5.5 if the leakage mechanism is described by trap-related tunneling processes).

A complete general JV equation in the same form as the Shockley equation can be written based on the Complete EEC model;

$$\begin{aligned} J &= \sum_i J_{diode,i} + J_{leak} + J_{leak,dark} - qJ_X \\ &= \sum_i J_{si} \left[ \exp\left(\frac{E_{fn,I} - E_{fp,I}}{n_i k_B T}\right) - 1 \right] + \frac{E_{fn,I} - E_{fp,I}}{R_{p\_PP}} + \frac{E_{fn,I} - E_{fp,I}}{R_{p,dark}} - qJ_X \end{aligned} \quad (5.10)$$

where i runs over the free-carrier recombination types (i.e. SRH or fn-tp + fp-tn and/or f-f),  $J_{leak} = qJ_X(1 - \eta_{PPd})$  is the PP leakage current,  $J_{leak,dark}$  is the dark leakage current that is usually smaller than  $J_{leak}$ , and  $J_{si}$  is the diode saturated current for the recombination type i ( $R_i$ ). If an analytic form for  $R_i$  is known,  $J_{si}$  can be written explicitly, for instance, Eq. 2.6 for  $R_{f-f}$ , Eq. 2.15 for  $R_{fn\text{-}tp}$  and Eq. 2.16 for  $R_{fp\text{-}tn}$ . If it is not known,  $J_{si}$  can always be written in the general form as

$$J_{si} = qa_0(1 - \eta_{PPd})R_{i,eq}, \quad (5.11)$$

according to Eq. 2.1.  $n_i$  is the ideality factor associated with the recombination  $R_i$ . For the f-f recombination,  $n = 1$ .  $n_D$  in Eq. 2.17 and  $n_A$  in Eq. 2.18 are the ideality factors for the fn-tp and the fp-tn recombinations respectively. If the SRH recombination is used, Eq. 2.23 can be used to calculate the SRH ideality factor function.

### 5.5.1 Total Parallel Resistance under Illumination Conditions

We can see that there are two parallel resistances ( $R_{p\_PP}$  and  $R_{p,dark} = R_{p\_tun}$ ) if the device is under illumination conditions. In this section, the total parallel resistance is explored.

Figure 5.13 shows  $R_s$ ,  $R_{p\_PP}$ ,  $R_{p,dark} = R_{p\_tun}$  as a function of applied voltage calculated by Eqs. 2.27, 2.28 and 5.5 as well as the total resistance  $R = [\partial J/\partial V_a]^{-1}$ , using  $\mu_{tun} = 5 \times 10^{-10} \Omega m^2$  from Section 5.4. According to the results,  $R_{p\_PP}$  is much lower than  $R_{p\_tun}$ , so that the total parallel resistance under illumination is

$$R_{p,illu} = \left( \frac{1}{R_{p\_pp}} + \frac{1}{R_{p\_tun}} \right)^{-1} \approx R_{p\_PP}, \quad (5.12)$$

i.e.  $R_{p,dark}$  (or  $R_{p\_tun}$ ) and the possible leakage processes in Section 5.4 can be ignored altogether under illumination conditions, unless the light intensity is low enough so that the leakage photo-current ( $qJ_X(1 - \eta_{PPS})$ ) is comparable to  $J_{leak,dark}$  [137]. The values of  $R_{p\_PP}$  in the reverse- and small-bias regimes are around  $0.1 \Omega m^2$  which agrees with the total  $R_p$  under illumination predicted by the Shockley equation in Fig. 5.6a. The graph of  $R = [\partial J/\partial V_a]^{-1}$  also points to the same conclusion. It converges to  $R_{p\_PP}$  at highly negative voltage where  $R_p$  dominates.

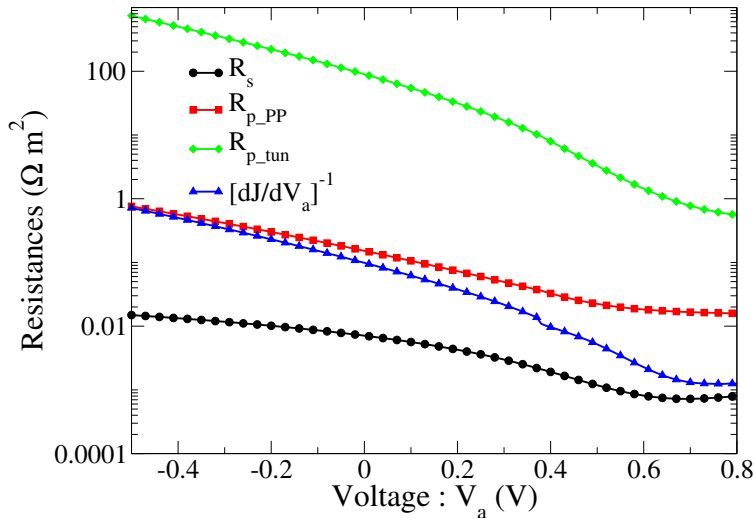


Figure 5.13: A comparison between  $R_s$ ,  $R_{p\_PP}$ ,  $R_{p\_tun}$  and total device resistance calculated by Eqs. 2.27, 2.28, 5.5 and  $[\partial J/\partial V_a]^{-1}$  respectively. The device is from Section 5.4 with  $\mu_{tun} = 5 \times 10^{-10} m^2/Vs$  and under illumination conditions

## 5.6 Shockley Parameters: Dark Versus Light

We have seen in Sections 4.2 and 4.4 that physics of OPVs under dark and illumination conditions are different because there are many more free carriers under illumination conditions than in the dark. Nevertheless, only one set of extracted Shockley parameters;  $J_0$ ,  $n$ ,  $R_s$  and  $R_p$ , is usually reported and used to describe JV curves under both conditions. In this part, we compare the differences between the Shockley parameters under the two conditions, and discuss errors of using the parameters interchangeably.

Here, we choose to simulate the CyTRIS:C<sub>60</sub> device using the parameters shown in Table 5.1 with a constant  $R_{p,dark} = 800\Omega m^2$  as proposed in Section 5.4.3, and the P3HT:PCBM device using the same parameters as in Table 4.5, but the recombination is replaced by the SRH recombination (Eq. 1.43) and a constant  $R_{p,dark} = 100\Omega m^2$  is included. We use this value of  $R_{p,dark}$  because it results in  $J_{leak,dark}$  that has similar magnitude to those in literature [138, 139]. Simulating the two devices provides us conclusions that can be applied to a variety of OPV systems.

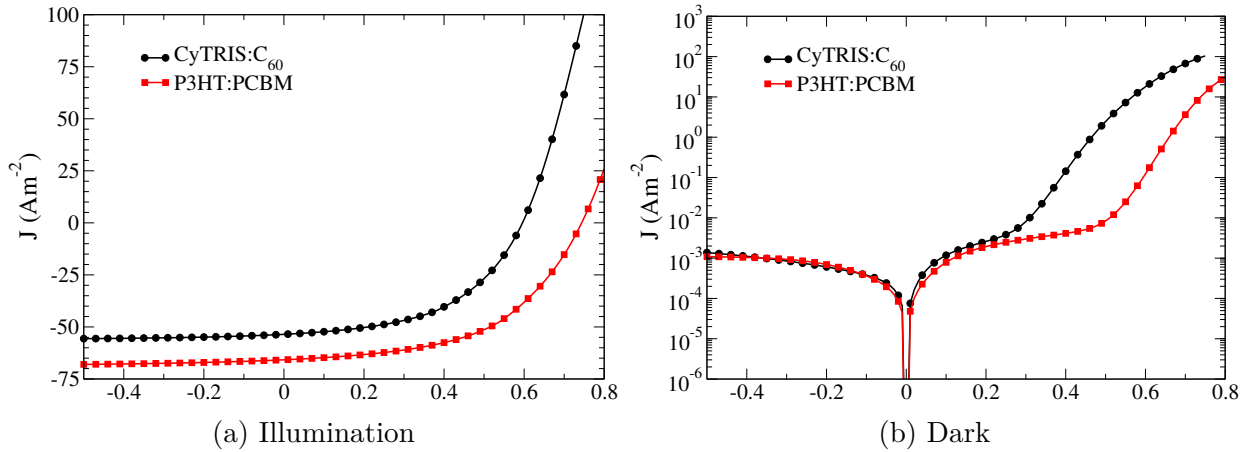


Figure 5.14: JV curves of the CyTRIS:C<sub>60</sub> (black lines with circles) and the P3HT:PCBM (red lines with squares) devices under (a) illumination and (b) dark conditions.

Figure 5.14 shows JV curves under illumination and dark conditions of the CyTRIS:C<sub>60</sub> and P3HT:PCBM devices. The following are comparisons of  $J_0$ ,  $R_s$ ,  $R_p$  and  $n$  as a function of  $V_a$  that are extracted from the figure.

### 5.6.1 Diode Saturation Current ( $J_0$ )

$J_0$  functions that are extracted from dark and illumination JV curves are not significantly different and can be used interchangeably. This is shown in Figure 5.15 where the  $J_0(V_a)$  functions of the two devices are plotted. The reason is that  $J_0$  which is expressed through Eq. 5.11 only depends on  $q$ ,  $a_0$ ,  $\eta_{PPd}$  and  $R_{eq}$  (recombination rate in equilibrium) that do not change between the two conditions.

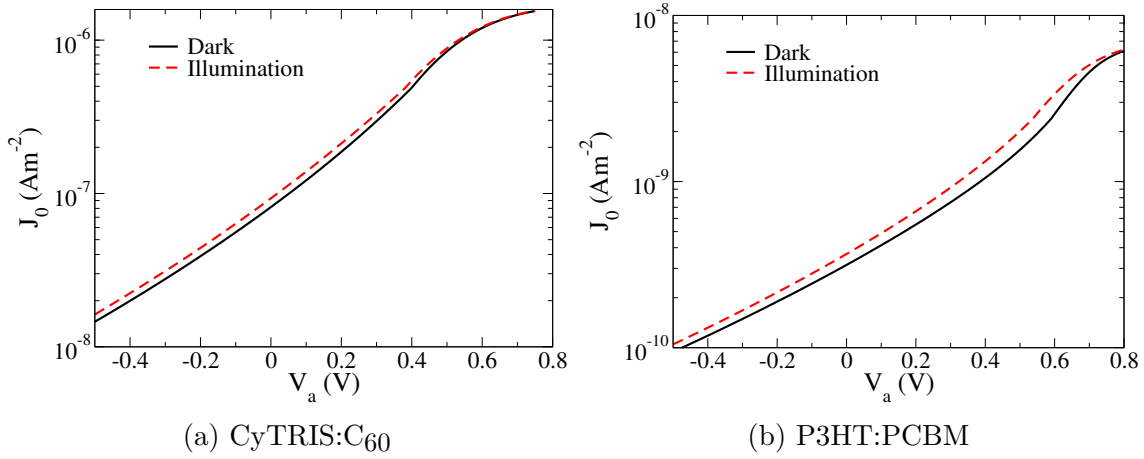


Figure 5.15: Plots of  $J_0$  as a function of  $V_a$  extracted from (a) the CyTRIS:C<sub>60</sub> and (b) P3HT:PCBM devices ( Figs. 5.14) under dark (black solid lines) and illumination (red dashed line) conditions.

Figures 5.16a and 5.16b show  $k_{PPd}$ ,  $k_{PPr}$ , interface electric field ( $F_I$ ) and  $\eta_{PPd}$  as a function of  $V_a$  of the CyTRIS:C<sub>60</sub> device both under dark and illumination conditions. Even though free carrier densities under illumination increase considerably from photo-generation processes (see Fig. 4.7), the device potential profile ( $\psi(x)$ ) still mainly depends on the voltage difference between the anode and the cathode ( $V_{bi} - V_a$ ), and band bending near the electrodes.  $\psi(x)$  and the resulting  $F_I$  in Fig. 5.16b are slightly altered by the photo-generated charges, so  $k_{PPd}$ ,  $k_{PPr}$  and  $\eta_{PPd} = k_{PPd}/(k_{PPd} + k_{PPr})$  that depend primarily on  $F_I$  do not change significantly. As a result,  $J_0 = qa_0(1 - \eta_{PPd})R_{eq}$  hardly changes when light is introduced.

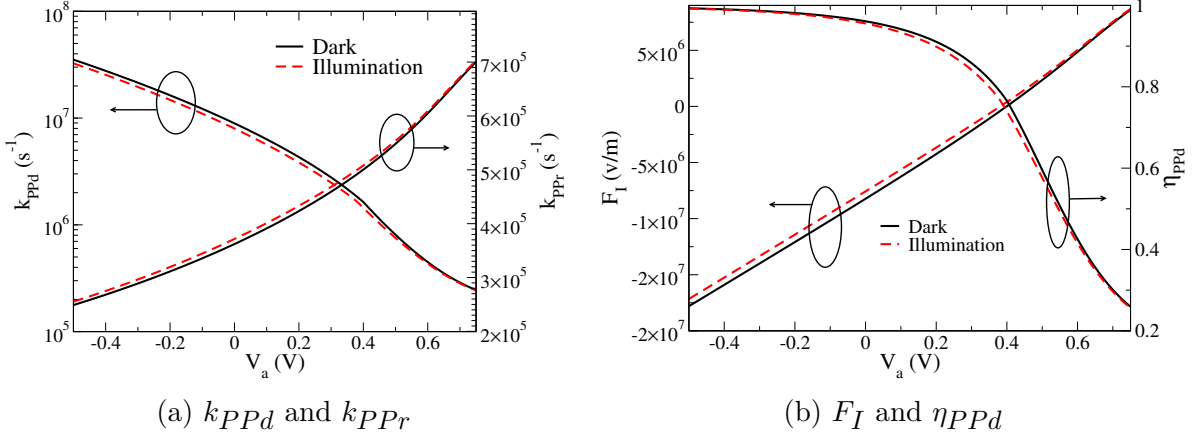


Figure 5.16: Comparisons between illumination and dark conditions of (a)  $k_{PPd}(V_a)$ ,  $k_{PPr}(V_a)$ , (b)  $F_I(V_a)$  and  $\eta_{PPd} = k_{PPd}/(k_{PPd} + k_{PPr})$  of the CyTRIS:C<sub>60</sub> device.

### 5.6.2 Series Resistance ( $R_s$ )

Figure 5.17 shows graphs of  $R_s$  versus  $V_a$  of the two devices under consideration, in the presence and the absence of light. In order to describe a JV curve correctly,  $R_s$  has to be a function of  $V_a$ , but due to limitations of finding  $R_s(V_a)$ , a constant  $R_s$  is normally extracted, using  $R_s = [\partial J/\partial V_a]_{V_{oc}}^{-1}$  [32, 140]. Accordingly, we compare  $R_s(V_a)$  around  $V_{oc}$  in Figure 5.17, where the CyTRIS:C<sub>60</sub> and the P3HT:PCBM devices have  $V_{oc} = 0.60V$  and  $0.74V$ , respectively.

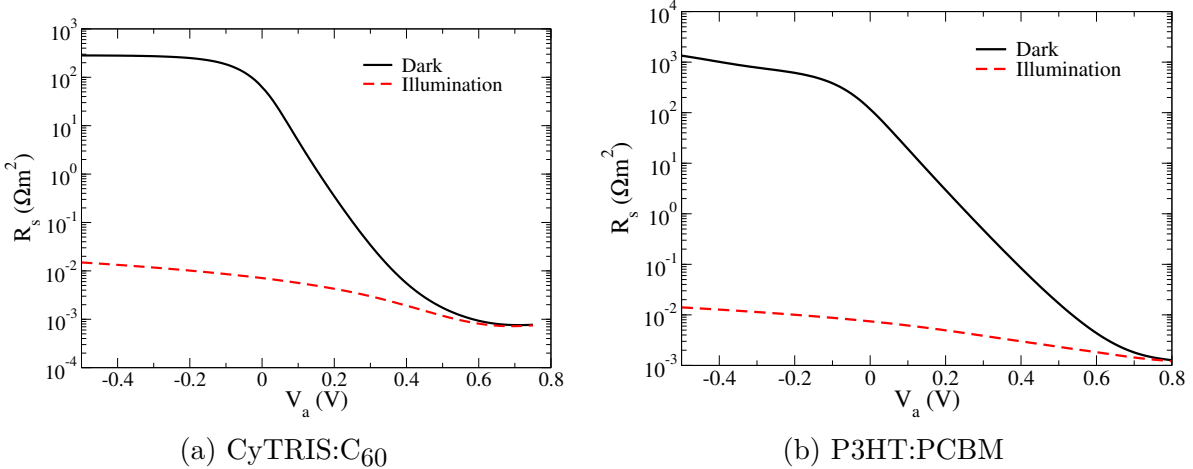


Figure 5.17: Comparisons between illumination (red dashed lines) and dark (black solid lines) series resistances of (a) the CyTRIS:C<sub>60</sub> and (b) P3HT:PCBM devices.

Based on the data,  $R_s(V_{oc})$  values of the CyTRIS:C<sub>60</sub> device are  $9.32 \times 10^{-4} \Omega\text{m}^2$  and

$8.12 \times 10^{-4} \Omega m^2$  under dark and illumination conditions, respectively. For P3HT:PCBM, dark and illumination  $R_s(V_{oc})$  are  $1.49 \times 10^{-3} \Omega m^2$  and  $1.33 \times 10^{-3} \Omega m^2$ , respectively. Hence,  $R_s(V_{oc})$  values under the two conditions are about 12-14% different in these two devices. These agree with the  $R_s$  values shown in Ref. [138], where  $R_s$  values from six different devices are different around 10-50% between under dark and illumination conditions.

### 5.6.3 Ideality Factor ( $n$ )

According to Section 4.5, ideality factor is related to the split of quasi-Fermi levels at the interface ( $E_{fn,I} - E_{fp,I}$ ) and trap characteristic temperatures ( $T_{t,D}$  and  $T_{t,A}$ ). In general form, it is expressed by Equation 2.23, which also depends on  $E_{fn,I} - E_{fp,I}$  and  $R(V_a)/R_{eq}$  where  $R(V_a)$  is recombination rate at  $V_a$  and  $R_{eq}$  is the equilibrium recombination rate. Due to that  $R(V_a)$ ,  $E_{fn,I}$  and  $E_{fp,I}$  under illumination and dark conditions are different because of the different amounts of charges, ideality factor values under the two conditions are also different, but the degree of the difference varies from system to system.

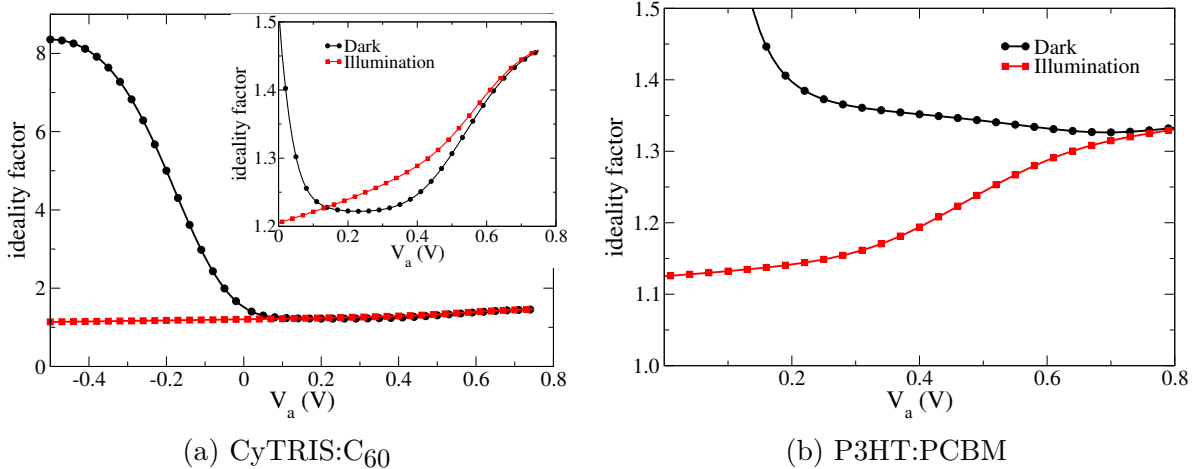


Figure 5.18: Ideality factor functions calculated by Eq. 2.23 of (a) the CyTRIS:C<sub>60</sub> and (b) the P3HT:PCBM devices under dark and illumination conditions. (inset) zoomed portion of figure (a) for  $V_a > 0V$

Figure 5.18 shows comparisons of dark and illumination ideality factor functions calculated using Eq. 2.23 of the two devices. For the P3HT:PCBM graph, we only show the positive bias regime because the dark  $n(V_a)$  function diverge around  $V = 0V$  from

$\ln(R(V_a)/R_{eq}) \approx 0$  in the denominator of Eq. 2.23. For the CyTRIS:C<sub>60</sub> case, the dark and illumination  $n(V_a)$  functions are close to each other (i.e. less than 10% different) in the positive bias regime, which is where  $n$  relevant the most according to Sections 5.2 and 5.3. This is in accordance with the results from Ref. [1] where extracted ideality factors from dark curves are close to those calculated by light intensity dependent  $V_{oc}$  data. On the other hand, the  $n(V_a)$  functions of the P3HT:PCBM device are significantly different because of the term  $E_{fn,I} - E_{fp,I}$  (not shown here).  $E_{fn,I} - E_{fp,I}$  is related to the interface charge densities and can be affected by many parameters, for example, dielectric constant, mobilities, and density of states near the HOMO or LUMO edges.

#### 5.6.4 Parallel Resistance ( $R_p$ )

Unlike the other three parameters whose values under dark and illumination conditions can be close or different by a small factor,  $R_p$  values under illumination and dark conditions are totally different because they arise from different origins. Figure 5.19 shows plots of illumination  $R_p$  functions ( $R_{p\_PP}$  from Section 5.5), which are recombination resistances of the recombined exciton currents;  $qJ_X(1 - \eta_{PPd})$ . Their values are lower than  $R_{p,dark}$ ;  $R_{p,dark} = 800\Omega m^2$  for CyTRIS:C<sub>60</sub> and  $100\Omega m^2$  for P3HT:PCBM, by at least two orders of magnitude. Similar results are observed experimentally in Ref. [138] where  $R_p$  values under dark are higher than the ones under illumination by  $10 - 10^5$  times.

#### 5.6.5 Errors of Using Dark and Illumination Shockley Parameters Interchangeably

According to the results of the four Shockley parameters,  $J_0$  is the only parameter that can be used interchangeably between dark and illumination conditions.  $R_p$  is on the opposite end of the spectrum because its values under dark and illumination are different by orders of magnitude. Extracted  $R_p$  values from dark JV curves must not be applied to fit other Shockley parameters or derive any physical properties from JV curves under illumination.

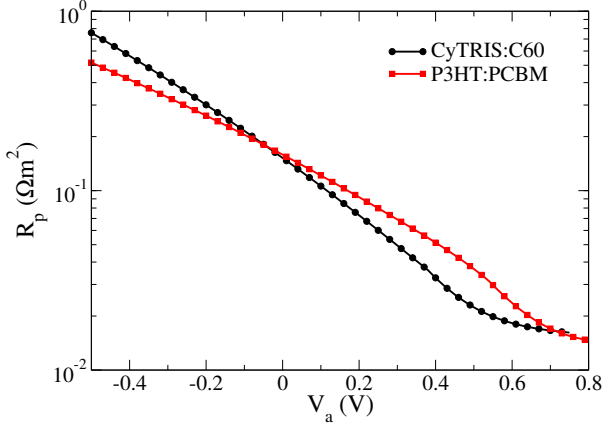


Figure 5.19: Plots of parallel resistances under illumination ( $R_p\_PP$ ) of the CyTRIS:C<sub>60</sub> (black with circles) and the P3HT:PCBM (red with squares) devices calculated using Eq. 2.28.

For  $R_s$  and n, their differences between dark and illumination conditions are not very high, and vary from system to system. However, using extracted values from one conditions with the other conditions can cause errors and wrong interpretations of the results. For example, if a dark  $R_s$  value, which is slightly higher than the illumination value (see Fig. 5.17), is applied to describe an illumination curve, the diode voltage ( $V_a - JR_s$ ) is underestimated. In order to maintain the right diode current ( $J_0[\exp((V_a - JR_s)/nk_B T) - 1]$ ), n has to be reduced from the actual value to compensate the error caused by  $R_s$ . Therefore, it is best to use two sets of the shockley parameters to describe JV curves under illumination and dark conditions.

## 5.7 Conclusions

In this chapter, we focus on applying the DD-BI and SCD models and the theories of OPVs that are discussed in the previous chapters to describe an actual bilayer device in terms of Shockley parameters;  $R_s$ ,  $R_p$ ,  $J_0$  and  $n$ . The device is a cyanine organic salt solar cell with TRIS counterion (CyTRIS:C<sub>60</sub>), which has an interesting kink-shaped JV behavior under dark conditions. We start this chapter with studying the effects of the Shockley parameters on JV curves under dark (Section 5.2) and illumination (Section 5.3) conditions. The results

show that the kink-shaped JV behavior is caused by a leakage current in the dark due to low  $R_p$  and low  $J_0$ .

In addition to the illumination leakage current and  $R_p$  in Section 2.2, we include a leakage current and  $R_p$  in the dark in our models by using the trap-to-trap (t-t) recombination and the standard Shockley form of leakage current with a constant  $R_p$ . Both methods result in a dark leakage current that can bring about the kink-shaped JV behavior. However, leakage currents from the two models do not fit perfectly with experimental results especially in the reverse bias regime, so better descriptions of dark leakage current in bilayer OPVs are still needed.

With the dark  $R_p$  processes, we now have a complete electrical equivalent circuit (EEC) model that includes physical processes of bilayer OPVS, having a dark  $R_p$  resistance connected to the illumination  $R_p$  resistance in parallel. In Section 5.6, we use the DD-BI, the SCD and the complete EEC to study differences of the Shockley parameters' values under dark and illumination conditions and possible errors of using the parameters interchangeably. According to the results, only  $J_0$  can be used interchangeably, and  $R_s$  and  $n$  values under the two conditions can be significantly different, but most importantly dark and illumination  $R_p$  values are different by many of orders of magnitude. Hence, it is best to use two sets of the parameters to avoid errors and misinterpretations of fitting results.

## CHAPTER 6

### ***AB INITIO CALCULATION OF AN EPITAXIAL PEROVSKITE***

Since the first photovoltaic application in 2009[141], perovskite solar cells have attracted tremendous attraction from the research community, and this discovery is among the top ten *Breakthrough of the Year*, ranked by the *Science* magazine in 2013. A type of perovskite material of particular interest is caesium tin halide ( $\text{CsSnX}_3$  where  $\text{X} = \text{Cl}, \text{Br}$  or  $\text{I}$ ). Even though they have been known since the 1980s[142, 143], the availability of atomistic calculations and advanced computer technologies have just allowed us recently to understand them fundamentally.

A research group at MSU lead by professor Richard R. Lunt is now concentrating on synthesizing  $\text{CsSnBr}_3$  using an epitaxy technique. It allows an epitaxial  $\text{CsSnBr}_3$  film to grow on the (100) surface of a  $\text{NaCl}$  substrate, from gaseous precursor of  $\text{CsBr}:\text{SnBr}_2$ . The  $\text{CsSnBr}_3$  crystal usually maintains cubic phase at room temperature[142], but the film undergoes a phase transition during the growth process. This is possibly caused by the induced compressive strain from lattice mismatch (i.e.  $a = 5.64 \text{ \AA}$  for  $\text{NaCl}$  and  $a = 5.804 \text{ \AA}$ [144] for  $\text{CsSnBr}_3$ ) or chemical interactions between the gaseous precursors. Different ratios of the precursors also affect the phase transition. For example, for  $\text{CsBr}:\text{SnBr}_2$  at 1:1 ratio, the first several layers are in the cubic phase and then another unknown phase forms in the thick film limit. For the ratio of 2:1, the structure maintains a cubic structure regardless of the thickness of the film.

Based on ultraviolet-visible (UV-Vis) spectrophotometry measurements, the cubic phase of  $\text{CsSnBr}_3$  has an energy gap of around 1.8eV and the unknown phase in the thick film limit has a gap of around 3.4eV. X-ray photoelectron (XPS) spectroscopy results show that the actual ratio of Sn:Br in the unknown phase is about 1:1 to 1:2, instead of 1:3, and the amount of Cs ion is less than that of  $\text{CsSnBr}_3$ . With this information and measured X-ray diffraction (XRD) patterns, the unknown phase/structure could be cesium pentabromodistannate (II)

or  $\text{CsSn}_2\text{Br}_5$  [145]. Hence, the objective of the study described in this chapter is to calculate properties of the two compounds using *Ab initio* calculations and compare the simulation results with experimental results, so the identity of  $\text{CsSn}_2\text{Br}_5$  can be confirmed. Mechanisms related to the film growth and the phase transition are also considered.

All calculations in this chapter are performed using the *Vienna Ab initio Simulation Package* (VASP), which is a quantum solid-state simulator. The method implemented in the package is density functional theory (DFT). Necessary background of the related quantum mechanics and the DFT are summarized in the appendix. The contents of this chapter start with an introduction to perovskites and cesium pentabromodistannate (II) in Section 6.1. Simulated electronic band structures are described and compared in Section 6.2. In Section 6.3, adsorption of the precursor atoms onto the (100) NaCl surface is investigated to find the lowest energy atomic configuration of the  $\text{CsSnBr}_3/\text{NaCl}$  interface. Section 6.4 then shows effects of the NaCl substrate on the band structures. Section 6.5 shows simulations of the  $\text{CsSnBr}_3$  film growing processes by depositing the structure layer by layer. Finally, in Section 6.6, possible explanations behind the phase transition are suggested.

## 6.1 Crystal Structures

### 6.1.1 Cubic Perovskite

The chemical formula of perovskite materials is  $\text{ABX}_3$  where its stoichiometry can be I-VI<sub>3</sub>, II-IV-VI<sub>3</sub>, III-III-VI<sub>3</sub> and I-II-VII<sub>3</sub>[146]. For the I-II-VII<sub>3</sub> family that  $\text{CsSnBr}_3$  belongs to, A is a cation with 1+ charge and 12 nearest neighbors (NN), B is a 2+ cation with 6 NN, and X is a 1- halide anion. The structure and the unit cells are shown in Figure 6.1. There exist more complex structures of perovskite materials which are beyond the scope of this study.

The structure under investigation consists of ions B and X forming  $\text{BX}_6$  octahedra throughout the bulk, and the A cations occupy the cuboctahedral voids[147, 148]. There are

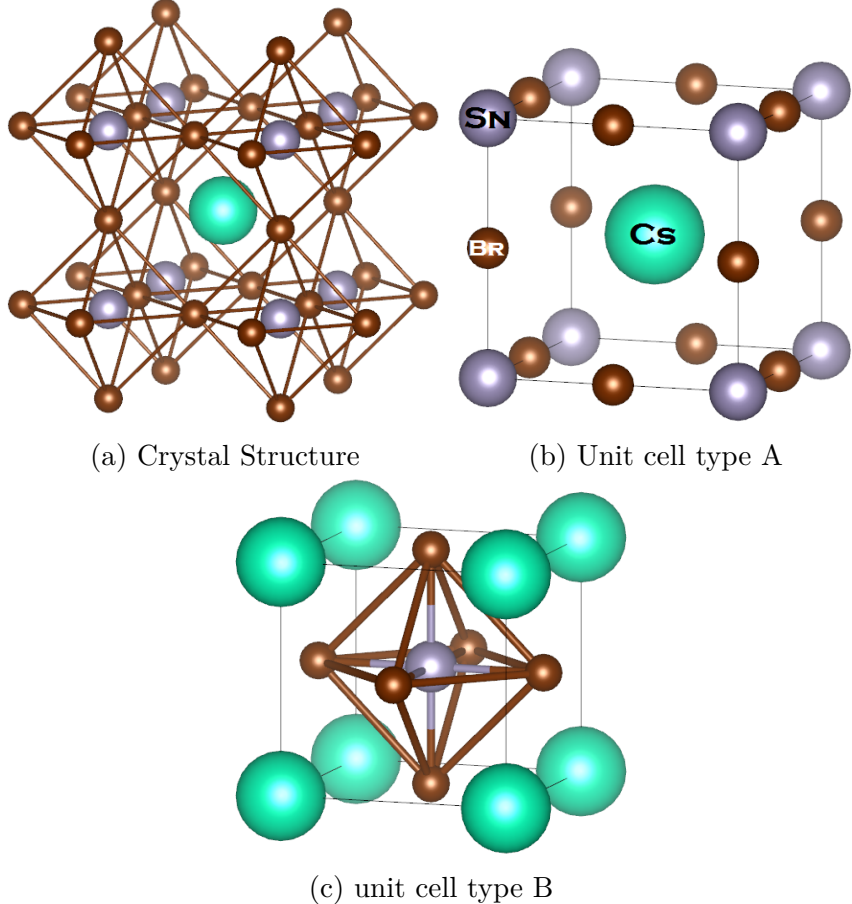


Figure 6.1: (a) Structure of a cubic perovskite showing octahedra of  $\text{BX}_6$  and the cation A filling the cuboctahedral void. (b) and (c) Two representations of the perovskite unit cell with the labels of the Cs, Sn, and Br ions in figure (b) for the case of  $\text{CsSnBr}_3$ .

two representations of the unit cell, shown in Figures 6.1b and 6.1c. There are many possible choices of the ions A, B, and X, however a perovskite material will be stable only if its geometric tolerance factor ( $t$ ) is close to one;  $t = (r_A + r_X)/\sqrt{2}(r_B + r_X)$ , where  $r_i$  is the effective radii of the ion  $i$ [148]. The factor  $t$  is derived from the ratio between the lattice constants (a) calculated from the AB plane (i.e. the middle plane in Fig. 6.1b);  $a_1 = \sqrt{2}(r_A + r_X)$  and from the AX<sub>2</sub> plane (i.e. the bottommost plane in Fig. 6.1b);  $a_2 = 2(r_B + r_X)$ , so  $t = a_1/a_2$ . For a list of the effective radii, see the paper by Shanon[149]. The BX<sub>6</sub> octahedra can be considered as a scaffold with the cations A supporting it. Accordingly, the size of the cation A is quite specific and large alkali metals like caesium suit the position. Too small A cation results in  $t < 1$  and octahedral distortion results. Alkali metal halide perovskites (e.g.

$\text{CsSnBr}_3$ ) should have  $0.813 < t < 1.107$  [150] in order to be stable. Examples of possibly stable perovskites are  $\text{CsCuX}_3$ ,  $\text{KCuX}_3$ ,  $\text{KCoX}_3$ ,  $\text{KMnX}_3$ , etc., where  $\text{X} = \text{Cl}, \text{Br}, \text{I}$ .

### 6.1.2 $\text{CsSn}_2\text{Br}_5$ Structure

The crystal structure of cesium pentabromodistannate (II) ( $\text{CsSn}_2\text{Br}_5$ ) is shown in Figure 6.2, which is proposed by Abrahams *et al.* in their paper [145]. The following is a brief description of the structure that is summarized from the paper.

The structure is composed by two-dimensional sheets of polymeric anion  $[\text{Sn}_2\text{Br}_5]_n^{n-}$  and inter-layer planes of Cs cations. Its tetragonal unit cell is shown in Figure 6.2a along with the definitions of the basis vectors. Projection of the unit cell onto the b/c plane is shown in Figure 6.2b, and Figure 6.2c shows the 2D  $[\text{Sn}_2\text{Br}_5]_n^{n-}$  sheet when it is viewed along the c direction. The polymeric sheet is composed of four-sided rings of 4 Sn atoms and 4 Br atoms, with each side shared with other rings. Each Sn atom forms 4 bonds with 4 neighboring Br atoms (note that there are Br atoms right under the dangling Br atoms in Fig. 6.2c) and has a pair of non-bonding valence electrons, so the bond shape at each Sn site is pyramidal.

Figure 6.3 shows another way of choosing  $\text{CsSn}_2\text{Br}_5$  unit cell that has different c basis vector from that in Figure 6.2, but the same a and b basis vectors. Instead of including 2 sheets of  $[\text{Sn}_2\text{Br}_5]_n^{n-}$  and 2 planes of Cs into the tetragonal unit cell in Fig. 6.2, the unit cell in Fig. 6.3, which is triclinic, has only one sheet of  $[\text{Sn}_2\text{Br}_5]_n^{n-}$  and one Cs plane. Thus, the triclinic unit cell is more economic than the tetragonal unit cell.

One unit cell can be transformed into another by using a transformation matrix in the relation;

$$\begin{pmatrix} a' & b' & c' \end{pmatrix} = \begin{pmatrix} a & b & c \end{pmatrix} \begin{pmatrix} P_{11} & P_{12} & P_{13} \\ P_{21} & P_{22} & P_{23} \\ P_{31} & P_{32} & P_{33} \end{pmatrix}, \quad (6.1)$$

where basis vectors a, b and c are transformed into new basis vectors a', b' and c' by the transformation matrix  $\mathbf{P}$ . In the case of  $\text{CsSn}_2\text{Br}_5$ , the transformation matrices to transform

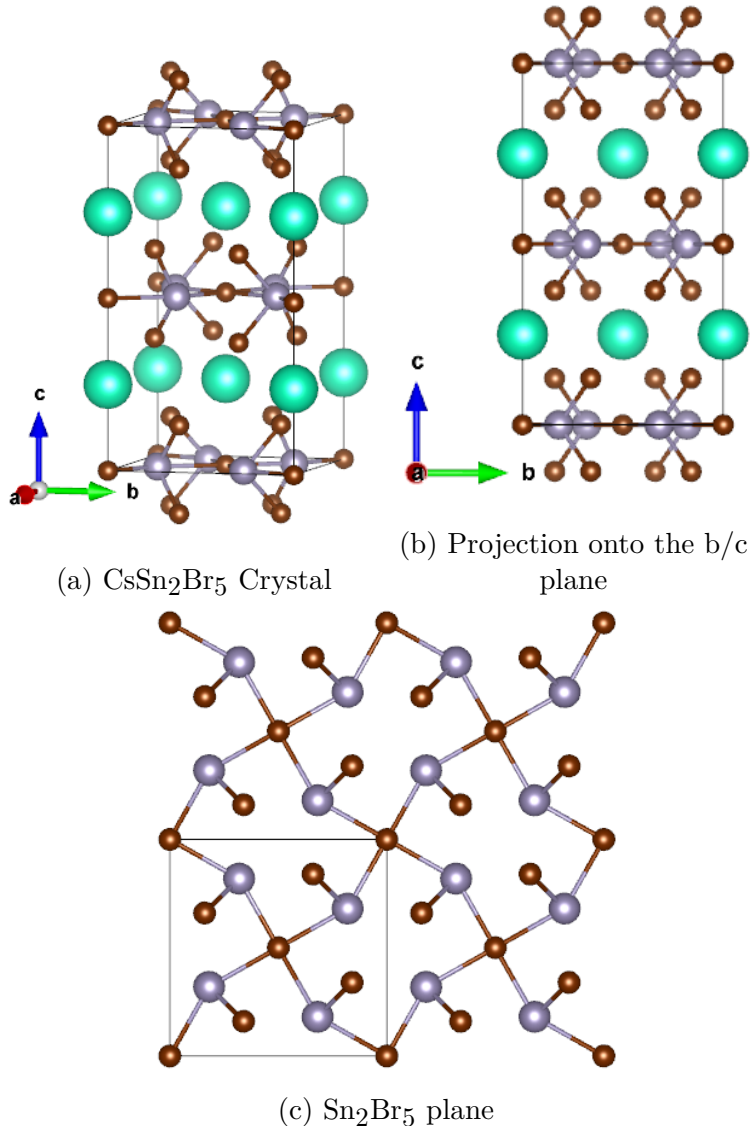


Figure 6.2: a) Tetragonal unit cell of  $\text{CsSn}_2\text{Br}_5$  with the definitions of the basis vectors and b) its projection onto the  $b/c$  plane. c) Projection onto the  $a/b$  plane of the  $[\text{Sn}_2\text{Br}_5]_n^{n-}$  polymeric sheet. Gray, purple and brown spheres represent Cs, Sn and Br atoms, respectively.

from the triclinic unit cell to the tetragonal unit cell and *vice versa* are given by;

$$\mathbf{P} = \begin{pmatrix} 1 & 0 & 1 \\ 0 & 1 & 1 \\ 0 & 0 & 2 \end{pmatrix}, \text{ and } \mathbf{P}' = \begin{pmatrix} 1 & 0 & -0.5 \\ 0 & 1 & -0.5 \\ 0 & 0 & 0.5 \end{pmatrix}, \quad (6.2)$$

respectively.

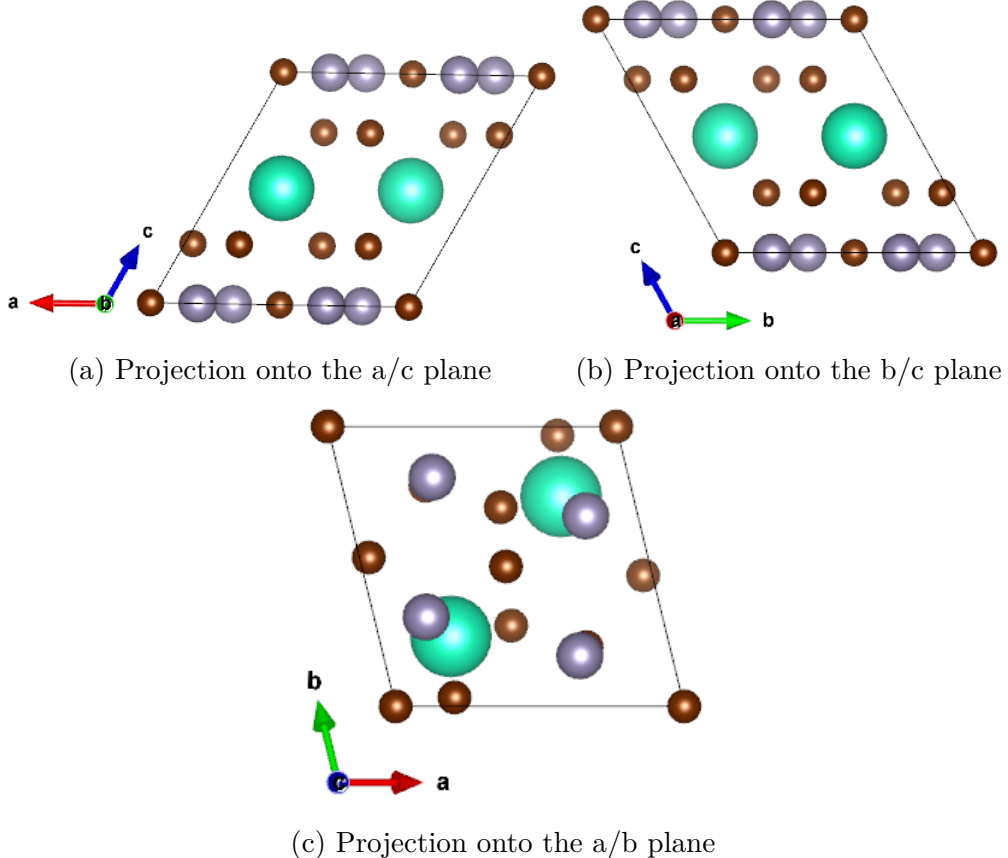


Figure 6.3: Triclinic unit cell of  $\text{CsSn}_2\text{Br}_5$  that is projected into a) the  $a/c$  plane, b) the  $b/c$  plane and c) the  $a/b$  plane. Gray, purple and brown spheres represent Cs, Sn and Br atoms, respectively.

## 6.2 Band Structure and Density of States Calculations of CsSnBr<sub>3</sub> and CsSn<sub>2</sub>Br<sub>5</sub>

In this part, we calculate electronic band structures and densities of states of  $\text{CsSnBr}_3$  and  $\text{CsSn}_2\text{Br}_5$  at the DFT level using the program VASP. We use the Perdew-Burke-Ernzerhof (PBE) functional [151]; which belongs to the class of generalized gradient approximations (GGA), and the Heyd-Scuseria-Ernzerhof (HSE06) functional [152]; which is a screened hybrid approximation for the exchange-correlation functional. In the case of  $\text{CsSn}_2\text{Br}_5$ , we use the triclinic unit cell primarily because of the smaller number of atoms, but the tetragonal unit cell is also calculated for comparison purposes. First of all, we perform structural relaxations on the unit cells that are described in the previous section using the

PBE functional to find the optimized unit cells. The optimized cubic unit cell of  $\text{CsSnBr}_3$  has the lattice constant of  $5.888\text{\AA}$ , and the optimized triclinic unit cell of  $\text{CsSn}_2\text{Br}_5$  has the following parameters;  $a = 8.6177\text{\AA}$ ,  $b = 8.6190\text{\AA}$ ,  $c = 10.1028\text{\AA}$ ,  $\alpha = 115.28^\circ$ ,  $\beta = 115.25^\circ$  and  $\gamma = 90^\circ$ . Computational details are as follows.

### 6.2.1 Computational Details

The structural optimizations are performed in two steps; rough and fine optimizations. During the rough optimizations, we use a conjugate gradient algorithm (IBRION = 2) to relax the initial structures until total force on each ion is less than  $0.3 \text{ eV}/\text{\AA}$  (EDIFFG = -0.3),, and then the structures are further optimized using a quasi-Newton algorithm (IBRION = 1) until the total force is less than  $0.01 \text{ eV}/\text{\AA}$ .

For band structure calculations, the first Brillouin zones of cubic, triclinic and tetragonal unit cells are illustrated in Figure 6.4. For cubic band structures, the path along the high symmetry k-points is chosen as  $\Gamma\text{-X}\text{-M}\text{-R}\text{-}\Gamma$ . The paths for the cases of triclinic or tetragonal systems follow the suggestions by Setyawan and Curtarolo[7] which are  $\text{X}\text{-}\Gamma\text{-Y}|\text{L}\text{-}\Gamma\text{-Z}|\text{N}\text{-}\Gamma\text{-M}|\text{R}\text{-}\Gamma$  and  $\Gamma\text{-X}\text{-M}\text{-}\Gamma\text{-Z}\text{-R}\text{-A}\text{-Z}|\text{X}\text{-R}|\text{M}\text{-A}$  respectively. Details of the high symmetry  $k$  vectors can be found in the paper [7] as well.

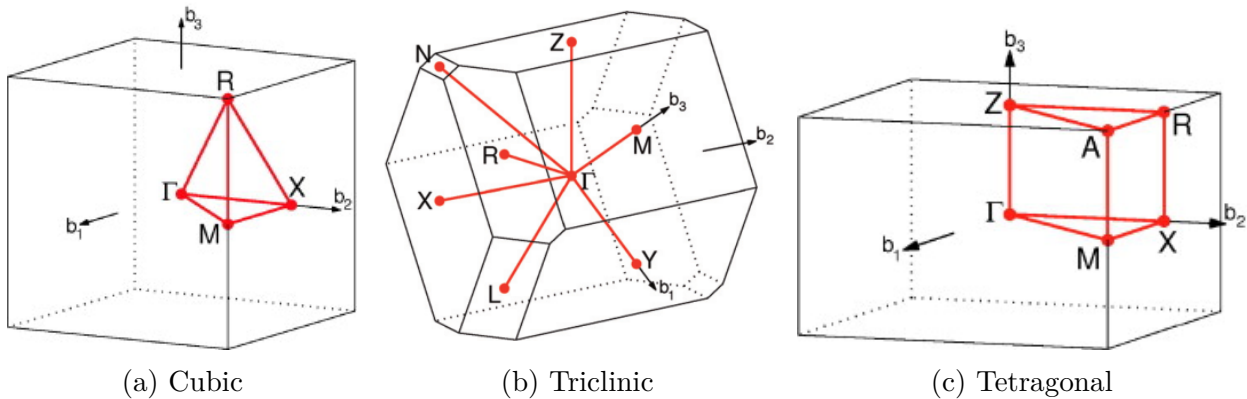


Figure 6.4: The first brillouin zones of (a) a cubic, (b) a triclinic and (c) a tetragonal unit cell with a path along the edges of the irreducible brillouin zones. *adapted from [7]*

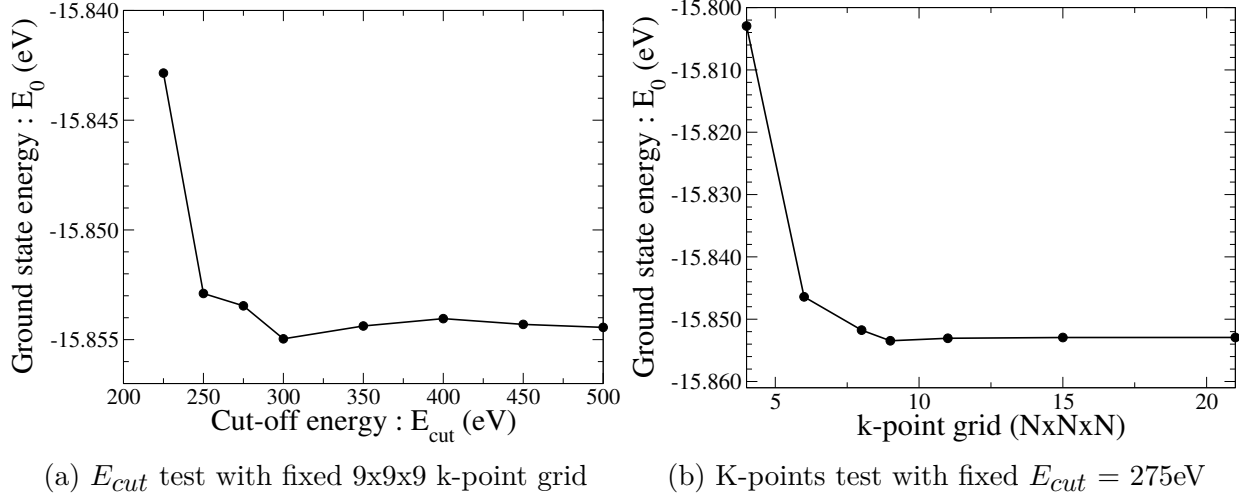


Figure 6.5: Ground state energy ( $E_0$ ) convergence tests of the cubic phase as a function of (a) cut off energy ( $E_{cut}$ ) using a  $\Gamma$ -centered k-point grid  $9 \times 9 \times 9$  and (b) k-point grid of  $N \times N \times N$  where  $N$  is the x-axis value with  $E_{cut} = 275$ eV.

Convergence tests of the ground state energy ( $E_0$ ) due to the choices of k-point grid and cut-off energy ( $E_{cut}$ ) of the plane wave basis set are shown in Figure 6.5 for the optimized cubic phase. The tests are based on the PBE functional. Throughout this chapter, the Gaussian smearing (ISMEAR = 0) with the width of 0.05eV (SIGMA = 0.05) are used, unless stated otherwise. The precision of the calculation is set to  $10^{-5}$  eV/atom (EDIFF = 1E-5), although EDIFF = 1E-4 is sufficient according to the VASP manual. The graph shows that  $E_{cut} = 300$ eV, or 275eV if the computational time is needed to be reduced, are sufficient and result in an error of about 1-2 meV. These  $E_{cut}$ 's are considerably higher than the default value set by VASP at 220eV, based on the Cs\_sv PAW potential. Change of  $E_0$  caused by k-point grids finer than  $8 \times 8 \times 8$  is not clearly observed, so it is chosen.

Figure 6.6 shows the  $E_0$  convergence tests of the optimized  $\text{CsSn}_2\text{Br}_5$  triclinic unit cell. Figure 6.6a shows that  $E_0(E_{cut})$  has considerable fluctuation for  $E_{cut} < 300$ eV, so  $E_{cut} = 300$ eV; which brings about an error of about 1-2meV as compared to that of  $E_{cut} = 350$ eV, is chosen. According to Fig. 6.6b where the major scale separation of the  $E_0$  axis is 0.01meV, k-point grids finer than  $6 \times 6 \times 4$  result in an negligible improvement of the accuracy. However, if a symmetric k-point grid (e.g.  $6 \times 6 \times 6$ ) is used, the program will show an error message

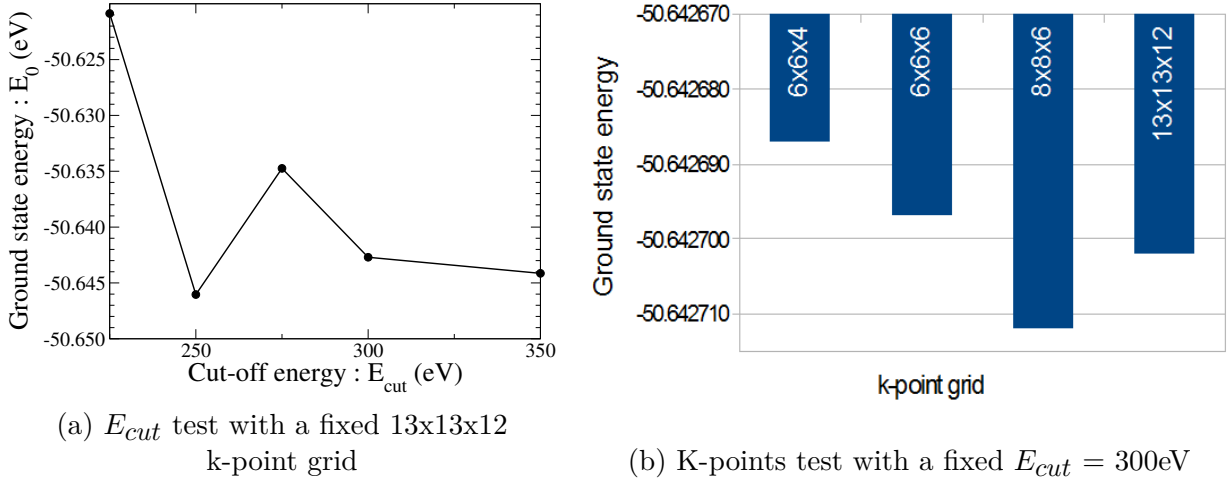


Figure 6.6: Ground state energy ( $E_0$ ) convergence tests of the optimized triclinic unit cell of  $\text{CsSn}_2\text{Br}_5$  as a function of (a) cut off energy ( $E_{cut}$ ) using a  $\Gamma$ -centered k-point grid 13x13x12 and (b)  $\Gamma$ -centered k-point grids with a fixed  $E_{cut} = 300\text{eV}$ .

about unmatched k-points in the irreducible Brillouin zone (IBZ) to the lattice type. This is because of the unequal lengths of the reciprocal lattice vectors; which are determined by

$$\vec{b}_1 = 2\pi \frac{\vec{a}_2 \times \vec{a}_3}{\vec{a}_1 \cdot (\vec{a}_2 \times \vec{a}_3)}, \quad \vec{b}_2 = 2\pi \frac{\vec{a}_3 \times \vec{a}_1}{\vec{a}_2 \cdot (\vec{a}_3 \times \vec{a}_1)} \quad \text{and} \quad \vec{b}_3 = 2\pi \frac{\vec{a}_1 \times \vec{a}_2}{\vec{a}_3 \cdot (\vec{a}_1 \times \vec{a}_2)}, \quad (6.3)$$

where  $\vec{a}_i$  is the Bravais lattice vector. For the optimized triclinic unit cell,  $|\vec{b}_1| = 0.131\text{\AA}^{-1}$ ,  $|\vec{b}_2| = 0.131\text{\AA}^{-1}$  and  $|\vec{b}_3| = 0.124\text{\AA}^{-1}$ , i.e.  $|\vec{b}_i|$  is approximately inversely proportional to  $|\vec{a}_i|$ . In order to have an equally-spaced k-point grid in the IBZ, the grid has to be roughly  $\frac{1}{a} \times \frac{1}{b} \times \frac{1}{c}$ . In this case, the grid 6x6x4 does not result in the error message and is sufficient.

The projected augmented-wave (PAW) potentials[153, 154]; which are the default methods in VASP, are used to replace the complex potentials of the core electrons. For Cs atoms, semi-core s electrons have to be treated as valence electrons, so the potential file Cs\_sv is used.

## 6.2.2 The PBE Calculations

### 6.2.2.1 CsSnBr<sub>3</sub> Bands and DOS

Figure 6.7 shows the calculated band structure and projected density of states (PDOS) of the cubic phase ( $a = 5.888 \text{ \AA}$ ) CsSnBr<sub>3</sub>, using the PBE functional. The PBE functional is known to underestimate band gaps[155], and this character happens here as well. A direct gap of 0.639 eV occurs at the  $R$  point (0.5 0.5 0.5). Figure 6.8 shows the magnified PDOS around the valence band maximum (VBM) and the conduction band minimum (CBM). In order to clearly understand effects of atomic orbitals on the bands, consider the electron orbitals that are treated as valence orbitals in the following PAW potential files:

- the Cs\_sv PAW potential : 5s2 5p6 6s1;
- the Sn PAW potential : 5s2 5p2;
- the Br PAW potential : 4s2 4p5.

Energies in the following analysis are referenced to the Fermi level which is set to zero. The dominant band in the energy range -8.5 to -6 eV is mainly from the Sn 5s orbitals; while from energies -5 to -2 eV, the bands are dominated by the Br 4p states. Near the VBM, the bands are a mixture of the Sn 5s and the Br 4p states. According to Huang and Lambrecht [156], these VBM bands are from anti-bonding interactions of the Sn 5s and Br 4p. Above the gap, the Sn 5p orbitals mainly comprise the CBM bands, until around the energy 2 to 4 eV, the bands are mixed between the Sn 5p, the Br 4p and the Cs semi-core d states. Over 4eV, the bands of these highly excited states belong to the Cs semi-core d states. Except for the gap, these results agree well with those of Huang and Lambrecht[156] where the more accurate GW method is employed.

### 6.2.2.2 CsSn<sub>2</sub>Br<sub>5</sub> Bands and DOS

The band structure and the PDOS of CsSn<sub>2</sub>Br<sub>5</sub> are shown in Figure 6.9. The VBM and the CBM are at the Z point (-0.5 0.0 0.5) and M point (0.0 0.0 0.5), respectively, resulting

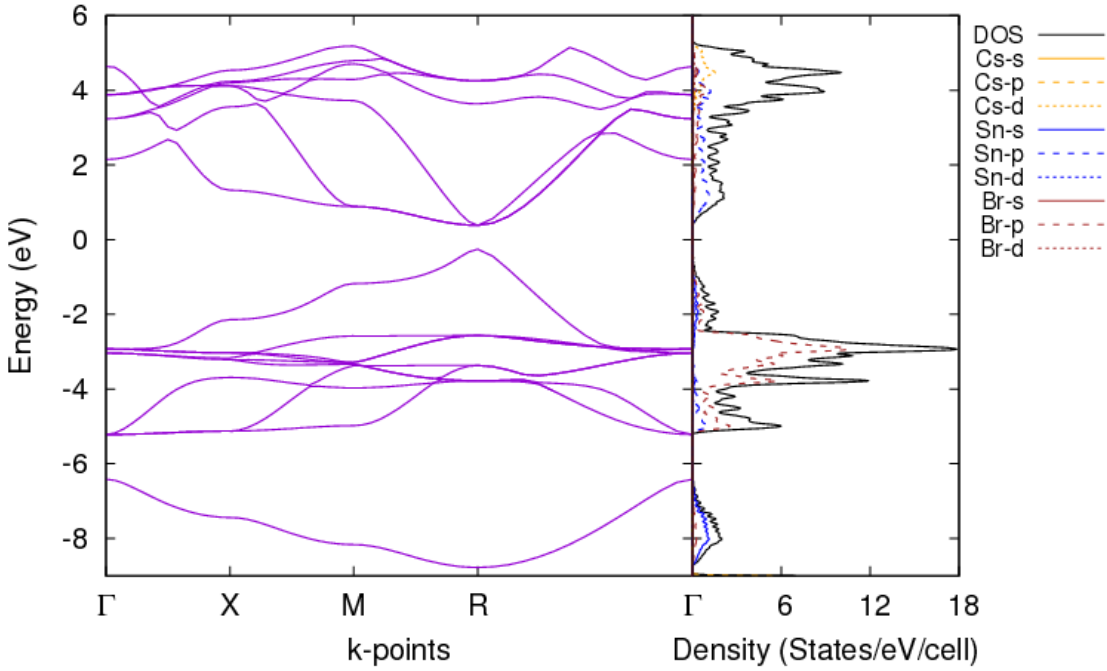


Figure 6.7: Electronic band structure and projected density of states the cubic  $\text{CsSnBr}_3$  structure calculated using the PBE functional.

in an indirect band gap of 2.467eV. However, the bands near the VBM are quite flat and the energies at the symmetry points at the edges of the Brillouin zone (i.e. X, Y, L, Z, N, M and R) are very close to each other. In the CBM bands, the energy at  $\Gamma$  point is also very close to the CBM at M point. The flat VBM bands indicate that effective hole masses ( $m_h^* = \hbar^2(\partial^2 E_k / \partial k^2)^{-1}$ ) are high; possibly resulting in a low hole mobility; which is not preferable in photovoltaic applications.

Atomic orbital characteristics of the bands are as follows. At -7 eV, the flat bands and the corresponding high DOS peak belong to the localized, full-shell semi-core Cs 5p states. The peaks at around -6eV are contributed by the Sn 5s states. From the energy about -3.5 to -0.5 eV, the bands are mainly from to the Br 4p orbitals. Near the VBM, the bands are due to a mixture of Sn 5s and Br 4p states; which are similar to the case of  $\text{CsSnBr}_3$ , and a small contribution from the Sn 5p orbitals. The bands near the CBM are mainly composed of the Sn 5p states, and approximately over 4eV, the bands are from both the Sn 5p and Br

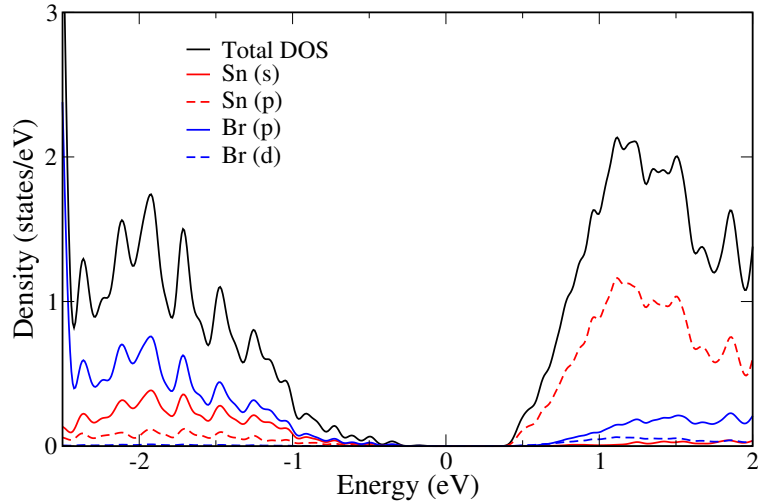


Figure 6.8: Zoomed in projected density of states around the VBM and the CBM of the cubic  $\text{CsSnBr}_3$  calculated using the PBE functional.

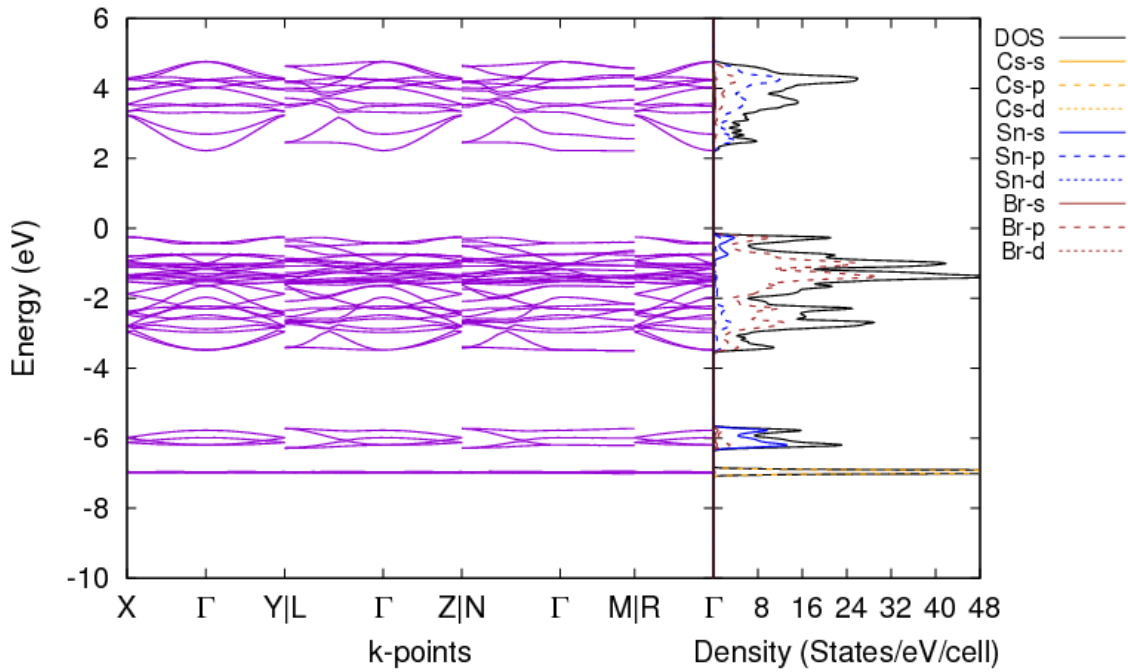


Figure 6.9: Electronic band structure and projected density of states of  $\text{CsSn}_2\text{Br}_5$  calculated using the optimized triclinic unit cell and the PBE functional.

4p orbitals.

Figure 6.10 is a plot of band structure and PDOS functions of  $\text{CsSn}_2\text{Br}_5$  calculated using the optimized tetragonal unit cell; whose unit cell parameters are  $a = 8.591\text{\AA}$ ,  $b = 8.591\text{\AA}$

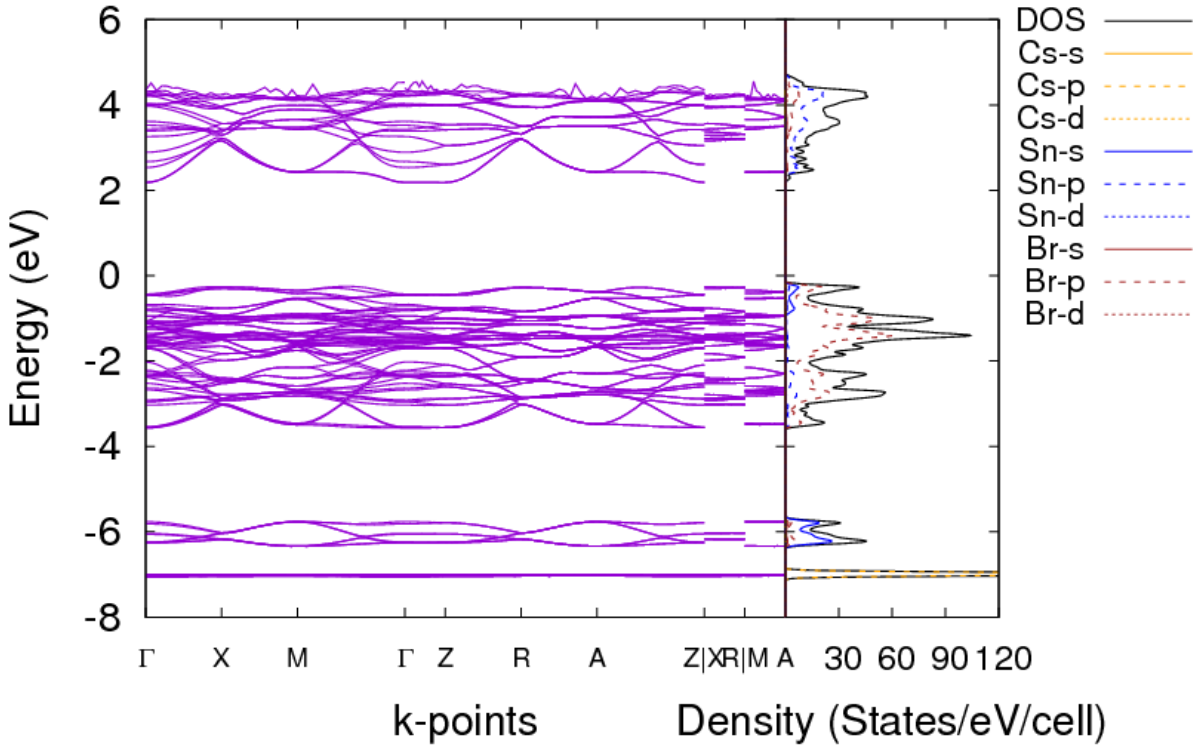
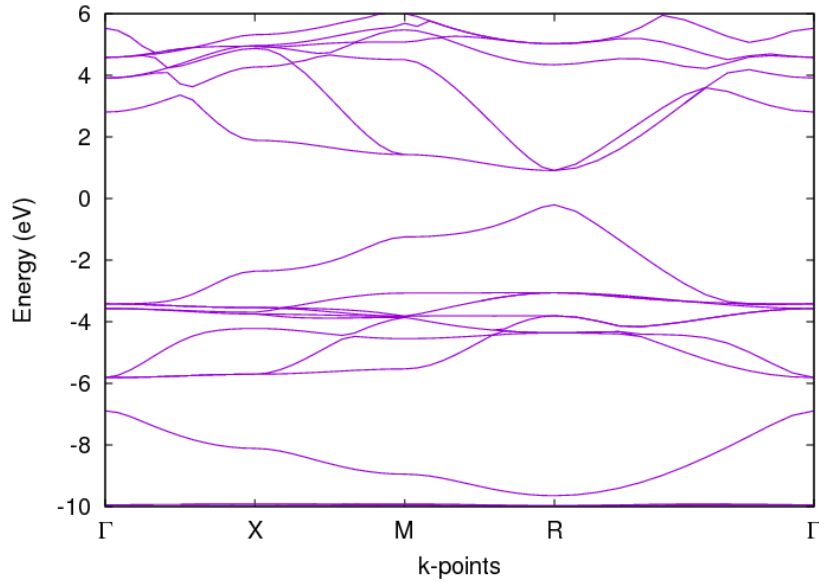


Figure 6.10: Electronic band structure and projected density of states of  $\text{CsSn}_2\text{Br}_5$  calculated using the optimized tetragonal unit cell and the PBE functional.

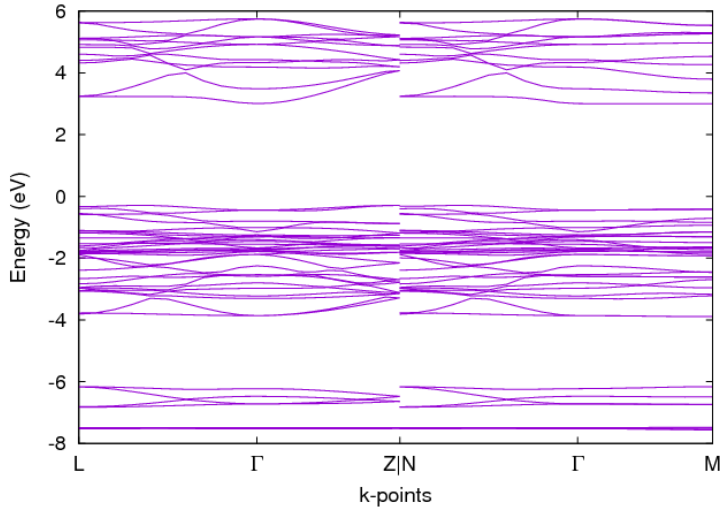
and  $c = 16.133\text{\AA}$ , and the PBE functional. The contributions of atomic orbitals as a function of energy that are shown in the graph agree well with those of the optimized triclinic unit cell in Fig. 6.9. The band structure also shows similar flat VBM bands and an indirect band gap of 2.430 eV, which is close to the value of 2.467 eV in the triclinic case.

### 6.2.3 The HSE06 Calculations

The HSE06[152] functional is employed for the band gap calculations as an effort to improve the accuracy. It is considerably more accurate than the local density approximations (LDA) or generalized gradient approximations (GGA) (e.g. the PBE functional) and is even more accurate than the single-shot  $G_0W_0$  calculation in binary compounds of GaAs, InAs, GaN and InN[157]



(a) HSE06 band structure of the cubic CsSnBr<sub>3</sub>



(b) HSE06 band structure of the triclinic CsSn<sub>2</sub>Br<sub>5</sub>

Figure 6.11: Calculated band structures of a) the cubic CsSnBr<sub>3</sub> and b) the triclinic CsSn<sub>2</sub>Br<sub>5</sub> using the HSE06 functional.

Figure 6.11 represents band structures of the cubic CsSnBr<sub>3</sub> and CsSn<sub>2</sub>Br<sub>5</sub> with the optimized triclinic unit cell, calculated using the HSE06 hybrid functional. For the CsSn<sub>2</sub>Br<sub>5</sub>, we use the path L- $\Gamma$ -Z|N- $\Gamma$ -M instead of the full path as shown in the PBE calculation to reduce the computational time. The shapes of the band structures are not significantly

different from the PBE results, but the gaps are broadened to 1.112eV for  $\text{CsSnBr}_3$  and 3.287 eV for  $\text{CsSn}_2\text{Br}_5$ .

#### 6.2.4 Summary and Discussion of Band Gaps

Table 6.1 summarizes the values of the band gaps and the optimized lattice parameters used in the band calculations.

material	lattice parameters	PBE gap (eV)	HSE06 gap (eV)
$\text{CsSnBr}_3$	$a = 5.888 \text{ \AA}$	0.639	1.112
$\text{CsSn}_2\text{Br}_5$ (triclinic)	$a = 8.618 \text{ \AA}, b = 8.619 \text{ \AA}, c = 10.10 \text{ \AA},$ $\alpha = 115.28^\circ, \beta = 115.25^\circ, \gamma = 90^\circ$	2.467	3.287
$\text{CsSn}_2\text{Br}_5$ (tetragonal)	$a = 8.591 \text{ \AA}, b = 8.591 \text{ \AA}, c = 16.133 \text{ \AA},$	2.430	-

Table 6.1: Summary of the band gap values and lattice parameters of  $\text{CsSnBr}_3$  and  $\text{CsSn}_2\text{Br}_5$ .

For  $\text{CsSnBr}_3$ , an actual compound is stable in a cubic phase at room temperature [142] with a lattice constant of 5.804 Å [144], showing a black color and has an energy gap of 1.8eV [143]. According to the simulation results, the optimized lattice constant is 5.888Å, and the band gaps are 0.639eV and 1.112eV when the PBE and the HSE06 functionals are used respectively. The underestimated PBE gap is unsurprising and expected because the PBE functional is commonly known to underestimate band gaps by around 1-2 eV or even 3 eV in some wide-gap semiconductors or insulators[158, 159]. In this case, the underestimation is around 1.2eV. For the HSE06 functional, the result is considerably improved but still underestimates the gap. The improvement comes from the fact that the HSE06 functional includes an exact Hartree-Fock exchange energy in short-range coulomb interactions but screens coulomb interactions in the long-range limit.

For the case of  $\text{CsSn}_2\text{Br}_5$ , if the same underestimation is assumed, the estimated gap should be around 3.6 - 3.8 eV according to the simulation results of the two functionals. These wide gap values agree with the colorlessness of the film and are in reasonable agreement with the experimental band gap value of 3.3eV.

In conclusion, it is likely that the unknown phase in the thick-film limit is CsSn<sub>2</sub>Br<sub>5</sub> based on the band calculations. This agrees with Ref. [145], which states that the CsSnBr<sub>3</sub> and CsSn<sub>2</sub>Br<sub>5</sub> compounds usually forms simultaneously during sample preparation of CsSn<sub>2</sub>Br<sub>5</sub>.

### 6.3 Adsorption of the Precursor Atoms Onto the NaCl(100) Surface

The purpose of the study described in this section is to find the atomic configuration at the interface between the NaCl(100) surface and the cubic CsSnBr<sub>3</sub>. This can be done by studying adsorption of the precursor atoms during the film deposition. The situation is that there is a clean surface of NaCl(100) and free atoms of Cs, Sn, and Br, suspended over it. The VASP package can be used to perform atomic relaxations to see if the free atoms attach to the surface. Considering the adsorption energy ( $E_{ads}$ ) also helps to determine the most probable absorption configuration.  $E_{ads}$  is a released energy as a result of an adsorption process, which is given by

$$E_{ads} = E_{surface+atom} - (E_{surface} + E_{atom}), \quad (6.4)$$

where  $E_{surface}$ ,  $E_{atom}$  and  $E_{surface+atom}$  are the total energies of the clean surface, the free single atom and the surface with the adsorbed atom respectively. They can be calculated from the relaxed structures using VASP.

The calculation procedure is as follows. First,  $E_{surface}$  is calculated using the unit cell of the NaCl(100) surface shown in Figure 6.12, using the lattice parameter of 5.64 Å, which is the experimental value. Since VASP is implemented with 3D periodic boundary conditions, large vacuum (>15Å in this simulation) has to be included to represent the surface. Second, an atom of Cs, Sn or Br is placed near the surface, and then relaxed to the lowest energy position. It is relaxed freely in any direction, while the surface is kept frozen. With the hypothesis that the atom should be adsorbed on top of a surface atom, there are six possibilities to put the atoms on, which are listed in Table 6.2. Finally, the total energies of a single Cs, Sn and Br atom are calculated and used in the  $E_{ads}$  equation.

All the calculations are based on the DFT with the PBE[151] version of the GGA functional. A k-point grid of 8x8x2 is used in calculations involving the surface, and 4x4x4 k-points are used in the single-atom calculations. A cut-off energy of 340eV is used. During the relaxations, the two-step relaxation method as described in Section 6.2.1 is carried out.

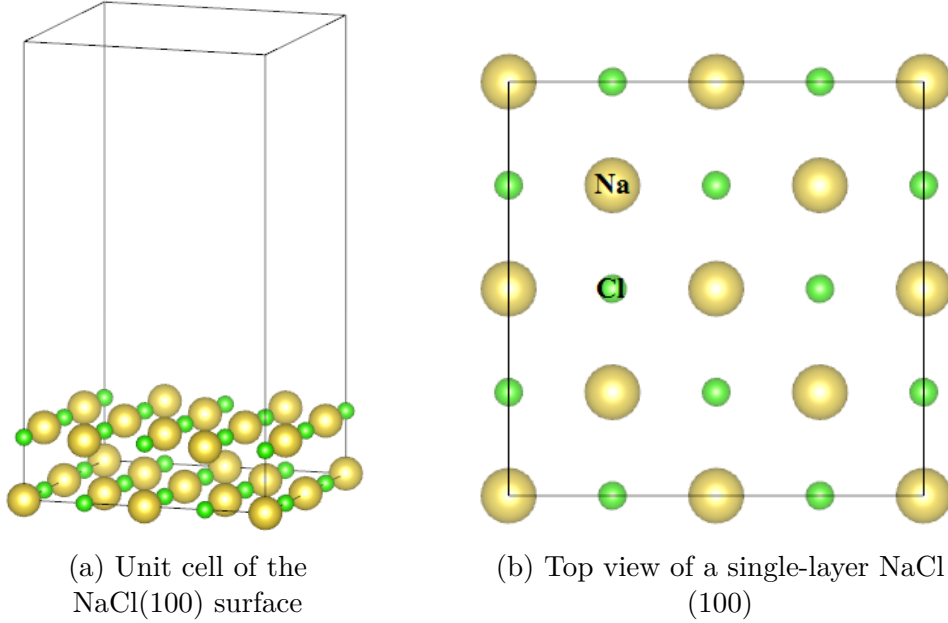


Figure 6.12: (a) The unit cell used for the infinite NaCl(100) surface under 3D periodic boundary conditions. The larger yellow spheres represent Na atoms, and the smaller green spheres represent Cl atoms. (b) Top view of a single-layer NaCl(100) surface.

The simulation results are shown in Table 6.2 in terms of  $E_{ads}$  and the perpendicular distances between the relaxed atoms and the surface. The most probable case is that a Sn atom is adsorbed onto a Cl surface atom. Its adsorption energy is much higher than that of the other atoms. Its distance of 2.7 Å suggests formation of a chemical bonding. For the other cases, the lower  $E_{ads}$  and the higher distances indicate non-bonding, especially in the Br cases where Br atoms are repelled from the surface.

Based on these results, it is hypothesized that the CsSnBr<sub>3</sub> crystal is attached to the NaCl(100) surface by a Sn-Cl bond. This is natural as the bottom-most Br ion in each SnBr<sub>6</sub> octahedron is replaced by the surface Cl ion. The structure is shown in Figure 6.13. It is further confirmed by VASP calculations that this is stable. The chemical bonding in the

Adsorbing site	Adsorbed atom	$E_{ads}$ (eV)	Distance from the surface (Å)
Cl	Cs	-0.1712	3.639
	Sn	-0.5790	2.717
	Br	-0.1192	6.741
Na	Cs	-0.0945	4.392
	Sn	-0.0827	3.532
	Br	-0.1239	6.089

Table 6.2: Resulting adsorption energies ( $E_{ads}$ ) and perpendicular distances in the study of adsorption of Cs, Sn and Br precursor atoms on the NaCl(100) surface.

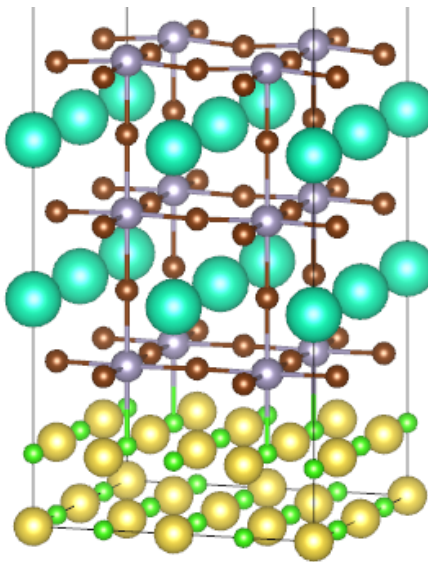


Figure 6.13: Structure of the  $\text{CsSnBr}_3$  crystal bonded to the  $\text{NaCl}(100)$  surface by the  $\text{Sn}^{2+}\text{Cl}^-$  ionic bonds.

metal halide octahedral network is considered to be mixed ionic/covalent interactions, so the standard ionic model (i.e.  $\text{Sn}^{2+} + \text{Br}^-$ ) is applicable[146]. The NaCl crystal is also formed by ionic bonding of  $\text{Na}^+$  and  $\text{Cl}^-$ . Hence, ionic bonding in the  $\text{SnBr}_5\text{Cl}$  surface octahedra is likely possible.

## 6.4 Effects of the NaCl Substrate on the $\text{CsSnBr}_3$ band structure

In the experiments, properties of the films, e.g. band gaps and crystal structures, are measured on samples that are still attached to the NaCl substrate. Hence, it is interesting to examine if the NaCl substrate has any effects on the films. In this part, we calculate and

compare band structures and PDOS functions of two cubic  $\text{CsSnBr}_3$  films; one is attached to the  $\text{NaCl}$  substrate and the other is not.

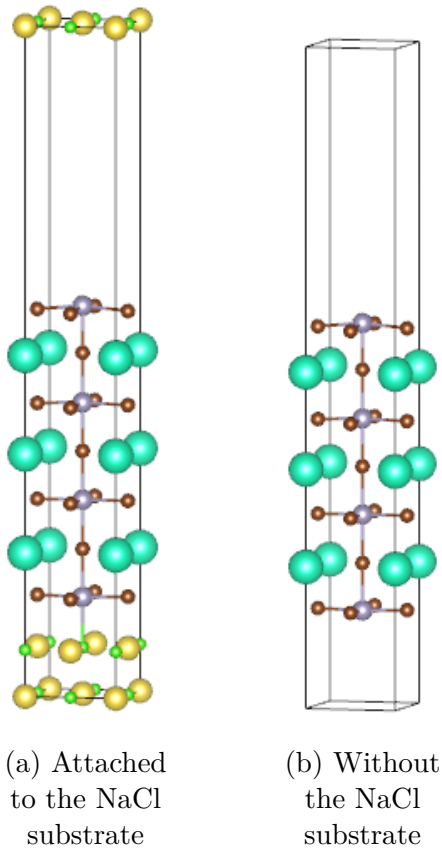


Figure 6.14: Unit cells of the cubic  $\text{CsSnBr}_3$  perovskite films having the thicknesses of 1.7 nm that are used to study effects of the  $\text{NaCl}$  substrate.

The atomic configuration result from the previous section is used in this study. Figure 6.14 shows the unit cells of the two films. The structures are relaxed using the PBE functional but the  $\text{NaCl}$  substrate is kept frozen similarly to that in the previous section. The perovskite films are composed of three layers of the  $\text{CsSnBr}_3$  cubic unit cell, resulting in the film thicknesses of 1.7 nm. Both unit cells are tetragonal unit cells with the same parameters;  $a = 5.64\text{\AA}$ ,  $b = 5.64\text{\AA}$  and  $c = 40.64\text{\AA}$ . The DFT calculation procedures that are described in Section 6.2.1 are applied to these systems, using  $E_{cut}$  of 300eV and k-point grids of 9x9x1 for band structure calculations and 17x17x2 for density of states calculations.

The band structure and DOS calculation results are shown in Figures 6.15 and 6.16.

There are higher number of non-degenerate bands as compared to the bulk result in Figure 6.7 because the unit cell is a super cell with distorted atomic positions that are caused by relaxations near the vacuum and the NaCl surfaces. The differences between the results of the films with and without the substrate can be categorized as follows.

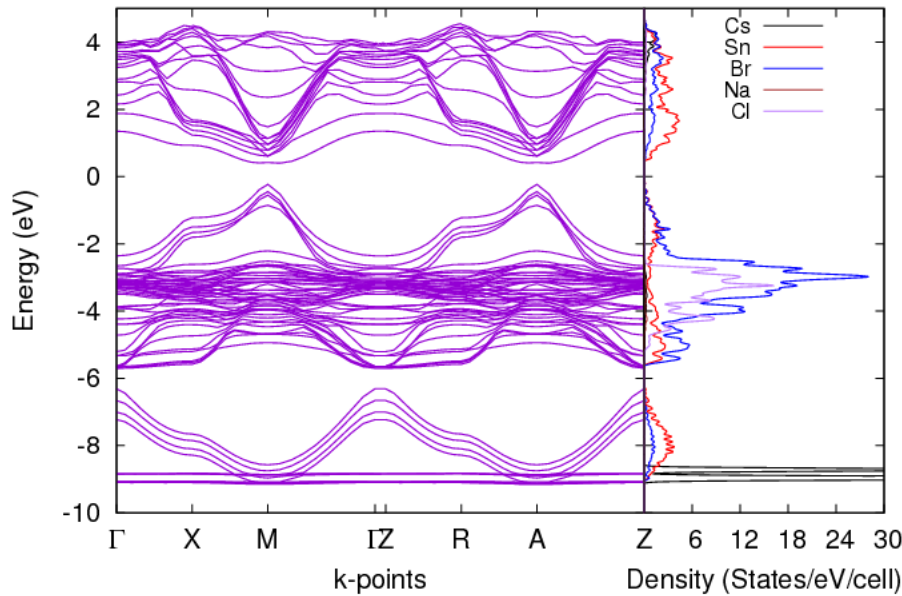


Figure 6.15: Band structure and PDOS functions of the  $\text{CsSnBr}_3$  film that is attached to the NaCl substrate, calculated using the PBE functional.

First, the NaCl substrate gives rise to additional bands around the energies -5 to -3 eV and around 4eV, with respect to the Fermi level at 0eV. The extra bands at the negative energies are contributed by the Cl 3p orbitals. The origins of the extra bands at the energy 4eV are not clear as the PDOS plot indicates that they arise from increased DOS's of Cs and Br. This may be caused by coulomb interactions at the interface and more insights are needed. Contributions from Na DOS can be seen around these bands, but they are negligibly small.

The extra bands do not noticeably change the original bands of  $\text{CsSnBr}_3$  and hence lead to a change of the band gap by only around 10meV, i.e. the energy gap of the film with the NaCl substrate is 0.633eV and the gap of the film without the substrate is 0.645eV. This is

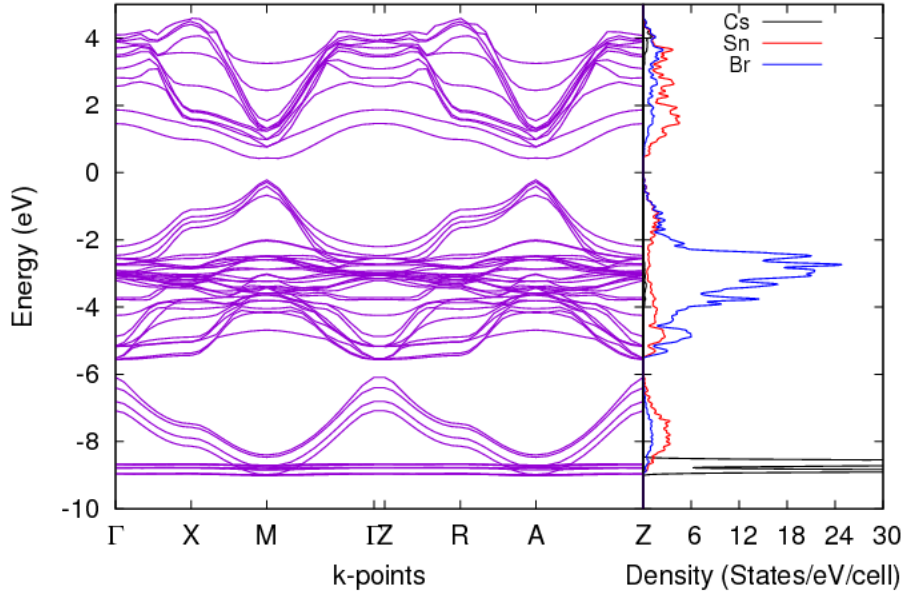


Figure 6.16: Band structure and PDOS functions of the  $\text{CsSnBr}_3$  film without the NaCl substrate, calculated using the PBE functional.

because NaCl crystals are formed by ionic bonding of full-shell  $\text{Na}^+$  and  $\text{Cl}^-$  ions, resulting in an insulating crystal with a very wide band gap of 8.97eV [160]. Hence, there should be no electron transfer or electron sharing at the  $\text{CsSnBr}_3/\text{NaCl}$  interface, so electronic structures of the  $\text{CsSnBr}_3$  film are almost unchanged.

We can see that the effects caused by the NaCl substrate are not very significant, even when the  $\text{CsSnBr}_3$  film is very thin. In the thick-film limit where the film is around 40 nm, properties of the samples should be of those the bulk perovskite and the substrate effects can be neglected.

## 6.5 $\text{CsSnBr}_3$ Film Growing Processes: Layer by Layer Deposition

Now we have the most probable atomic configuration at the  $\text{CsSnBr}_3/\text{NaCl}$  interface as shown in Figure 6.13, which has the unit cell as shown in Figure 6.14. This part of thesis shows the dynamics of the film growth processes based on that configuration, by simulating

depositions of the  $\text{CsSnBr}_3$  film; one atomic layer after another.

For the simulations, we use the two-step structural optimization that is described in Section 6.2.1 to relax the film structures until the total force acting on each atom is less than  $0.01 \text{ eV}/\text{\AA}$ . The unit cells are similar to that in Fig. 6.14, including a large vacuum space over the film. We allow all atoms to relax including Na and Cl atoms in the substrate, but the unit cells' shape and volume are fixed (ISIF = 2 in VASP) to represent the induced strain as a result of the lattice mismatch between the cubic  $\text{CsSnBr}_3$  crystal and the NaCl substrate.  $E_{cut}$  of  $340 \text{ eV}$  and k-point grid of  $8 \times 8 \times 2$  are used in all the simulations.

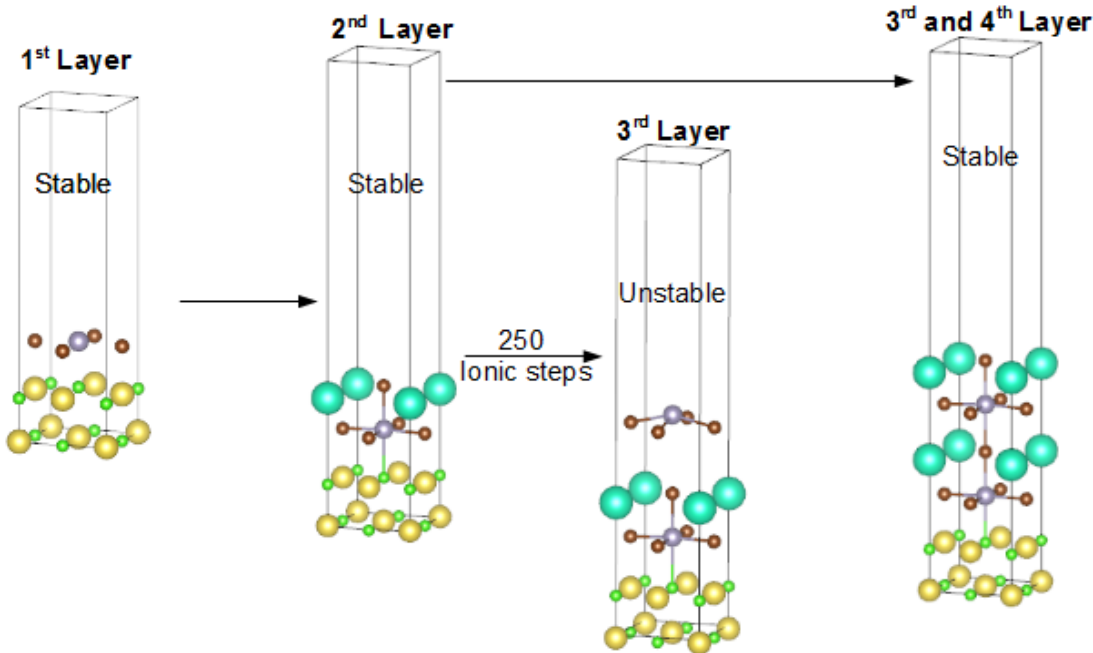


Figure 6.17: Simulation results of depositing atomic layers of  $\text{CsSnBr}_3$  onto the NaCl substrate. Na, Cl, Cs, Sn, Br atoms are represented by yellow, green, gray, purple and brown spheres, respectively.

Figure 6.17 shows the simulations results. For the first layer, a Sn atom is put on top of the Cl atom in the middle of the cell, and then Br atoms are placed over Na atoms at the edges of the unit cell. This first layer will result in the complete cubic  $\text{CsSnBr}_3$  structure as shown in Figures 6.13 and 6.14. Note that the Cl atoms at the corners of the unit cell are not covered by Sn atoms because these spaces will form cuboctahedral voids for Cs atoms.

Based on the simulation, this first  $\text{SnBr}_2$  layer attaches to the substrate and is stable.

For the second layer; which is an atomic layer of Cs and Br atoms, a Br atom is placed on top of the middle Sn atom of the first layer and forms a bond. Cs atoms are placed at the corners of the unit cell to fill the cuboctahedral voids. The relaxed structure; which is a sheet of  $\text{SnBr}_5\text{Cl}$  octrahedra attached to the  $\text{NaCl}$  substrate, is stable.

A surprising result is observed in the third layer, which is an atomic  $\text{SnBr}_2$  layer similar to the first layer. The structural relaxation does not converge to the required force even at the 250<sup>th</sup> ionic step, while the other relaxations usually converge within 50 ionic steps. The introduced layer is repelled from the film as shown in the Figure. However, if the third and the fourth layers are deposited simultaneously as shown by the rightmost structure in Fig. 6.17. The structure is stable, and the convergence of the relaxation is obtained. The most probable explanation is that, in cubic  $\text{CsSnBr}_3$  perovskites, Sn and Br atoms bond with each other and form the octahedron scaffold. If the octahedra are incomplete (e.g. the third layer situation), the bonds' strength may be less than those of the complete one (e.g. the third and the fourth layers together), so a coulomb repulsion dominates and repels the layer.

Figure 6.18 shows another situation that can occur for the third layer. Instead of depositing the same  $\text{SnBr}_2$  layer as the first layer that covers only half of the Cl atoms, we deposit a  $\text{SnBr}$  layer that cover all atoms of the layer beneath it. This full-cover  $\text{SnBr}$  layer results in a surprising outcome, as it attaches and is stable. However, if other layers can attach on top of this layer, the structure will not cubic  $\text{CsSnBr}_3$  anymore. We try a couple of atomic configurations for the fourth layer after the full-cover  $\text{SnBr}$  layer (see Figure 6.18 for example), but they do not form a bond or attach to the third  $\text{SnBr}$  layer.

In conclusion, we simulate the film growing processes in this section and arrive at two interesting results. First, the deposited film has to form complete octahedra  $\text{SnBr}_6$  layers in order to from cubic perovskite, or, second, other more energetically favorable layers like the full-cover  $\text{SnBr}$  layer in the third layer may form and cause a phase transition.

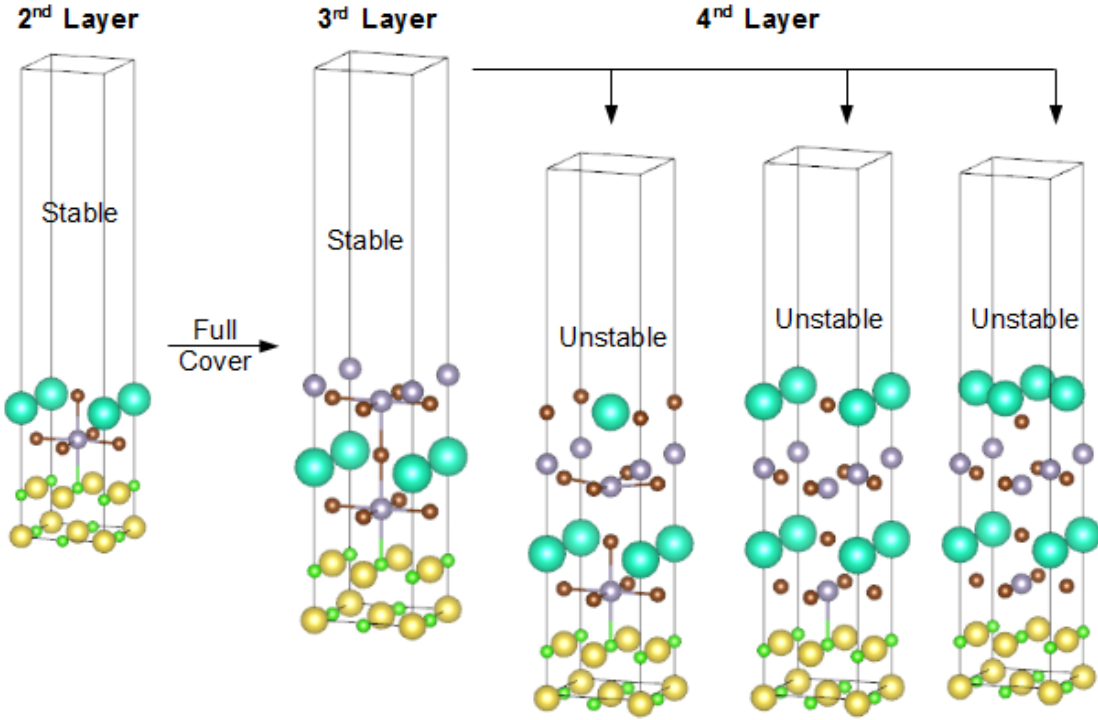


Figure 6.18: Simulation results showing film deposition processes after the third full-cover SnBr layer. Na, Cl, Cs, Sn, Br atoms are represented by yellow, green, gray, purple and brown spheres, respectively.

## 6.6 Useful Research Directions : Heteroepitaxy, Critical Thickness and Phase Transition

Heteroepitaxy, which is the technique of growing a crystal film of one material on a crystal substrate of another material used in this study, usually leads to a lattice mismatch between the film and the substrate and a mismatch (or misfit) strain. The misfit strain ( $f$ ) is defined by [161]

$$f = \frac{a_s - a_e}{a_e}, \quad (6.5)$$

where  $a_s$  and  $a_e$  are the lattice constants of the substrate and the epitaxial film, respectively. The strain can be a tensile strain ( $a_s > a_0$ ;  $f > 0$ ) or a compressive strain ( $a_s < a_0$ ;  $f < 0$ ) [161]. In the present study, the relaxed lattice constant of  $\text{CsSnBr}_3$  in the cubic phase is  $5.888\text{\AA}$ , and  $\text{NaCl}$  has the lattice constant of  $5.64\text{\AA}$ , resulting in a misfit strain of  $-4.21\%$ . This strain is not very high, so the first several layers of the epitaxial  $\text{CsSnBr}_3$  film are

pseudomorphic, i.e. they match their in-plane lattice constant with that of the substrate and adjust their out-of-plane lattice constant accordingly. The pseudomorphic layers can be grown until the film thickness reaches a critical thickness where atom dislocations (or misfit dislocations) occur to reduce the strain energy [161], after which the film lattice approaches its natural states. In a similar perovskite system [162], an epitaxial film of  $\text{LaAlO}_3$  is grown on a  $\text{SrTiO}_3(100)$  substrate, resulting in a lattice mismatch of -3.17% and a critical thickness of 3.8 nm.

Based on the physics of heteroepitaxy and the results we find in Section 6.5, there seems to be a connection between the misfit strain and the transition from  $\text{CsSnBr}_3$  to  $\text{CsSn}_2\text{Br}_5$ . Studying this relation is crucial to understanding physics of the phase transition and the  $\text{CsSnB}_3/\text{CsSn}_2\text{Br}_5$  interface. Here, we suggest the following steps for future work. First, total and surface energies of a  $\text{CsSnBr}_3/\text{NaCl}$  sample as a function of the  $\text{CsSnBr}_3$  thickness can be calculated using DFT to find the critical thickness, and then this thickness is compared to experimental thicknesses at which transitions occur. Secondly, the interface between  $\text{CsSnBr}_3$  and  $\text{CsSn}_2\text{Br}_5$  can be studied directly by first finding surface configurations that bring about the lowest energies in the two materials. The two surfaces are then taken into contact, and the total energy can be calculated. With information of crystal orientations from experiments, the correct interface configuration can be predicted.

## 6.7 Conclusions

In this chapter, we present our numerical studies regarding growing of cubic  $\text{CsSnBr}_3$  perovskite films on  $\text{NaCl}(100)$  substrates using a vapor phase epitaxy technique. Based on experimental measurements of band gap and lattice constants, the hypothesis is that the cubic  $\text{CsSnBr}_3$  perovskite undergoes a phase transition to  $\text{CsSn}_2\text{Br}_5$ . We test this hypothesis by simulating electronic band structures using DFT with the PBE and the HSE06 functionals. The results indicate that  $\text{CsSn}_2\text{Br}_5$  has an energy gap of around 3.6 - 3.8eV, which agrees with the experimental band gaps and its transparency. Therefore, it is likely that the

hypothesis is true.

We also study interface between the NaCl substrate and CsSnBr<sub>3</sub>. Considering adsorption energies of the precursor atoms reveals that CsSnBr<sub>3</sub> attaches to the substrate through bondings between Sn atoms and surface Cl atoms. This configuration is then used to study effects of the substrate on electronic properties of the film. The results show that the effects are not significant and can be negligible in the thick-film limit.

Finally, the film growing processes are studied by simulating depositions of CsSnBr<sub>3</sub> atomic layers onto the NaCl substrate, one layer at a time. Structural relaxation calculations confirm that several layers of the cubic CsSnBr<sub>3</sub> perovskite can be stably grown on the NaCl(100) surface, but the film may be unstable if the topmost layer does not form complete SnBr<sub>6</sub> octahedra. This may be the origin of the phase transition and can be a topic of future studies.

## CHAPTER 7

### CONCLUSIONS AND OUTLOOKS

#### 7.1 Conclusions

Working principles of bilayer organic photovoltaics (OPVs) and electronic properties of an epitaxial  $\text{CsSnBr}_3$  perovskite film are the focuses of this dissertation.

For bilayer OPVs, we developed the DD-BI model, which is a numerical model in the form of a computer software, to simulate fundamental mechanisms of bilayer OPVs and the SCD equations, which are analytic equations that can describe results from the DD-BI model. These models are based on the GWWF model, which is a diode equation model bilayer OPVs. We consider three types of carrier recombination: free-carrier to free-carrier (f-f) (or bimolecular) recombination; free-carrier to trapped-charge (f-t) recombination; and the Shockley-Read-Hall (SRH) recombination. The SCD equations are in the same form as the Shockley diode equation, which is universally used to fit current-voltage (JV) curves of solar cells resulting in fitting parameters: series and parallel resistances ( $R_s$  and  $R_p$ ); ideality factor ( $n$ ); and diode saturation current ( $J_0$ ). Together with short-circuit current ( $J_{sc}$ ), open-circuit voltage ( $V_{oc}$ ) and fill factor (FF), these parameters are figures of merit of solar cells.

The DD-BI and the SCD models were shown to be extensions of the GWWF model to include space charge effects, correct physical definitions of  $R_s$  and self-consistent interface properties. A drawback of the GWWF model is that it estimates interface charge densities using relations in terms of empirical potential drops across the donor and the acceptor that do not include space charge effects and cancel out the definition of  $R_s$  in the derivation. The GWWF model does not show space charge accumulation around the interface and results in overestimations of interface electric field and polaron pair dissociation rate and efficiency ( $k_{PPd}$  and  $\eta_{PPd}$ ).

In Section 4.2, we studied influences of carrier mobilities on space charge accumulation

and quasi-Fermi levels (chemical potentials). We find that space charge accumulation around the interface raises electron quasi-Fermi energy ( $E_{fn,I}$ ) in the accepter and reduces hole quasi-Fermi energy ( $E_{fp,I}$ ) in the donor, resulting in a split of quasi-Fermi energies ( $E_{fn,I} - E_{fp,I}$ ) at the interface. This split is a driving potential of the interface recombination and can be defined as the diode voltage ( $V_d$ ); which equals to  $V_a - JR_s$ . Hence, the definition of  $R_s$  is obtained as the total change of quasi-Fermi energies from the electrodes to the interface divided by the total current density. The degrees of charge accumulation and quasi-Fermi energy splitting increase with reducing mobilities, giving rise to greater values of  $R_s$ . Parallel resistance under illumination conditions is also studied. It is a recombination resistance of the recombined exciton current ( $qJ_X(1 - \eta_{PPd})$ ). Higher accumulation of charge caused by low mobilities results in a higher recombination rate and higher  $qJ_X(1 - \eta_{PPd})$ , which is represented by lower recombination resistance ( $R_p$ ) values. This agrees with the conventional picture of  $R_p$  as a shunt path for a leakage current, but  $qJ_X(1 - \eta_{PPd})$  is the actual leakage current of bilayer OPVs under illumination.

In Sections 4.3 and 4.4 we studied effects of injection barriers, which are defined as the differences between the electrode work functions and the donor HOMO energy and the acceptor LUMO energy. High injection barriers cause s-shaped JV behaviors, resulting in lower  $J_{sc}$  and FF values, but they do not significantly affect  $V_{oc}$  as interface charge densities and interface quasi-Fermi levels are not significantly affected. Interestingly, injection barriers smaller than about 0.3 eV do not have any noticeable effects on JV curves. The reason behind this is quasi-Fermi level pinning due to charge transfer between the active layers and the electrodes, which can be explained by the integer charge transfer (ICT) model. If the cathode work function is between the acceptor LUMO level and the acceptor  $E_{fn}$ , charge transfer from the cathode to  $E_{fn}$  occurs and the quasi-Fermi level is pinned, and *vice versa* for the anode work function that sits between the donor HOMO level and the donor  $E_{fp}$ . If the electrodes' work functions are out of these ranges, charge transfer does not occur, and quasi-Fermi levels drop across the contacts, giving rise to extra components of  $R_s$ .

In Section 4.5, relations between ideality factors and trap characteristics are studied. In general, ideality factors depend on  $E_{fn,I} - E_{fp,I}$  and the ratio of recombination rate to recombination rate at equilibrium. In terms of interface quasi-Fermi energies, ideality factors indicate deviations of  $E_{fn,I}$  and  $E_{fp,I}$  from the equilibrium Fermi energy. These mechanisms can result in ideality factor values of around 1-2 which can be used as rough indicators of trap characteristics. However, actual relations between ideality factors and traps are complicated, and interpretations of fitted ideality factors have to be careful. For example, a total current may be composed of many currents from different trap-assisted recombination types, each of which has a different ideality factor and may not be the same as that of the total current, so deducing a trap characteristic energy (Urbach tail energy) value from the fitted ideality factor is likely misleading. Furthermore, we show that our ideality factor equations are general forms of a famous definition of ideality factor.

In Section 4.6, the SRH recombination is compared with the f-t recombination, which is understood as a reduced form of the SRH recombination. According to the results, even though their recombination rates are comparable at voltage lower than  $V_{oc}$ , they are actually different processes, because the SRH recombination includes capturing of free carriers by unoccupied trap states into account, while the f-t recombination does not. The differences are clearer at voltage higher than  $V_{oc}$  when many more free carriers are injected. The f-t recombination rate reduces because traps cannot capture the injected charges, but the SRH recombination increases as the injected charges can fill empty trap states.

In Chapter 5, we apply the DD-BI and the SCD models to describe an experimental JV curve of a cyanine organic salt solar cell. The JV curve has an interesting kink-shaped behavior under dark conditions that is caused by a leakage current. However, the definition of leakage current under illumination conditions as  $qJ_X(1 - \eta_{PPd})$  does not apply in the dark where  $J_X = 0$ , so we include another mechanism for the dark leakage current. Two processes are proposed: (1) recombination between localized states; (2) using an empirical dark  $R_p$  as a constant in the standard Shockley form. The two processes are in reasonable

agreement with the experimental results in the positive voltage regime. Hence, the total  $R_p$  value is the total resistance of dark  $R_p$  and illumination  $R_p$  that are connected in parallel. Under illumination conditions, illumination  $R_p$  dominates the total  $R_p$  because illumination  $R_p$  values are much lower than dark  $R_p$  values. In the dark, dark  $R_p$  is the only process that governs interface leakage current, so it becomes dominant. We also study differences between Shockley parameters under illumination and dark conditions. The results show that only  $J_0$  can be used interchangeably between the two conditions because it depends on intrinsic properties that are not affected by illumination. On the other hand,  $R_s$ , n and most importantly  $R_p$  between the two conditions can be different by orders of magnitude. Using extracted parameters from one condition to describe devices under the other conditions results in misinterpretations and errors.

In Chapter 6 we focus on electronic properties of an epitaxial  $\text{CsSnBr}_3$  film that is grown on a  $\text{NaCl}(100)$  substrate using a vapor phase heteroepitaxy technique.  $\text{CsSnBr}_3$  is stable in a black cubic phase at room temperature and has a band gap of around 1.8 eV. Growing a  $\text{CsSnBr}_3$  film using the technique results in a colorless film with a band gap of around 3.3 - 3.5 eV in the thick-film limit, which is hypothesized to be  $\text{CsSn}_2\text{Br}_5$ . Band structure calculations using DFT show that  $\text{CsSn}_2\text{Br}_5$  is a wide band gap semiconductor with an agreeable estimated band gap with the experimental result, and thus the film is likely  $\text{CsSn}_2\text{Br}_5$ . We also study atomic configurations at the interface between the  $\text{NaCl}$  substrate and  $\text{CsSnBr}_3$  and effects of the  $\text{NaCl}$  substrate on the growth film. The result is that the  $\text{NaCl}$  substrate does not significantly affect electronic properties of the grown film. Finally, we consider the growth process of a  $\text{CsSnBr}_3$  film and find that a phase transition to  $\text{CsSn}_2\text{Br}_5$  is possible if the topmost layer of the  $\text{CsSnBr}_3$  film does not form a complete octahedron structure of  $\text{SnBr}_6$ .

## 7.2 Outlook

For OPVs, there are many possibilities for future research. First, a more accurate description of dark leakage current is needed. We suggest including a trap-assisted tunneling process for the leakage current. Second, at the present, the research community tends to go toward perovskite solar cells for the next generation of solar cell. Many efficient perovskite solar cells are based on bilayer structures. Hence, it is interesting to adapt the DD-BI and the SCD models for bilayer perovskite solar cells. Additionally, due to the fact that the true bilayer organic interface is difficult to achieve because of fast interpenetration between the donor and the acceptor, our models can be modified to have a bulk-heterojunction region around the interface for better descriptions of bilayer OPVs.

For  $\text{CsSnBr}_3$  perovskite, the interface between  $\text{CsSnBr}_3$  and  $\text{CsSn}_2\text{Br}_5$  and the conditions under which the phase transition occurs are interesting directions.  $\text{CsSn}_2\text{Br}_5$  is not suitable for photovoltaic applications because of the wide band gap. Hence, understanding the transition conditions is important to determine the film growth conditions that result in a more perfect cubic  $\text{CsSnBr}_3$  crystal. Additionally, according to the Shockley-Queisser limits, the optimal band gap for single-junction solar cells is around 1.3 eV. Tuning the CBM and the VBM to optimize band gap of  $\text{CsSnBr}_3$  using a doping process is an interesting study and can be done using DFT simulations.

## **APPENDIX**

## APPENDIX

### QUANTUM MECHANICS BACKGROUND FOR *AB INITIO* CALCULATIONS

This appendix provides an overview of quantum mechanics necessary to understand some important basics of *ab initio* calculations. Although the Schrodinger equation can accurately describe atomic systems, solving the equation for an exact solution is difficult in practice, as stated by Dirac four years after the advent of the Schrodinger equation:

*"The underlying physical laws necessary for the mathematical theory of a large part of physics and the whole of chemistry are thus completely known, and the difficulty is only that the exact application of these laws leads to equations much too complicated to be soluble. It therefore becomes desirable that approximate practical methods of applying quantum mechanics should be developed, which can lead to an explanation of the main features of complex atomic systems without too much computation".*

— P. A. M. Dirac, *Proc. R. Soc. Lond. A* **123**, 714 (1929)

Hence, approximations are needed to deduce useful information from the equation. One of the most preferred approximations, which is used in this study, is density functional theory (DFT). The main principle of DFT is that total energy of a system is treated as a functional of charge density instead of wave function.

In order to introduce to DFT, the Schrodinger equation for many-body systems, the Born - Oppenheimer approximation, the Hartree-Fock (HF) approximation and the Kohn-Sham DFT have to be introduced first. The latter can be considered as the basis of current atomistic DFT simulations. Beyond this overview, in-depth discussions of the theories can be found in quantum chemistry books and review papers, for example, the book by David Sholl and Janice Steckel [163], which is an introduction to the HF theory, and the book by Szabo and Ostlund [164]. The narrative review paper *Nobel Lecture* by W. Kohn [165] who

is the founder of modern DFT is also recommended. For more thorough reviews, see the papers by Jones and Gunnarsson[166] and by Geerlings *et al.*[167].

## A.1 The Schrodinger Equation and the Born-Oppenheimer Approximation

The primary goal of computational quantum calculations is to have the most accurate solution for the time-independent, non-relativistic Schrodinger equation of many-body systems. Consider a system of  $M$  nuclei with masses  $M_A$  and charges  $Z_A$  at positions  $\vec{R}_A$  and  $N$  electrons with spin coordinates  $\omega_i$  at positions  $\vec{r}_i$ . Let  $\vec{x}_i = \{\vec{r}_i, \omega_i\}$  denote the set of the four coordinates necessary to describe the electron  $i$ . The Schrodinger equation can be written as

$$\hat{H}\Psi(\vec{x}_1, \dots, \vec{x}_n, \vec{R}_1, \dots, \vec{R}_M) = E\Psi(\vec{x}_1, \dots, \vec{x}_n, \vec{R}_1, \dots, \vec{R}_M), \quad (\text{A.1})$$

where the Hamiltonian is

$$\hat{H} = -\frac{1}{2} \sum_{i=1}^N \nabla_i^2 - \frac{1}{2} \sum_{A=1}^M \frac{1}{M_A} \nabla_A^2 - \sum_{i=1}^N \sum_{A=1}^M \frac{Z_A}{r_{iA}} + \sum_{i=1}^N \sum_{j>i}^N \frac{1}{r_{ij}} + \sum_{A=1}^M \sum_{B>A}^M \frac{Z_A Z_B}{R_{AB}}. \quad (\text{A.2})$$

The Hamiltonian is written in atomic units where the electron mass ( $m_e$ ), the elementary charge ( $q$ ), the factor  $4\pi\epsilon_0$  and the reduced Planck's constant ( $\hbar$ ) are set to 1. There are five energy terms in the Hamiltonian. The first two terms are kinetic energies of the electrons and the nuclei. The third term represents attractive electrostatic potentials between the electrons and the nuclei. The fourth and fifth terms are repulsive electron-electron and nucleus-nucleus electrostatic potentials, respectively.

According to the Born-Oppenheimer approximation, nuclei are much heavier and move much slower than electrons, so nuclei can be considered stationary. As a result, the nuclear kinetic energy in the second term can be neglected, and the total nucleus-nucleus repulsive potential can be considered as a constant;  $E_{nuc} = \sum_{A=1}^M \sum_{B>A}^M \frac{Z_A Z_B}{R_{AB}}$ , which can be separated from the Hamiltonian. The remaining terms depend only on electrons' positions, and

we can write the electron Hamiltonian ( $\hat{H}_{el}$ ) as

$$\hat{H}_{el} = -\frac{1}{2} \sum_{i=1}^N \nabla_i^2 - \sum_{i=1}^N \sum_{A=1}^M \frac{Z_A}{r_{iA}} + \sum_{i=1}^N \sum_{i < j}^N \frac{1}{r_{ij}} = \hat{T} + \hat{V}_{Ne} + \hat{V}_{ee}. \quad (\text{A.3})$$

Thus, the total energy of the Schrodinger equation in Eq. A.1 is reduced to  $E_{total} = E_{el} + E_{nuc}$ , where  $E_{el}$  is total electron energy from the relation;

$$\hat{H}_{el} \Psi_{el} = E_{el} \Psi_{el}, \quad (\text{A.4})$$

where  $\Psi_{el}$  is the electronic wave function.

## A.2 Hartree-Fock Approximation

As a result of the Born-Oppenheimer approximation, the electron wave function  $\Psi_{el}$ ; which has to be antisymmetric, is sought for. One way to describe the antisymmetric ground state wave function ( $\Psi_{el,0}$ ) is using the Slater determinant;

$$\Psi_{el,0} = \frac{1}{\sqrt{N!}} \begin{vmatrix} \chi_1(\vec{x}_1) & \chi_2(\vec{x}_1) & \cdots & \chi_N(\vec{x}_1) \\ \chi_1(\vec{x}_2) & \chi_2(\vec{x}_2) & \cdots & \chi_N(\vec{x}_2) \\ \vdots & \vdots & & \vdots \\ \chi_1(\vec{x}_N) & \chi_2(\vec{x}_N) & \cdots & \chi_N(\vec{x}_N) \end{vmatrix}, \quad (\text{A.5})$$

where  $\chi_i(\vec{x}_j)$  are orthogonal *spin orbitals*, which are a product of spatial orbitals  $\psi_i(\vec{r}_j)$  and a spin function;  $\alpha(\omega)$  (spin up) or  $\beta(\omega)$  (spin down). This formulation of  $\Psi_{el,0}$  satisfies the antisymmetry because an interchange between any two sets of the spatial-spin coordinates  $\vec{x}$  results in  $-\Psi_{el,0}$ . Note that the Pauli exclusion principle, which does not allow two electrons to have exactly the same set of  $\vec{x}$ , is already included in the antisymmetry. Using the Hamiltonian in Equation A.3 and the *variational principle*, a trial function of the Slater determinant can be minimized so that  $\Psi_{el,0}$  is obtained.

The Hartree-Fock approximation states that there exists a set of orthogonal spin orbitals that minimizes the energy, and hence the ground state Hartree-Fock wave function is found

(i.e.  $\Psi_{HF} = \Psi_{el,0}$ ). The Hamiltonian in Eq. A.3 can be written as a summation;

$$\hat{H}_{el} = \sum_{i=1}^N \left( -\frac{1}{2} \nabla_i^2 - \sum_{A=1}^M \frac{Z_A}{r_{iA}} + \sum_{i < j} \frac{1}{r_{ij}} \right). \quad (\text{A.6})$$

Using this form of the Hamiltonian and the orthogonality of spin orbitals;  $\int \chi_i^*(\vec{x}) \chi_j(\vec{x}) d\vec{x} = \delta_{ij}$ , the electron energy can be calculated;  $E_{el} = \langle \Psi_{HF} | \hat{H}_{el} | \Psi_{HF} \rangle$ . This results in the Hartree-Fock differential equations;

$$\hat{f} \chi_i = \epsilon_i \chi_i, \quad i = 1, 2, \dots, N \quad (\text{A.7})$$

where  $\hat{f}$  is the *Fock operator* which is expressed by

$$\hat{f} = -\frac{1}{2} \nabla_i^2 - \sum_{A=1}^M \frac{Z_A}{r_{iA}} + V_{HF}(\vec{x}_i), \quad (\text{A.8})$$

where  $V_{HF}(\vec{x}_i)$  is the Hartree-Fock potential which is given by

$$V_{HF}(\vec{x}_i) = \sum_{j \neq i}^N (\hat{J}_j(\vec{x}_i) - \hat{K}_j(\vec{x}_i)). \quad (\text{A.9})$$

The operator  $\hat{J}_j(\vec{x}_i)$ , which is called *the Coulomb operator*, represents a repulsive potential perceived by an electron at  $\vec{x}_i$  due to the distribution of other electrons at  $\vec{x}_j$ . The operator is given by  $\hat{J}_j(\vec{x}_1) = \int |\chi_j(\vec{x}_2)|^2 r_{12}^{-1} d\vec{x}_2$ . The operator  $\hat{K}_j(\vec{x}_i)$ , which is called *the exchange term*, has no meaning in the classical sense but arises mathematically from the Hartree-Fock approximation. When it operates onto a spin orbital, it is defined by  $\hat{K}_j(\vec{x}_1) \chi_i(\vec{x}_1) = \int \chi_j^*(\vec{x}_2) r_{12}^{-1} \chi_i(\vec{x}_2) d\vec{x}_2 \chi_j(\vec{x}_1)$ .

The essence of the Hartree-Fock approximation is that instead of dealing with the many-body Schrodinger equation, each electron can be treated independently under averaged influences of the nuclei (the  $2^{nd}$  term in Equation A.8) and other electrons (through  $V_{HF}$ ). In other words, the atomic system is reduced to non-interacting electron systems in a mean potential field, which can be solved self-consistently.

### A.3 Density Functional Theory

The theory that kindled the idea behind DFT was the Thomas-Fermi (TF) model of electron gas, which results in an expression for total kinetic energy of electrons in terms of spatial

electron density ( $n(\vec{r})$ ). Hohenberg and Kohn (HK) then derived the first theorem of DFT with the purpose of using  $n(\vec{r})$  instead of wave function  $\Psi$  in solving the Schrodinger equation. The theorem states that the ground-state Hamiltonian and energy of the Schrodinger equation are unique functionals of electron density[168]. Two keywords that have to be understood here are "unique" and "functional". The former means that it is not possible for different systems with different Hamiltonians to have the same ground state  $n(\vec{r})$ . Hence, a ground state electron density can be used to find  $\hat{H}_{el}$  and  $\Psi_{el}$ . For the latter, an energy functional, which is usually written as  $E[n(\vec{r})]$ , takes the entire vector field  $n(\vec{r})$  as an input and gives a scalar field of energy as an output.

In the same paper by Hohenberg and Kohn[168], they also show that  $E[n(\vec{r})]$  obeys the variational principle, so minimizing  $E[\tilde{n}(\vec{r})]$  where  $\tilde{n}(\vec{r})$  is any trial electron density will yield the ground state energy:

$$E_0 = \min_{\tilde{n}(\vec{r})} E[\tilde{n}(\vec{r})]. \quad (\text{A.10})$$

Consequently, the energy functional can be written similarly to the Hamiltonian in Equation A.3 as

$$E[n(\vec{r})] = T[n(\vec{r})] + E_{ee}[n(\vec{r})] + E_{Ne}[n(\vec{r})] = F_{HK}[n(\vec{r})] + E_{Ne}[n(\vec{r})]. \quad (\text{A.11})$$

The kinetic energy functional ( $T[n(\vec{r})]$ ) and the electron-electron potential functional ( $E_{ee}[n(\vec{r})]$ ) are usually combined together as the Hohenberg-Kohn functional  $F_{HK}[n(\vec{r})]$ . The term  $E_{Ne}[n(\vec{r})]$  is the nucleus-electron potential energy functional that can be expressed through

$$E_{Ne}[n(\vec{r})] = \int n(\vec{r}) V_{Ne}(\vec{r}) d\vec{r}, \quad (\text{A.12})$$

where the nucleus-electron potential  $V_{Ne}(\vec{r})$  is sometimes called external potential ( $V_{ext}(\vec{r})$ ). Note that  $E[n(\vec{r})]$  in Eq. A.11 is still exact.  $F_{HK}[n(\vec{r})]$  is a universal functional that is absolutely invariant from system to system. If it was known, DFT could solve any problems for the exact ground state energies. Unfortunately, its expression is not known exactly.  $E_{ee}[n(\vec{r})]$  can be written in terms of the classical coulomb interaction ( $J[n(\vec{r})]$ ) and a non-

classical coulomb interaction ( $E_{ncl}[n(\vec{r})]$ ) as;

$$E_{ee}[n(\vec{r})] = J[n(\vec{r})] + E_{ncl}[n(\vec{r})], \quad \text{where } J[n(\vec{r})] = \frac{1}{2} \int \int \frac{n(\vec{r})n(\vec{r}')}{|\vec{r}-\vec{r}'|} d\vec{r}d\vec{r}'. \quad (\text{A.13})$$

## A.4 Kohn-Sham Equations

Inspired by the non-interacting electron system in the Hartree-Fock formalism, Kohn and his post-doc L. Sham overcame the unavailability of  $F_{HK}[n(\vec{r})]$  by introducing the fictitious Kohn-Sham (KS) system[169]. It is a system of non-interacting particles that can be described by the Kohn-Sham orbitals ( $\phi_i$ ) and obeys the following single-particle Schrodinger equation;

$$\hat{h}_{KS}\phi_i(\vec{r}) = \left( -\frac{1}{2}\nabla^2 + V_{KS}(\vec{r}) \right) \phi_i(\vec{r}) = \epsilon_i \phi_i(\vec{r}), \quad (\text{A.14})$$

where  $\hat{h}_{KS}$  is the single-particle Kohn-Sham Hamiltonian,  $V_{KS}(\vec{r})$  is the Kohn-Sham potential and  $\epsilon_i$  is the orbital energy of the KS orbital  $\phi_i(\vec{r})$ . With the following constraints of total energy and particle density;

$$E = \sum_{i=1}^N \epsilon_i, \quad n(\vec{r}) = \sum_{i=1}^N |\phi_i(\vec{r})|^2, \quad (\text{A.15})$$

where  $E$  and  $n(\vec{r})$  are the same as those in the original electron system, one can solve the Kohn-Sham equations for the ground state properties.

The question is: What should the KS potential be? First, the HK functional ( $F_{HK}[n(\vec{r})]$ ) is rewritten as

$$F_{HK}[n(\vec{r})] = T_S[n(\vec{r})] + J[n(\vec{r})] + E_{XC}[n(\vec{r})], \quad (\text{A.16})$$

where  $T_S[n(\vec{r})]$  is the Kohn-Sham kinetic energy, which is given by

$$T_S[n(\vec{r})] = \sum_{i=1}^N \langle \phi_i | \frac{1}{2} \nabla^2 | \phi_i \rangle, \quad (\text{A.17})$$

$J[n(\vec{r})]$  is the classical Coulomb interaction in Eq. A.13, and  $E_{XC}[n(\vec{r})]$  is the *exchange-correlation* functional. The **Exchange energy** refers a reduction of Coulomb energy from spatial separations of electrons with the same spin, and the **correlation energy** refers to

the energy difference between the actual many-body system and the one that is calculated by the Hartree-Fock approximation[170].  $E_{XC}[n(\vec{r})]$  also contains all unknown or additional functionals.

Using the new  $F_{HK}[n(\vec{r})]$  in the Euler-Lagrange equation[167];

$$V_{Ne}(\vec{r}) + \frac{\delta F_{HK}[n(\vec{r})]}{\delta n(\vec{r})} = V_{KS}(\vec{r}) + \frac{\delta T_S[n(\vec{r})]}{\delta n(\vec{r})}, \quad (\text{A.18})$$

we have

$$V_{KS}(\vec{r}) = V_{Ne}(\vec{r}) + \int \frac{n(\vec{r}')}{|\vec{r} - \vec{r}'|} d\vec{r}' + V_{XC}(\vec{r}), \quad (\text{A.19})$$

where the exchange correlation potential ( $V_{XC}(\vec{r})$ ) is a functional derivative in the form

$$V_{XC}(\vec{r}) = \frac{\delta E_{XC}[n(\vec{r})]}{\delta n(\vec{r})}. \quad (\text{A.20})$$

With  $V_{KS}(\vec{r})$  in Eq. A.19, Equations A.14 become the Kohn-Sham equations.

## A.5 Exchange-Correlation Functionals

Based on the previous discussion about the Kohn-Sham DFT, the exchange-correlation (XC) term in Eq. A.20 is the only term that has no explicit expression and has to be approximated. There are many classes and many functionals within a class. The Perdew-Burke-Ernzerhof (PBE) functional [151], which belongs to the generalized gradient approximation (GGA) class, is used mainly in this work. It does not require a lot of computational resources but provides moderate accuracy. However, it usually underestimates energy gaps. The HSE06 function[152, 171], which is a hybrid XC functional, is also included in this work. The following are brief explanations of these functionals.

### A.5.1 The PBE functional

The local density approximations (LDA) are the simplest approximations for the XC functional. The principle is that electrons are considered as a homogeneous electron gas with density  $n(\vec{r})$ . Assuming that the homogeneous XC energy per electron is  $\epsilon_{XC}(\vec{r}) = \epsilon_{XC}^{hom}[n(\vec{r})]$ ,

the XC energy functional is given by

$$E_{XC}^{LDA}[n(\vec{r})] = \int n(\vec{r})\epsilon_{XC}(\vec{r})d\vec{r}. \quad (\text{A.21})$$

Even though it is based on local approximations [170] and is not highly accurate, it is overwhelmingly successful and is the basis of more sophisticated functionals.

Including electron spins in the LDA yields the local spin density approximations (LSDA), and the XC functional is given by

$$E_{XC}^{LSDA}[n_{\uparrow}(\vec{r}), n_{\downarrow}(\vec{r})] = \int n(\vec{r})\epsilon_{XC}(n_{\uparrow}, n_{\downarrow})d\vec{r}. \quad (\text{A.22})$$

The generalized gradient approximations (GGA) take another step further than the LSDA by including inhomogeneities of  $n(\vec{r})$  about  $\vec{r}$  in terms of gradients of the spin density. Perdew-Burke-Ernzerhof[151] approach this approximation by adding a correction term  $H(n_{\uparrow}, n_{\downarrow}, \nabla n)$  to the homogeneous exchange functional  $\epsilon_X^{homo}(n_{\uparrow}, n_{\downarrow})$ , which finally results in

$$E_{XC}^{PBE}[n_{\uparrow}(\vec{r}), n_{\downarrow}(\vec{r})] = \int n(\vec{r})\epsilon_X^{homo}[n(\vec{r})]F_{XC}[n(\vec{r}), \nabla n(\vec{r})]d\vec{r}, \quad (\text{A.23})$$

where  $F_{XC}$  is an enchantment factor.

### A.5.2 Hybrid Functionals

As an effort to increase the accuracy beyond the GGA approximations, a certain amount of Hartree-Fock (HF) exact exchange energy is included, resulting in a hybrid functional. One example of hybrid functionals is the PBE0 functional [172], which treats the exchange-correlation energy ( $E_{xc}$ ) as

$$E_{xc}^{PBE0} = \frac{1}{4}E_x^{HF} + \frac{3}{4}E_x^{PBE} + E_c^{PBE}, \quad (\text{A.24})$$

where the exchange energy is a mixture of PBE and HF exchange energies in a ratio of 3:1, but the correlation energy is taken to be the PBE result. This full-range (or global) hybrid functional is usually expensive and difficult to converge, and often overestimates band gaps of materials [173].

Heyd-Scuseria-Ernzerhof (HSE) [152, 171] propose a hybrid functional that includes effects of screened Coulomb potential by separating the Coulomb operator into short-range (SR) and long-range (LR) parts. The resulting XC energy ( $E_{xc}^{HSE06}$ ) is given by

$$E_{xc}^{HSE06} = \frac{1}{4}E_x^{HF,SR}(w) + \frac{3}{4}E_x^{PBE,SR}(w) + E_x^{PBE,LR} + E_c^{PBE}, \quad (\text{A.25})$$

where  $w$  is an adjustable parameter determining the range of the short-range part. According to the equation, the short-range part of the exchange energy is a combination of HF and PBE energies similar to that of the PBE0 functional, but the long-range part and the correlation energy are from PBE results. If the parameter  $w$  is set to zero, the short-range part diminishes and the HSE06 functional reduces to the PBE0 functional. The HSE06 functional predicts band gaps more accurately than the global PBE0 functional but uses significantly less computational resources [173].

## **BIBLIOGRAPHY**

## BIBLIOGRAPHY

- [1] John Suddard-Bangsund, Christopher J Traverse, Margaret Young, Tyler J Patrick, Yimu Zhao, and Richard R Lunt. Organic salts as a route to energy level control in low bandgap, high open-circuit voltage organic and transparent solar cells that approach the excitonic voltage limit. *Advanced Energy Materials*, 6(1), 2016.
- [2] Nevena Marinova, Silvia Valero, and Juan Luis Delgado. Organic and perovskite solar cells: Working principles, materials and interfaces. *Journal of Colloid and Interface Science*, 488:373–389, 2017.
- [3] Yunfei Zhou, Michael Eck, and Michael Krüger. Bulk-heterojunction hybrid solar cells based on colloidal nanocrystals and conjugated polymers. *Energy & Environmental Science*, 3(12):1851–1864, 2010.
- [4] Noel C Giebink, Gary P Wiederrecht, Michael R Wasielewski, and Stephen R Forrest. Ideal diode equation for organic heterojunctions. i. derivation and application. *Physical Review B*, 82(15):155305, 2010.
- [5] Jonathan D Servaites, Mark A Ratner, and Tobin J Marks. Organic solar cells: a new look at traditional models. *Energy & Environmental Science*, 4(11):4410–4422, 2011.
- [6] M Kröger, S Hamwi, J Meyer, T Riedl, W Kowalsky, and A Kahn. Role of the deep-lying electronic states of mno<sub>3</sub> in the enhancement of hole-injection in organic thin films. *Applied physics letters*, 95(12):251, 2009.
- [7] Wahyu Setyawan and Stefano Curtarolo. High-throughput electronic band structure calculations: Challenges and tools. *Computational Materials Science*, 49(2):299–312, 2010.
- [8] David JC MacKay. Sustainable energy—without the hot air. *UIT Cambridge, England*, 2009.
- [9] International Energy Agency. Key world energy statistics, 2016.
- [10] Shahriar Shafiee and Erkan Topal. When will fossil fuel reserves be diminished? *Energy policy*, 37(1):181–189, 2009.
- [11] M King Hubbert and David G Willis. Mechanics of hydraulic fracturing. 1972.
- [12] Volker Krey, Josep G Canadell, Nebojsa Nakicenovic, Yuichi Abe, Harald Andruleit, David Archer, Arnulf Grubler, Neil TM Hamilton, Arthur Johnson, Veselin Kostov, et al. Gas hydrates: entrance to a methane age or climate threat? *Environmental Research Letters*, 4(3):034007, 2009.
- [13] Peter M Vitousek. Beyond global warming: ecology and global change. *Ecology*, 75(7):1861–1876, 1994.

- [14] The National Aeronautics and Space Administration. Global temperature, 2016.
- [15] Stephen H Schneider. The greenhouse effect: Science and policy. *Science*, 243(4892):771–781, 1989.
- [16] Jeff Tsao, Nate Lewis, and George Crabtree. Solar faqs.
- [17] Jenny Nelson. *The physics of solar cells*, volume 1. World Scientific, 2003.
- [18] Charles R Coble, Elaine G Murray, and Dale R Rice. *Prentice-Hall earth science*. Prentice-Hall, 1986.
- [19] Salvador Izquierdo, Marcos Rodrigues, and Norberto Fueyo. A method for estimating the geographical distribution of the available roof surface area for large-scale photovoltaic energy-potential evaluations. *Solar Energy*, 82(10):929–939, 2008.
- [20] Marius Paulescu, Eugenia Paulescu, Paul Gravila, and Viorel Badescu. *Solar Radiation Measurements*, pages 17–42. Springer London, London, 2013.
- [21] Francisco G Montoya, Maria J Aguilera, and Francisco Manzano-Agugliaro. Renewable energy production in spain: A review. *Renewable and Sustainable Energy Reviews*, 33:509–531, 2014.
- [22] Martin A Green, Keith Emery, Yoshihiro Hishikawa, Wilhelm Warta, and Ewan D Dunlop. Solar cell efficiency tables (version 45). *Progress in photovoltaics: research and applications*, 23(1):1–9, 2015.
- [23] Martin A Green. Crystalline and thin-film silicon solar cells: state of the art and future potential. *Solar energy*, 74(3):181–192, 2003.
- [24] Junfeng Yan and Brian R Saunders. Third-generation solar cells: a review and comparison of polymer: fullerene, hybrid polymer and perovskite solar cells. *RSC Advances*, 4(82):43286–43314, 2014.
- [25] Maria-Eleni Ragoussi and Tomás Torres. New generation solar cells: concepts, trends and perspectives. *Chemical Communications*, 51(19):3957–3972, 2015.
- [26] Paul Breeze. Chapter 9 - types of solar cells. In Paul Breeze, editor, *Solar Power Generation*, pages 57 – 70. Academic Press, 2016.
- [27] Florian Machui, Markus Hösel, Ning Li, George D Spyropoulos, Tayebeh Ameri, Roar R Søndergaard, Mikkel Jørgensen, Arnulf Scheel, Detlef Gaiser, Kilian Kreul, et al. Cost analysis of roll-to-roll fabricated ito free single and tandem organic solar modules based on data from manufacture. *Energy & Environmental Science*, 7(9):2792–2802, 2014.
- [28] Askari Mohammad Bagher. Comparison of organic solar cells and inorganic solar cells. *Int J Renew Sustain Energy*, 3:53–58, 2014.

- [29] C Del Canizo, G Del Coso, and WC Sinke. Crystalline silicon solar module technology: Towards the 1€ per watt-peak goal. *Progress in photovoltaics: research and applications*, 17(3):199–209, 2009.
- [30] Frederik C Krebs, Nieves Espinosa, Markus Hösel, Roar R Søndergaard, and Mikkel Jørgensen. 25th anniversary article: rise to power–opv-based solar parks. *Advanced Materials*, 26(1):29–39, 2014.
- [31] William Shockley. The theory of p-n junctions in semiconductors and p-n junction transistors. *Bell Syst. Tech. J.*, 28(3):435–489, 1949.
- [32] André Moliton and Jean-Michel Nunzi. How to model the behaviour of organic photovoltaic cells. *Polymer International*, 55(6):583–600, 2006.
- [33] D Chirvase, Z Chiguvare, M Knipper, J Parisi, V Dyakonov, and JC Hummelen. Temperature dependent characteristics of poly (3 hexylthiophene)-fullerene based heterojunction organic solar cells. *Journal of Applied Physics*, 93(6):3376–3383, 2003.
- [34] Koen Vandewal, Kristofer Tvingstedt, Abay Gadisa, Olle Inganäs, and Jean V Manca. On the origin of the open-circuit voltage of polymer–fullerene solar cells. *Nature materials*, 8(11):904–909, 2009.
- [35] Jonathan D Servaites, Sina Yeganeh, Tobin J Marks, and Mark A Ratner. Efficiency enhancement in organic photovoltaic cells: consequences of optimizing series resistance. *Advanced Functional Materials*, 20(1):97–104, 2010.
- [36] V Dyakonov. Mechanisms controlling the efficiency of polymer solar cells. *Applied Physics A*, 79(1):21–25, 2004.
- [37] William J Potscavage Jr, S Yoo, and Bernard Kippelen. Origin of the open-circuit voltage in multilayer heterojunction organic solar cells. *Applied physics letters*, 93(19):193308, 2008.
- [38] Jiangeng Xue, Soichi Uchida, Barry P Rand, and Stephen R Forrest. 4.2% efficient organic photovoltaic cells with low series resistances. *Applied Physics Letters*, 84:3013, 2004.
- [39] Liyuan Han, Naoki Koide, Yasuo Chiba, and Takehito Mitake. Modeling of an equivalent circuit for dye-sensitized solar cells. *Applied Physics Letters*, 84(13):2433–2435, 2004.
- [40] Gert-Jan AH Wetzelaer, Max Scheepers, Araceli Miquel Sempere, Cristina Momblona, Jorge Ávila, and Henk J Bolink. Trap-assisted non-radiative recombination in organic–inorganic perovskite solar cells. *Advanced Materials*, 27(11):1837–1841, 2015.
- [41] Jeong-Hyeok Im, In-Hyuk Jang, Norman Pellet, Michael Grätzel, and Nam-Gyu Park. Growth of ch<sub>3</sub>nh<sub>3</sub>pbi<sub>3</sub> cuboids with controlled size for high-efficiency perovskite solar cells. *Nature nanotechnology*, 9(11):927–932, 2014.

- [42] Brian A Gregg and Mark C Hanna. Comparing organic to inorganic photovoltaic cells: Theory, experiment, and simulation. *Journal of Applied Physics*, 93(6):3605–3614, 2003.
- [43] Anders Hagfeldt, Gerrit Boschloo, Licheng Sun, Lars Kloo, and Henrik Pettersson. Dye-sensitized solar cells. *Chemical reviews*, 110(11):6595–6663, 2010.
- [44] Uli Würfel, Dieter Neher, Annika Spies, and Steve Albrecht. Impact of charge transport on current-voltage characteristics and power-conversion efficiency of organic solar cells. *Nature communications*, 6, 2015.
- [45] Jae-Wook Kang, Sung-Pil Lee, Do-Geun Kim, Sunghun Lee, Gun-Hwan Lee, Jong-Kuk Kim, Sun-Young Park, Joo Hyun Kim, Han-Ki Kim, and Yong-Soo Jeong. Reduction of series resistance in organic photovoltaic using low sheet resistance of ito electrode. *Electrochemical and Solid-State Letters*, 12(3):H64–H66, 2009.
- [46] Yang Shen, Kejia Li, Nabanita Majumdar, Joe C Campbell, and Mool C Gupta. Bulk and contact resistance in p3ht: Pcbm heterojunction solar cells. *Solar Energy Materials and Solar Cells*, 95(8):2314–2317, 2011.
- [47] Akinobu Hayakawa, Osamu Yoshikawa, Takuya Fujieda, Kaku Uehara, and Susumu Yoshikawa. High performance polythiophene/fullerene bulk-heterojunction solar cell with a tiox hole blocking layer. *Applied Physics Letters*, 90(16):163517–163900, 2007.
- [48] Chih-Tang Sah, Robert Noyce, and William Shockley. Carrier generation and recombination in pn junctions and pn junction characteristics. *Proceedings of the IRE*, 45(9):1228–1243, 1957.
- [49] We Shockley and WT Read Jr. Statistics of the recombinations of holes and electrons. *Physical review*, 87(5):835, 1952.
- [50] Re N Hall. Electron-hole recombination in germanium. *Physical Review*, 87(2):387, 1952.
- [51] Thomas Kirchartz, Bart E Pieters, James Kirkpatrick, Uwe Rau, and Jenny Nelson. Recombination via tail states in polythiophene: fullerene solar cells. *Physical Review B*, 83(11):115209, 2011.
- [52] A Foertig, J Rauh, V Dyakonov, and C Deibel. Shockley equation parameters of p3ht: Pcbm solar cells determined by transient techniques. *Physical Review B*, 86(11):115302, 2012.
- [53] Ching W Tang. Two-layer organic photovoltaic cell. *Applied Physics Letters*, 48(2):183–185, 1986.
- [54] MS White, DC Olson, SE Shaheen, N Kopidakis, and David S Ginley. Inverted bulk-heterojunction organic photovoltaic device using a solution-derived zno underlayer. *Applied Physics Letters*, 89(14):143517, 2006.

- [55] Martin Brinkmann and J-C Wittmann. Orientation of regioregular poly (3-hexylthiophene) by directional solidification: A simple method to reveal the semicrystalline structure of a conjugated polymer. *Advanced Materials*, 18(7):860–863, 2006.
- [56] NS Sariciftci, L Smilowitz, Alan J Heeger, F Wudl, et al. Photoinduced electron transfer from a conducting polymer to buckminsterfullerene. *Science*, 258(5087):1474–1476, 1992.
- [57] Gang Yu, Jun Gao, Jan C Hummelen, Fred Wudl, and Alan J Heeger. Polymer photovoltaic cells: Enhanced efficiencies via a network of internal donor-acceptor heterojunctions. *Science*, 270(5243):1789, 1995.
- [58] JJM Halls, CA Walsh, NC Greenham, EA Marseglia, RH Friend, SC Moratti, and AB Holmes. Efficient photodiodes from interpenetrating polymer networks. 1995.
- [59] Alexander L Ayzner, Christopher J Tassone, Sarah H Tolbert, and Benjamin J Schwartz. Reappraising the need for bulk heterojunctions in polymer- fullerene photovoltaics: the role of carrier transport in all-solution-processed p3ht/pcbm bilayer solar cells. *The Journal of Physical Chemistry C*, 113(46):20050–20060, 2009.
- [60] Kwan H Lee, Paul E Schwenn, Arthur RG Smith, Hamish Cavaye, Paul E Shaw, Michael James, Karsten B Krueger, Ian R Gentle, Paul Meredith, and Paul L Burn. Morphology of all-solution-processed “bilayer” organic solar cells. *Advanced Materials*, 23(6):766–770, 2011.
- [61] Neil D Treat, Michael A Brady, Gordon Smith, Michael F Toney, Edward J Kramer, Craig J Hawker, and Michael L Chabinyc. Interdiffusion of pcmb and p3ht reveals miscibility in a photovoltaically active blend. *Advanced Energy Materials*, 1(1):82–89, 2011.
- [62] Shuangyong Sun, Teddy Salim, Nripan Mathews, Martial Duchamp, Chris Boothroyd, Guichuan Xing, Tze Chien Sum, and Yeng Ming Lam. The origin of high efficiency in low-temperature solution-processable bilayer organometal halide hybrid solar cells. *Energy & Environmental Science*, 7(1):399–407, 2014.
- [63] Qi Wang, Yuchuan Shao, Qingfeng Dong, Zhengguo Xiao, Yongbo Yuan, and Jin-song Huang. Large fill-factor bilayer iodine perovskite solar cells fabricated by a low-temperature solution-process. *Energy & Environmental Science*, 7(7):2359–2365, 2014.
- [64] Mingzhen Liu, Michael B Johnston, and Henry J Snaith. Efficient planar heterojunction perovskite solar cells by vapour deposition. *Nature*, 501(7467):395–398, 2013.
- [65] Sibel Y Leblebici, Teresa L Chen, Paul Olalde-Velasco, Wanli Yang, and Biwu Ma. Reducing exciton binding energy by increasing thin film permittivity: an effective approach to enhance exciton separation efficiency in organic solar cells. *ACS applied materials & interfaces*, 5(20):10105–10110, 2013.
- [66] Slawomir Braun, William R Salaneck, and Mats Fahlman. Energy-level alignment at organic/metal and organic/organic interfaces. *Advanced Materials*, 21(14-15):1450–1472, 2009.

- [67] Carsten Deibel, Thomas Strobel, and Vladimir Dyakonov. Role of the charge transfer state in organic donor–acceptor solar cells. *Advanced materials*, 22(37):4097–4111, 2010.
- [68] Askat E Jailaubekov, Adam P Willard, John R Tritsch, Wai-Lun Chan, Na Sai, Raluca Gearba, Loren G Kaake, Kenrick J Williams, Kevin Leung, Peter J Rossky, et al. Hot charge-transfer excitons set the time limit for charge separation at donor/acceptor interfaces in organic photovoltaics. *Nature materials*, 12(1):66–73, 2013.
- [69] JA Barker, CM Ramsdale, and NC Greenham. Modeling the current-voltage characteristics of bilayer polymer photovoltaic devices. *Physical Review B*, 67(7):075205, 2003.
- [70] LJA Koster, ECP Smits, VD Mihailescu, and PWM Blom. Device model for the operation of polymer/fullerene bulk heterojunction solar cells. *Physical Review B*, 72(8):085205, 2005.
- [71] Gavin A Buxton and Nigel Clarke. Computer simulation of polymer solar cells. *Modelling and simulation in Materials Science and Engineering*, 15(2):13, 2006.
- [72] Gavin A Buxton and Nigel Clarke. Predicting structure and property relations in polymeric photovoltaic devices. *Physical Review B*, 74(8):085207, 2006.
- [73] Young Min Nam, June Huh, and Won Ho Jo. Optimization of thickness and morphology of active layer for high performance of bulk-heterojunction organic solar cells. *Solar Energy Materials and Solar Cells*, 94(6):1118–1124, 2010.
- [74] Benjamin Y Finck and Benjamin J Schwartz. Understanding the origin of the s-curve in conjugated polymer/fullerene photovoltaics from drift-diffusion simulations. *Applied Physics Letters*, 103(5):053306, 2013.
- [75] Girish Lakhwani, Akshay Rao, and Richard H Friend. Bimolecular recombination in organic photovoltaics. *Annual review of physical chemistry*, 65:557–581, 2014.
- [76] C Groves and NC Greenham. Bimolecular recombination in polymer electronic devices. *Physical Review B*, 78(15):155205, 2008.
- [77] M Kuik, LJA Koster, GAH Wetzelaer, and PWM Blom. Trap-assisted recombination in disordered organic semiconductors. *Physical review letters*, 107(25):256805, 2011.
- [78] William Shockley and Hans J Queisser. Detailed balance limit of efficiency of p-n junction solar cells. *Journal of applied physics*, 32(3):510–519, 1961.
- [79] Anssi Hovinen. Fitting of the solar cell iv-curve to the two diode model. *Physica Scripta*, 1994(T54):175, 1994.
- [80] Kashif Ishaque, Zainal Salam, and Hamed Taheri. Simple, fast and accurate two-diode model for photovoltaic modules. *Solar Energy Materials and Solar Cells*, 95(2):586–594, 2011.

- [81] WY Liang. Excitons. *Physics Education*, 5(4):226, 1970.
- [82] Noel C Giebink, Brian E Lassiter, Gary P Wiederrecht, Michael R Wasielewski, and Stephen R Forrest. Ideal diode equation for organic heterojunctions. ii. the role of polaron pair recombination. *Physical Review B*, 82(15):155306, 2010.
- [83] Charles L Braun. Electric field assisted dissociation of charge transfer states as a mechanism of photocarrier production. *The Journal of chemical physics*, 80(9):4157–4161, 1984.
- [84] James C Blakesley and Dieter Neher. Relationship between energetic disorder and open-circuit voltage in bulk heterojunction organic solar cells. *Physical Review B*, 84(7):075210, 2011.
- [85] VD Mihailetti, LJA Koster, JC Hummelen, and PWM Blom. Photocurrent generation in polymer-fullerene bulk heterojunctions. *Physical review letters*, 93(21):216601, 2004.
- [86] Peter Mark and Wolfgang Helfrich. Space-charge-limited currents in organic crystals. *Journal of Applied Physics*, 33(1):205–215, 1962.
- [87] Steven A Hawks, Gang Li, Yang Yang, and Robert A Street. Band tail recombination in polymer: fullerene organic solar cells. *Journal of Applied Physics*, 116(7):074503, 2014.
- [88] Lior Tzabari and Nir Tessler. Shockley–read–hall recombination in p3ht: Pcbm solar cells as observed under ultralow light intensities. *Journal of Applied Physics*, 109(6):064501, 2011.
- [89] Sarah R Cowan, Wei Lin Leong, Natalie Banerji, Gilles Dennler, and Alan J Heeger. Identifying a threshold impurity level for organic solar cells: Enhanced first-order recombination via well-defined pc84bm traps in organic bulk heterojunction solar cells. *Advanced Functional Materials*, 21(16):3083–3092, 2011.
- [90] HT Nicolai, MM Mandoc, and PWM Blom. Electron traps in semiconducting polymers: exponential versus gaussian trap distribution. *Physical Review B*, 83(19):195204, 2011.
- [91] Nir Tessler, Yevgeni Preezant, Noam Rappaport, and Yohai Roichman. Charge transport in disordered organic materials and its relevance to thin-film devices: A tutorial review. *Advanced Materials*, 21(27):2741–2761, 2009.
- [92] Peter Stallinga. *Two-Terminal Devices: DC Current*, pages 45–64. John Wiley & Sons, Ltd, 2009.
- [93] LF Hernández-García, O Ramírez-Sánchez, V Cabrera-Arenas, and LM Reséndiz-Mendoza. A gaussian model for recombination via carrier-trap distributions in organic solar cells. *Journal of Computational Electronics*, pages 1–7, 2016.

- [94] Lars Onsager. Deviations from ohm's law in weak electrolytes. *The Journal of Chemical Physics*, 2(9):599–615, 1934.
- [95] HK Gummel. A self-consistent iterative scheme for one-dimensional steady state transistor calculations. *Electron Devices, IEEE Transactions on*, 11(10):455–465, 1964.
- [96] Riaz A Usmani. Inversion of a tridiagonal jacobi matrix. *Linear Algebra and its Applications*, 212:413–414, 1994.
- [97] DL Scharfetter and H\_K Gummel. Large-signal analysis of a silicon read diode oscillator. *Electron Devices, IEEE Transactions on*, 16(1):64–77, 1969.
- [98] Simon J Martin, Geraldine LB Verschoor, Matthew A Webster, and Alison B Walker. The internal electric field distribution in bilayer organic light emitting diodes. *Organic electronics*, 3(3):129–141, 2002.
- [99] E Tutiš, Detlef Berner, and Libero Zuppiroli. Internal electric field and charge distribution in multilayer organic light-emitting diodes. *Journal of applied physics*, 93(8):4594–4602, 2003.
- [100] JC Wang, XC Ren, SQ Shi, CW Leung, and Paddy KL Chan. Charge accumulation induced s-shape j–v curves in bilayer heterojunction organic solar cells. *Organic electronics*, 12(6):880–885, 2011.
- [101] Alexander Wagenpfahl, Daniel Rauh, Moritz Binder, Carsten Deibel, and Vladimir Dyakonov. S-shaped current-voltage characteristics of organic solar devices. *Physical Review B*, 82(11):115306, 2010.
- [102] Hin-Lap Yip, Steven K Hau, and Alex K-Y Jen. Interface engineering of stable, efficient polymer solar cells. *Solar & Alternative Energy*, 2009.
- [103] Ralf Mauer, Marcel Kastler, and Frédéric Laquai. The impact of polymer regioregularity on charge transport and efficiency of p3ht: Pcbm photovoltaic devices. *Advanced Functional Materials*, 20(13):2085–2092, 2010.
- [104] Valentin D Mihailetti, Jeroen KJ van Duren, Paul WM Blom, Jan C Hummelen, René AJ Janssen, Jan M Kroon, Minze T Rispens, Wil Jan H Verhees, and Martijn M Wienk. Electron transport in a methanofullerene. *Advanced Functional Materials*, 13(1):43–46, 2003.
- [105] FJ Zhang, A Vollmer, J Zhang, Z Xu, JP Rabe, and N Koch. Energy level alignment and morphology of interfaces between molecular and polymeric organic semiconductors. *Organic Electronics*, 8(5):606–614, 2007.
- [106] Zheng Xu, Li-Min Chen, Mei-Hsin Chen, Gang Li, and Yang Yang. Energy level alignment of poly (3-hexylthiophene):(6, 6-phenyl c61 butyric acid methyl ester bulk heterojunction. *Appl. Phys. Lett.*, 95(1):13301, 2009.

- [107] Youngkyoo Kim, Amy M Ballantyne, Jenny Nelson, and Donal DC Bradley. Effects of thickness and thermal annealing of the pedot: Pss layer on the performance of polymer solar cells. *Organic Electronics*, 10(1):205–209, 2009.
- [108] Wanli Ma, Cuiying Yang, Xiong Gong, Kwanghee Lee, and Alan J Heeger. Thermally stable, efficient polymer solar cells with nanoscale control of the interpenetrating network morphology. *Advanced Functional Materials*, 15(10):1617–1622, 2005.
- [109] Morteza Eslamian and Joshua E Newton. Spray-on pedot: Pss and p3ht: Pcbm thin films for polymer solar cells. *Coatings*, 4(1):85–97, 2014.
- [110] Jian Wang, Liang Xu, Yun-Ju Lee, Manuel De Anda Villa, Anton V Malko, and Julia WP Hsu. Effects of contact-induced doping on the behaviors of organic photovoltaic devices. *Nano letters*, 15(11):7627–7632, 2015.
- [111] Yong Seok Eo, Hee Woo Rhee, Byung Doo Chin, and Jae-Woong Yu. Influence of metal cathode for organic photovoltaic device performance. *Synthetic Metals*, 159(17):1910–1913, 2009.
- [112] Sylvain Chambon, Yolande Murat, Guillaume Wantz, Lionel Hirsch, and Pascal Tardy. Lanthanum hexaboride as novel interlayer for improving the thermal stability of p3ht: Pcbm organic solar cells. *ACS applied materials & interfaces*, 7(45):25334–25340, 2015.
- [113] Jo-Lin Lan, Zhiqiang Liang, Yi-Hsun Yang, Fumio S Ohuchi, Samson A Jenekhe, and Guozhong Cao. The effect of srtio 3: Zno as cathodic buffer layer for inverted polymer solar cells. *Nano Energy*, 4:140–149, 2014.
- [114] Boyuan Qi and Jizheng Wang. Open-circuit voltage in organic solar cells. *Journal of Materials Chemistry*, 22(46):24315–24325, 2012.
- [115] H Ishii, N Hayashi, E Ito, Y Washizu, K Sugi, Y Kimura, M Niwano, Y Ouchi, and K Seki. Kelvin probe study of band bending at organic semiconductor/metal interfaces: examination of fermi level alignment. *Physica status solidi (a)*, 201(6):1075–1094, 2004.
- [116] C Van Berkel, MJ Powell, AR Franklin, and ID French. Quality factor in a-si: H nip and pin diodes. *Journal of applied physics*, 73(10):5264–5268, 1993.
- [117] Attila J Mozer and Niyazi Serdar Sariciftci. Negative electric field dependence of charge carrier drift mobility in conjugated, semiconducting polymers. *Chemical physics letters*, 389(4):438–442, 2004.
- [118] Yuan Li, Wenxiao Huang, Huihui Huang, Corey Hewitt, Yonghua Chen, Guojia Fang, and David L Carroll. Evaluation of methods to extract parameters from current–voltage characteristics of solar cells. *Solar Energy*, 90:51–57, 2013.
- [119] O Ya Olikh. Review and test of methods for determination of the schottky diode parameters. *Journal of Applied Physics*, 118(2):024502, 2015.

- [120] Anna C Veron, Hui Zhang, Anthony Linden, Frank Nuesch, Jakob Heier, Roland Hany, and Thomas Geiger. Nir-absorbing heptamethine dyes with tailor-made counterions for application in light to energy conversion. *Organic letters*, 16(4):1044–1047, 2014.
- [121] Tobias Stubhan, Tayebeh Ameri, Michael Salinas, Johannes Krantz, Florian Machui, Marcus Halik, and Christoph J Brabec. High shunt resistance in polymer solar cells comprising a  $\text{moo}_3$  hole extraction layer processed from nanoparticle suspension. *Applied Physics Letters*, 98(25):253308, 2011.
- [122] RA Street, M Schoendorf, A Roy, and JH Lee. Interface state recombination in organic solar cells. *Physical Review B*, 81(20):205307, 2010.
- [123] Xin Guo and TP Ma. Tunneling leakage current in oxynitride: dependence on oxygen/nitrogen content. *IEEE Electron Device Letters*, 19(6):207–209, 1998.
- [124] EJ Miller, ET Yu, P Waltereit, and JS Speck. Analysis of reverse-bias leakage current mechanisms in gan grown by molecular-beam epitaxy. *Applied Physics Letters*, 84(4):535–537, 2004.
- [125] GAM Hurkx, DBM Klaassen, MPG Knuvers, and FG O’Hara. A new recombination model describing heavy-doping effects and low-temperature behaviour. In *Electron Devices Meeting, 1989. IEDM’89. Technical Digest., International*, pages 307–310. IEEE, 1989.
- [126] GAM Hurkx, DBM Klaassen, and MPG Knuvers. A new recombination model for device simulation including tunneling. *IEEE Transactions on Electron Devices*, 39(2):331–338, 1992.
- [127] Marco Mandurrino, Michele Goano, Marco Vallone, Francesco Bertazzi, Giovanni Ghione, Giovanni Verzellesi, Matteo Meneghini, Gaudenzio Meneghesso, and Enrico Zanoni. Semiclassical simulation of trap-assisted tunneling in gan-based light-emitting diodes. *Journal of Computational Electronics*, 14(2):444–455, 2015.
- [128] Marco Mandurrino, Giovanni Verzellesi, Michele Goano, Marco Vallone, Francesco Bertazzi, Giovanni Ghione, Matteo Meneghini, Gaudenzio Meneghesso, and Enrico Zanoni. Physics-based modeling and experimental implications of trap-assisted tunneling in ingan/gan light-emitting diodes. *physica status solidi (a)*, 212(5):947–953, 2015.
- [129] Konrad Sakowski, Leszek Marcinkowski, Stanislaw Krukowski, Szymon Grzanka, and Elzbieta Litwin-Staszewska. Simulation of trap-assisted tunneling effect on characteristics of gallium nitride diodes. *Journal of Applied Physics*, 111(12):123115, 2012.
- [130] Chanho Yoo and Tae Whan Kim. Tunneling processes and leakage current mechanisms of thin organic layer sandwiched between two electrodes. *Current Applied Physics*, 16(2):170–174, 2016.
- [131] Chi-Feng Lin, Mi Zhang, Shun-Wei Liu, Tien-Lung Chiu, and Jiun-Haw Lee. High photoelectric conversion efficiency of metal phthalocyanine/fullerene heterojunction photovoltaic device. *International journal of molecular sciences*, 12(1):476–505, 2011.

- [132] Jeihyun Lee, Soohyung Park, Younwoo Lee, Hyein Kim, Dongguen Shin, Junkyeong Jeong, Kwangho Jeong, Sang Wan Cho, Hyunbok Lee, and Yeonjin Yi. Electron transport mechanism of bathocuproine exciton blocking layer in organic photovoltaics. *Physical Chemistry Chemical Physics*, 18(7):5444–5452, 2016.
- [133] S Fares. Influence of gamma-ray irradiation on optical and thermal degradation of poly (ethyl-methacrylate)(pema) polymer. *Natural Science*, 4(07):499, 2012.
- [134] Rocco P Fornari, Juan Aragó, and Alessandro Troisi. A very general rate expression for charge hopping in semiconducting polymers. *The Journal of chemical physics*, 142(18):184105, 2015.
- [135] WF Pasveer, Jeroen Cottaar, C Tanase, Reinder Coehoorn, PA Bobbert, PWM Blom, DM De Leeuw, and MAJ Michels. Unified description of charge-carrier mobilities in disordered semiconducting polymers. *Physical review letters*, 94(20):206601, 2005.
- [136] Jose M Montero and Juan Bisquert. Trap origin of field-dependent mobility of the carrier transport in organic layers. *Solid-State Electronics*, 55(1):1–4, 2011.
- [137] Christopher M Proctor and Thuc-Quyen Nguyen. Effect of leakage current and shunt resistance on the light intensity dependence of organic solar cells. *Applied Physics Letters*, 106(8):23\_1, 2015.
- [138] Victor S Balderrama, Josep Albero, Pedro Granero, Josep Ferré-Borrull, Josep Pallarés, Emilio Palomares, and Lluis F Marsal. Design, fabrication and charge recombination analysis of an interdigitated heterojunction nanomorphology in p3ht/pc 70 bm solar cells. *Nanoscale*, 7(33):13848–13859, 2015.
- [139] Claudia N Hoth, Stelios A Choulis, Pavel Schilinsky, and Christoph J Brabec. On the effect of poly (3-hexylthiophene) regioregularity on inkjet printed organic solar cells. *Journal of Materials Chemistry*, 19(30):5398–5404, 2009.
- [140] Sayantan Das and TL Alford. Improved efficiency of p3ht: Pcbm solar cells by incorporation of silver oxide interfacial layer. *Journal of Applied Physics*, 116(4):044905, 2014.
- [141] Akihiro Kojima, Kenjiro Teshima, Yasuo Shirai, and Tsutomu Miyasaka. Organometal halide perovskites as visible-light sensitizers for photovoltaic cells. *Journal of the American Chemical Society*, 131(17):6050–6051, 2009.
- [142] Masahiro Mori and Haruo Saito. An x-ray study of successive phase transitions in csnbr3. *Journal of Physics C: Solid State Physics*, 19(14):2391, 1986.
- [143] Stephen J Clark, Colin D Flint, and John D Donaldson. Luminescence and electrical conductivity of csnbr3, and related phases. *Journal of Physics and Chemistry of Solids*, 42(3):133–135, 1981.
- [144] J Barrett, SRA Bird, JD Donaldson, and J Silver. The mössbauer effect in tin (ii) compounds. part xi. the spectra of cubic trihalogenostannates (ii). *Journal of the Chemical Society A: Inorganic, Physical, Theoretical*, pages 3105–3108, 1971.

- [145] I Abrahams, DZ Demetriou, RT Kroemer, H Taylor, and M Motavalli. Evidence for cluster orbital formation in  $\text{cssn}$   $2 \times 5$  compounds ( $x = \text{cl}, \text{br}$ ). *Journal of Solid State Chemistry*, 160(2):382–387, 2001.
- [146] Aron Walsh. Principles of chemical bonding and band gap engineering in hybrid organic-inorganic halide perovskites. *The Journal of Physical Chemistry C*, 119(11):5755–5760, 2015.
- [147] Michael Grätzel. The light and shade of perovskite solar cells. *Nature materials*, 13(9):838–842, 2014.
- [148] Nam-Gyu Park. Perovskite solar cells: an emerging photovoltaic technology. *Materials Today*, 18(2):65–72, 2015.
- [149] RD t Shannon. Revised effective ionic radii and systematic studies of interatomic distances in halides and chalcogenides. *Acta Crystallographica Section A: Crystal Physics, Diffraction, Theoretical and General Crystallography*, 32(5):751–767, 1976.
- [150] Chonghea Li, Xionggang Lu, Weizhong Ding, Liming Feng, Yonghui Gao, and Ziming Guo. Formability of  $\text{abx}_3$  ( $x = \text{f}, \text{cl}, \text{br}, \text{i}$ ) halide perovskites. *Acta Crystallographica Section B: Structural Science*, 64(6):702–707, 2008.
- [151] John P Perdew, Kieron Burke, and Matthias Ernzerhof. Generalized gradient approximation made simple. *Physical review letters*, 77(18):3865, 1996.
- [152] Jochen Heyd, Gustavo E Scuseria, and Matthias Ernzerhof. Hybrid functionals based on a screened coulomb potential. *The Journal of Chemical Physics*, 118(18):8207–8215, 2003.
- [153] Peter E Blöchl. Projector augmented-wave method. *Physical Review B*, 50(24):17953, 1994.
- [154] Georg Kresse and D Joubert. From ultrasoft pseudopotentials to the projector augmented-wave method. *Physical Review B*, 59(3):1758, 1999.
- [155] M Shishkin and G Kresse. Self-consistent g w calculations for semiconductors and insulators. *Physical Review B*, 75(23):235102, 2007.
- [156] Ling-yi Huang and Walter RL Lambrecht. Electronic band structure, phonons, and exciton binding energies of halide perovskites  $\text{cssncl}_3$ ,  $\text{cssnbr}_3$ , and  $\text{cssni}_3$ . *Physical Review B*, 88(16):165203, 2013.
- [157] RR Pela, M Marques, and LK Teles. Comparing lda-1/2, hse03, hse06 and g 0 w 0 approaches for band gap calculations of alloys. *Journal of Physics: Condensed Matter*, 27(50):505502, 2015.
- [158] Jochen Heyd, Juan E Peralta, Gustavo E Scuseria, and Richard L Martin. Energy band gaps and lattice parameters evaluated with the heyd-scuseria-ernzerhof screened hybrid functional. *The Journal of chemical physics*, 123(17):174101, 2005.

- [159] Jong-Won Song, Giacomo Giorgi, Koichi Yamashita, and Kimihiko Hirao. Communication: singularity-free hybrid functional with a gaussian-attenuating exact exchange in a plane-wave basis. *The Journal of chemical physics*, 138(24):241101, 2013.
- [160] DM Roessler and WC Walker. Electronic spectra of crystalline nacl and kcl. *Physical Review*, 166(3):599, 1968.
- [161] John E Ayers, Tedi Kujofsa, Paul Rago, and Johanna Raphael. *Heteroepitaxy of semiconductors: theory, growth, and characterization*. CRC press, 2016.
- [162] C Merckling, M El-Kazzi, G Delhaye, V Favre-Nicolin, Y Robach, M Gendry, G Grenet, G Saint-Girons, and G Hollinger. Strain relaxation and critical thickness for epitaxial laalo 3 thin films grown on srtio 3 (001) substrates by molecular beam epitaxy. *Journal of crystal growth*, 306(1):47–51, 2007.
- [163] David Sholl and Janice A Steckel. *Density functional theory: a practical introduction*. John Wiley & Sons, 2011.
- [164] Attila Szabo and Neil S Ostlund. *Modern quantum chemistry: introduction to advanced electronic structure theory*. Courier Corporation, 1989.
- [165] Walter Kohn. Nobel lecture: Electronic structure of matter—wave functions and density functionals. *Reviews of Modern Physics*, 71(5):1253, 1999.
- [166] Robert O Jones and Olle Gunnarsson. The density functional formalism, its applications and prospects. *Reviews of Modern Physics*, 61(3):689, 1989.
- [167] Paul Geerlings, F De Proft, and W Langenaeker. Conceptual density functional theory. *Chemical reviews*, 103(5):1793–1874, 2003.
- [168] Pierre Hohenberg and Walter Kohn. Inhomogeneous electron gas. *Physical review*, 136(3B):B864, 1964.
- [169] Walter Kohn and Lu Jieu Sham. Self-consistent equations including exchange and correlation effects. *Physical review*, 140(4A):A1133, 1965.
- [170] Mike C Payne, Michael P Teter, Douglas C Allan, TA Arias, and JD Joannopoulos. Iterative minimization techniques for ab initio total-energy calculations: molecular dynamics and conjugate gradients. *Reviews of Modern Physics*, 64(4):1045, 1992.
- [171] Jochen Heyd, Gustavo E Scuseria, and Matthias Ernzerhof. Erratum:“hybrid functionals based on a screened coulomb potential”[j. chem. phys. 118, 8207 (2003)]. *The Journal of Chemical Physics*, 124(21):219906, 2006.
- [172] John P Perdew, Matthias Ernzerhof, and Kieron Burke. Rationale for mixing exact exchange with density functional approximations. *The Journal of Chemical Physics*, 105(22):9982–9985, 1996.
- [173] Alejandro J Garza and Gustavo E Scuseria. Predicting band gaps with hybrid density functionals. *arXiv preprint arXiv:1608.04796*, 2016.